Measurement and control of electronic coherences

Clément Cabart

Numéro National de Thèse : 2018LYSEN031

Thèse de doctorat de l'université de Lyon
opérée par
l'École Normale Supérieure de Lyon

École Doctorale N° 52
Physique & Astrophysique de Lyon

Spécialité de doctorat : Physique

Soutenue publiquement le 18/09/2018, par :
Clément CABART

Measurement and control of electronic coherences

Mesure et contrôle de cohérences électroniques

Devant le jury composé de :

Audrey COTTET, *CR CNRS, ENS*	Examinatrice
Benjamin HUARD, *Professeur, ENS de Lyon*	Président
Michael MOSKALETS, *Professeur, Kharkiv Polytechnic Institute*	Examinateur
Patrice ROCHE, *DR CEA, CEA Saclay*	Rapporteur
Maura SASSETTI, *Professeure, Genoa University*	Rapporteure
Pascal DEGIOVANNI, *DR CNRS, ENS de Lyon*	Directeur de thèse

Remerciements

Il s'est écoulé plusieurs semaines depuis ma soutenance, mais je n'ai toujours pas eu le temps d'écrire ces quelques lignes qui ouvriront ma thèse, celles qui seront sûrement les plus lues au fur et à mesure des années quand quelqu'un tombera sur ce manuscrit, chez moi ou ailleurs. J'espère qu'elles rendront justice à ce qu'a pu être l'expérience de ma thèse au cours de ces dernières années, ainsi qu'à l'ensemble des personnes qui ont permis que ce travail se déroule dans les meilleures conditions.

Je souhaite tout d'abord remercier l'ensemble des membres de mon jury pour leurs commentaires sur ce travail, et j'espère que cette version définitive répondra aux quelques attentes laissées en suspens en amont de la soutenance. Je remercie en particulier Maura Sassetti et Patrice Roche pour leur relecture attentive du manuscrit, malgré le temps limité dont ils ont disposé. Audrey Cottet, Michael Moskalets et Benjamin Huard m'ont également permis de réfléchir à de nouveaux aspects de mon travail par leurs nombreuses questions le jour J, et je les en remercie.

Au premier rang des personnes qui ont influencé mon travail, et en tant que dernier membre du jury, il me paraît essentiel de remercier Pascal pour ces nombreuses années de travail et de complicité. Pascal est tout d'abord un très bon physicien, capable de faire ressortir la physique d'équations bien peu engageantes ou de mener des calculs compliqués en un temps record (pour peu que quelqu'un vérifie les signes ou les changements de variables après coup). Il est également un encadrant laissant une grande liberté à ses doctorants, sans pour autant les abandonner en rase campagne. Son intérêt pour la physique en général, et non seulement le destin des électrons dans des fils quantiques, m'a permis de réfléchir à de nombreux problèmes qui ne figurent pas dans ce manuscrit sans être laissé à moi-même. Cependant, ce n'est pas uniquement pour ses capacités d'encadrant que j'ai tant apprécié ces dernières années, mais également pour ses capacités humaines, son amitié et sa joie de vivre. Sa bonne humeur très communicative et son envie de

discuter d'absolument tous les sujets possibles (oui oui, vraiment tous) a rendu cette thèse très enrichissante d'un point de vue personnel. Je ne pensais pas discuter d'une AI contrôlant le monde comme système politique optimal à 5h du matin dans un aéroport émirati, et pourtant...

Ce travail de thèse n'aurait également pas été le même sans les allers-retours régulier (à la fois de personnes et d'idées) entre Lyon et Paris. Ce sont ces échanges constants entre théorie et expérience qui ont donné forme à mon travail. Pour tous ces échanges, merci à l'ensemble des personnes avec qui j'ai eu l'occasion de travailler au Laboratoire Pierre Aigrain : Gwendal, Arthur et Vincent, pour m'avoir accueilli au sein du laboratoire pendant un an, faisant de moi l'un des rares théoriciens de l'ENS de Lyon ayant fait des micro-soudures ou des transferts d'Helium liquide ; Bernard et Jean-Marc pour les nombreux repas partagés et leurs bons conseils ; et plus récemment Rémi et Hugo pour tous les échanges que nous avons eus lors de nos visites à Paris et leur présence à ma soutenance.

En revenant à Lyon, le laboratoire de Physique a été pour moi l'environnement de travail le plus intéressant qui soit pour un physicien. Le large spectre thématique des gens qui y travaillent permet d'acquérir une vision de la physique extrêmement complète, et je pense que discuter dans le même repas de cristaux liquides ou de théorie des boucles n'arrive pas dans tant de laboratoires que cela. Le travail de Thierry à la tête du labo permet de maintenir ce mélange des thèmes au quotidien. Cependant, pour pouvoir discuter de nombreux sujets, il faut également des gens avec qui en parler, et c'est pourquoi je remercie ici toutes les personnes avec qui j'ai partagé un bureau durant ces diverses années. J'ai une pensée spécifique pour mes deux derniers co-bureaux, Grimaud et Valentin, avec qui nous avons vécu un dernier semestre marqué par une triple rédaction de thèse, avec les divers moments difficiles que cela implique. Je pense cependant que l'ambiance dans ce bureau "à l'étage qui n'existe pas" est restée optimale pendant tout ce temps, et je les remercie encore pour cela. Bien entendu, cette ambiance a également été maintenue par les personnes avec qui j'ai partagé l'essentiel de mes repas, et pour certains d'entre eux mes 7 années de présence à l'ENS : Félix, Guilhem, Alexandre et Benjamin.

Alexandre a été notamment un colocataire et un cuisinier hors-pair, le responsable d'un très grand nombre d'heures perdues devant des consoles ou des jeux en flash, et la liste des jeux devant lesquels je l'ai vu s'énerver pourrait remplir quelques pages supplémentaires. Citons seule-

ment ici le fameux World's Hardest Game, dont la musique continuera à me hanter bien trop longtemps. Il m'a également maintenu éveillé un très grand nombre de soirées autour de discussions animées ou de bières triples, les deux pouvant facilement aller ensemble.

Benjamin, quant à lui, a été à la fois une aide précieuse dans mon travail et dans ma vie personnelle, un inventeur très créatif (une partie de labo se souviendra longtemps de son robot se baladant dans les couloirs) et la personne qui m'a le plus charrié depuis mon arrivée à Lyon (mais je pense lui avoir bien rendu). Il a également été un partenaire de voyage hors-pair, partageant notamment l'envie de tester l'ensemble des restaurants les plus "locaux" possible lors de nos conférences asiatiques, parfois avec des résultats particulièrement improbables. Le bureau qu'il occupait avec Alexandre était de plus la meilleure salle de repos dont on puisse rêver, bien que cela ne soit sûrement pas l'avis de leurs voisins. Si l'ambiance avec Pascal a été aussi bonne, c'est sûrement également à cause d'eux deux, et je pense que certains ont été heureux d'apprendre que les Daltons s'en allaient pour récupérer un peu de tranquillité.

Ces dernières années ont également été occupées par bien plus de choses que l'étude des électrons uniques sous l'effet d'interactions. Toujours avec les mêmes compères, l'écriture du livre dit infernal de "Physique quantique, information et calcul" s'est révélée une expérience des plus sympathiques bien que très chronophage. Nul ne peut prédire quand (et même si) ce livre sortira un jour, mais il s'agit de toute manière d'une activité qui dépasse de loin le produit final. Pour les potentiels lecteurs de ce livre, sachez que j'ai fait tout mon possible pour vous éviter des migraines (ce qui en dit long sur la difficulté initiale du produit...).

Enfin, comment ne pas mentionner ce que certains appelaient "mon vrai travail" : ma position de trésorier au sein de l'ASUL Ultimate m'a occupé pendant plus de deux ans durant ma thèse, et c'est une expérience qui m'a apporté bien plus que je ne l'espérais. J'ai eu la chance de voir mon club grandir de 60 à plus de 100 licenciés, de lancer des disques avec un nombre incroyable de coéquipiers, et de jouer au plus haut niveau possible pour un joueur d'ultimate : championnat d'Europe des clubs, première division française... Un grand merci à tous les coachs qui m'ont permis de progresser et qui m'ont fait confiance, et en particulier à Ivan et Aurélien qui auront la lourde tâche de continuer le travail de ces dernières années pour la saison qui démarre. Je n'oublie pas non plus les nombreuses autres occasions que j'ai eu de faire de l'ultimate durant ma thèse, que ce soit en championnat universitaire avec l'ENS

ou lors de tournois plus amusants avec l'ensemble des PhDisc, une fine équipe de joueurs invétérés de jeux de société avec qui j'ai passé tant de week-ends. Merci aux vieux (Tim, Guilhem, Félix, Bertrand, Grimaud, pour ne citer que les Lyonnais) et aux plus jeunes qui prendront la relève (Quentin, Robin, Charles...). Si mes comptes sont bons, j'aurai joué dans plus de 40 week-ends d'ultimate durant ces 3 années, et c'est grâce à l'ensemble de ces personnes que je m'y suis amusé.

Dans un autre registre, merci à Léo, Julien, Matthieu et Guilhem pour les festivals réguliers et leur passion pour la musique qui a mené à tant de belles découvertes. Ils n'étaient pas toujours les week-ends les plus sobres, mais ils font partie de ceux qui laissent le plus de souvenirs.

Enfin, comment ne pas finir en remerciant ma famille pour le soutien qu'ils m'ont apporté toutes ces années. Je sais que le sujet exact de ma thèse restera pour longtemps un mystère, et je sais également que la distance Lyon-Caen est un peu trop grande à leur goût, mais je ne peux que les remercier de tous les efforts qu'ils ont fait. Enfin, merci infiniment à Sarah, pour sa relecture attentive de ce manuscrit et pour tout le reste... Ce n'est que le début !

Contents

Introduction

> Its beauty calls us, we can't go back. Our quest begins now, even if the ice should crack.
>
> The Great Old Ones
> *Antarctica*

The Nobel Prize in Physics 2012 was awarded jointly to Serge Haroche and David J. Wineland "for ground-breaking experimental methods that enable measuring and manipulation of individual quantum systems".

This small line on the Nobel prize website crowns what is, in my opinion, one of the most groundbreaking experimental achievement of the last 30 years: the demonstration that our degree of control on quantum systems is now sufficiently good to perform the thought experiments of the founding fathers of quantum mechanics in the laboratory. Schrödinger cats or entangled states are now routinely generated on demand for single quantum systems, as are the completely non-classical Fock states, containing a fixed number of photons, for electromagnetic fields in a cavity.

One particular point that strikes me in this quest for the control and manipulation of individual quantum systems are the measurements performed in these experiments. We are now able to analyze one of the most important issues in quantum mechanics: projective measurements. Even more, we are able to tune extensively the measurement process, going from standard projective measures to non-destructive ones, in which the state of the system is left pretty much unchanged, at the expense of the information we are able to recover on it. All this work proves the crucial role of entanglement between the system and external degrees of freedom. It gradually leads to the emergence of quantum states for the system that are relative to the state of the environment and somehow more robust than a generic quantum state of the system [185, 89, 124,

186]. This process, called decoherence, has now been monitored with great precision in several experiments, and is an important piece of the puzzle towards clarifying the link between our everyday experience of the classical world and the mysteries of the quantum world [187]. Pioneering experiments on decoherence [20] have sparked a great line of research aiming at understanding, and ultimately tame, this decoherence processes. In particular, decoherence is one of the main challenges that prevents us from everyday life use of quantum mechanics for communication and computation, two areas that have really taken off in recent years precisely due to the degree of control attained on quantum systems [77].

Among possible quantum information systems, quantum optics starts with a clear advantage: because of their nature, photons do not interact easily with each other, in general couple weakly to matter degrees of freedom, and can thus be well isolated from decoherence. This has led, for example, to the demonstration of entangled pairs of photons propagating over several hundreds of kilometers in optical fibers or in space [165, 131] while retaining their coherence. However, this advantage may also be a limitation of photon based quantum information processing: in order to use quantum systems for computation or communication, we need to be able to make them act on each other. This is where solid state physics comes into play.

Solid state devices can allow us to engineer the coupling between matter and electromagnetic degrees of freedom. Superconducting circuits are one of the mainstream alleys for building quantum computation systems [178] whereas quantum spintronics is viewed as a promising challenger that would combine the relative isolation of a single nuclear or electronic spin to the electric controlabillity of mesoscopic devices, as originally proposed in [92]. In this context, understanding and controlling quantum electrical currents down to the single electron level as well as their coupling to the electromagnetic field is a very important problem.

From this perspective, one specific class of system has appeared very promising at the end of the 20th century, owing to its clear analogy with standard quantum optics: bi-dimensional electron gases in the quantum Hall regime. It had long been envisioned that, in this system, electronic transport occurs within quasi one-dimensional chiral edge channels which could constitute an electronic analogue of optical fibers [22]. The demonstration of tunable beamsplitters for electrons [172, 173] has

been an important step in this direction and has lead to the first demonstrations of electronic Mach-Zehnder interferometers [88], demonstrating the coherence of electrons in quantum Hall edge channels over several micrometers [137]. At the same time, experimental techniques for measuring electrical current fluctuations drastically improved both in sensitivity and accessible frequency range [60, 122], thus opening the way to the exploration of electron dynamics on subnanosecond timescales. However, it was the advent of single electron sources a decade ago [44] that truly ignited the domain. This emerging field has since been dubbed "Electron Quantum Optics" and should be viewed as a subfield or, maybe more appropriately, as an evolution of quantum coherent nano-electronics [17]. Since then, several efforts have been made to close the gap between electron quantum optics and its photon counterpart, through the demonstration of several interferometry experiments reviewed in [111]. In the meantime, a lot of effort has been devoted to the development of new single electron sources [38, 4] as well as to the extension of electron quantum optics concepts beyond its original birthplace (quantum Hall edge channels) [43], thus contributing to the maturation and expansion of this rapidely developing field whose state of the art has been reviewed quite extensively in a recent volume of Physica Status Solidi [151].

If on the bright side the real advantage of photons over electrons is their reduced sensibility to decoherence, then on the dark side the main pitfall of electron quantum optics is the charged nature of the excitations. Electrons propagating in the edge channels of the quantum Hall effect will experience the effect of screened Coulomb interactions with every other electron present in the system, and in particular with all the electrons present within the conductor. Under the effect of interactions, electronic states will then lose their coherence over lengthscales which are of the order of the size of experimental setups, thus preventing their use as good quantum information carriers up to now, even though this had been a huge motivation [10, 86, 11, 184] for developing single electron sources and electron quantum optics setups.

This is where my work comes into play. Since the effect of interaction seems to prohibit the use of electron quantum optics systems for quantum information processing (at least naively), it was natural to shift our focus towards the study of these interactions themselves. A research program has thus been started aiming at predicting the effect of screened Coulomb interactions on electronic excitations [32] in experimentally relevant cases, while at the same time the experimental group

led by G. Fève in Laboratoire Pierre Aigrain worked on testing these ideas in the lab in order to confirm or infirm our scenarios. This collaboration has led to fruitful developments both in the experimental and theoretical sides, most of which are presented in this manuscript. In particular, we have developed a computation scheme predicting the effect of several interaction models on any single-electron wavepacket [OP2], which has since been confirmed by experiments [OP3]. Joint work between our two groups has also led to the demonstration of a quantum signal analyzer extracting the single electron wavefunctions present in a quantum electrical current [OP4].

Finally, building on these developments, we felt that it was time to tackle decoherence, motivating us for studying decoherence control protocols [OP1]. Our main motivation was that getting an in-depth understanding of single to few electron decoherence is now crucial both for our understanding of electronic quantum transport as well as for developing applications of electron quantum optics such as quantum information processing[1] and the quantum metrology of charge and electric currents.

From a personal point of view, the strong link between theory and experiment has been a great advantage of my doctoral research project, as I think that doing theoretical physics is meaningful only when results can at least shed some light on forthcoming experiments and, if possible, be tested by actually performed experiments. The fruitful collaboration between our group in Lyon and the experimental group of G. Fève has given me the opportunity to spend one year within the experimental group in Paris, prior to the start of my PhD, in order to familiarize myself with these experiments.

This one year stay has allowed me to understand better the challenges which await an experimentalist trying to study electron quantum optics, the difficulties to overcome, and finally which theoretical situations might be reasonably attainable and which are still relying on much more prospective experimental developments. This double vision on my scientific field has remained intact all along my PhD, and I hope that this manuscript will show it, explaining the scientific construction of a theoretical work heavily inspired by experiments, and how and why we were led to explore more prospective questions.

[1] As we shall see in this manuscript, a proper choice of material may restore some of the original hopes in the field.

Outline of the manuscript

Let me now describe the content of this thesis from a more down-to-earth point of view. This manuscript is divided into three chapters with clear focuses: the first one is devoted to a presentation of electron quantum optics and the associated tools. The second chapter presents the experimental setups and protocols that are studied in the laboratory. Finally, the third chapter is devoted to the effect of screened Coulomb interactions on electronic excitations. In both chapter 2 and chapter 3, we will present work that has been fully completed and published, as well as work in progress and more preliminary results that will lead to forthcoming publications.

Chapter 1 will present an overview of the tools and concepts at the core of the electron quantum optics framework, both from an experimental and a theoretical point of view. Its first section will be devoted to the experimental toolbox used on a daily basis in experimental groups such as the one at Laboratoire Pierre Aigrain. We will review in detail how bi-dimensional electron gases under strong magnetic fields can be used to engineer ballistic conduction channels, as well as the equivalent of a beamsplitter for electrons. Then, we will turn ourselves to the sources that are used in electron quantum optics experiments, with a specific emphasis on single-electron sources used at LPA.

After this overview, section 1.2 will be devoted to introducing the theoretical framework of electron quantum optics and, in particular, the main concept that will be used throughout this manuscript: the electronic coherence function. This quantity introduced by C. Grenier [66, 67] is the direct equivalent in electronics of Glauber's coherence function for photons [62]. We will spend quite some time showing this analogy and explaining how it relates to physically observable quantitites. On our way, we will introduce several representations of single electron coherence, among which a time-frequency representation called the electronic Wigner function [41]. In order to forge our intuition on the electronic Wigner function, a variety of examples will be discussed, including in particular the ones relevant for single-electron sources or sinusoidal drives.

Section 1.3 will continue this exploration of coherence functions by going beyond single particle quantities and defining second and n-th order coherence functions. These functions have several symmetry properties reflecting the fermionic statistics of electrons, as well as quite complicated representations. However, this will prove useful, as we will

be able to extract several interesting physical properties from them, and will use these functions at several points of the manuscript.

We will end this first chapter with another theoretical tool that will be used extensively to treat Coulomb interactions: bosonization. As will be explained, there is an equivalence between the creation of low-energy electrons above a Fermi sea and the excitation of bosonic degrees of freedom called edge-magnetoplasmons in a vacuum. This last section will therefore give all the necessary equations allowing us to translate quantities from one language to the other, thus providing a dictionary between electrons and bosons.

The second chapter of this manuscript, devoted to how actual experiments work, will review first which physical quantities can be accessed using current technology, explaining the challenges that need to be overcome for such measurements to be possible.

Then, section 2.2 will give a complete overview of the different interferometry experiments that have been realized in the framework of electron quantum optics. Two interferometers will be discussed: the Mach-Zehnder interferometer, which is an amplitude interferometer, and Hong-Ou-Mandel interferometer, which is an intensity interferometer. We will discuss the pros and cons of each interferometer, as well as the main physical quantities that they give access to. Another point of view on these problems is presented in one of our publications [OP5], in which we have developed a re-interpretation of all electron quantum optics interferometry experiments in terms of analog quantum signal processing.

Using Hong-Ou-Mandel interferometry, we can also perform another type of measurement that was, once again, reserved to quantum optics up to these last few years: a complete tomography of an unknown quantum current. Section 2.3 will be devoted both to the presentation of the protocol that can be used to reconstruct the full Wigner function of an unknown state, and to its actual implementation in the experiment. I have had the opportunity to work both on the experimental and theoretical parts of this work, and I have performed the benchmarking of a completely new tool that we expect to become a standard procedure in the study of quantum currents [OP4]. However, while the tomographic reconstruction of single electron coherence is an impressive experimental achievement, it is not the only thing that is done by our quantum signal analyzer. Indeed, B. Roussel has invented during his PhD in our theory group in Lyon a numerical analysis of the signal allowing the extraction of all single-electron and single-hole wavefunctions present in a periodic

quantum electrical current. This enablies us to understand any quantum current in terms of its elementary single particle excitations, which we have called electronic atoms of signal [OP5]. While I have participated in this part of the work, I was not the main researcher on this topic, and I will thus only briefly review it here, refering the interested reader to the PhD thesis by B. Roussel [138] and to our forthcoming publications.

Finally, we will turn ourselves to more prospective experiments, aiming at transposing the results presented up to now for first order coherences in the case of second order ones. This work started during the PhD of E. Thibierge [OP6, 159], and I have participated to its further development. This work which aims at providing a new protocol for reconstructing second electron coherence is, to my great sorrow, not yet fully complete but I will nevertheless present our results here.

The third and last chapter will then be devoted to the study of Coulomb interaction in electron quantum optics, their effect, their characterization and control. As can be expected from its length, this was the main focus of my PhD: it will thus constitute the main part of this manuscript.

I will first state how bosonization can be used to treat screened Coulomb interaction in our framework. Using the dictionary from chapter 1, we are able to express the coherence after a finite-length interaction region for any incoming single-electronic wavepacket located above the Fermi sea. As we will see, the result can be casted under a quite compact form, but needs to be expanded as a quite tedious sum of terms in order to be evaluated. This analytical approach is a first necessary step, which I developed. The second step, which I did not develop due to a lack of the necessary coding skills, is feeding this development to a computer. I will briefly present the very clever numerical implementation that is used to evaluate the resulting expressions. This implementation was done by B. Roussel, whithout whom explicit results could not have been obtained. The main part of my work is then the third step of this treatment: having a powerful tool allowing the computation of single electron coherence taking into account interaction effects for any type of interaction and any incoming wavepacket, we have to extract physically relevant results for the experiments as well as use this tool to enlighten us on the physics of decoherence in the many body (strongly) interacting electron fluid. In this thesis, I will focus on three important situations in which interesting physics can be extracted from our modelization.

The first one, presented in section 3.2 directly concerns actual ex-

periments: we consider single electron decoherence within a two channel system capacitively coupled by short-range effective screened Coulomb interactions. This section will be devoted to the physical interpretation of how this modifies incoming currents, and more specifically to the differences it implies between classically driving an Ohmic contact and emitting energy-resolved single electron excitations. In particular, we will show that our model can predict single electron coherence and Hong-Ou-Mandel experimental signals with a very good agreement with experimental results. Moreover, we will discuss how it should be possible, with our current experimental sensibility and taking into account the limitations of the experimental setup, to discriminate between different microscopic interaction models, namely short- and long-range ones.

Then, section 3.3 will discuss how a clever engineering of the electromagnetic environment of an edge channel can be used to protect electronic excitations from decoherence. This will be done by giving a complete study, within our framework and with our numerical approach, of an idea that has been used in the DC regime by our community for some years now [2, 83]. This will provide useful insights both on the way that such systems can allow some decoherence protection, and on how electronic relaxation and decoherence could be useful in cases where this protection fails.

The third case of interest for us will simply be the case where only one conduction channel is present in the system and the edge channel is not coupled to external degrees of freedom. This seems a rather academical problem but it deals with a basic physics issue: single particle decoherence within a quantum coherent interacting many-body system. Moreover, it also addresses the question of the velocity of electronic excitations within the 1D channel. More precisely, it answers whether single electron quantum currents propagate at the Fermi velocity or at the plasmon velocity, these two being different in the presence of interactions. As we shall see, the answer to this questions turns out to be subtle and illuminating. As a byproduct, it will shed some light on the role of the material in single electron decoherence, an issue that has often been overlooked due to the fact that experience have, up to very recently, only been performed within GaAs bi-dimensional gases.

As we will see, in this ideal single edge channel case, interactions only lead to a frequency-dependent plasmonic velocity. Yet, we will show that even such a simple case can lead to pretty interesting results and in particular provides clear answers to the above questions. We will

also discuss an effective electrical circuit approach to the finite frequency transport, which we think is a good way to introduce bulk dissipation in our treatment of the system.

Finally, this chapter will end with what may be the most complicated section of this manuscript formula-wise: the computation of a generic n-th order coherence after an interaction region, in a case where we injected p electrons in the system. This is a very interesting problem since higher order electronic coherences are the key to understand and quantify entanglement within the electronic fluid. Entanglement within a many body quantum system is a very important and subtle problem [3] which is of high interest, for example in the cold atom community. It has also been a hot topic in the field of electronic quantum transport, from the unraveling of entanglement generation from the Fermi sea at a quantum point contact by Beenakker [6], entanglement measurement proposals before the advent of electron quantum optics [27, 143, 58, 59, 95] to the recent proposals for generating and detecting entanglement in electron quantum optics setups [147, 30, 29, 160, 81]. Although this aspect has not been developed so much during my PhD, E. Thibierge's thesis [159] as well as one of our papers [OP5] explain how to connect electronic coherences to quantum information quantities relevant for quantifying entanglement.

In section 3.5, we also provide the complete analytical solution to the problem of computing the effect of effective screened Coulomb interactions on any electronic coherence for an initial state involing a p-electron Slater determinant on top of the Fermi sea. The bad news is that, even with B. Roussel's programming skills, apart from the case already treated by us, a numerical implementation of the full solution seems to be out of reach, or with a cost to benefit ratio that may exceed the enthusiasm of any academic funding agency. However, we have looked beyond these formidable equations and we have been able to extract some clear physical information in some specific and physically relevant cases, such as the high energy regime already discussed for first order coherence in [32]. In particular, I will show that the effect of Coulomb interaction between the injected electrons takes quite a nice form, leading to some interesting results and possibly giving us hopes to obtain explicit numerical results under the proper assuptions.

As a side note before leaving the reader with the rest of my text, let me stress here that most of this work has been published in 6 papers, which are denoted by [OPx], as a way to make them more distinct from

standard bibliography. The complete publication list can be found on the very last page of this manuscript.

Chapter 1

Electron Quantum Optics

> Durch leeren Raum bricht ein Schein.
>
> Der Weg einer Freiheit
> *Lichtmensch*

This introductory chapter aims at presenting the evolution of electronic transport during the last decades from a purely condensed matter to a quantum optics-inspired paradigm. This shift has been catalyzed by new experimental developments allowing for the controlled preparation and manipulation of new states of the electronic fluid, all the way down to single-electronic excitations in the equivalent of optical fibers for the electrons. New theoretical concepts have then been developed for interpreting the new experiments built upon these breakthroughs. They are inspired by the corresponding concepts of quantum optics such as coherence functions introduced by Roy Glauber in the 1960s.

In this chapter, we will first focus on the experimental tools that have lead to the transition from coherent electronic transport to electron quantum optics. These tools somehow mirror the usual components that can be found on an optical table: *optical fibers* which will be provided by the chiral edge channels in the integer quantum Hall effect; *beamsplitters* tunable via metallic top gates; and *single to few electron sources*, two families of which will be presented in section 1.1.2. These elements can then be combined to design new experiments that mirror the famous quantum optics ones, as will be explained in details in chapter 2.

The second part of this chapter will then be devoted to the presentation of the theoretical arsenal that has been developed to understand

and conceptualize these new experiments. Two main concepts will be presented here and used extensively through the whole manuscript. We will first introduce *electronic coherence functions* and discuss their main properties, their various representations and the physical quantities they give access to. Then, we will discuss *bosonization* which provides the dictionary between electron and photon quantum optics. This technique will be at the heart of my work, as will be made clear in chapter 3, where we will see that going back and forth between the two ways of looking at excitations in our system allows us to treat non-trivial problems such as Coulomb interaction induced electronic decoherence in a transparent and unified way.

1.1 Experimental tools

1.1.1 From condensed matter to optics-like elements

The first goal of an experimentalist trying to make electron quantum optics is to find a way to control electronic propagation as cleanly as possible. This means first of all that we need to have a sufficiently small system. Indeed, there are several length scales to consider when looking at the conduction properties of a conductor, and two of them are really important for us.

One of these length scales is the inelastic scattering length, l_{in}, defined as the mean distance over which an electron can propagate without loosing energy. It is mostly limited by the strength of electron-phonon and electron-electron interactions, and is the one we experience in our everyday life. Indeed, these inelastic processes are the ones responsible for the heating of classical electric wires when we send current through. As we will see, controlling l_{in} is not an easy feat, and will occupy us for a long time in a much further section (3.3).

The other length scale of interest in our setup is the elastic scattering length, which describes collisions over static impurities which do not change the energy. The mean distance between two such collisions is denoted by l_{el}, and our goal is to find a system in which this length is longer than the typical size of our experiments, to put ourselves in what is called the ballistic regime of conduction.

Of course, this is only a small part of all possible regimes of conduction that could appear in general, but we are not going to detail those any further and rather refer the reader to the book by Montambaux [115] for more information.

2DEG under a magnetic field

A system of choice for realizing a ballistic conductor has been found in bi-dimensional electron gases, or 2DEG. They are heterostructures obtained at the interface between two semiconductors, which will mostly be GaAs and AlGaAs in our case. At such junctions, a triangular potential well is created which leads to the quantization of the transverse quasi-momentum. In the optimal regime, only the electronic bands associated with the lowest quantized transverse quasi-momentum matters and a bi-dimensional electron gas located at the interface can be obtained. The corresponding electrons usually arise from donor atoms located about 100 nm away from the gas. The potential associated with these ionized impurities is thus smoothed out by this 100 nm distance, which leads to high mobility in the material. This is why these materials are so interesting: the electronic elastic mean free path l_{el} can exceed several hundreds of micrometers [17]. Since typical samples for electron quantum optics experiments involve 1 to few tens of micrometers propagation lengths, we can expect the two dimensional electron gas to be in the ballistic propagation regime at sufficiently low temperature.

Using state-of-the-art lithography techniques, it is indeed possible to etch samples or to deposit metallic gates with submicronic precision, meaning that the ballistic regime can be obtained in a real experiment. However, without any other assumptions, propagation in our 2DEG can happen in any direction of the plane and elastic scattering effects may limit the possible applications of such systems for electron quantum optics when increasing their size. However, the application of a perpendicular magnetic field has proven useful to circumvent this potential difficulty. It turns out that applying a strong magnetic field (a few Teslas) to a cryogenically cooled 2DEG allows one to enter a new regime of electronic transport, called the integer quantum Hall regime. This groundbreaking discovery by Klitzing, Dorda, and Pepper [96] was awarded the Nobel prize five years later. Its very specific properties, which we shall review now, are precisely what makes this regime so useful for electron quantum optics.

In the integer quantum Hall regime, the longitudinal resistivity vanishes, while the transverse resistivity takes quantized values:

$$\rho_{xy} = \frac{R_{\mathrm{K}}}{\nu},\ \nu \in \mathbb{N} \quad \text{and} \quad R_{\mathrm{K}} = \frac{h}{e^2} \tag{1.1}$$

where e is the electron charge and h is Planck's constant. The quantity $R_{\mathrm{K}} = h/e^2$, called the von Klitzing resistance, has a value of about

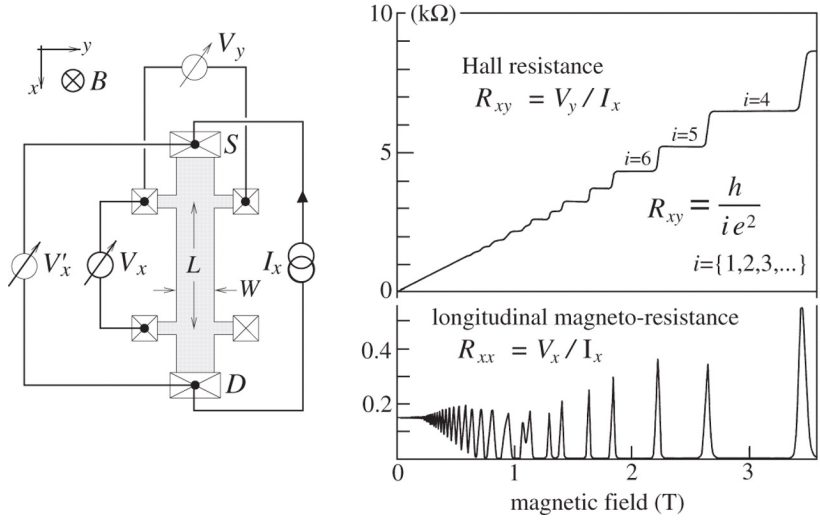

Figure 1.1: Figure extracted from [175]. *Left*: A schematic view of a quantum Hall experiment. A bi-dimensional electron gas is put in a strong perpendicular magnetic field and we apply some current along one of the plane direction (here along the x-axis). We can then measure resistivities either in the same direction (R_{xx}) or along the transverse one (R_{xy}) by measuring the potential difference between either contacts 1 and 2 or 1 and 3. *Right*: Experimental results. When the magnetic field varies, R_{xy} goes from one quantized plateau to another, and R_{xx} vanishes whenever we are on a plateau.

25.8 kΩ. Finally, the integer ν is called the filling factor and we will see why in a few paragraphs. The remarkable discovery by von Klitzing is that this regime is exceptionally stable under a variation of the magnetic field: the transverse resistance only varies from one integer value of ν to another in narrow transition regions where the longitudinal resistivity is non-zero, as can be seen on figure 1.1. Between two transitions, it is stable up to 10^{-9}, a remarkable property of great interest for metrology [175] which explains why physicists talk about quantum Hall plateaus.

How can we explain such a behaviour? The idea is simply to look at the energy levels of our system under a magnetic field, which are called Landau levels. These highly degenerated levels are, in the case of an infinite plane, equivalent to harmonic oscillator levels, and are therefore equally spaced with an energy $\hbar\omega_c$ between them. ω_c is called the

cyclotron pulsation, as it is the pulsation associated with the classical circular motion of electrons in a magnetic field. Moreover, due to the magnetic field, the spin degeneracy of electrons is lifted, and a Zeeman energy separation $\hbar\omega_Z$ appears between the two spin populations. With only this simple spectrum, conduction in our sample would be quite easy to understand: either the chemical potential μ set by our voltage is inside one Landau level, in which case the whole system is a conductor and both resistivities have finite values, or it is between two possible levels, in which case we have an insulating system, where resistivity becomes infinite. Here, we must make a small remark on the role of disorder for the existence of the plateaus. Indeed, the existence of disorder in our system is unexpectedly advantageous for us! Disorder leads to the presence of localized states that will trap extra electrons when the chemical potential is between two Landau levels, thus stabilizing the insulating behaviour of the sample. Of course, we need the disorder to be not too strong, since it will also change the degeneracy of Landau levels, so that too strong disorder will even make us lose the energy-localization of levels. A good review of this topic can be found in the lectures given by D. Tong at Cambridge University [163].

However, in reality, a quantum Hall sample is not insulating: it has a non-zero transverse resistivity. The above discussion indeed overlooks a crucial point of real samples: they are not infinite. Equivalently, they have edges which are precisely where they are connected to electronic reservoirs. Therefore, our energy spectrum must be modified to take into account the confinement potential at the edge. This confinement potential will bend the energy levels as can be seen on figure 1.2, and our discussion of conduction properties must be refined. Not much changes when the chemical potential is at the same energy as one of the original Landau levels, but the picture becomes radically different when it lies between them which is the integer quantum Hall regime. In this case, the chemical potential crosses every filled Landau level near the edges of the system, therefore creating one dimensional metallic states which are electronic conduction channels. Moreover, since the electronic velocity is linked to the gradient of the potential, electrons within a given channel system will propagate in the opposite direction than those of the opposite edge: electronic propagation is thus chiral. Chirality implies that no backscattering is possible along one edge of the sample and, when the two edges are sufficiently far apart, any backscattering event from one channel to the other one is prohibited [22], since it would

require a very improbable tunneling event from one edge to the other. This explains why the longitudinal resistivity vanishes on a quantum Hall plateau. It also explains why the transverse resistivity (or equivalently conductivity) is quantized since transport can only occur via an integer number of conduction channels. At a given chemical potential, changing the magnetic field therefore allows us to change the number of conduction channels in our system by modifying the energies of the Landau levels. As can directly be seen on the spectrum, the number of channels ν is equal to the number of filled Landau levels situated below the chemical potential, explaining why we called the integer factor appearing in equation (1.1) the filling factor. A last interesting property of those edge channels is the fact that inter-channel tunneling events are rare, and therefore only happen over long propagation distances (typically a few hundreds of nanometers). Since our experiments will always be smaller than such sizes in order to be in the ballistic propagation regime, we can always consider adjacent channels as independent. This does not mean that they do not interact with each other, as we will extensively see in chapter 3, but it will greatly simplify the way in which we can treat a system of several copropagating channels.

To conclude this small overview of quantum Hall edge channels, we showed that they have all the properties we could ask of optical fibers: unidimensional propagation, with no backscattering possible. This will put them at the heart of our implementation of electron quantum optics experiments, and next section will be devoted to how we can better control these channels to manipulate the propagation of electrons.

Controlled propagation of electrons

Now that we have access to a controlled medium for the propagation of electrons, what we need to find is a way to modify this propagation at will, and to interact with the edge channels. Parallel to the understanding of the quantum Hall effect, the 1980s also saw a great deal of experimental evolutions allowing to transition from bi-dimensional electron gases to one-dimensional ones. The first results, obtained both in silicon [31] and GaAs-based heterojunctions [8, 161], made clear that the main tool for this was to create a constriction in the 2DEG. Such a constriction can be made directly by design of the sample, but the real result allowing its practical use in many successful experiments is the fact that it can be obtained by using metallic gates deposited on the top of the sample, and applying a negative bias to them in order to de-

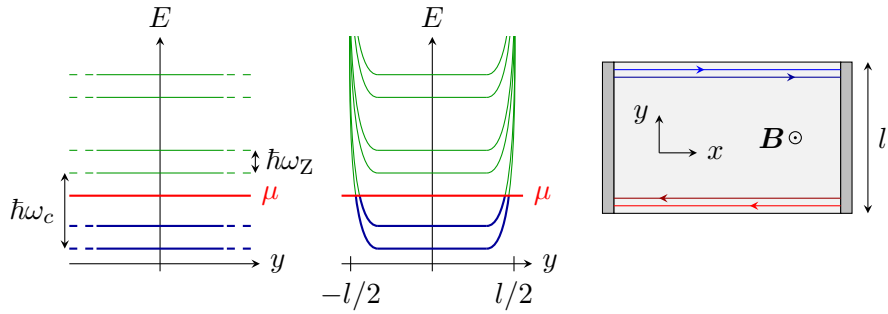

Figure 1.2: *Left*: Energy spectrum of an infinite 2DEG under a perpendicular magnetic field $\boldsymbol{B} = B\mathbf{e}_z$. Landau levels are separated by an energy $\hbar\omega_c$, while the two spins populations are separated by Zeeman splitting $\hbar\omega_\mathrm{Z}$. Since the chemical potential is between two levels, this sample is insulating. *Middle*: Schematic energy spectrum of a finite 2DEG under a magnetic field. Levels are bent due to the confining potential. Chemical potential therefore crosses energy levels near the edges, creating conduction channels. *Right*: Schematic vision of the edge channels created in the case described by the previous spectrum. Propagation along the edges is chiral.

plete the gas from electrons under them. This setup, called a quantum point contact (or QPC), is represented on figure 1.3. It was first demonstrated by Wees et al. [172] and independently by Wharam et al. [179], as a way to show that ballistic transport in one-dimensional systems leads to a quantization of resistance. In terms of edge channels, what this means is that it is possible to change the number of channels that can go through the sample by varying the gate potential. It even allows for partial transmission of a channel when the potential is precisely tuned, as was theoretically understood by Büttiker [23]. Therefore, the quantum point contact can be seen as a tunable beamsplitter for electrons, and will obviously be of great practical use for any electron quantum optics experiment.

Let us now take a brief moment to examine how the QPC works. From the point of view of an electron in the 2DEG, the negative bias applied to the top gates creates a repulsive potential, in much the same way as the edges of the samples. These gates therefore allow for a smooth and tunable additional confinement potential, which leads to a modification of the path followed by conduction channels. When we take

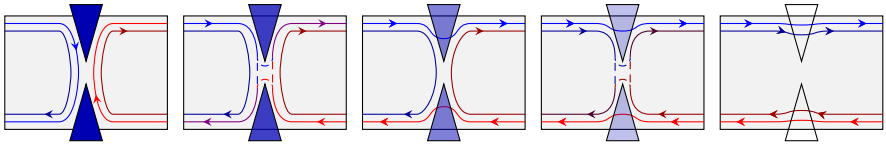

Figure 1.3: Schematic representation of a quantum point contact action on the edge channels. *From left to right*: starting from a strong negative bias applied to the top gates, all channels are reflected. As we relax the bias, repelling potential becomes weaker and one channel can be partially transmitted, and then fully transmitted. This goes on until every channel is transmitted. In cases where channels are not fully transmitted, we observe some mixing between the incoming channels from both sides of the QPC in the output. This will be of particular interest in chapter 2.

a look at the shape of the quantum point contact in figure 1.3, it is clear that if this confinement potential is strong enough, all edge channels will stay on one side of the barrier and we will be in a fully reflective situation. When relaxing a bit this confinement, it will become possible for electrons in the outer channel to tunnel from one side of the barrier to the other, leading to a partial transmission of this channel. If we relax it even more, electrons from the outer channel are no more sufficiently repelled to be backscattered, and only follow a modified edge, while other edge channels are still reflected. This goes on until all channels are transmitted through the QPC.

1.1.2 On-demand single electron sources

In the previous section, we have studied the means of propagation of electrons through a sample, and discovered the existence of electronic equivalent to optical fibers and to beamsplitters. Let us now focus on the excitations that propagate within these elements and ask ourselves: what are the electronic sources of interest in electron quantum optics? Performing electron quantum optics-like experiments calls for sources that are able to emit simple, few-particles electronic excitations, or even better single electron (or hole) excitations.

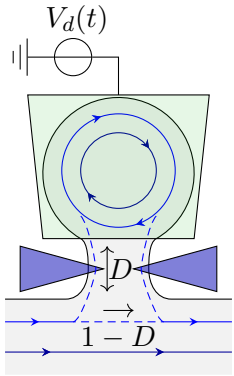

Figure 1.4: A schematic view of the quantum dot source. A small cavity of the 2DEG is closed by a quantum point contact, leading to a Fabry-Pérot type quantization of levels in the cavity. The energy position of these levels can then be tuned by applying some voltage to a metallic top gate.

Landau quasiparticle source

The first on-demand single electron source has first been demonstrated by Fève et al. [44] in the Laboratoire Pierre Aigrain. It is shown in figure 1.4 and is based on the rearrangement of single particle states within an electronic cavity. A quantum point contact defines this electronic cavity, which we call a quantum dot, in a controlled way. By tuning the transmission D of the dot, the spectrum inside the cavity can go from a continuum at full transmission $D = 1$ to a discrete one at $D = 0$ with energy levels separated by an energy gap Δ. It is analogous to a Fabry-Pérot interferometer in classical optics. In an equilibrium situation, all quantized levels up to the Fermi level are filled, and nothing happens.

The idea of this source is to rapidly shift the position of all levels by applying a square drive voltage $V_d(t)$ to a top gate placed above the dot. In an ideal case, as shown in figure 1.5, all levels inside the dot are shifted upwards in energy when $-eV_d(t)$ increases. Appropriately tuning the amplitude of the drive so that this shift is equal to the gap between levels Δ ensures that exactly one discrete level is promoted above the Fermi level. The corresponding electron can therefore tunnel out of the dot and propagate into the sample. When $-eV_d(t)$ decreases back to its initial value, the now-empty discrete level fills up again: our source

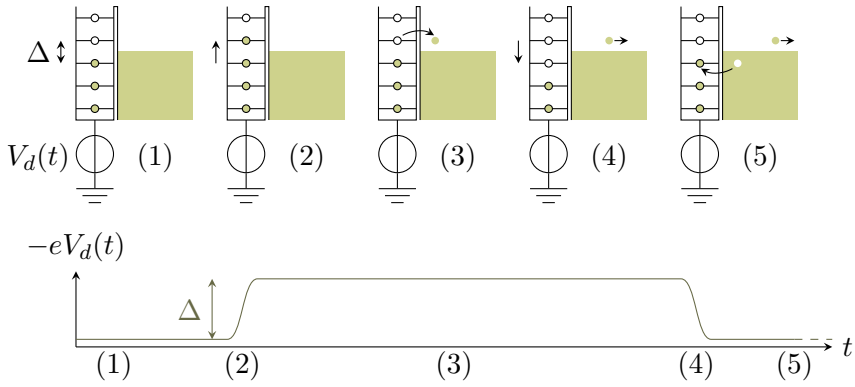

Figure 1.5: Schematic view of the ideal operating cycle of the source obtained when applying a square voltage of well-tuned amplitude to the top gate. (1) At the beginning, all levels below the Fermi level are filled. (2) A brutal raise of voltage leads to a fast shift in energy of all levels. One level is promoted above the Fermi level. (3) After some typical dwelling time τ_0, the promoted electron tunnels out of the cavity and propagates into the sample. (4) We brutally decrease back the voltage and thus shift an empty level below the Fermi level. (5) After some time, an electron tunnels into the dot to fill this empty level, and a hole is emitted into the sample. We are back to the initial situation. By repeating this cycle, we obtain a source emitting an electron and a hole per period, separated from each other by half a period

emits a single hole excitation. In the ideal regime, this source emits one single energy resolved electron and one single energy resolved hole excitation per period.

In a realistic situation, this ideal picture needs to be precised: the Heisenberg principle forbids a fully energy-resolved excitation to be emitted within a finite time, and in particular during a half period. However, the dot transmission D controls both the width $\hbar\gamma$ of the quantized levels and the typical escape time (or dwelling time) $\tau_0 = 1/\gamma$ of the cavity. Closing the dot improves the energy resolution of the emitted excitations but τ_0 may exceed the half-period and we may thus enter a regime in which no excitation is emitted. In the opposite regime of a short dwelling time, the transparency D has to be close to 1 and charge quantization, which is a hallmark of single electron emission, may break down. Designing and operating such a system as a single electron source

thus requires some compromise between several requirements:

- The dwelling time τ_0 has to be much longer than the typical rising time of our square voltage, in order for the single particle levels to be rearranged before any hybridization with continuum single particle states of the edge channel. This ensures electronic emission well above the Fermi level[1].
- τ_0 has to be shorter than the half-period of the drive, in order to maximize the probability to emit an electron per cycle.
- The energy level width $\hbar\gamma$ has to be smaller than half the gap between levels, in order to promote only one level above the Fermi level.
- The repetition rate of the source must be high enough to generate measurable quantities.

The importance of the last point will appear clearly in the next chapter when discussing how to perform measurements in electron quantum optics experiments. A realistic implementation of this source typically uses a drive frequency in the 1 to 3 GHz range and the geometry of the dot is such that $\Delta \simeq 120\,\mu\text{eV}$, corresponding to a 30 GHz frequency. This leaves one decade for the escape time around 100 ps since we ask for

$$3\,\text{GHz} < \frac{1}{\tau_0} < 30\,\text{GHz}\,, \tag{1.2}$$

which can be obtained experimentally. Let us stress that even if source parameters seem to be tightly constrained, we still have access to a variety of regimes by tuning the transmission of the dot or the position of the levels with respect to the Fermi sea. This versatility will be of particular importance when studying Coulomb interaction effects on energy-resolved excitations in chapter 3.

A single electron classical drive?

Due to the associated nanofabrication constraints, quantum dot based sources are challenging devices to build and operate within a real sample. People have thus looked for simpler single to few electron sources. Of

[1] In the opposite case, the electron would tunnel out of the cavity as soon as it crosses the Fermi level, and we would have a low energy emission instead of the resolved, high-energy one we are looking for.

course, the simplest device that can be imagined is a simple Ohmic contact, driven by a classical time dependent voltage. In full generality, the state created by such a drive is not built from a well defined number of electron and hole excitations on top of the Fermi sea. Nevertheless, lowering the amplitude will certainly give access to a regime where the average number of such excitations emitted per period is close to unity and, in some well controlled regimes, such sources lead to very interesting electronic states.

The first one is the adiabatic regime, in which the only thing that happens is that the Fermi sea chemical potential directly follows the drive. Everything is then equivalent to a slowly varying DC potential. While this state is not of huge interest in terms of electronic wavefunctions, it will often be used throughout this manuscript, and will be covered in much more details in the corresponding sections.

The second regime of interest is indeed a remarkable one, and has been predicted by Levitov, Lee, and Lesovik [104]: using a Lorentzian voltage pulse of total charge $-e$, we can emit exactly one single electron excitation on top of the Fermi sea, which is called a Leviton. More generally, for a Lorentzian voltage drive $V_d(t)$

$$i(t) = \frac{V_d(t)}{R_{\mathrm{K}}} = \frac{q}{\pi\tau_0}\frac{1}{1+(t/\tau_0)^2} \tag{1.3}$$

with controlled duration τ_0 and total charge q, the resulting state when $q = -ne$ is an n-electronic state built as a Slater determinant of an n electron excitation on top of the Fermi sea [93]. This n-Leviton state is emitted around $t = 0$, with a typical width τ_0 around the emission time. In the case $n < 0$, the equivalent hole excitation obtained by removing the Slater determinant from the Fermi sea is generated, and will be called an n-anti-Leviton. Another interesting property for single electronic Levitons or anti-Levitons is that any train of Lorentzian voltage pulses of charges $-e$ leads to a state containing only electronic excitations and no electron-hole pairs on top of the Fermi sea. This means that we can repeat the emission of Levitons to create a periodic source of single-electronic Lorentzian wavepackets. Such a source has been recently demonstrated in the group of D. C. Glattli [38] and will be very useful in the study of Coulomb interaction effects on electronic excitations.

Evidently, there are some drawbacks to this simpler electron source, and the main one is the fact that all electronic excitations obtained by applying a voltage to an Ohmic contact have, by design, an energy

content localized close to the Fermi level. High energy scenarios, and more importantly situations studying electronic wavepackets located far above the Fermi sea can therefore not be attained using Leviton sources. The existence of both types of sources will then provide complementary information on the underlying physics.

1.2 First order coherence

Now that we have seen a quick overview of the experimental tools allowing us to do optics-like experiments, we need to turn ourselves to the theoretical tools at work in optics (both classical and quantum) and search for their electronic equivalent. In this work, we are mainly interested in interference experiments, as we will see in chapter 2. In optics, the good tool to study such experiments is called coherence, and it is presented in a great number of books [183, 48]. We will only give some reminders about its definition and properties in a first section, before going to electronic coherence.

1.2.1 Coherence in optics

Classical optics

Let us start with a simple interferometry experiment in classical optics, Young's experiment. We are interested in the light intensity I that can be measured by some detector at position $\mathbf{r}_d$ and time t. We know that this intensity can be related to two things: the response function of the detector, given by some function $K_d(\tau)$, and the electric field at the detector's location, $E(\mathbf{r}_d, t)$. To simplify things, we suppose here that the light used is linearly polarized and monochromatic with pulsation ω, such that we can use a complex scalar to describe the field. This gives the following equation

$$I(\mathbf{r}_d, t) = \int_{t-\tau_d}^{t+\tau_d} K_d(\tau - t) E(\mathbf{r}_d, \tau) E^*(\mathbf{r}_d, \tau) \mathrm{d}\tau \tag{1.4}$$

which is just a way of saying that the detector gives an average, with some response function, of the energy flux that goes through it during some duration $2\tau_d$ around t. Due to the specific form of the double hole experiment, we know that the field at the detector's location and time t can be linked to the field at positions of the holes $\mathbf{r}_1$ and $\mathbf{r}_2$ at previous

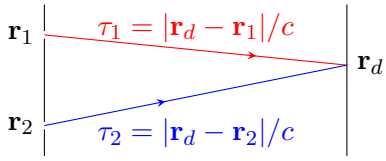

Figure 1.6: A schematic representation of Young's interferometry experiment. The field at the detector's location $\mathbf{r}_d$ can be linked to its values at the two sources at previous times.

times, as can be seen in figure 1.6, giving

$$E(\mathbf{r}_d, t) = E(\mathbf{r}_1, t - \tau_1) + E(\mathbf{r}_2, t - \tau_2)\,. \tag{1.5}$$

When going back to intensity, this leads to a three terms equation

$$I(\mathbf{r}_d, t) = I_1(\mathbf{r}_d, t) + I_2(\mathbf{r}_d, t) \tag{1.6a}$$

$$+ 2\mathrm{Re}\left(\int_{t-\tau_d}^{t+\tau_d} K_d(\tau - t) E(\mathbf{r}_1, \tau - \tau_1) E^*(\mathbf{r}_2, \tau - \tau_2) \mathrm{d}\tau\right) \tag{1.6b}$$

in which we recognize the intensity coming from each source in term 1.6a and an interference effect between the fields in term 1.6b. From this equation, we understand that the relevant quantity to compute in order to know if interference effects will be observed in this experiment is the classical coherence function defined as

$$G(\mathbf{r}_1, t_1 | \mathbf{r}_2, t_2) = \langle E(\mathbf{r}_1, t - t_1) E^*(\mathbf{r}_2, t - t_2) \rangle \tag{1.7}$$

where the average is a time average over t. From this function, we can define a normalized quantity as

$$g(\mathbf{r}_1, t_1 | \mathbf{r}_2, t_2) = \frac{G(\mathbf{r}_1, t_1 | \mathbf{r}_2, t_2)}{\sqrt{G(\mathbf{r}_1, t_1 | \mathbf{r}_1, t_1) G(\mathbf{r}_2, t_2 | \mathbf{r}_2, t_2)}} \tag{1.8}$$

such that $|g| = 1$ if the fields are perfectly correlated, meaning that the contrast in the interference pattern will be maximal, and $|g| = 0$ if the fields are completely decorrelated, so that no interference pattern can be observed. A simple Cauchy-Schwartz inequality gives

$$|G(\mathbf{r}_1, t_1 | \mathbf{r}_2, t_2)|^2 \leq G(\mathbf{r}_1, t_1 | \mathbf{r}_1, t_1) G(\mathbf{r}_2, t_2 | \mathbf{r}_2, t_2) \tag{1.9}$$

such that g cannot take values bigger than 1.

Quantum optics

In order to describe quantum sources, the idea of a quantum version of optical coherence had to be developed. This became especially true, as can be expected from their name, after the development of coherent sources such as the MASER in the 1950s. Then, in 1963, Roy Glauber defined what would become the quantum theory of optical coherence in a series of three articles [61, 62, 63]. From the classical equation, we would expect that all we would need to do is to replace the classical field by an operator and complex conjugation by hermitian conjugation. Things are unfortunately not as simple, because the quantum field operator $\mathbf{E}(\mathbf{r},t)$ at position $\mathbf{r}$ and time t is hermitian. The great idea of Glauber was to define two sub-operators from this one, taking either only the positive frequencies of its Fourier transform or only its negative frequencies:

$$\mathbf{E}(\mathbf{r},t) = \mathbf{E}^{(-)}(\mathbf{r},t) + \mathbf{E}^{(+)}(\mathbf{r},t) \tag{1.10a}$$

$$\mathbf{E}^{(-)}(\mathbf{r},t) = \int_{-\infty}^{0} \widetilde{\mathbf{E}}(\mathbf{r},\omega)\mathrm{e}^{-\mathrm{i}\omega t}\frac{\mathrm{d}\omega}{2\pi} \tag{1.10b}$$

$$\mathbf{E}^{(+)}(\mathbf{r},t) = \int_{0}^{+\infty} \widetilde{\mathbf{E}}(\mathbf{r},\omega)\mathrm{e}^{-\mathrm{i}\omega t}\frac{\mathrm{d}\omega}{2\pi} \tag{1.10c}$$

These operators are hermitian conjugates of each other, and can be interpreted respectively as the annihilation (for $\mathbf{E}^{(+)}$) and creation (for $\mathbf{E}^{(-)}$) operators for a photon at position $\mathbf{r}$ and time t. Using these operators, it is possible to describe an interferometry experiment in a quantum optics manner, for example with a destructive measurement such as photodetection at the end of the experiment. What Glauber then found is that the probability to detect a photon on the interval $[0,t]$ for a quantum state described by the density matrix ρ is given by

$$P^{\mathrm{1ph}}_{[0,t]} = \int_0^t K_d(t_1-t_2)\mathcal{G}^{(1)}_\rho(\mathbf{r}_d,t_1|\mathbf{r}_d,t_2)\mathrm{d}t_1\mathrm{d}t_2 \tag{1.11}$$

where

$$\mathcal{G}^{(1)}_\rho(\mathbf{r}_1,t_1|\mathbf{r}_2,t_2) = \mathrm{Tr}\left[\mathbf{E}^{(+)}(\mathbf{r}_1,t_1)\rho\mathbf{E}^{(-)}(\mathbf{r}_2,t_2)\right] \tag{1.12}$$

is the quantum optics equivalent of the coherence function, and K_d is as before the response function of the detector. Let us try to understand it in quite the same way as we did for classical fields. The density matrix ρ corresponds in the general case to a statistical mixture of quantum pure states, meaning that the coherence function contains information both on statistical properties of the source and on the quantum properties

of each state in the mixture. In the case of a pure quantum state, the coherence function can be seen as the transition amplitude between the initial state minus a photon removed at the detector's position $\mathbf{r}_d$ at time t_1 (the action of $\mathbf{E}^{(+)}(\mathbf{r}_1, t_1)$ on the "ket") and the same state with the photon removed at time t_2 (the action of $\mathbf{E}^{(-)}(\mathbf{r}_2, t_2)$ on the "bra"). During that period of time, the photodetector has some probability to "click" given by its response function. This is indeed what we expect from a photodetector: it needs to remove one photon from the field it probes in order to detect something. Here, the coherence function directly encodes the average over all the pure states that constitute our full quantum state.

Without going into more detail, we can use Glauber's first order coherence $\mathcal{G}^{(1)}$ in exactly the same way as its classical equivalent. We can for example define a coherence degree by creating some normalized quantity $g^{(1)}(\mathbf{r}, t|\mathbf{r}', t') = \mathcal{G}^{(1)}(\mathbf{r}, t|\mathbf{r}', t')/\sqrt{\mathcal{G}^{(1)}(\mathbf{r}, t|\mathbf{r}, t)\mathcal{G}^{(1)}(\mathbf{r}', t'|\mathbf{r}', t')}$ and use it to define different regimes of light. But, in this work, we are not interested that much in quantum optics coherence functions, and we will therefore go directly to the electronic case, where we will give much more detail about the properties and interpretation of coherence.

1.2.2 Electronic first order coherence

Definitions

The electronic equivalent of quantum optics coherence function is simply defined by replacing the photonic field operators by electronic ones. Let us denote by $\psi(\mathbf{r}, t)$ the annihilation operator at position $\mathbf{r}$ and time t, and by $\psi^\dagger(\mathbf{r}, t)$ its creation counterpart. Given these operators, the electronic first order coherence function has been defined by Grenier [67] as

$$\mathcal{G}^{(e)}_\rho(\mathbf{r}, t|\mathbf{r}', t') = \left\langle \psi^\dagger(\mathbf{r}', t')\psi(\mathbf{r}, t) \right\rangle_\rho = \mathrm{Tr}\left[\psi(\mathbf{r}, t)\rho\psi^\dagger(\mathbf{r}', t')\right] \tag{1.13}$$

where ρ denotes, as before, the density matrix of the state under consideration. In most of this manuscript, position dependence of the coherence function will be dropped as the position variable will be fixed by the actual position of detectors in our system. At first glance, this may seem like a loss of generality but, fortunately, several properties of our system ensure that all information in the coherence function can be recovered from its temporal dependence. Within an interaction free region, electronic propagation is chiral and ballistic at a fixed velocity v_F which

is the Fermi velocity along the edge channel. In this free propagation regime, position and time are closely related along the edge: anything happening at position x and time t will be happening at position $x+v_{\mathrm{F}}\tau$ at time $t+\tau$. The position dependence of single electron coherence can then be recovered from its time dependence at a fixed position x, thus showing that the real quantity of interest for us can simply be denoted $\mathcal{G}^{(e)}_{\rho,x}(t|t')$. Let us stress that, for 1D systems, single electron coherence is dimensionally equivalent to the inverse of a length.

Contrary to the photonic case, the electronic vacuum in edge channels is not the true electronic vacuum which we denote by $|\emptyset\rangle$, but a Fermi sea $|F_\mu\rangle$ in which all single particle energy levels are filled up to a certain chemical potential μ, following Fermi-Dirac statistics. As a consequence, our first difference with photon optics is that even when all sources are switched off, first order coherence is not zero but is equal to its Fermi sea value, which we will denote either by $\mathcal{G}^{(e)}_{\mathrm{F}}(t|t')$ for $\mu=0$ or $\mathcal{G}^{(e)}_{\mu}(t|t')$ for the specific case of chemical potential μ. An important property of the Fermi sea is that it is a stationary state. Its coherence function only depends on the difference between the two times: $\mathcal{G}^{(e)}_{\mathrm{F}}(t|t')=\mathcal{G}^{(e)}_{\mathrm{F}}(t-t')$.

Since we are interested in the specific contribution of a source to single electron coherence, we define the excess single electron coherence by

$$\Delta\mathcal{G}^{(e)}_{\rho}(t|t')=\mathcal{G}^{(e)}_{\rho}(t|t')-\mathcal{G}^{(e)}_{\mathrm{F}}(t|t')\,. \tag{1.14}$$

As the presence of the Fermi sea allows for creation of hole excitations, obtained by removing an electron from the Fermi sea, defining the hole coherence function as

$$\mathcal{G}^{(h)}_{\rho}(x,t|x',t')=\Big\langle\psi(x',t')\psi^{\dagger}(x,t)\Big\rangle_{\rho}\,. \tag{1.15}$$

enables us to analyze the many body state in terms of hole excitations.

Properties

Let us now derive a few properties of interest which are valid for any state ρ. First of all, it is straightforward that

$$\mathcal{G}_{\rho}(t|t')=\mathcal{G}^{*}_{\rho}(t'|t)\,. \tag{1.16}$$

As we will see later, this property ensures that the probability of finding an electron in some particular state is real.

Another property of interest deals with the link between electron and hole coherences. It can be derived simply by using the anticommutation relation between the creation and destruction operators

$$\mathcal{G}^{(e)}_{\rho,x}(t|t') + \mathcal{G}^{(h)}_{\rho,x}(t'|t) = \frac{1}{v_{\mathrm{F}}}\delta(t-t')\,, \tag{1.17}$$

the $1/v_{\mathrm{F}}$ factor coming from the combination of the anticommutator $\left\{\psi(x), \psi^\dagger(x')\right\} = \delta(x-y)$ with the time dependence $\psi(x,t) = \psi(x - v_{\mathrm{F}}t)$ in a free propagation region, as is always assumed for the place where the detectors are located.

Finally, single electron coherence satisfies a Cauchy-Schwartz inequality of the form:

$$\left|\mathcal{G}^{(e)}(t|t')\right|^2 \leq \mathcal{G}^{(e)}(t|t)\mathcal{G}^{(e)}(t'|t')\,. \tag{1.18}$$

It can be derived in the following way: since the many body density operator is positive definite, $\mathrm{Tr}\left[A\rho A^\dagger\right] \geq 0$ for any operator A. Using $A = \alpha\psi(t) + \beta\psi(t')$ where $(\alpha, \beta) \in \mathbb{C}^2$, we have

$$|\alpha|^2\mathcal{G}^{(e)}(t|t) + |\beta|^2\mathcal{G}^{(e)}(t'|t') + \alpha\beta^*\mathcal{G}^{(e)}(t|t') + \alpha^*\beta\mathcal{G}^{(e)}(t'|t) \geq 0\,. \tag{1.19}$$

This equation being valid for any α and β, it implies that the matrix defined by single electron coherences defines a definite positive sesquilinear form, which implies equation (1.18)[2]. More generally, using the same idea, we have

$$\det\left[\mathcal{G}^{(e)}(t_i|t_j)\right] \geq 0 \tag{1.20}$$

for any given list of times t_i. Equation (1.18) imposes a clear constraint on possible values for the non-diagonal coherence $\mathcal{G}^{(e)}(t|t')$: diagonal coherences need to be non-zero at both t and t' for it to be non-zero.

Wick's theorem

Before discussing simple examples, let us discuss a final property of single electron coherence that is not valid for any many-body state ρ but which relies on specific physical hypotheses: Wick's theorem [180].

This theorem applies only for a certain class of states called Gaussian, which are described by a reduced density matrix that can be written as

[2] Even if this does not seem obvious when using the standard mathematical formulation, which states that all leading principals minor of $A\rho A^\dagger$ are positive.

the exponential of a quadratic form in terms of creation and destruction operators. In that case, we can use anticommutation relations and properties of the exponential function to show that every average over a balanced number of ψ and $\psi^\dagger$ operators can be expressed as the sum over all possible pairings of one ψ with one $\psi^\dagger$. Fermionic statistics add moreover the constraint that pairings should come with a minus sign if there is an odd number of "crossings" in the corresponding pairing graph. In order to put that in a more visual manner, figure 1.7 shows some simple examples of how to use Wick's theorem. For a more mathematical approach and definition of this theorem, books such as [101, 125] are great resources.

The fact that only averages of the form $\langle\psi\psi^\dagger\rangle$ appear in the result comes from superselection rules. The most general superselection rule is called the parity superselection rule [181] and states that no many-body states containing superpositions between states with different fermion numbers are allowed. In a metallic conductor, no state containing superpositions between different total charges are allowed which is even a stronger requirement. Consequently, any average containing different numbers of ψ and $\psi^\dagger$ operators is directly equal to 0 in a normal metal. Let us stress that superconductors allow for superpositions between states differing by a charge $2e$, meaning that averages of ψ^2 – the superconducting order parameter – can be non-zero.

This theorem is of particular importance and will be used extensively in this manuscript, as a wide variety of physical many body states of the electronic fluid are indeed Gaussian. This is the case of equilibrium states, such as the Fermi sea at any temperature, but also of states generated by a driven Ohmic contact, or more generally states that can be obtained from an equilibrium state by time dependent single particle scattering theory. However, Wick's theorem is generically no longer valid is in the presence of interactions, but we will see in section 3.1.2 that a generalized version of Wick's theorem can be obtained.

Simple examples

Let us now review simple examples to get a more intuitive understanding of the physical content of single electron coherence. First, consider a state $|\Psi_1\rangle$ containing an electron in some wavefunction φ_1. In the second quantification picture, it is obtained from the action of a creation

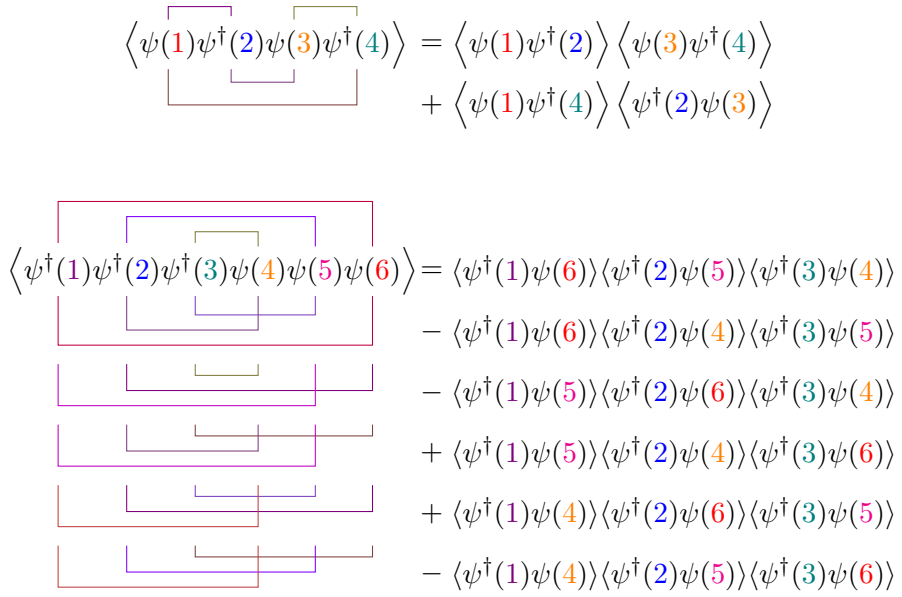

Figure 1.7: A visualization of Wick's theorem. For any Gaussian state, the average of a balanced number of ψ and $\psi^\dagger$ operators can be expressed as the sum of products of two-operators averages. Minus signs appear in those sums when the pairing graph has an odd number of crossing, a fact coming from Fermionic anticommutation relations.

operator on the true fermionic vacuum:

$$|\Psi_1\rangle = \psi^\dagger[\varphi_1]\,|\emptyset\rangle \;\text{ with }\; \psi^\dagger[\varphi_1] = \int \varphi_1(t)\psi^\dagger(t)\mathrm{d}t\,. \tag{1.21}$$

The first order coherence for that state is simply

$$\mathcal{G}^{(e)}_{|\Psi_1\rangle}(t|t') = \varphi_1(t)\varphi_1^*(t')\,. \tag{1.22}$$

It contains all the information on the single-electronic wavefunction φ_1, not only on its square modulus but also on its phase, which can be read from the $t-t'$ dependence. What happens when using states with more electrons? Let $|\Psi_N\rangle$ be the state containing N electrons in the mutually orthogonal wavefunctions $(\varphi_n)_{n\in\{1,\dots,N\}}$. In a second quantification picture, in which antisymmetry of the resulting state is naturally obtained, this state is written as

$$|\Psi_N\rangle = \prod_{n=1}^{N} \psi^\dagger[\varphi_n]\,|\emptyset\rangle \tag{1.23}$$

and, using Wick's theorem, we obtain

$$\mathcal{G}^{(e)}_{|\Psi_N\rangle}(t|t') = \sum_{n=1}^{N} \varphi_n(t)\varphi_n^*(t')\,. \tag{1.24}$$

Once again, single electron coherence contains information on all the single-electronic wavefunctions present within the many-body state. This object allows us to answer any question regarding single-particle properties.

For example, let us compute the probability to find an electron in some specific wavefunction φ given a possibly multi-electronic state described by the density matrix ρ. The electron number operator for this single particle state is

$$n[\varphi] = \psi^\dagger[\varphi]\psi[\varphi]\,. \tag{1.25}$$

Because of Fermi statistics, its spectrum consists of 0 and 1. The probability to find an electron in φ is therefore directly given by its average, which can be expressed simply using first order coherence

$$p[\varphi] = \langle n[\varphi]\rangle = \int \varphi^*(t)\varphi(t')\mathcal{G}^{(e)}(t|t')\mathrm{d}t\mathrm{d}t'\,. \tag{1.26}$$

For example, in the case of the state $|\Psi_1\rangle$ described before, this probability would simply be the square modulus of the scalar product between wavefunctions φ and φ_1, as expected from standard quantum mechanics.

Another important quantity that can be recovered quite easily from the coherence function is the average time dependent electrical current. Indeed, the average current at time t is directly linked to the excess number of electrons (with respect to the Fermi level) at the detector's location at time t:

$$\langle i(t)\rangle_\rho = -ev_{\mathrm{F}}\Delta\mathcal{G}^{(e)}_\rho(t|t) \tag{1.27a}$$

$$= -ev_{\mathrm{F}}\left(\left\langle\psi^\dagger(t)\psi(t)\right\rangle_\rho - \left\langle\psi^\dagger(t)\psi(t)\right\rangle_{\mathrm{F}}\right) \tag{1.27b}$$

where the v_{F} factor arises from the dimensionality of $\mathcal{G}^{(e)}(t|t)$. As expected, the time representation of coherence is relevant when looking at time-dependent quantities. It should be noted here that most figures in this manuscript will plot the quantity $\langle i_e(t)\rangle = -\langle i(t)\rangle/e$, which corresponds to the current of particles and not the electrical current. For more information on how to link detection events and first order coherence, I recommend reading E. Thibierge's PhD [159] (unfortunately only available in French).

Energy representation

Suppose that we are not interested in time-dependent quantities, but rather on energy-dependent ones. In that case, is first order coherence rendered useless? The answer is no, but we need to change our representation of it. Such another possible representation of coherence can be obtained by using a double Fourier transform in order to go to the frequency domain:

$$\widetilde{\mathcal{G}}^{(e)}(\omega|\omega') = v_{\mathrm{F}}^2 \int \mathcal{G}^{(e)}(t|t')\mathrm{e}^{\mathrm{i}(\omega t - \omega' t')}\mathrm{d}t\mathrm{d}t' \,. \tag{1.28}$$

In terms of fermionic operators, we have

$$\widetilde{\mathcal{G}}^{(e)}_{\rho}(\omega|\omega') = 2\pi v_{\mathrm{F}} \left\langle c^\dagger(\omega')c(\omega)\right\rangle_\rho \tag{1.29}$$

where $c(\omega)$ is the operator annihilating an electron at energy[3] $\hbar\omega$, defined from its time-domain counterpart by

$$c(\omega) = \sqrt{\frac{v_{\mathrm{F}}}{2\pi}} \int \psi(t)\mathrm{e}^{\mathrm{i}\omega t}\mathrm{d}t \tag{1.30}$$

so that c and $c^\dagger$ satisfy the anticommutation relation $\left\{c(\omega), c^\dagger(\omega')\right\} = \delta(\omega - \omega')$.

To understand the advantages of this representation, let us consider a state obtained by adding a single electron and a single hole to a Fermi sea at a chemical potential $\mu = 0$, at zero temperature[4]

$$|\Psi_{e/h}\rangle = \psi[\varphi_h]\psi^\dagger[\varphi_e]\,|F_{\mu=0}\rangle \ . \tag{1.31}$$

For this state to be non-zero, the energy content of the electronic wavefunction φ_e needs to be entirely above the Fermi level: $\varphi_e(\omega < 0) = 0$. In the same way, for the electron removed from the Fermi sea, $\varphi_h(\omega > 0) = 0$. The excess coherence of this state is given, in the energy domain, by

$$\Delta\widetilde{\mathcal{G}}^{(e)}_{|\Psi_{e/h}\rangle}(\omega|\omega') = \varphi_e^*(\omega)\varphi_e(\omega') - \varphi_h^*(\omega)\varphi_h(\omega') \,. \tag{1.32}$$

Given the constraints on the wavefunctions, this directly shows that all electronic contributions to the coherence will be contained in the

[3] Throughout this manuscript, the words "energy" and "frequency" will be used most of the time without distinction.

[4] We choose $\mu = 0$ for simplicity, but everything developed here can be done by shifting all frequencies limits to $\mu/\hbar$ instead.

($\omega \geq 0, \omega' \geq 0$) quadrant, whereas hole contributions only contribute in the ($\omega \leq 0, \omega' \leq 0$) quadrant. What about the two others quadrants, characterized by $\omega\omega' < 0$? They correspond to electron-hole coherences, but they cannot be obtained by elementary electron-hole pairs created by moving an electron from below the Fermi level to above it, as is made clear by equation (1.32). In reality, the simplest type of excitation leading to a non-zero contribution in these off-diagonal quadrants is a coherent superposition between the emission of such an elementary pair and doing nothing to the Fermi sea:

$$|\Psi_{\mathrm{coh}}\rangle = \frac{1}{\sqrt{2}}\left(1 + \psi[\varphi_h]\psi^\dagger[\varphi_e]\right)|F_{\mu=0}\rangle \ . \tag{1.33}$$

We can also interpret this state as presenting one electron in a coherent superposition of an electronic and a hole wavefunction $(|\varphi_e\rangle + |\varphi_h\rangle)/\sqrt{2}$ instead than on $|\varphi_h\rangle$ as in the Fermi sea. The excess coherence of such an excitation is, using once again Wick's theorem:

$$\Delta\widetilde{\mathcal{G}}^{(e)}_{|\Psi_{\mathrm{coh}}\rangle} = \frac{1}{2}\Big(\varphi_e(\omega)\varphi_e^*(\omega') - \varphi_h(\omega)\varphi_h^*(\omega') \tag{1.34a}$$

$$-\varphi_e(\omega)\varphi_h^*(\omega') - \varphi_h(\omega)\varphi_e^*(\omega')\Big) \ . \tag{1.34b}$$

The contribution (1.34a) is the excess coherence of the electron-hole pair $|\Psi_{e/h}\rangle$, while equation (1.34b) encodes the contribution within the electron-hole quadrants presented in figure 1.8. The frequency representation of first order coherence therefore allows a direct access to the nature of the excitations which was hidden in the off-diagonal phase of the time-domain representation.

There is another case in which the frequency representation of coherence can have an advantage over the time-domain one: stationary sources. In this case, $\mathcal{G}^{(e)}(t|t') = \mathcal{G}^{(e)}(t - t')$. The Fourier transform of such a function only depends on the average energy $\overline{\omega} = (\omega + \omega')/2$ and is singular in the difference of ω and ω':

$$\widetilde{\mathcal{G}}^{(e)}_{\mathrm{stat}}(\omega|\omega') = 2\pi v_{\mathrm{F}} f(\overline{\omega})\delta(\omega - \omega') \ . \tag{1.35}$$

In this equation, $f(\overline{\omega})$ is the occupation number at energy $\hbar\overline{\omega}$ for the stationary state under consideration.

Let us look at an example of such a state using the Fermi sea at some temperature T_{el} and chemical potential $\mu = 0$. Its many-body state can

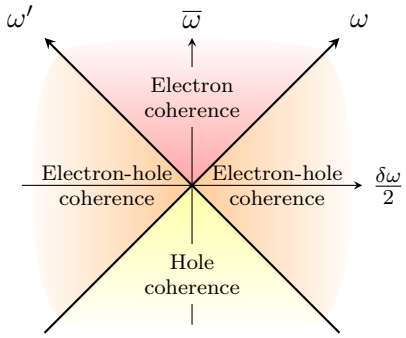

Figure 1.8: A visual representation of the frequency quadrants of coherence. Electronic-only excitations have a non-zero contribution to the quadrant with both frequencies positive and holes-only in the quadrant with both frequencies negative. The two last quadrants are signatures of electron-hole coherences.

be represented by the density matrix

$$\rho_{\mathrm{F},T_{\mathrm{el}}} = \bigotimes_{\omega\in\mathbb{R}} \Big(f_{T_{\mathrm{el}}}(\omega) c^\dagger(\omega)|0_\omega\rangle\langle 0_\omega|c(\omega) + (1 - f_{T_{\mathrm{el}}}(\omega))|0_\omega\rangle\langle 0_\omega| \Big) \quad (1.36)$$

where $f_{T_{\mathrm{el}}}$ is the Fermi-Dirac distribution at temperature T_{el}. This density matrix simply represents a collection of statistical mixtures at all energies $\hbar\omega$, between a state occupied with probability $f_{T_{\mathrm{el}}}(\omega)$ and its empty counterpart[5]. Using equation (1.29), we obtain

$$\begin{aligned} \widetilde{\mathcal{G}}^{(e)}_{T_{\mathrm{el}},\mu=0}(\omega|\omega') &= 2\pi v_{\mathrm{F}} \left\langle c^\dagger(\omega') c(\omega) \right\rangle_{\rho_{\mathrm{F},T_{\mathrm{el}}}} \\ &= 2\pi v_{\mathrm{F}} \delta(\omega - \omega') f_{T_{\mathrm{el}}}(\omega)\,. \end{aligned} \quad (1.37)$$

This result is expected from equation (1.35) for a Fermi sea at temperature T_{el}.

1.2.3 Wigner representation

Up to now, we have seen that coherence functions can be represented in two possible ways. In the time domain, they give information on all time-dependent quantities, like the current associated with a state for

[5] At zero temperature, we would recover the pure state $|F_{\mu=0}\rangle$ used before, corresponding to all negative-energy states occupied and all positive-energy states empty.

example, but no direct information on the energy content of the state. Equivalently, in the frequency domain, it is easy to recover information on the energy of single particle excitations present in a many body state, but difficult to read the temporal evolution. It then seems quite natural to look for a representation of coherence that would give us access to both informations at once. It is indeed possible to do so, by using a representation called the Wigner representation of coherence, inspired from the one developed by Wigner [182] in the context of quantum mechanics and independently by Ville [169] for classical signal processing. It is simply defined as a time-frequency representation, obtained by taking a single Fourier transform of any of the two preceding representations with respect to the difference of parameters [41]:

$$\mathcal{W}^{(e)}(\bar{t},\overline{\omega}) = v_{\mathrm{F}} \int_{-\infty}^{+\infty} \mathcal{G}^{(e)}\left(\bar{t}+\frac{\tau}{2}\middle|\, \bar{t}-\frac{\tau}{2}\right) \mathrm{e}^{\mathrm{i}\overline{\omega}\tau}\mathrm{d}\tau \tag{1.38a}$$

$$= \frac{1}{v_{\mathrm{F}}} \int_{-\infty}^{+\infty} \widetilde{\mathcal{G}}^{(e)}\left(\overline{\omega}+\frac{\Omega}{2}\middle|\, \overline{\omega}-\frac{\Omega}{2}\right) \mathrm{e}^{-\mathrm{i}\bar{t}\Omega}\frac{\mathrm{d}\Omega}{2\pi}\,. \tag{1.38b}$$

In the following, we will drop the $\bar{\cdot}$ superscript for simplicity, and denote the Wigner function $\mathcal{W}^{(e)}(t,\omega)$, which depends on one time and one frequency. Note that τ and ω are conjugated variables, as well as t and Ω. This will be used in particular for higher order coherences in section 1.3. The excess Wigner distribution function is defined in the same way from the excess single electron coherence

$$\Delta\mathcal{W}_{\rho}^{(e)}(t,\omega) = \mathcal{W}_{\rho}^{(e)}(t,\omega) - \mathcal{W}_{\mathrm{F}}^{(e)}(t,\omega)\,. \tag{1.39}$$

Finally, a Wigner distribution function for holes $\mathcal{W}^{(h)}$ as well as its excess $\Delta\mathcal{W}^{(h)}$ can also be defined in the same way from $\mathcal{G}^{(h)}$.

Properties of the Wigner function

A first nice property comes from the hermiticity of the first order coherence function: $\mathcal{W}^{(e)}(t,\omega)$ is a real-valued function. This means that it will be easily represented on a bi-dimensional density plot, contrary to coherence functions which require plots of their modulus as well as of their phase.

The marginals of the Wigner function also contain relevant information for us: integrating over one of the two variables is completely equivalent, with some v_{F} factors, to looking at the diagonal of the coherence function in the other variable. And, as was already shown in

equations (1.27a) and (1.35), those diagonal quantities can be directly linked to physical properties: average current at time t, or occupation number at energy $\hbar\omega$. This gives the following equations:

$$\int_{-\infty}^{+\infty} \Delta\mathcal{W}^{(e)}(t,\omega)\frac{\mathrm{d}\omega}{2\pi} = -\frac{\langle i(t)\rangle}{e} \tag{1.40a}$$

$$\lim_{T\to\infty}\left(\frac{1}{T}\int_{-T/2}^{+T/2}\mathcal{W}^{(e)}(t,\omega)\mathrm{d}t\right) = f(\omega)\,. \tag{1.40b}$$

In order to better visualize physical states, marginals of the Wigner functions will be plotted alongside their density plot in most figures presented in this manuscript.

Finally, a classicality criterion can be defined as

$$0 \leq \mathcal{W}^{(e)}(t,\omega) \leq 1\,. \tag{1.41}$$

Whenever this criterion holds, the Wigner function can be interpreted as a probability distribution, *i.e.* as the probability to detect an electron of energy $\hbar\omega$ at time t. This classicality criterion extends to hole excitations, as equation (1.17) expressed in the Wigner representation gives $\mathcal{W}^{(h)}(t,\omega) = 1 - \mathcal{W}^{(e)}(t,-\omega)$. Yet, as we will later see, we need to be careful when using the name "classical". For example, only a subset of all states obtained with a driving of an Ohmic contact fulfill this classicality criterion, even if one would usually call them "classically driven states". This will be made clear in next section, which is devoted to the coherence of all sources used in this manuscript, and how they compare to one another.

1.2.4 Wigner functions of useful sources

After these general considerations, it is time to turn ourselves to specific examples. Four of them will be discussed in this section: we will first discuss the equilibrium state characterized by a given electronic temperature T_{el} and chemical potential μ and how its single electron coherence is affected by the application of a classical voltage drive. We will then briefly discuss the form of single electron coherence for time-periodic sources in general and review the two single-electron sources introduced in section 1.1.2.

The driven Fermi Sea

As a starting point, let us talk about the base element of our system: the Fermi sea. As we have seen in equation (1.37), its coherence is easy

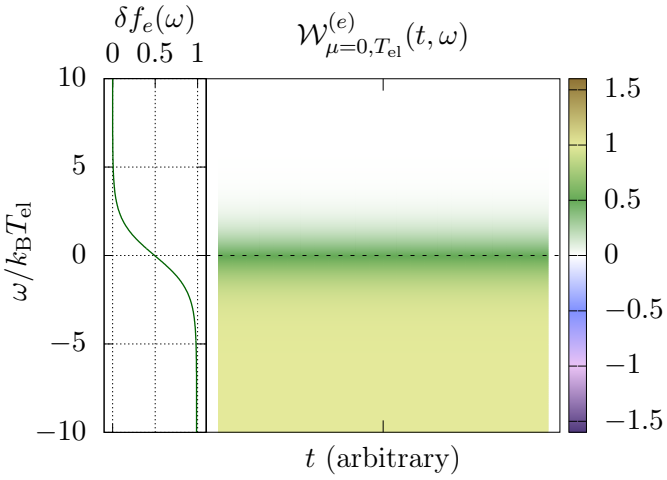

Figure 1.9: Wigner function of the Fermi sea at temperature $T_{\rm el}$ and chemical potential $\mu = 0$. At all times, we recover a Fermi-Dirac distribution in energy. The energy marginal plotted on the left of the graph is therefore a Fermi-Dirac distribution as well.

to compute in the energy representation. Starting from that, it is direct to find the Wigner function of a Fermi sea at chemical potential μ and temperature $T_{\rm el}$:

$$\mathcal{W}^{(e)}_{\mu,T_{\rm el}}(t,\omega) = f_{\mu,T_{\rm el}}(\omega)\,. \tag{1.42}$$

As expected from the stationarity of the state, this Wigner function does not depend on time. It is shown for the case $\mu = 0$ in figure 1.9, as $\mu \neq 0$ corresponds only to a global shift in energies.

Now, let us see how this Wigner function is modified when applying some time dependent voltage to an Ohmic contact. Each electron feels the effect of the applied time dependent potential and accumulates the corresponding electric phase $\phi_V(t) = \int^t V(\tau)\mathrm{d}\tau$. Consequently, the single electron coherence is modified by a time dependent phase

$$\mathcal{G}^{(e)}_{\rm drive}(t|t') = \exp\left(\mathrm{i}\frac{e}{\hbar}\int_{t'}^{t} V(\tau)\mathrm{d}\tau\right)\mathcal{G}^{(e)}_{\mu,T_{\rm el}}(t-t')\,. \tag{1.43}$$

For a constant (DC) potential $V(t) = V_0$, we then have

$$\mathcal{W}^{(e)}_{\rm DC}(t,\omega) = \mathcal{W}^{(e)}_{\mu,T_{\rm el}}\left(t, \omega + \frac{eV_0}{\hbar}\right) \tag{1.44}$$

which is completely equivalent, as expected, to a chemical potential shift: $\mu' = \mu - eV_0/\hbar$.

In the case of an AC drive, the simplest case is a sinusoidal drive, $V(t) = V_0 \cos(2\pi f t)$. For this specific voltage, we can compute analytically the additional phase in the coherence [41]:

$$\exp\left(\mathrm{i}\frac{e}{\hbar}\int_{t'}^{t} V(\tau)\mathrm{d}\tau\right) = \exp\left(\mathrm{i}\frac{2eV_0}{hf}\sin(\pi f\delta t)\cos(2\pi f\bar{t})\right) \tag{1.45}$$

which is equal, using the Bessel decomposition $\mathrm{e}^{\mathrm{i}z\sin(\theta)} = \sum_{n\in\mathbb{Z}} \mathrm{e}^{\mathrm{i}n\theta} J_n(z)$, to

$$\sum_{n\in\mathbb{Z}} \mathrm{e}^{\mathrm{i}n\pi f\delta t} J_n\left(\frac{2eV_0}{hf}\cos(2\pi f\bar{t})\right) . \tag{1.46}$$

From this equation, the full Wigner function is obtained as:

$$\mathcal{W}^{(e)}_{\cos}(t,\omega) = \sum_{n\in\mathbb{Z}} J_n\left(\frac{2eV_0}{hf}\cos(2\pi f t)\right) f_{\mu,T_{\mathrm{el}}}(\omega + n\pi f) . \tag{1.47}$$

This formula shows that three energy scales need to be compared in order to understand the resulting coherence. The first one is the temperature scale $k_{\mathrm{B}}T_{\mathrm{el}}$, which corresponds to the smoothing of the electronic distribution function by thermal fluctuations. When T_{el} goes to 0, the Wigner function (1.47) will present a series of steps of width πf in the ω variable. In the opposite limit $T_{\mathrm{el}} \gg hf$, these steps are smoothed out by thermal fluctuations. The energy scale hf can be interpreted as the energy carried by a monochromatic photon of frequency f such as the one associated with the sinusoidal drive. As it directly appears in the argument of the Bessel function, this energy scale needs to be compared to the electric energy scale eV_0, which represents the classical energy exchanged between the drive and the electronic fluid per half period. The ratio eV_0/hf then estimates the average number of photons absorbed and exchanged by the electronic fluid during a single period.

The classical regime for this type of driving corresponds to $hf \ll k_{\mathrm{B}}T_{\mathrm{el}}$ and $hf \ll eV_0$, respectively meaning that thermal fluctuations smooth the Wigner's behaviour in energy and that large number of photons are exchanged between the drive and the fluid. This is obviously the case for a standard AC drive (220 V, 50 Hz) at room temperature. In that regime, the Wigner function can be approximated by an adiabatic evolution of the Fermi distribution

$$\mathcal{W}^{(e)}_{\mathrm{classical}}(t,\omega) = f_{\mu,T_{\mathrm{el}}}\left(t, \omega + \frac{eV(t)}{\hbar}\right) . \tag{1.48}$$

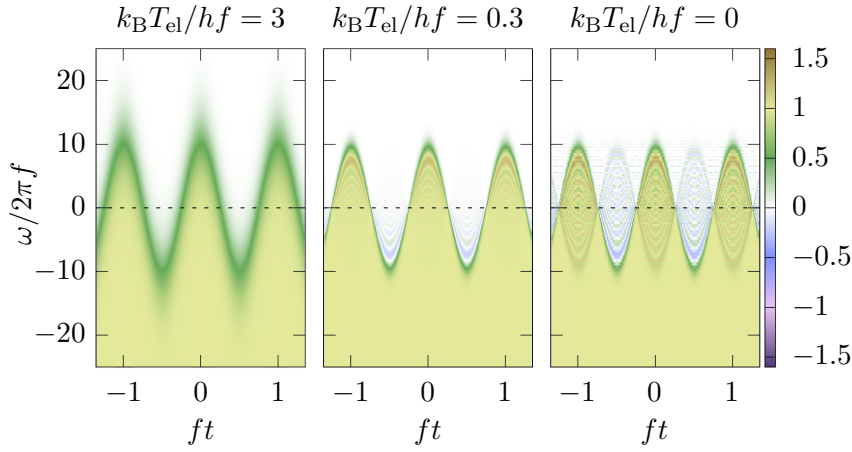

Figure 1.10: Wigner function of the state created when applying a sinusoidal drive to an Ohmic contact, with $eV_0 = 10hf$, for different temperatures. When the temperature is high enough, the evolution in energy is smoothed and everything behaves as an adiabatic evolution of the chemical potential. On the contrary, when the temperature goes to zero, the thermal coherence time of electrons becomes larger than the period and interferences appear, leading to non-classical values of the Wigner function. In this latter case, the Wigner function exhibits steps in the energy direction, a signature of the fact that all energy exchanges at zero temperature need to be multiples of hf.

This classical distribution is presented in the first panel of figure 1.10. When decreasing the electronic temperature below hf/k_B (other panels of that same figure), two things happen:

- The variation of $\mathcal{W}^{(e)}(t,\omega)$ along the energy axis is no longer smooth, but presents steps reflecting that, at low temperatures, all energy exchanges arises from photons of energy hf injected by the drive.

- Interference effects appear and with them values of $\mathcal{W}^{(e)}$ bigger than 1 and smaller than 0. In this case, our drive can no longer be called "classical", as per equation (1.41). This is due to the fact that the thermal coherence time of electrons in the system, $\hbar/k_B T_{el}$, becomes larger than the period $1/f$ of the drive.

The other regime of interest, which may be coined as a "quantum"

regime[6] is the opposite limit where hf becomes the dominant energy scale: $k_\mathrm{B}T_\mathrm{el} \ll eV_0 \ll hf$. In this regime, less than one photon is exchanged per period on average between the drive and the electronic fluid. Only the first few Bessel functions will contribute to the Wigner function, which can thus be expanded as

$$\mathcal{W}^{(e)}_{\cos}(t,\omega) = \mathcal{W}^{(e)}_{\mu,T_\mathrm{el}}(t,\omega) \tag{1.49a}$$

$$- F_{\mu,T_\mathrm{el}}(\omega)\cos(2\pi f t)\left(\frac{eV_0}{hf}\right) \tag{1.49b}$$

$$+ g_{\mu,T_\mathrm{el}}(\omega)\cos^2(2\pi f t)\left(\frac{eV_0}{hf}\right)^2 + \mathcal{O}\left(\left(\frac{eV_0}{hf}\right)^3\right) \tag{1.49c}$$

where we have used the auxiliary functions

$$F_{\mu,T_\mathrm{el}}(\omega) = f_{\mu,T_\mathrm{el}}(\omega+\pi f) - f_{\mu,T_\mathrm{el}}(\omega-\pi f) \tag{1.50a}$$

$$g_{\mu,T_\mathrm{el}}(\omega) = \frac{1}{2}f_{\mu,T_\mathrm{el}}(\omega+2\pi f) + \frac{1}{2}f_{\mu,T_\mathrm{el}}(\omega-2\pi f) - f_{\mu,T_\mathrm{el}}(\omega)\,. \tag{1.50b}$$

At zero temperature, F_{μ,T_el} is equal to -1 in a range $2\pi f$ around the chemical potential μ and zero everywhere else, while g_{μ,T_el} is equal to $1/2$ for $\omega \in]\mu, \mu+2\pi f]$, to $-1/2$ for $\omega \in]\mu-2\pi f, \mu]$, and to zero elsewhere.

Let us have a closer look at the different terms of this development. The first order term given by equation (1.49b) can be interpreted as an harmonic modulation of weak amplitude of the Wigner function for energies between $-hf/2$ and $hf/2$ around the base chemical potential. As the average of a cosine function on a period is zero, no change to the occupation number are linked to this term, meaning that no photon is absorbed by the electronic fluid at first order. This term contributes to the average current with

$$\langle i(t)\rangle_{\text{1st order}} = \frac{e^2}{h}V(t)\,. \tag{1.51}$$

We recover directly the expected response of an edge channel, *i.e.* Ohm's law with a resistance R_K. We will see in section 2.3.1 that this contribution is of particular interest for the tomography protocol used to reconstruct any coherence function from interferometry measurements.

The second order contribution (1.49c) has no effect on the average current, since the integration over ω of g_{μ,T_el} is equal to 0, but it contributes to a change of occupation number. Electrons are added in a

[6] Even though we just saw that quantum effects are by no mean limited to such a regime!

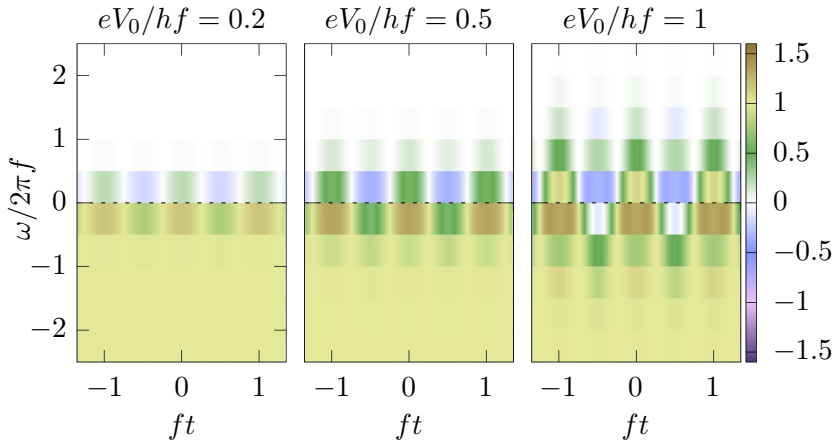

Figure 1.11: Wigner function for a low-amplitude sinusoidal drive applied to an Ohmic contact, at zero temperature. From left to right, as we increase the voltage, we see that the different orders appearing in equation (1.49) lead to processes in wider energy bands. Of course, this type of drive dominated by few-photon processes is completely non-classical.

band of energy hf over the chemical potential and removed in a band of the same width below μ. This is actually the signature of the absorption of a photon of energy hf which creates electron-hole pairs by promoting electrons from below the Fermi level to higher energies. To recover multiphotonic processes in which several photons are absorbed by the system, the drive amplitude needs to be increased. The next terms in the development from equation (1.49) then start to play a role, as depicted in figure 1.11 for excitations of increasing voltage at zero temperature.

Periodic sources

The case we just studied is in reality a specific type of periodic source and we managed to solve it without really using the periodicity property. However, in a completely general case, there are still things to say about coherence and Wigner functions using only the fact that the source is periodic. Indeed, for a generic $T = 1/f$ periodic source, single electron coherence in the time domain has a time-translation invariance

$$\mathcal{G}^{(e)}_{\text{periodic}}(t + T|t' + T) = \mathcal{G}^{(e)}_{\text{periodic}}(t|t')\,. \tag{1.52}$$

Equation (1.52) is completely equivalent to saying that coherence is periodic in the $\bar{t}$ variable, which translates into a direct periodicity of the Wigner function in the time domain, $\mathcal{W}^{(e)}(t,\omega) = \mathcal{W}^{(e)}(t+T,\omega)$ as was the case in the previous paragraph's example.

Time periodicity also greatly simplifies the expression of single electron coherence in the frequency domain, since the variable conjugated to $\bar{t} = (t+t')/2$ is now periodic:

$$\widetilde{\mathcal{G}}^{(e)}_{\text{periodic}}(\omega|\omega') = v_{\text{F}} \sum_{n\in\mathbb{Z}} \delta(\omega - \omega' - 2\pi n f) \widetilde{\mathcal{G}}_n \left(\frac{\omega+\omega'}{2} \right) . \tag{1.53}$$

The functions $\widetilde{\mathcal{G}}_n(\omega)$ are nothing but the harmonics of the Wigner distribution function $\mathcal{W}^{(e)}(t,\omega)$ when expressing its T-periodicity in the t variable:

$$\mathcal{W}^{(e)}(t,\omega) = \sum_{n\in\mathbb{Z}} \widetilde{\mathcal{G}}_n(\omega) \mathrm{e}^{2\mathrm{i}\pi n f t} \tag{1.54}$$

Now, can we find the form of functions $\widetilde{\mathcal{G}}_n$ in a generic case? We already did, without saying it, for the case of a sinusoidal drive: the first few ones can be pretty easily extracted from equation (1.49).

Floquet scattering theory

In a more generic case, there is another possibility to find the form of functions $\widetilde{\mathcal{G}}_n$: we can use Floquet theorem [45, 119], which states that if we apply some periodic potential in a finite region of space, we can find a scattering matrix[7] relating the incoming electronic modes to the outgoing ones in the following form:

$$c_{(\text{out})}(\omega) = \sum_{n\in\mathbb{Z}} S_n(\omega) c_{(\text{in})}(\omega - 2\pi n f) . \tag{1.55}$$

In the case of a periodic driving through an Ohmic contact, we already saw in equation (1.43) that, in the time domain, first order coherence is modified by a phase which depends on the integral of the applied voltage over time. Another way to express the same result is given when looking at the fermionic operators. Under a driving by $V(t)$, they are modified in the following way:

$$\psi_{(\text{out})}(t) = \exp\left(\mathrm{i}\frac{e}{\hbar} \int_{-\infty}^{t} V(\tau)\mathrm{d}\tau \right) \psi_{(\text{in})}(t) . \tag{1.56}$$

[7] In full generality, this matrix can relate modes in different edge channels. Here, we only look at the single channel case.

This is directly equivalent, in the time domain, to the definition given in equation (1.55). By taking a Fourier transform of equation (1.56), we find that the matrix elements S_n are in fact the Fourier coefficients of the added phase, denoted by α_n, given by

$$\exp\left(\mathrm{i}\frac{e}{\hbar}\int_{-\infty}^{t} V(\tau)\mathrm{d}\tau\right) = \sum_{n\in\mathbb{Z}} \alpha_n \mathrm{e}^{-2\mathrm{i}\pi n f t}\,. \tag{1.57}$$

The scattering matrix coefficients $S_n(\omega) = \alpha_n$ do not depend on ω here. The first order coherence in the frequency domain then depends on $\widetilde{\mathcal{G}}_n$ functions of the form

$$\widetilde{\mathcal{G}}_n(\omega) = \sum_{p\in\mathbb{Z}} \alpha_p \alpha_{n-p}^{*} f_{\mu,T_{\mathrm{el}}}(\omega + (n-2p)\pi f) \tag{1.58}$$

and the corresponding Wigner function is given by

$$\mathcal{W}^{(e)}(t,\omega) = \sum_{p,q} \alpha_p \alpha_q^{*} \mathrm{e}^{2\mathrm{i}\pi(q-p)ft} f_{\mu,T_{\mathrm{el}}}(\omega - \pi(p+q)f)\,. \tag{1.59}$$

How can the coefficients α_n be interpreted? Let us look at the transition amplitude to go from an incoming state at energy $\hbar\omega$ to another state of energy $\hbar\omega'$. This amplitude is given by

$$\begin{aligned}\mathcal{A}(\omega\to\omega') &= \left\langle 0 \left| c_{(\mathrm{out})}(\omega') c_{(\mathrm{in})}^{\dagger}(\omega) \right| 0 \right\rangle \\ &= \sum_{n\in\mathbb{Z}} \alpha_n(\omega')\delta(\omega' - \omega - 2\pi n f)\,.\end{aligned} \tag{1.60}$$

The α_n are therefore directly associated with a transition in energy of multiples of hf. They are therefore called photo-assisted transition amplitudes: for $n > 0$, α_n corresponds to the amplitude of probability to absorb n photons of energy hf coming from the drive, and for $n < 0$ it corresponds to the emission of n photons. α_0 is directly the elastic scattering amplitude for an electron at energy $\hbar\omega$. To confirm this interpretation, we can also use the Wigner function to compute the outgoing occupation number per period

$$f(\omega) = \frac{1}{T}\int_{-T/2}^{+T/2} \mathcal{W}^{(e)}(t,\omega)\mathrm{d}t = \sum_{n\in\mathbb{Z}} |\alpha_n|^2 f_{\mu,T_{\mathrm{el}}}(\omega - 2\pi n f)\,. \tag{1.61}$$

As expected from what was said before, this clearly shows that $|\alpha_n|^2$ is the probability to have an event shifting the energy by nhf.

After these considerations on time periodic sources, let us consider the single electron sources described in section 1.1.2. Of course, in a realistic experiment, these sources are operated in a periodic way such that measurements can be made, as will be explained in chapter 2. Yet, for most applications, we can consider single electron sources as one-shot emitters and only study the coherence of a single emitted wavepacket, which we will then repeat over time.

The Leviton source

Let us start with the Leviton source, corresponding to a driving of the Fermi sea with some voltage given in equation (1.3). Its excess Wigner function can be computed analytically for charges that are integer factors of the electron charge [41], but its expression is not that much interesting for us. It is sufficient to know that it is done starting from the energy representation of coherence, as

$$\Delta\widetilde{\mathcal{G}}^{(e)}_{\mathrm{Lev}}(\omega|\omega') = \varphi_{\mathrm{Lev}}(\omega)\varphi^{*}_{\mathrm{Lev}}(\omega') \tag{1.62}$$

with φ_{Lev} the electronic wavefunction describing a Leviton quasiparticle, whose expression is given by

$$\varphi_{\mathrm{Lev}}(\omega) = \sqrt{4\pi\tau_0 v_{\mathrm{F}}}\mathrm{H}(\omega)\mathrm{e}^{-\omega\tau_0}\,, \tag{1.63}$$

τ_0 being the typical width of the Lorentzian pulse, and $\mathrm{H}(\omega)$ the Heaviside distribution.

The corresponding excess Wigner function is displayed in the $q = -e$ case in figure 1.12, and we can see that it exhibits all the features we could expect from such a time-resolved drive:

- It has only low energy contributions, as expected for any classical drive of the Fermi sea, energy levels close to the Fermi levels are populated first.
- It leads to a Lorentzian current centered around the emission time of the excitation.
- It has no hole contribution at negative energies, as expected from the fact that such an excitation should be purely electronic.

We also recover the fact that it contains exactly one excitation, which can be checked by seeing that the integration of a Lorentzian shape of

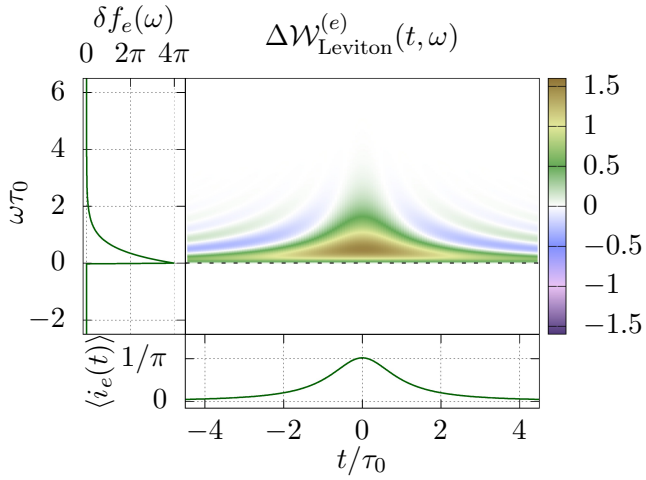

Figure 1.12: Excess Wigner function of a Leviton excitation obtained by applying a Lorentzian voltage to an Ohmic contact. This leads to a Lorentzian shape for the current. As expected, this type of excitation is located mainly near the Fermi level, as can be also seen on the excess occupation number. We can furthermore see that it only has contributions above the Fermi level, meaning that it is a purely electronic excitation. Finally, the negative values of the excess Wigner function at $\omega > 0$ are the signature of the quantum nature of this excitation.

height $1/\pi$ is equal to 1, as is the integral $\int_0^\infty 4\pi \mathrm{e}^{-2\omega}\mathrm{d}\omega/2\pi$. Moreover, we see that this Wigner function exhibits values outside of the $[0, 1]$. As a single electron state, the Leviton is not quasi-classical. This is due to its proximity with the Fermi sea. Indeed, it is known that a single particle wavefunction with a positive Wigner function is Gaussian. As such, its Wigner function is also Gaussian and therefore has infinite spreading in the (t, ω) plane. Any purely electronic wave-function leading to a vanishing Wigner function for $\omega < 0$ cannot be Gaussian and therefore should exhibit negativities.

Energy-resolved excitations

The last case of interest for us is the energy-resolved excitation emitted by the quantum dot, which is called the Landau quasiparticle by analogy with the famous problem of relaxation of energy-resolved excitations originally considered by Landau for justifying his approach to

the interacting electron fluid within normal metals.

This excitation is emitted at some given energy $\hbar\omega_0$ controlled by the amplitude of the drive, and has a typical width in energy $\hbar\gamma$ given by the width of the levels inside the dot, therefore controlled by the transmission of the tunneling barrier. The average current is a decaying half-exponential with timescale $\tau_0 = 1/\gamma$. In the frequency domain, its wavefunction is given by a Lorentzian shape (coming from the shape of levels in the dot), centered around ω_0, with a typical width γ, and truncated so that it is non-zero only for positive energies as expected from an electronic-only wavefunction:

$$\varphi_{\text{Landau}}(\omega) = \sqrt{\frac{v_{\text{F}}\gamma}{\mathcal{N}}}\frac{\mathrm{H}(\omega)}{\omega - \omega_0 + \mathrm{i}\gamma/2} \tag{1.64}$$

with $\mathrm{H}(\omega)$ the Heaviside function and $\mathcal{N}$ the normalization factor ensuring that this wavefunction follows the conventions defined in appendix A. Intuitively, equation (1.64) is justified by making an analogy with the problem of a discrete level coupled to a continuum: once the voltage has been risen above the Fermi level, the dot's populated level is connected by tunneling amplitudes to a continuum of extended single particle levels. In this case, it is known to leak into the continuum and the long time leaked wavefunction is of Weisskopf-Wigner form [176] because of the broad band tunneling coupling [28]. Within the framework of Floquet scattering theory, this form has been justified more rigorously by Moskalets, Haack, and Büttiker [118].

The excess Wigner function associated with such a wavefunction is displayed in figure 1.13 for values of γ and ω_0 close to the one available experimentally: $\hbar\omega_0 = 0.7\,\mathrm{K}$ and $\tau_0 = 1/\gamma = 140\,\mathrm{ps}$. As expected, it has no contribution at negative energies since it has only electronic contributions to coherence, and it exhibits values outside of the $[0, 1]$ range, sign of its quantum nature. It looks very similar to the Leviton Wigner function tilted by 90 degrees, which could be expected since they are both Lorentzian wavepackets, either in the time domain or the energy domain. In particular, the excess Wigner function is very broad in energy at short times and becomes more and more resolved in the energy domain when considered over a broader time interval: this is a direct consequence of Heisenberg uncertainty principle. This is dual to the fact that, when looking close to the Fermi sea, the Leviton's Wigner function spreads over a large time interval.

But this duality is not exact: due to the specific shape of the wavefunction in the energy domain, the Wigner function exhibits a kind of

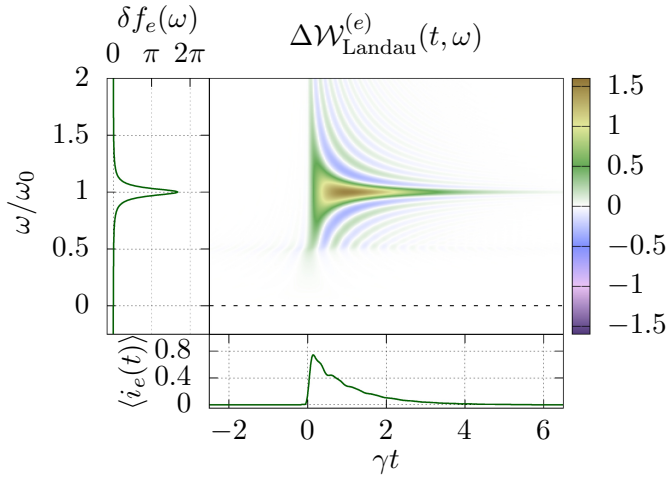

Figure 1.13: Excess Wigner function of an energy-resolved excitation of the form given by equation (1.64) (Landau excitation). Parameters are close to the ones observed experimentally: $\hbar\omega_0 = 0.7\,\text{K}$ and $\tau_0 = 1/\gamma = 140\,\text{ps}$. As for the Leviton, this is a purely electronic and quantum excitation. It is located away from the Fermi sea.

cutoff around $\omega = \omega_0/2$, which can be understood by looking at the coherence in the energy domain, as is shown in figure 1.14. The cutoff in the energy domain at $\omega < 0$ and $\omega' < 0$ means that the Fourier transform along an axis parallel to the x axis is bound to be close to zero whenever we are below $\overline{\omega} = \omega_0/2$. This is why the Leviton and Landau quasi-particle Wigner functions are not exactly deduced from each over by a 90 degrees rotation in the (t, ω) plane.

After half a period, the quantum dot will emit a hole in the system, as can be seen in figure 1.15. The full Wigner function is simply given by a Fermi sea in which we have removed one electron, giving quite the same shape as what was seen before, albeit symmetrically with respect to the chemical potential $\mu = 0$. The excess Wigner function is also show in that same figure, as a way to familiarize ourselves with the excess Wigner functions for "missing electrons". Here, we need to take some extra caution in interpreting the data: even if it mainly exhibits negative values, we need to remember that it is the full Wigner function that needs to be between 0 and 1 for it to be interpreted as a classical probability density. Therefore, for negative energies and at $T_{\text{el}} = 0$, the

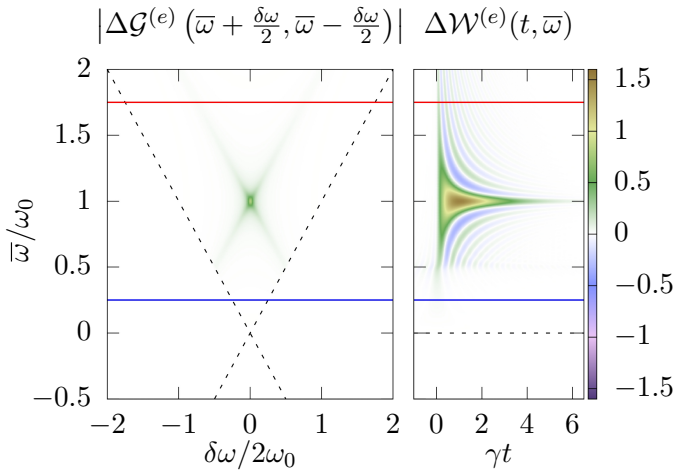

Figure 1.14: *Left*: Modulus of the coherence in the energy domain, for the same excitation as figure 1.13. *Right*: Wigner function of that same excitation. Since both of them are linked *via* Fourier transforms along horizontal lines of this graph, it is clear why the cutoff of $\varphi_{\text{Landau}}(\omega)$ at $\omega < 0$ leads to a vanishing of the Wigner function at $\omega \lesssim \omega_0/2$. For example, the Wigner function along the red and blue lines would have been identical if the coherence was not restrained to the electronic quadrant.

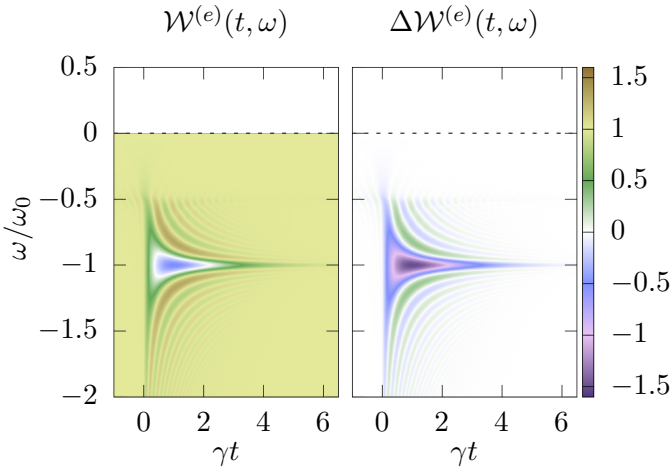

Figure 1.15: *Left*: Electronic Wigner function, for the hole corresponding to the excitation of figure 1.13. We have removed an electron in the wavefunction seen before (with opposite ω_0) from a Fermi sea at zero temperature. *Right*: excess electronic Wigner function for the same hole.

classicality condition can be expressed as $-1 \leq \Delta\mathcal{W}^{(e)} \leq 0$. Here, it does not change the result, but it will be interesting to remember this fact later in this work.

Of course, when looking at the real source emitting a periodic train of such electron-then-hole excitations, we need to change things a bit and be careful, as excitations emitted at one period may share coherences with the ones emitted at other periods. One way to do that is by modelling the full source using Floquet scattering theory [67], which allows to compute the full coherence using a scattering matrix of the form

$$S_n(\omega) = \sum_{p\in\mathbb{Z}} \alpha_p \alpha^*_{p+n} S_{\mathrm{dot}}(\omega - 2\pi p f) \tag{1.65}$$

where the coefficients α_n are defined as before from the square voltage applied to the dot, and the S_{dot} function is the scattering matrix of the dot itself with no voltage applied. It can be obtained rather easily in the time domain by modelling the dot as a Fabry-Pérot interferometer, as was presented in figure 1.4 in which electrons can make a certain number

of turns around an l-sized loop:

$$S_{\mathrm{dot}}(t-t') = \sqrt{1-D}\delta(t-t') - D\sum_{k=1}^{+\infty}\sqrt{1-D}^{k-1}\delta(t-t'-kl/v_{\mathrm{F}})\,. \quad (1.66)$$

Equation (1.66) confirms the intuitive idea that either the electron goes through the dot region without going in ($\sqrt{1-D}\delta(t-t')$) or it goes into the dot, makes k turn and goes out. In the energy domain, this directly leads to

$$S_{\mathrm{dot}}(\omega) = \frac{\sqrt{1-D} - \mathrm{e}^{\mathrm{i}\omega l/v_{\mathrm{F}}}}{1-\sqrt{1-D}\mathrm{e}^{\mathrm{i}\omega l/v_{\mathrm{F}}}}\,. \quad (1.67)$$

The full single electron coherence emitted by the dot can be computed numerically from equation (1.67). In most cases, the result will be quite different from the repeated single-electron emission we studied just before, which means that some work is needed to recover what are the wavepackets emitted by the source and to characterize in which regime and to which extent it really works as a single-excitation emitter. This will be discussed extensively in section 2.3.3.

1.3 Higher order coherences

In his seminal papers [62, 63], Glauber realized that first order photonic coherences are not sufficient to describe all possible experiments. In particular, his approach to photodetection showed that describing multiple photo-detections required more than the first order coherence of the electromagnetic field. In fact, only Gaussian states may be characterized by their first order coherence function alone, a fact that directly comes from the application of Wick's theorem, as seen in section 1.2.2 on page 38. In full generality, we need to define higher order electronic coherences functions of the form

$$\mathcal{G}_{\rho}^{(2e)}(t_1,t_2|t_1',t_2') = \left\langle \psi^{\dagger}(t_1')\psi^{\dagger}(t_2')\psi(t_2)\psi(t_1)\right\rangle_{\rho} \quad (1.68a)$$

$$\mathcal{G}_{\rho}^{(ne)}(t_1,\cdot\cdot,t_n|t_1',\cdot\cdot,t_n') = \left\langle \psi^{\dagger}(t_1')\cdot\cdot\psi^{\dagger}(t_n')\psi(t_n)\cdot\cdot\psi(t_1)\right\rangle_{\rho}\,. \quad (1.68b)$$

$\mathcal{G}^{(2e)}$ is called the second order electronic coherence function, and $\mathcal{G}^{(ne)}$ the n-th order one. Of course, we can define their holes equivalent denoted by $\mathcal{G}^{(nh)}$ by simply reversing the order of annihilation and creation operators. The remainder of this section will be devoted to the properties of these functions, first in the simpler second order case, before

using the knowledge gained in that case to discuss their n-th order generalizations.

1.3.1 Second order coherence

In this section, I will summarize the results obtained by Étienne Thibierge during his PhD [159] concerning the symmetry properties of second order coherence and the definition of excess second order coherence for any source. I will also briefly review the energy and Wigner representations of second order coherence, and introduce simple examples which will be discussed throughout the text when appropriate. It should be noted here that second order coherence has also been defined by Moskalets [117] who has focused on the specific case of sources described by Floquet scattering theory. So far, the difficulty to perform measurements of this quantity has prevented the development of thorough studies of second order coherence in electron quantum optics whereas it is routinely used in the photonics community.

Simple properties

We can derive properties equivalent to the first order coherence ones in the second order case. For example, anticommutation relations impose that

$$\begin{aligned}\mathcal{G}^{(2e)}(t_1,t_2|t_1',t_2') = \mathcal{G}^{(2h)}(t_1',t_2'|t_1,t_2) \\ - \frac{1}{v_\mathrm{F}}\delta(t_1-t_1')\mathcal{G}^{(h)}(t_2'|t_2) + \frac{1}{v_\mathrm{F}}\delta(t_1-t_2')\mathcal{G}^{(h)}(t_1'|t_2) \\ - \frac{1}{v_\mathrm{F}}\delta(t_2-t_1')\mathcal{G}^{(e)}(t_1|t_2') + \frac{1}{v_\mathrm{F}}\delta(t_2-t_2')\mathcal{G}^{(e)}(t_1|t_1')\end{aligned} \tag{1.69}$$

which is the direct equivalent of equation (1.17).

In the same way, by using the same reasoning as the one developed on page 38 for equation (1.18) but with another operator, a Cauchy-Schwartz inequality for second order coherence is obtained

$$\left|\mathcal{G}^{(2e)}(t_1,t_2|t_1',t_2')\right|^2 \leq \mathcal{G}^{(2e)}(t_1,t_2|t_1,t_2)\mathcal{G}^{(2e)}(t_1',t_2'|t_1',t_2')\,. \tag{1.70}$$

This equation implies, as before, that non-diagonal coherences can exist only when the corresponding diagonal coherences are non-zero. Of course, for second order coherence, the diagonal is defined as a plane in the 4D space by taking $t_1 = t_1'$, $t_2 = t_2'$, rather than a standard line in the 2D space as before.

Symmetries and the Pauli principle

The second order coherence function exhibits antisymmetry properties coming directly from the fermionic nature of electrons:

$$\begin{aligned}\mathcal{G}^{(2e)}(t_1,t_2|t_1',t_2') &= -\mathcal{G}^{(2e)}(t_2,t_1|t_1',t_2') \\ &= -\mathcal{G}^{(2e)}(t_1,t_2|t_2',t_1') \\ &= \mathcal{G}^{(2e)}(t_2,t_1|t_2',t_1')\,.\end{aligned} \tag{1.71}$$

Note that the last equation $\mathcal{G}^{(2e)}(1,2|1',2') = \mathcal{G}^{(2e)}(2,1|2',1')$ reflects the indistinguishability of electrons. When combined with the hermiticity condition

$$\mathcal{G}^{(2e)}(t_1,t_2|t_1',t_2') = \mathcal{G}^{(2e)}(t_1',t_2'|t_1,t_2)^* \tag{1.72}$$

the antisymmetry properties show that we only need to compute the value of $\mathcal{G}^{(2e)}$ on one-eighth of the total 4D space of parameters in order to reconstruct its value everywhere.

Because of these symmetries, one must be careful when interpreting electronic second order coherence. The diagonal part of coherence, obtained by focusing on the plane $t_1 = t_1' \cap t_2 = t_2'$ corresponds to correlations between two successive electronic detections, regardless of their order. But all the non-diagonal parts of second order coherence will not be as easy to interpret as the off-diagonal part of first order electronic coherence. This comes directly from equation (1.71), which shows that for each non-zero point in the diagonal plane, three other points in the 4D space are non-zero, two of them being out of the diagonal plane. Consequently, even in the presence of strong electronic decoherence, there will always be a non-vanishing off-diagonal contribution to second order electronic coherence. We will come back to this when discussing the Wigner function representation of second order electronic coherence.

Another interesting feature of the antisymmetry relations (1.71) is the fact that second order coherence is zero on two full 3D hyperplanes of the space of parameters: those defined by $t_1 = t_2$ or $t_1' = t_2'$. This is a direct consequence of the Pauli principle that forbids the existence of two electrons in the same state.

Figure 1.16 depicts these symmetries in a graphical manner. The figure is based on specific variables that are either even or odd when we apply one of the exchanges presented in equation (1.71). These variables

are given by the transformation

$$\bar{t} = \frac{t_1 + t_1' + t_2 + t_2'}{4} = \frac{\bar{t}_1 + \bar{t}_2}{2} \tag{1.73a}$$

$$\delta\bar{t} = \frac{t_1 + t_1'}{2} - \frac{t_2 + t_2'}{2} = \bar{t}_1 - \bar{t}_2 \tag{1.73b}$$

$$\bar{\tau} = \frac{t_1 - t_1' + t_2 - t_2'}{2} = \frac{\tau_1 + \tau_2}{2} \tag{1.73c}$$

$$\delta\tau = t_1 - t_1' - t_2 + t_2' = \tau_1 - \tau_2 \tag{1.73d}$$

where $\bar{t}_i = (t_i + t_i')/2$ and $\tau_i = t_i - t_i'$ are directly equivalent to the ones introduced before for first order coherence. On the figure, we do not use the variable $\bar{t} = (\bar{t}_1 + \bar{t}_2)/2$ as it is the only one that does not change under any of the symmetries considered here. In these new variables, the Pauli principle leads to zero second order coherence on the hyperplanes defined by $\delta\bar{t} = \pm\frac{\delta\tau}{2}$.

A simple example

Before we continue to explore the different representations of second order coherence, let us take a break and have a look at really simple examples in order to understand the physical content of this quantity as well as its symmetries.

A good starting point is the N-electronic state from equation (1.23), $|\Psi_N\rangle = \prod_{n=1}^{N} \psi^\dagger[\varphi_n]\,|\emptyset\rangle$. To begin with, let us focus on the simple case $N = 2$ containing two electrons on top of the true electronic vacuum in orthogonal wavefunctions φ_1 and φ_2. Using Wick's theorem, the second order coherence is obtained as

$$\begin{aligned}\mathcal{G}^{(2e)}_{|\Psi_2\rangle}(t_1, t_2|t_1', t_2') = {} & \varphi_1(t_1)\varphi_2(t_2)\varphi_1^*(t_1')\varphi_2^*(t_2') \\ & - \varphi_1(t_2)\varphi_2(t_1)\varphi_1^*(t_1')\varphi_2^*(t_2') \\ & - \varphi_1(t_1)\varphi_2(t_2)\varphi_1^*(t_2')\varphi_2^*(t_1') \\ & + \varphi_1(t_2)\varphi_2(t_1)\varphi_1^*(t_2')\varphi_2^*(t_1')\,.\end{aligned} \tag{1.74}$$

As expected, it displays all the symmetries discussed before. In order to understand better the physical meaning of this function, let us rewrite it as

$$\mathcal{G}^{(2e)}_{|\Psi_2\rangle}(t_1, t_2|t_1', t_2') = \Phi_{12}(t_1, t_2)\Phi_{12}^*(t_1', t_2') \tag{1.75}$$

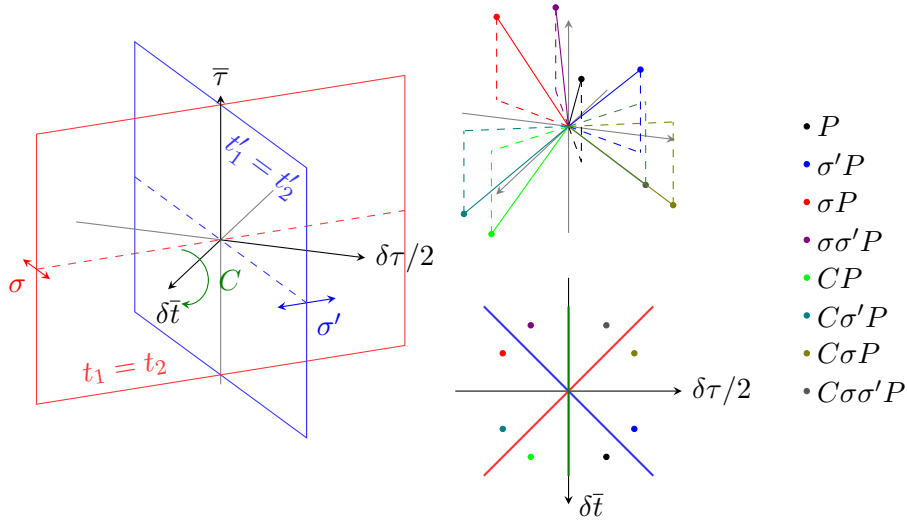

Figure 1.16: Representation of the symmetries of second order coherence. *Left*: at fixed $\bar{t}$, symmetries act on a 3D space parametrized by $(\delta\bar{t}, \bar{\tau}, \delta\tau)$. The mirror symmetry with respect to the red plane, denoted by σ, corresponds to the exchange of t_1 and t_2: coherences on these mirror points are opposite of each other. The same applies for the blue plane, corresponding to the exchange of t_1' and t_2' and denoted by σ'. Due to the Pauli principle, second order coherence is directly equal to 0 within the blue and red planes. The rotation C around the $\delta\bar{t}$ axis by an angle π is equivalent to the exchange of t_1 with t_1' and of t_2 with t_2'. Coherences at these points are complex conjugated. *Right*: Representation of the eight points of the orbit under the action of the three exchange operations in the 3D space (*Top*), and their projections in the 2D plane $\overline{\tau} = 0$ (*Bottom*). Starting from the black point, we create the red one by applying the symmetry with respect to the red plane, and so on for other colors. For example, violet corresponds to the red plane symmetry combined with the blue one. As the blue plane is the image of the red one with respect to the green rotation, there are two equivalent ways of obtaining two of the greenish points.

where we have defined the two-electron wavefunction $\Phi_{12}(t_1, t_2)$ as the Slater determinant built from single-electron wavefunctions φ_1 and φ_2:

$$\Phi_{12}(t_1, t_2) = \det \begin{bmatrix} \varphi_1(t_1) & \varphi_2(t_1) \\ \varphi_1(t_2) & \varphi_2(t_2) \end{bmatrix} . \tag{1.76}$$

Second order coherence therefore contains in this example all the information on the two-electron objects that constitute our system. In this simple case, of course, only one such object is present since we only have two electrons in the full quantum state.

Let us now turn ourselves to the N-electron case $|\Psi_N\rangle$. The electronic second order coherence is directly

$$\mathcal{G}^{(2e)}_{|\Psi_N\rangle}(t_1, t_2|t_1', t_2') = \sum_{n=2}^{N} \sum_{m=1}^{n-1} \Phi_{mn}(t_1, t_2)\Phi^*_{mn}(t_1', t_2') \tag{1.77}$$

where Φ_{mn} is once again the two-electron Slater determinant built from φ_m and φ_n. The antisymmetry of all these wavefunctions implies that $\mathcal{G}^{(2e)}$ still verifies all symmetries discussed before. This indeed shows that $\mathcal{G}^{(2e)}$ contains information on all the two-electron wavefunctions present in the electronic fluid.

Defining the excess 2nd order coherence

The above discussion makes it clear that the Fermi sea has non-zero second order coherence, since it is indeed built as a Slater determinant of a huge number of wavefunctions over the true fermionic vacuum. As for first order coherence, this rises the question of defining the excess second order coherence emitted by an electronic source. However, removing the contribution of the Fermi sea is not enough to really corner the intrinsic excess two-electron coherence which contains the contribution of two-particle states emitted by the source. Part of the total second order coherence comes from correlations between the source and the Fermi sea through classical and quantum processes, in such a way that the total electronic second order coherence can be decomposed as [OP6]

$$\begin{aligned} \mathcal{G}^{(2e)}_{\rho}(t_1, t_2|t_1', t_2') = & \\ & \mathcal{G}^{(2e)}_{\mathrm{F}}(t_1, t_2|t_1', t_2') && \text{(1.78a)} \\ & + \mathcal{G}^{(e)}_{\mathrm{F}}(t_1|t_1')\Delta\mathcal{G}^{(e)}_{\rho}(t_2|t_2') + \mathcal{G}^{(e)}_{\mathrm{F}}(t_2|t_2')\Delta\mathcal{G}^{(e)}_{\rho}(t_1|t_1') && \text{(1.78b)} \\ & - \mathcal{G}^{(e)}_{\mathrm{F}}(t_1|t_2')\Delta\mathcal{G}^{(e)}_{\rho}(t_2|t_1') - \mathcal{G}^{(e)}_{\mathrm{F}}(t_2|t_1')\Delta\mathcal{G}^{(e)}_{\rho}(t_1|t_2') && \text{(1.78c)} \\ & + \Delta\mathcal{G}^{(2e)}_{\rho}(t_1, t_2|t_1', t_2') \,. && \text{(1.78d)} \end{aligned}$$

This equation is represented schematically in figure 1.17: the full second order coherence can be seen as the joint "clicking" of two single electron detectors, one associated with times t_1 and t'_1, the other one with times t_2 and t'_2. What equation (1.78) means is that electrons making those detectors click do not always come from the source S. Obviously, both may come from the Fermi sea (1.78a), leading simply to the *Fermi* contribution to second order coherence. It is also possible to detect one electron from the Fermi sea and one from the source (1.78b). These two terms correspond to *classical correlations* between the source and the Fermi sea, and would also be present if we were discussing classical particles. The third line (1.78c) is of purely quantum nature: it corresponds to *quantum exchanges* between the source and the Fermi sea. This means that we cannot assign an origin to the detected electrons. Furthermore, the minus sign for these terms is a direct consequence of fermionic statistics. Finally, the last term (1.78d) is the intrinsic contribution of the source to second order coherence, which we will sometimes call the *excess* contribution. This full equation may indeed be understood as the definition of this intrinsic quantity from the full second order coherence and the excess single electron coherence. Of course, the intrinsic second order coherence satisfies the properties discussed in equations (1.71) and (1.72), as can be checked easily using the properties of first order coherence.

One additional property that can be derived directly from this decomposition, using Wick's theorem[8], is the fact that, for a single electron excitation on top of the Fermi sea $|\Psi_e\rangle = \psi^\dagger[\varphi_e]\,|F_\mu\rangle$, we have

$$\Delta\mathcal{G}^{(2e)}_{|\Psi_e\rangle}(t_1, t_2|t'_1, t'_2) = 0\,. \tag{1.79}$$

This is also valid for single-hole states of the form $|\Psi_h\rangle = \psi[\varphi_h]\,|F_\mu\rangle$. This was expected: since the source only corresponds to one excitation, there are no processes in which we could detect two electrons as coming from it. By contrast, a single electron-hole pair would lead to a non-zero intrinsic second order coherence.

More generally, the intrinsic second order coherence for any many-body state satisfying Wick's theorem is easy to compute. Using Wick's

[8]Remember that the Fermi sea is an equilibrium state, and therefore Gaussian.

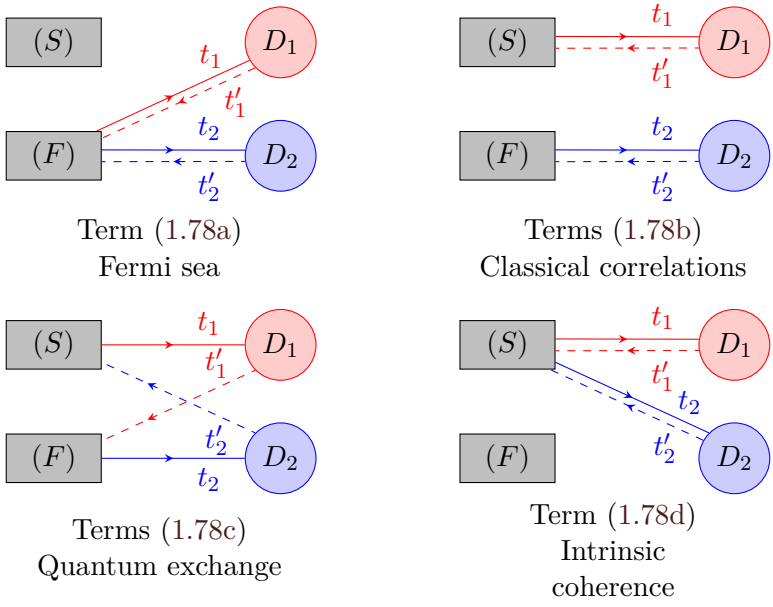

Figure 1.17: A schematic representation of second order coherence in the presence of the Fermi sea. $\mathcal{G}^{(2e)}(t_1, t_2|t'_1, t'_2)$ can be interpreted as a two-electron detection event by detectors D_1 associated with times t_1 and t'_1 and D_2 (times t_2 and t'_2). We can divide the contribution to coherence into four parts, depending on which of the incoming parts (Fermi sea or source) the ψ and $\psi^\dagger$ operators are applied.

theorem, the full second order coherence is obtained as

$$\begin{aligned}\mathcal{G}^{(2e)}_{\text{Wick}}(t_1,t_2|t_1',t_2') &= \mathcal{G}^{(e)}(t_1|t_1')\mathcal{G}^{(e)}(t_2|t_2') - \mathcal{G}^{(e)}(t_1|t_2')\mathcal{G}^{(e)}(t_2|t_1') \\ &= \det\begin{bmatrix}\mathcal{G}^{(e)}(t_1|t_1') & \mathcal{G}^{(e)}(t_1|t_2') \\ \mathcal{G}^{(e)}(t_2|t_1') & \mathcal{G}^{(e)}(t_2|t_2')\end{bmatrix}\end{aligned} \tag{1.80}$$

Using $\mathcal{G}^{(e)}(t|t') = \mathcal{G}^{(e)}_{\text{F}}(t|t') + \Delta\mathcal{G}^{(e)}(t|t')$ in equation (1.80), we recover all the terms from equation (1.78) and find that

$$\Delta\mathcal{G}^{(2e)}_{\text{Wick}}(t_1,t_2|t_1',t_2') = \det\begin{bmatrix}\Delta\mathcal{G}^{(e)}(t_1|t_1') & \Delta\mathcal{G}^{(e)}(t_1|t_2') \\ \Delta\mathcal{G}^{(e)}(t_2|t_1') & \Delta\mathcal{G}^{(e)}(t_2|t_2')\end{bmatrix} \tag{1.81}$$

which gives in a straightforward way equation (1.79) as soon as $\Delta\mathcal{G}^{(e)}_{|\Psi_e\rangle}(t|t') = \varphi_e(t)\varphi_e^*(t')$.

Energy representation

As for first order coherence function, we will sometimes use an energy representation of second order coherence, which is defined as

$$\begin{aligned}&\widetilde{\mathcal{G}}^{(2e)}(\omega_1,\omega_2|\omega_1',\omega_2') \\ &\quad = v_{\text{F}}^4 \int \mathcal{G}^{(2e)}(t_1,t_2|t_1',t_2')\mathrm{e}^{\mathrm{i}(\omega_1 t_1+\omega_2 t_2-\omega_1' t_1'-\omega_2' t_2')}\mathrm{d}t_1\mathrm{d}t_2\mathrm{d}t_1'\mathrm{d}t_2' \,.\end{aligned} \tag{1.82}$$

As expected, in terms of fermionic operators, we have

$$\widetilde{\mathcal{G}}^{(2e)}_{\rho}(\omega_1,\omega_2|\omega_1',\omega_2') = 4\pi^2 v_{\text{F}}^2 \left\langle c^\dagger(\omega_2')c^\dagger(\omega_1')c(\omega_1)c(\omega_2)\right\rangle_\rho \,. \tag{1.83}$$

The intrinsic second order coherence in the energy domain can also be defined using the process described by equation (1.78) in the time domain. Naturally, all symmetry properties linked to the exchange of two variables are still valid in this representation and the Pauli principle leads to a cancellation of coherence in the 3D spaces $\omega_1 = \omega_2$ and $\omega_1' = \omega_2'$.

More interestingly, in a direct analogy with what we saw for first order coherence, the energy representation allows a simple access to the nature of the excitations leading to coherences. Here, we need to divide the full 4-dimensional space into 6 sectors:

- (2e) : electron pairs, all frequencies positive.
- (2h) : hole pairs, all frequencies negative.

- (e+h) : one electron and one hole, $\omega_1\omega_2 < 0$ and $\omega_1'\omega_2' < 0$.
- (e+e/h) : one electron and one e/h pair, 3 frequencies positives, one negative.
- (h+e/h) : one hole and one e/h pair, 3 frequencies negative and one positive.
- (2e/h) : two e/h pairs, either $\omega_i > 0$ and $\omega_i' < 0$ or $\omega_i < 0$ and $\omega_i' > 0$.

These 6 sectors are stable under the effect of symmetries, as could be expected, and obviously do not overlap with each other. This will prove useful at the very end of this manuscript, in section 3.5, when we will try to discuss the physics behind interaction-induced second order coherence.

Of course, it might also be useful to change variables in the same way as was done in equation (1.73), and define

$$\overline{\omega} = \frac{\omega_1 + \omega_1' + \omega_2 + \omega_2'}{4} = \frac{\overline{\omega}_1 + \overline{\omega}_2}{2} \tag{1.84a}$$

$$\delta\overline{\omega} = \frac{\omega_1 + \omega_1'}{2} - \frac{\omega_2 + \omega_2'}{2} = \overline{\omega}_1 - \overline{\omega}_2 \tag{1.84b}$$

$$\overline{\Omega} = \frac{\omega_1 - \omega_1' + \omega_2 - \omega_2'}{2} = \frac{\Omega_1 + \Omega_2}{2} \tag{1.84c}$$

$$\delta\Omega = \omega_1 - \omega_1' - \omega_2 + \omega_2' = \Omega_1 - \Omega_2 \tag{1.84d}$$

where $\overline{\omega}_i = (\omega_i + \omega_i')/2$ and $\Omega_i = \omega_i - \omega_i'$ just like for first order coherence. Rewriting the Fourier transform using these reduced energy variables explicitly shows which one is conjugated with which reduced time variable:

$$\widetilde{\mathcal{G}}^{(2e)}(\overline{\omega}, \delta\overline{\omega}, \overline{\Omega}, \delta\Omega) = v_{\mathrm{F}}^4 \int \exp\left[\mathrm{i}\left(2\overline{\omega}\,\overline{\tau} + 2\overline{\Omega}\,\overline{t} + \frac{1}{2}\delta\Omega\delta\overline{t} + \frac{1}{2}\delta\overline{\omega}\delta\tau\right)\right] \mathcal{G}^{(2e)}(\overline{t}, \delta\overline{t}, \overline{\tau}, \delta\tau)\,\mathrm{d}\overline{t}\,\mathrm{d}\delta\overline{t}\,\mathrm{d}\overline{\tau}\,\mathrm{d}\delta\tau\,. \tag{1.85}$$

In these variables, the Pauli principle leads to an annulation of coherence in the 3D spaces defined by $\delta\overline{\omega} = \pm\frac{\delta\Omega}{2}$. The 6 sectors defined above are still valid, but they are not that easy to represent in a fully comprehensive manner. Yet, in the $\overline{\Omega} = 0$ subspace, we can draw quite easily the projection of most of these sectors, as can be seen in figure 1.18. The only sector that does not appear in this subspace is the (2e/h) one,

since it is impossible to satisfy both its condition of existence and $\overline{\Omega} = 0$. However, this $\overline{\Omega} = 0$ subspace is of much interest for us, as we will explain just now, and will be the one we use the most in this manuscript.

Fermi sea coherence and stationary states

As a first example of second order coherence, it is instructive to compute the second order of a Fermi sea with temperature T_{el} and chemical potential $\mu = 0$. As its first order coherence is, from equation (1.37),

$$\widetilde{\mathcal{G}}^{(e)}_{T_{\mathrm{el}},\mu=0}(\omega|\omega') = 2\pi v_{\mathrm{F}}\delta(\omega-\omega')f_{T_{\mathrm{el}}}\left(\frac{\omega+\omega'}{2}\right) \tag{1.86}$$

we can use Wick's theorem to get

$$\begin{aligned}
&\widetilde{\mathcal{G}}^{(2e)}_{T_{\mathrm{el}},\mu=0}(\omega_1,\omega_2|\omega_1',\omega_2') \\
&\quad= \widetilde{\mathcal{G}}^{(e)}(\omega_1|\omega_1')\widetilde{\mathcal{G}}^{(e)}(\omega_2|\omega_2') - \widetilde{\mathcal{G}}^{(e)}(\omega_1|\omega_2')\widetilde{\mathcal{G}}^{(e)}(\omega_2|\omega_1') && \text{(1.87a)} \\
&\quad= 4\pi^2 v_{\mathrm{F}}^2 \\
&\qquad\times\Big[\delta(\omega_1-\omega_1')\delta(\omega_2-\omega_2')f_{T_{\mathrm{el}}}(\omega_1)f_{T_{\mathrm{el}}}(\omega_2) && \text{(1.87b)} \\
&\qquad-\delta(\omega_1-\omega_2')\delta(\omega_2-\omega_1')f_{T_{\mathrm{el}}}(\omega_1)f_{T_{\mathrm{el}}}(\omega_2)\Big].
\end{aligned}$$

The Fermi sea contribution to first order coherence is located in two 2D subspaces $(\omega_1 = \omega_1') \cap (\omega_2 = \omega_2')$ or $(\omega_1 = \omega_2') \cap (\omega_2 = \omega_1')$, meaning that the $c^\dagger$ operators populate back one of the removed electronic excitation. In those subspaces, it can be non-zero only when both energies are populated, which is given by the Fermi-Dirac distribution. In order to visualize this coherence, it will be easier to use the reduced variables:

$$\begin{aligned}
\widetilde{\mathcal{G}}^{(2e)}_{T_{\mathrm{el}},\mu=0}(\overline{\omega},\delta\overline{\omega},\overline{\Omega},\delta\Omega) &= 4\pi^2 v_{\mathrm{F}}^2\delta(\overline{\Omega}) \\
&\quad\times\Big[\delta(\delta\Omega)f_{T_{\mathrm{el}}}\left(\overline{\omega}+\frac{\delta\overline{\omega}}{2}\right)f_{T_{\mathrm{el}}}\left(\overline{\omega}-\frac{\delta\overline{\omega}}{2}\right) \\
&\quad-\delta(\delta\overline{\omega})f_{T_{\mathrm{el}}}\left(\overline{\omega}+\frac{\delta\Omega}{2}\right)f_{T_{\mathrm{el}}}\left(\overline{\omega}-\frac{\delta\Omega}{2}\right)\Big].
\end{aligned} \tag{1.88}$$

We see here that the two planes of interest are both contained in the 3D subspace $\overline{\Omega} = 0$. We can therefore draw the second order coherence of the Fermi sea easily, as shown in figure 1.19 for the specific case of

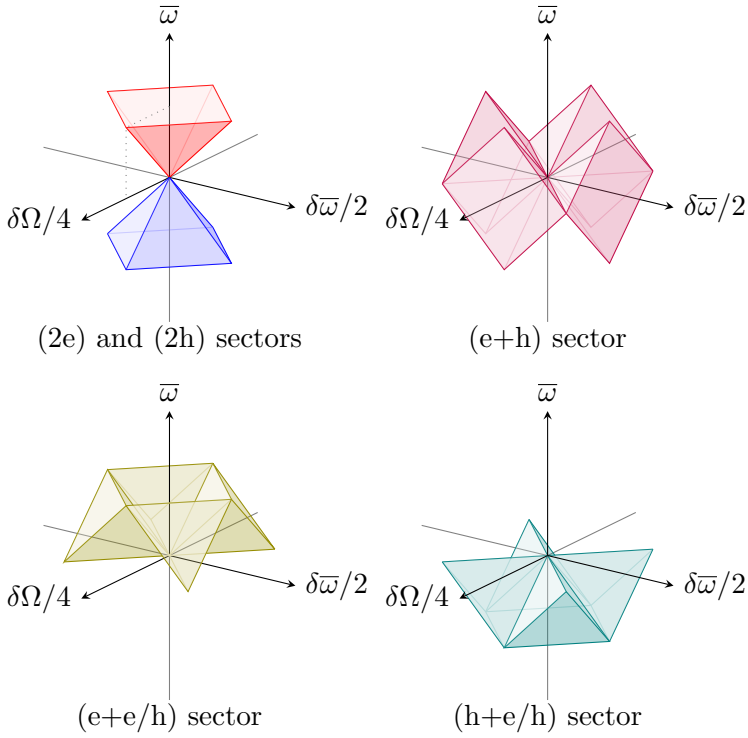

Figure 1.18: A drawing of the different two-excitations sectors that appear in second order coherence, in the subspace $\overline{\Omega} = 0$. This subspace will be the one we use most of the time in this manuscript, even if it does not give access to all possible types of coherences. In particular, the (2e/h) sector corresponding to coherences between two electron/hole pairs does not appear in this subspace. For any of the 5 others, we have only shown a finite part of the full sector. For example, the (2e) sector (in red) corresponds to the extension of the reversed pyramid seen here up to $\overline{\omega} = +\infty$, while the (2h) one (in blue), goes all the way down to $\overline{\omega} = -\infty$. The three others sectors would extend in the direction of their outward facing faces. It is easy to see that all 5 parts sum up to the full space displayed here.

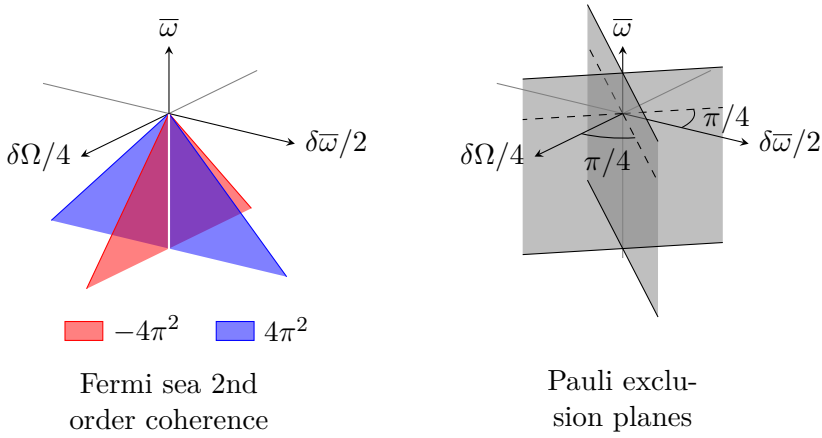

Fermi sea 2nd order coherence

Pauli exclusion planes

Figure 1.19: Second order coherence function of the Fermi sea (see equation (1.88)) at zero temperature and zero chemical potential, in the 3D subspace $\overline{\Omega} = 0$. It is non-zero only in two orthogonal planes, $\delta\Omega = 0$ and $\delta\overline{\omega} = 0$. In those planes, it is equal to the product of two Fermi-Dirac distributions, which explains the triangular shape. Due to the Pauli principle it is also equal to 0 at the intersection of the two planes discussed above. In the general case, the Pauli principle imposes that second order coherence vanishes on the two planes shown on the right panel.

zero temperature. As could be expected from our division into different excitations sectors, we see that the Fermi sea is fully contained within the (2h) sector.

As was already discussed for first order coherence, the Fermi sea is only a particular stationary state, and the only thing we need to change to recover the results for any stationary state is replacing the Fermi-Dirac distribution by the real electronic distribution of that particular state (see for example equation (1.35)). Defining the excess occupation number as before by subtracting the Fermi-Dirac distribution, $\delta f(\omega) = f(\omega) - f_{\mu,T_{\text{el}}}(\omega)$, the excess second order coherence in a stationary case has exactly the same form as the one of the Fermi sea, but with $\delta f(\omega)$

instead of $f_{\mu,T_{\rm el}}(\omega)$:

$$\begin{aligned}\Delta\widetilde{\mathcal{G}}^{(2e)}_{\rm stat}(\omega_1,\omega_2|\omega_1',\omega_2') = 4\pi^2 v_{\rm F}^2 \\ \times\Big[\delta(\omega_1-\omega_1')\delta(\omega_2-\omega_2')\delta f(\omega_1)\delta f(\omega_2) \\ -\delta(\omega_1-\omega_2')\delta(\omega_2-\omega_1')\delta f(\omega_1)\delta f(\omega_2)\Big]\,.\end{aligned} \tag{1.89}$$

Other simple examples

There are two more simple examples that we are going to discuss in this section: a single energy-resolved excitation above the Fermi sea, and two such excitations above the Fermi sea.

We first look at an electron emitted at an energy ω_0, $c^\dagger(\omega_o)\,|F\rangle$. In such a diverging case, we will not be interested in the real values of second order coherence, but rather in finding the points where it is non-zero. The result is displayed in figure 1.20. We recognize the Fermi sea contribution, as well as 4 lines corresponding to correlations and exchange terms, which are the product of the point-like first order coherence for the emitted electron with the half-line first order coherence of the Fermi sea. Note that this coherence is fully contained within the $\overline{\Omega}=0$ subspace.

The second simple example we are interested in is one with two excitations emitted above the Fermi sea, $c^\dagger(\omega_1)c^\dagger(\omega_2)\,|F\rangle$. Once again, second order coherence is fully contained within the $\overline{\Omega}=0$ subspace, and points where it is non-zero are displayed in figure 1.21. Just as before, we recognize the Fermi contribution and lines corresponding to the quantum exchanges and correlation terms. Yet, we also have a new contribution coming from coherences between the two emitted electrons, appearing in the (2e)-part of this coherence subspace. This contribution is simply the intrinsic coherence $\Delta\mathcal{G}^{(2e)}$ associated with our state!

At the very end of this manuscript, in section 3.5.2, we will use again this type of states and study their second order coherence in presence of interaction.

Wigner representation

To conclude this part on second order coherence, let us take a look at a mixed energy-time representation, which is the direct equivalent of

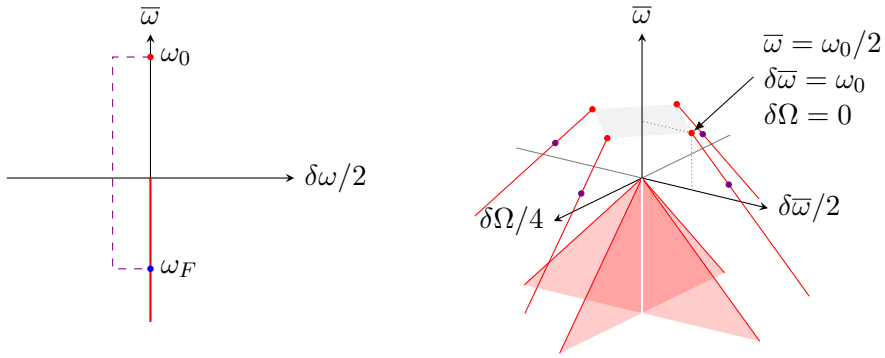

First order coherence

Second order coherence

Figure 1.20: A schematic vision of coherences for a single electron emitted with a resolved energy ω_0 above a Fermi sea at zero temperature. *Left*: First order coherence. It is completely contained in the $\delta\omega = 0$ subspace, and displays an half-line corresponding to the Fermi sea, and a single point at $\overline{\omega} = \omega_0$ corresponding to the injected excitation. *Right*: Second order coherence. With a single injected electron, all terms that appear are either coming from the Fermi sea contribution, or from correlations and quantum exchanges. This leads to 4 half-lines stopping at $\overline{\omega} = \omega_0/2$, that can be understood in a simple way. For example, all 4 purple points are coming from correlations and exchanges between the emitted excitation at ω_0 and the specific electron at energy ω_F from the Fermi sea highlighted on the first order coherence. Changing which specific electron from the Fermi sea we chose leads to the full red line.

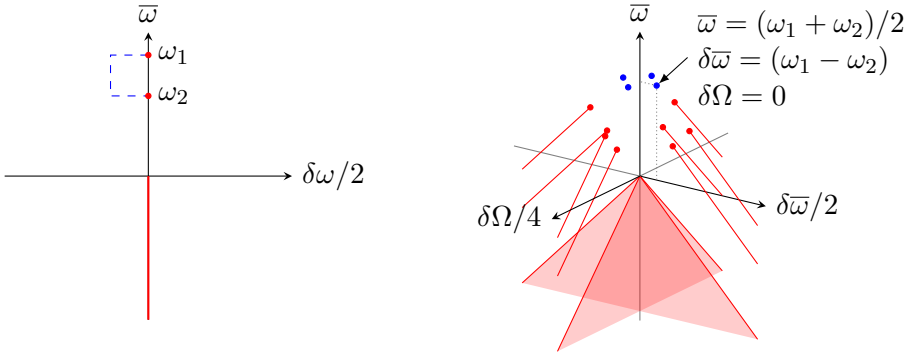

First order coherence

Second order coherence

Figure 1.21: A schematic vision of coherences for two electrons emitted with resolved energies ω_1 and ω_2 above a Fermi sea at zero temperature. *Left*: First order coherence. It is completely contained in the $\delta\omega = 0$ subspace, and displays an half-line corresponding to the Fermi sea, and two points corresponding to the injected excitations. *Right*: Second order coherence. We recover the Fermi sea contribution as well as the four terms coming from correlations and quantum exchanges, in the same way as for figure 1.20. Yet, 4 new points appear, corresponding to coherences between the two emitted excitations: the intrinsic second order coherence of our state.

Wigner representation:

$$\mathcal{W}^{(2e)}(\bar{t}_1,\overline{\omega}_1;\bar{t}_2,\overline{\omega}_2) \tag{1.90}$$
$$= v_{\mathrm{F}}^2 \int \mathcal{G}^{(2e)}\left(\bar{t}_1+\frac{\tau_1}{2},\bar{t}_2+\frac{\tau_2}{2}\middle|\,\bar{t}_1-\frac{\tau_1}{2},\bar{t}_2-\frac{\tau_2}{2}\right)\mathrm{e}^{\mathrm{i}(\overline{\omega}_1\tau_1+\overline{\omega}_2\tau_2)}\mathrm{d}\tau_1\tau_2\,.$$

As before, we will drop the $\bar{\cdot}$ superscript for simplicity when using only Wigner functions. The symmetry property of second order coherence implies that

$$\mathcal{W}^{(2e)}(t_1,\omega_1;t_2,\omega_2) = \mathcal{W}^{(2e)}(t_2,\omega_2;t_1,\omega_1) \tag{1.91}$$

reflecting the indistinguishability of electrons. Exactly as for the Wigner representation of single electron coherence, the Wigner representation of two-electron coherence within a single edge channel is also real. However, the anti-symmetry of the two-electron coherence which reflects the fermionic statistics of electrons has drastic implications.

As explained in our recent work [OP5], the Wigner representation of two electron coherence exhibits essential non-classical features. The natural extension of the definition of quasi-classicality to two-electron Wigner distribution would be that $0 \leq \mathcal{W}^{(2e)}(t_1,\omega_1,t_2,\omega_2) \leq 1$ so that it could be interpreted as a two-electron time dependent distribution function.

A natural example of a quasi-classical two electron Wigner distribution arises when considering two edge channels. In that case, we can define an inter-channel two-electron distribution, as the Fourier transform of $\mathcal{G}^{(2e)}(1t_1,2t_2|1t_1',2t_2')$, the 1 and 2 variables meaning that the corresponding ψ and $\psi^\dagger$ operators act on the specified channel. When computing this quantity, we find that

$$\mathcal{W}^{(2e)}(1,t_1,\omega_1;2,t_2,\omega_2) = \mathcal{W}_1^{(e)}(t_1,\omega_1)\,\mathcal{W}_2^{(e)}(t_2,\omega_2)\,. \tag{1.92}$$

This product expression reflects the role of the edge channel index as an orbital degree of freedom breaking the indistinguishability between electrons within edge channel 1 and electrons within edge channel 2. It also implies that if $\mathcal{W}_1^{(e)}$ and $\mathcal{W}_2^{(e)}$ are both quasi-classical, then $\mathcal{W}^{(2e)}(1,t_1,\omega_1;,2,t_2,\omega_2)$ is also quasi-classical.

On the other hand, considering the two-electron Wigner distribution for electrons within the same edge channel systematically leads to non classical $\mathcal{W}^{(2e)}$ because of quantum exchange. The case of a pure two-electron excitation on top of the Fermi sea $\psi^\dagger[\varphi_1]\psi^\dagger[\varphi_2]\,|F\rangle$ where $\varphi_{1,2}$

are identical wavepackets φ_e respectively shifted by times $\pm\tau/2$, already displays this property since we have in that case

$$\begin{aligned}\Delta\mathcal{W}^{(2e)}(t_1,\omega_1;t_2,\omega_2) = \\ \mathcal{W}^{(e)}_{\varphi_1}(t_1,\omega_1)\mathcal{W}^{(e)}_{\varphi_2}(t_2,\omega_2) &\quad (1.93a)\\ +\mathcal{W}^{(e)}_{\varphi_2}(t_1,\omega_1)\mathcal{W}^{(e)}_{\varphi_1}(t_2,\omega_2) &\quad (1.93b)\\ -2\cos((\omega_1-\omega_2)\tau))\mathcal{W}^{(e)}_{\varphi_e}(t_1,\omega_1)\mathcal{W}^{(e)}_{\varphi_e}(t_2,\omega_2)\,. &\quad (1.93c)\end{aligned}$$

The oscillating term (1.93c) arises from the antisymmetry of $\Delta\mathcal{G}^{(2e)}$ and is responsible for the non-classicality of the Wigner distribution function. Note that these oscillations happen in the energy difference. Energy shifted excitations would lead to oscillations in the variable $t_1 - t_2$. This is for example the case when computing $\mathcal{W}^{(2e)}$ for a thermal equilibrium state:

$$\begin{aligned}&\mathcal{W}^{(2e)}_{\mu=0,T_{\rm el}}(t_1,\omega_1;t_2,\omega_2) = \qquad (1.94)\\ &f_{T_{\rm el}}(\omega_1)f_{T_{\rm el}}(\omega_2) - 2\pi k_{\rm B}T_{\rm el}\delta(\omega_1-\omega_2)f_{\rm B}(\omega_{\rm tot})\frac{\sin(\omega_{\rm tot}t_{12})}{\sinh(t_{12}/\tau_{\rm th}(T_{\rm el}))}\end{aligned}$$

where $\omega_{\rm tot} = \omega_1 + \omega_2$, $t_{12} = t_1 - t_2$ and $\tau_{\rm th}(T_{\rm el}) = \hbar/k_B T_{\rm el}$ denotes the thermal coherence time for electrons at electronic temperature $T_{\rm el}$. Here $f_{\rm B}$ denotes the Bose distribution at temperature $T_{\rm el}$. The singular oscillating term occurring for $\omega_1 = \omega_2$ is a signature of the Pauli principle. These t_{12} oscillations correspond to the Friedel oscillations associated with two electrons at energies $\hbar\omega_1$ and $\hbar\omega_2$, and are damped over a time scale corresponding to the thermal electron coherence time $\tau_{\rm th}(T_{\rm el})$.

We will not go into any more details here on second order coherence, but will turn ourselves to the completely general case, for which we will briefly present the generalizations of most properties seen in this section.

1.3.2 n-th order coherence

Exactly as in photonics, the $\mathcal{G}^{(ne)}$ functions are natural generalizations of what we have just described for second order coherence. For the sake of brevity, we will denote the list $(t_1, t_2, \cdots, t_n)$ by $\mathbf{t}$, and its counterpart for primed variables by $\mathbf{t}'$ throughout the present section.

First properties and symmetries

Exactly as before, a Cauchy-Schwarz inequality is also valid for higher order electronic coherences:

$$\left|\mathcal{G}^{(ne)}(\mathbf{t}|\mathbf{t}')\right|^2 \leq \mathcal{G}^{(ne)}(\mathbf{t}|\mathbf{t})\mathcal{G}^{(ne)}(\mathbf{t}'|\mathbf{t}')\,. \tag{1.95}$$

It has the same exact implications as before, and we will still call diagonal coherence the part of coherence contained in the n-dimensional space defined by $\mathbf{t} = \mathbf{t}'$. A similar one is also valid in the frequency domain.

Of course, since the link between electronic and holes coherence comes from anticommutation properties, they will be related at higher orders. Yet, it is quite tedious to write in a general case as every smaller order appears in the relation. Since we will not be interested in hole n-th order coherences in this thesis, the full formula will not be given here.

Fermi statistics also lead to antisymmetry properties in this general case. If we exchange any two times t_i and t_j, the coherence function is just transformed in its opposite. This means that we can apply any permutation of indexes in the list $\mathbf{t}$, and find that the coherence in the new point is equal to its value in the old one, times the signature of the permutation. Since we can do the same thing to $\mathbf{t}'$, we can summarize it in the following form:

$$\forall\,(\sigma,\sigma')\in\mathfrak{S}_n^2,\quad \mathcal{G}^{(ne)}(\mathbf{t}|\mathbf{t}') = \epsilon(\sigma)\epsilon(\sigma')\mathcal{G}^{(ne)}\left(\sigma[\mathbf{t}]|\sigma'[\mathbf{t}']\right) \tag{1.96}$$

where $\sigma[\mathbf{t}]$ denotes the list $(t_{\sigma(1)}, t_{\sigma(2)}, \cdots, t_{\sigma(n)})$ obtained by applying the permutation σ to the different coordinates of the $\mathbf{t}$ vector, and $\epsilon(\sigma)$ is the signature of σ.

The hermiticity condition still implies

$$\mathcal{G}^{(ne)}(\mathbf{t}|\mathbf{t}') = \mathcal{G}^{(ne)}(\mathbf{t}'|\mathbf{t})^* \tag{1.97}$$

When putting all these properties together, we find that we only need to compute the value of the n-th order coherence function in $\frac{1}{2(n!)^2}$ of the full n-dimensional space[9], since the cardinal of $\mathfrak{S}_n$ is $n!$. For obvious reasons, we will not try to show graphically all the points that arise from all those symmetries, and we will not construct reduced variables in the general case even if it could in principle be done.

[9] We can directly verify that the $n = 2$ case corresponds to what we saw before.

Finally, the Pauli principle is still valid for n-th order coherence, which means that as soon as there is a pair $t_i = t_j$ or $t'_i = t'_j$, coherence will be zero. This means that there are $n(n-1)$ spaces of dimension $(2n-1)$ where the n-th order electronic coherence vanishes.

A simple example

Let us consider our favorite N-electron state $|\Psi_N\rangle = \prod_{k=1}^{N} \psi^\dagger[\varphi_k]\,|\emptyset\rangle$ once again. When $N > n$, this state has non-zero $\mathcal{G}^{(ne)}$ coherence. This means that the Fermi sea exhibits electronic coherence at all orders, since it is exactly such a state but with an infinite number of electrons. To compute $\mathcal{G}^{(ne)}_{|\Psi_N\rangle}$, we will do exactly the same steps as for equation (1.77), and find

$$\mathcal{G}^{(ne)}_{|\Psi_N\rangle}(\mathbf{t}|\mathbf{t}') = \sum_{i_1>i_2>\cdots>i_n} \Phi_{i_1,i_2,\cdots,i_n}(\mathbf{t})\Phi^*_{i_1,i_2,\cdots,i_n}(\mathbf{t}') \tag{1.98}$$

where $\Phi_{i_1,i_2,\cdots,i_n}$ is the n-electron wavefunction built from wavefunctions $\varphi_{i_1},\cdots,\varphi_{i_n}$, each index being taken in $\{1,\cdots,N\}$

$$\Phi_{i_1,i_2,\cdots,i_n}(t_1,t_2,\cdot\cdot,t_n) = \det\begin{bmatrix} \varphi_{i_1}(t_1) & \varphi_{i_2}(t_1) & \cdots & \varphi_{i_n}(t_1) \\ \varphi_{i_1}(t_2) & \varphi_{i_2}(t_2) & \cdots & \varphi_{i_n}(t_2) \\ \vdots & \vdots & \ddots & \vdots \\ \varphi_{i_1}(t_n) & \varphi_{i_2}(t_n) & \cdots & \varphi_{i_n}(t_n) \end{bmatrix}. \tag{1.99}$$

Naturally, we recover the fact that n-th order electronic coherence contains all the information on the n-electronic wavefunctions present in the system.

Excess coherence

As for first and second order electronic coherence, defining the intrinsic contribution of a source to n-th order electronic coherence is an important issue. Our approach is a generalization of the one followed for second order electronic coherence in equation (1.78): we proceed in a recursive way using all lower order coherences. Suppose that we have defined excess electronic coherences functions up to order $n-1$. Then, the n-th order coherence function can be decomposed in the following

way:

$$\mathcal{G}_\rho^{(ne)}(\mathbf{t}|\mathbf{t}') = \mathcal{G}_{\mathrm{F}}^{(ne)}(\mathbf{t}|\mathbf{t}') \tag{1.100a}$$

$$+ \sum_{\sigma\in\mathfrak{S}_n}\sum_{\sigma'\in\mathfrak{S}_n}\sum_{k=1}^{n-1}\epsilon(\sigma)\epsilon(\sigma')\times \tag{1.100b}$$

$$\Delta\mathcal{G}_\rho^{(ke)}\left(t_{\sigma(1)},\cdots,t_{\sigma(k)}|t'_{\sigma'(1)},\cdots,t'_{\sigma'(k)}\right)\times$$

$$\mathcal{G}_{\mathrm{F}}^{((n-k)e)}\left(t_{\sigma(k+1)},\cdots,t_{\sigma(n)}|t'_{\sigma'(k+1)},\cdots,t'_{\sigma'(n)}\right)$$

$$+ \Delta\mathcal{G}_\rho^{(ne)}(\mathbf{t}|\mathbf{t}')\,. \tag{1.100c}$$

This equation must be understood as the definition of the intrinsic n-th order coherence of the source (term 1.100c). The second term, 1.100b, contains all possible correlations between the Fermi sea and the source, both classical and coming from quantum exchanges as discussed in the second order case. Classical correlations correspond to all cases when the set $\{\sigma(1),\cdots,\sigma(k)\}$ is the same as $\{\sigma'(1),\cdots,\sigma'(k)\}$. We can easily check that this formula reduces to the one obtained previously in the $n=2$ case, as there are only two possible permutation in that case: the identity or the exchange of 1 and 2.

In the specific case of a state described by Wick's theorem, we have

$$\mathcal{G}_{\mathrm{Wick}}^{(ne)}(\mathbf{t}|\mathbf{t}') = \det\left[\mathcal{G}^{(e)}(t_i|t'_j)\right] \tag{1.101}$$

where $\mathcal{G}^{(e)}(t_i|t'_j)$ has to be understood as the matrix taking this value on line i and column j. Developing the determinant leads to an expression of the same form as equation (1.100) which implies that the intrinsic higher order electronic coherence is, in that case, equal to

$$\Delta\mathcal{G}_{\mathrm{Wick}}^{(ne)}(\mathbf{t}|\mathbf{t}') = \det\left[\Delta\mathcal{G}^{(e)}(t_i|t'_j)\right]\,. \tag{1.102}$$

Energy and Wigner representation

To end this brief overview of the properties of the coherence at any order, we can define the energy and Wigner representation of $\mathcal{G}^{(ne)}$ respectively as:

$$\widetilde{\mathcal{G}}^{(ne)}(\boldsymbol{\omega}|\boldsymbol{\omega}') = v_{\mathrm{F}}^{2n}\int\mathcal{G}^{(ne)}(\mathbf{t}|\mathbf{t}')\mathrm{e}^{\mathrm{i}(\boldsymbol{\omega}\cdot\mathbf{t}-\boldsymbol{\omega}'\cdot\mathbf{t}')}\mathrm{d}^n\mathbf{t}\,\mathrm{d}^n\mathbf{t}' \tag{1.103}$$

$$\mathcal{W}^{(ne)}(\mathbf{t}|\boldsymbol{\omega}) = v_{\mathrm{F}}^{n}\int\mathcal{G}^{(ne)}\left(\mathbf{t}+\frac{\boldsymbol{\tau}}{2}|\mathbf{t}-\frac{\boldsymbol{\tau}}{2}\right)\mathrm{e}^{\mathrm{i}\boldsymbol{\omega}\cdot\boldsymbol{\tau}}\mathrm{d}^n\boldsymbol{\tau} \tag{1.104}$$

where $\mathbf{a} \cdot \mathbf{b}$ has to be understood as the scalar product between the two vectors. These representations will not be used much in the rest of this manuscript, but are given for the sake of completeness.

1.4 From fermions to bosons (and back)

To conclude this chapter, we will present in this last section bosonization, a crucial tool for studying Coulomb interaction effects in electron quantum optics. The key idea is to describe all electrons in one dimension in terms of quantized charge density waves, which are bosonic degrees of freedom called edge-magnetoplasmons, or simply plasmons. This approach has two main limitations. First, it is only valid for low energy electrons (with respect to the Fermi sea) so that the energy spectrum can be linearized around the Fermi crossing points. Second, we are limited to the description of situation that are not to far from equilibrium, which means that we always need to be able to define a Fermi sea for this to work. In this section, we shall simply recall all useful equations relating electronic excitations to plasmonic ones without detailing their proof. Quoting the words from a review by Delft and Schoeller [35]: "ironing out all the subtleties [of the bosonization formalism] is substantially harder than simply applying it."

A reader interested in a more complete derivation of bosonization may then choose to read this review, which presents a constructive proof of all expressions used in this manuscript, or the collection of historical articles that was compiled by Stone [153]. In the specific case of condensed matter, and more particularly for one-dimensional systems, a book by Giamarchi [57] provides a complete overview of the way in which bosonization allowed us to solve quite a number of theoretical problems. To summarize history in a few lines, one problem encountered when trying to describe interacting electrons was the dimensionality of the system. Indeed, in one dimension, the standard Fermi liquid theory developed by Landau [99] to treat interacting electrons breaks down. This fact was first remarked in a model developed independently by Luttinger [107] and Tomonaga [162], which led to the coining of the term "Tomonaga-Luttinger liquid" for systems of fermions interacting in one dimension. A bosonization approach was developed by Mattis and Lieb [113] to solve this model, and lead to its exact resolution. A few years later, Haldane [74] used this bosonization approach as a basis to describe a general interacting gas of fermions in one dimension,

which proved useful to solve systems such as quantum 1D wires or spin chains. Later on, this was extended to the case that interests us here: edge channels of the quantum Hall effect, both in the integer and fractional regimes [177]. More recently, several works have started to develop bosonization schemes that are valid beyond the usual approximations. For example, Snyman and Florens [150] has developed new ideas to go beyond the linear dispersion relation needed in standard bosonization, while Gutman, Gefen, and Mirlin [72] are searching for a way to treat situation far from equilibrium. Of course, these more recent developments will not be used in the present manuscript.

After this quick summary, let us now present an overview of what we need to use bosonization in edge channels: a simple dictionary relating bosonic quantities and operators to fermionic ones.

1.4.1 The dictionary

Translation into bosonic fields

The two operators describing plasmons in our 1D chiral channels are defined as

$$b(\omega) = \frac{1}{\sqrt{\omega}} \int_{-\infty}^{+\infty} c^\dagger(\omega' - \omega) c(\omega') \, \mathrm{d}\omega' \tag{1.105a}$$

$$b^\dagger(\omega) = \frac{1}{\sqrt{\omega}} \int_{-\infty}^{+\infty} c^\dagger(\omega' + \omega) c(\omega') \, \mathrm{d}\omega' \tag{1.105b}$$

where $c(\omega)$ and $c^\dagger(\omega)$ respectively denote the electronic annihilation and creation operators at energy $\hbar\omega$. A plasmonic excitation is thus nothing but a coherent superposition of all electron/hole pairs of energy $\hbar\omega$. To verify that they are indeed bosonic excitations, let us compute the commutator of b and $b^\dagger$:

$$\begin{aligned} \Big[b(\omega), b^\dagger(\omega')\Big] &= \frac{1}{\sqrt{\omega\omega'}} \int \Big[c^\dagger(\omega_+ - \omega)c(\omega_+), c^\dagger(\omega_- + \omega')c(\omega_-)\Big] \, \mathrm{d}\omega_+ \mathrm{d}\omega_- \\ &= \frac{1}{\sqrt{\omega\omega'}} \int \Big(c^\dagger(\omega_- + \omega' - \omega)c(\omega_-) \\ &\qquad - c^\dagger(\omega_- + \omega')c(\omega_- + \omega) \Big) \mathrm{d}\omega_- \, . \end{aligned} \tag{1.106}$$

We need to be especially cautious here, as we are looking at the difference of two infinite quantities. To regularize this expression, we need to use

normal ordering. We will denote by $:A:$ the normal ordered version of expression A with respect to the Fermi sea:

$$:A:= A - \langle A \rangle_{\mathrm{F}} \,. \tag{1.107}$$

In reality, we already did such a conversion without saying it when linking the current to first order coherence in equation (1.27), which we could rewrite as $i(t) = -ev_{\mathrm{F}} :\psi^\dagger(t)\psi(t):$. Let us continue the calculation of our commutator:

$$\begin{aligned}\Big[b(\omega), b^\dagger(\omega')\Big] = & \\ \int \Big(:c^\dagger(\omega_- + \omega' - \omega)c(\omega_-): - :c^\dagger(\omega_- + \omega')c(\omega_- + \omega): \Big) \frac{\mathrm{d}\omega_-}{\sqrt{\omega\omega'}} & \\ + \int \Big(\Big\langle c^\dagger(\omega_- + \omega' - \omega)c(\omega_-)\Big\rangle_{\mathrm{F}} - \Big\langle c^\dagger(\omega_- + \omega')c(\omega_- + \omega)\Big\rangle_{\mathrm{F}} \Big) \frac{\mathrm{d}\omega_-}{\sqrt{\omega\omega'}} \,. &\end{aligned} \tag{1.108}$$

The first term of this equation corresponds to regularized, finite value integrals that therefore cancel each other. The second term corresponds to a correlator of which we know the value, see equation (1.37). This means that the corresponding integrand is, at zero temperature, equal to zero almost everywhere, except in $[0, \omega]$ where it is equal to one. This leads finally to

$$\Big[b(\omega), b^\dagger(\omega')\Big] = \delta(\omega - \omega') \frac{\omega}{\sqrt{\omega\omega'}} = \delta(\omega - \omega') \tag{1.109}$$

Back-translation

Having defined bosonic operators from fermionic ones, let us give the inverse relations and construct fermionic operators from the bosonic ones and discuss their interpretation. The link between fermions and bosons is given by

$$\psi(t) = \frac{\mathcal{U}}{\sqrt{2\pi a}} \exp\left[\int_0^{+\infty} \Big(b(\omega)\mathrm{e}^{-\mathrm{i}\omega t} - b^\dagger(\omega)\mathrm{e}^{\mathrm{i}\omega t}\Big) \frac{\mathrm{d}\omega}{\sqrt{\omega}}\right] \tag{1.110}$$

where a is the short distance cutoff below which bosonization is not valid and $\mathcal{U}$ is called the Klein ladder operator which removes one electron from the fluid. The Klein operator and its hermitian conjugate $\mathcal{U}^\dagger$ are needed in order to take into account that applying ψ or $\psi^\dagger$ changes the number of charges present in the system, something that can not be done by the b and $b^\dagger$. The Klein operators act simply by changing

the chemical potential of the fluid in exactly the right way to remove or add one excitation from the ground state. Let me comment a bit on what it means in terms of physical states. At a given number of electrons N, the ground state is given by a Fermi sea with N electrons $|F_N\rangle$. From a bosonic point of view, this is a vacuum state: the plasmons are coherent superpositions of electron/hole pairs, and there are no such pairs in the Fermi sea. However, it is a specific vacuum linked to the fact that there are N electrons. As we said, applying $\mathcal{U}$ correspond to the removal of one electron, leading to the Fermi sea $|F_{N-1}\rangle$. Of course, this state is still a vacuum for plasmons, but we need to keep in mind that it differs from the previous one. In a way, in terms of bosons, we have a family of vacuums given by $|O_i\rangle$, where i is a counter of the number of fermions in the system, over which we can create states using the $b^\dagger$ operators. In the case where we bosonize several species of fermions, for examples two different spins or different edge channels, we will have different Klein operators for each species. They anticommute with each other in order to implement the anticommutation relations of the fermionic operators. They also commute with all bosonic operators, so that changing the chemical potential before or after applying the bosonic part of ψ is completely equivalent.

The exponential, bosonic, part of the fermionic operators can be seen as a generalized version of coherent displacement operators from quantum optics. For a single bosonic mode, the displacement operator creating the coherent state $|\alpha\rangle$ is given by

$$D(\alpha) = \mathrm{e}^{\alpha b^\dagger - \alpha^* b} \tag{1.111}$$

such that $D(\alpha)\,|0\rangle = |\alpha\rangle$. Here, we use a generalized version

$$\mathcal{D}\,[\alpha] = \exp\left(\int_0^{+\infty} \Big(\alpha(\omega)b^\dagger(\omega) - \alpha(\omega)b(\omega)\Big)\,\mathrm{d}\omega\right) \tag{1.112}$$

that creates a multimode coherent state

$$\mathcal{D}\,[\alpha]\,|0\rangle = \bigotimes_{\omega>0} D(\alpha(\omega))\,|0_\omega\rangle = \bigotimes_{\omega>0} |\alpha(\omega)\rangle = |[\alpha]\rangle\ . \tag{1.113}$$

The notation $|[\alpha]\rangle$ will be used throughout this manuscript for that multimode state, as a way to keep equations as compact as possible. Displacement operators and coherent states will be of particular importance for us, especially in chapter 3, so let us devote a few lines to list

their most useful properties:

$$\mathcal{D}\left[\alpha\right]\mathcal{D}\left[\beta\right] = \exp\left(\mathrm{i}\int_0^\infty \mathrm{Im}\left(\beta^*(\omega)\alpha(\omega)\right)\mathrm{d}\omega\right)\mathcal{D}\left[\alpha+\beta\right] \tag{1.114a}$$

$$\mathcal{D}\left[\alpha\right] = \exp\left(-\int_0^\infty \frac{|\alpha(\omega)|^2}{2}\mathrm{d}\omega\right) :\mathcal{D}\left[\alpha\right]: \tag{1.114b}$$

These two properties together allow us to compute, for example, the scalar product between two coherent states $\langle[\beta]|[\alpha]\rangle$,

$$\langle[\beta]|[\alpha]\rangle = \exp\left(\int_0^\infty \mathrm{i}\,\mathrm{Im}\left(\beta^*(\omega)\alpha(\omega)\right) - \frac{|\alpha(\omega)-\beta(\omega)|^2}{2}\mathrm{d}\omega\right) \tag{1.115}$$

as well as the following matrix elements:

$$\langle[\alpha]|\,:\mathcal{D}\left[\gamma\right]:\,|[\beta]\rangle = \exp\left(\int_0^\infty \gamma(\omega)\alpha^*(\omega) - \gamma^*(\omega)\beta(\omega)\mathrm{d}\omega\right)\langle[\alpha]|[\beta]\rangle\,. \tag{1.116}$$

After this small technical parenthesis, let us refocus on the operators ψ and $\psi^\dagger$. Using the above definitions, they are connected to generalized displacement operators by

$$\psi(t) = \frac{\mathcal{U}}{\sqrt{2\pi a}}\mathcal{D}\left[\Lambda_t\right] \tag{1.117a}$$

$$\psi^\dagger(t) = \frac{\mathcal{U}^\dagger}{\sqrt{2\pi a}}\mathcal{D}\left[-\Lambda_t\right] \tag{1.117b}$$

where we have defined

$$\Lambda_t(\omega) = -\frac{\mathrm{e}^{\mathrm{i}\omega t}}{\sqrt{\omega}}\,. \tag{1.118}$$

Creating an electron at time t thus corresponds, in the bosonic domain, to the creation of an infinite dimensional coherent state with functional parameter $\omega \mapsto \Lambda_t(\omega)$. Let us now discuss the physical meaning of this specific parameter.

1.4.2 Creating coherent plasmonic excitations

Equivalently, one may ask how we can create such a coherent plasmonic state in a real experiment. The answer to that question is simple: as for standard quantum optics, any classical forcing applied to our system will lead to a coherent state. This of course raises the following important

question: what is the coherent state created by applying some classical voltage $V(t)$ to an Ohmic contact?

To answer it, let us look at the electric current operator in our system, $i(t)$. It is straightforward to show that the finite-frequency components of the current, obtained by Fourier transforming $i(t)$, are directly linked to plasmonic operators by

$$i(\omega) = -e\sqrt{\omega}\, b(\omega)\,. \tag{1.119}$$

As discussed in section 1.1.2 devoted to Leviton sources, applying some time dependant AC voltage $V(t)$ to an Ohmic contact directly creates the current $i(t) = e^2 V(t)/h$ in the edge channel of interest. The coherent state created by that same voltage is therefore such that all finite-frequency components of the current are equal to the one created by the voltage of interest,

$$\forall \omega > 0,\ -e\sqrt{\omega}\,\langle b(\omega)\rangle = \frac{e^2}{h}\widetilde{V}(\omega) \tag{1.120}$$

where $\widetilde{V}$ is the Fourier transform of V. The coherent state we are searching for is thus given by

$$\mathcal{D}\left[-\frac{e\widetilde{V}(\omega)}{h\sqrt{\omega}}\right]|0\rangle\ . \tag{1.121}$$

This leads to two main remarks:

- Since all states created by applying some voltage to an Ohmic contact are coherent plasmonic states, this is in particular true for Levitons!
- The coherent state associated with $\psi^\dagger(t_0)$, of parameter $-\Lambda_{t_0}(\omega)$, corresponds to the state created by a percussional voltage drive $V(t) = -\frac{h}{e}\delta(t - t_0)$. This is indeed what we would expect, as we want to express the idea that we added some charge $-e$ exactly at time t_0.

If we look closely at equation (1.121), there is still a property that seems to be important: if we want to avoid any infra-red divergence, we need $\lim_{\omega\to 0}\widetilde{V}(\omega) = 0$. How can we regularize our state when this is not the case? Suppose that we have some voltage with a non-zero limit at low frequency. In that case, let us look at a periodic source emitting

this voltage with a frequency f. Such a periodic source will only have non-zero $\widetilde{V}(\omega)$ when $\omega = 2\pi n f$. The only diverging part is then exactly at $\omega = 0$, and thus corresponds to a DC current. Such a DC part will simply lead to a change of chemical potential, and thus implies a change from one bosonic vacuum to another. It can be completely absorbed by changing the vacuum state on which we would apply the displacement operator corresponding to the AC-only part of that periodic voltage, which has no divergence at all.

1.4.3 Electrons as superpositions of plasmons

A last point that will be useful for us in the following of this work is the ability to express any electronic state as a plasmonic state, and back. To begin, let us look at single electronic states above the Fermi sea, of the form $\psi^\dagger[\varphi_e]\,|F\rangle$. We can express it in terms of bosons as

$$\psi^\dagger[\varphi_e]\,|F\rangle = \left(\int \varphi_e(t)\psi^\dagger(t)\mathrm{d}t\right)|F\rangle = \frac{\mathcal{U}^\dagger}{\sqrt{2\pi a}}\int \varphi_e(t)\,|[\Lambda_t]\rangle\,\mathrm{d}t\,. \quad (1.122)$$

From the bosonic point of view, any added excitation on top of the Fermi sea is thus simply a superposition of coherent states. As an example, let us look at an electron emitted by our usual single-electron source. From equation (1.122), we expect it to be built as a continuous superposition of bosonic coherent states, each of these states corresponding in the electronic point of view to a time-localized excitation. To test this point of view, we can try to construct artificially such superpositions of bosonic coherent states, and see if we recover the Wigner distribution function of our usual wavepacket in the continuous limit. Figure 1.22 shows this reconstruction at work through the lens of Wigner functions. By superposing more and more time-resolved excitations, with weights given by $\varphi_{\mathrm{Landau}}(t)$, the interference pattern between them visible on the Wigner functions gives rise to the energy-localization and to all other features we talked about in section 1.2.4. On the other hand, a well known theorem by Levitov, Lee, and Lesovik [104] states that the only single electron excitations on top of the Fermi sea that correspond to coherent plasmonic states are the Levitons (see also [138] for an alternating proof).

In other words, a Landau quasi-particle, as well a a generic single electron excitation on top of the Fermi sea, is a continuous Schrödinger cat state of coherent plasmon states. This plasmonic interpretation of

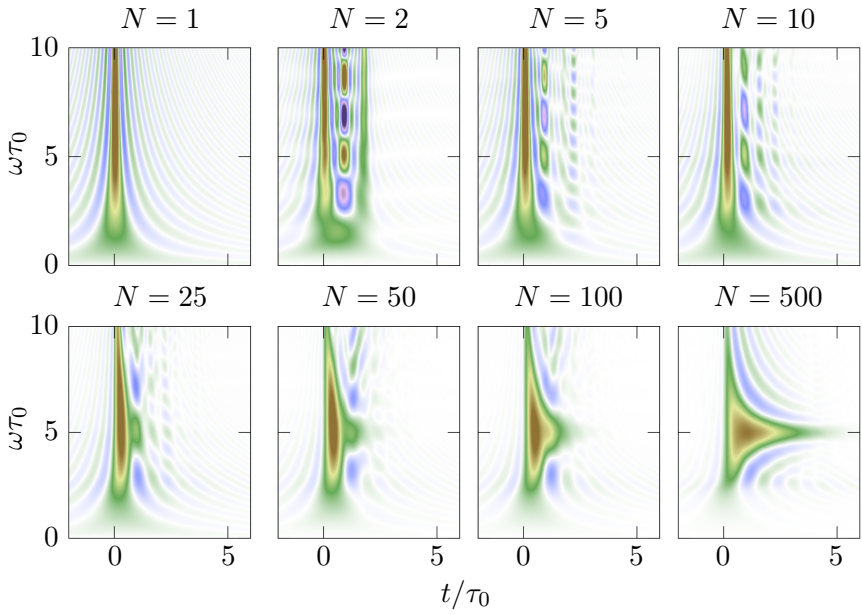

Figure 1.22: Reconstruction of the excess Wigner function for a Landau excitation (see equation (1.64)) with parameters such that $\omega_0\tau_0 = 5$. Each panel depicts the Wigner function associated with a finite superposition $\sum_{j=1}^{N} \varphi_{\mathrm{e}}(t_j)\psi^{\dagger}(t_j)|F\rangle$ where the times t_j are picked up randomly through probability distribution $|\varphi_{\mathrm{e}}(t)|^2$. The final form of the wavepacket's Wigner distribution function can thus be interpreted as arising from quantum interferences between its different time-localized contributions.

single electron excitations will prove particularly useful when we will later discuss Coulomb interaction induced relaxation.

Chapter 2

Measuring coherences

> The traces we leave are vague,
> but they still catch sight
>
> Harakiri for the Sky
> *The Traces We Leave*

In this chapter, I will discuss the challenges linked to electron quantum optics experiments, focusing mainly on the experiment I worked on. I will also explain how these experiments give access to electron quantum optics quantities such as electronic coherences. This chapter will thus connect the concept-oriented previous chapter to more advanced models and experiments that have been developped in electron quantum optics. In particular, I will discuss several interferometry experiments directly inspired by classical and quantum optics which have been demonstrated over the last few years. I will mainly review them within the framework of electron quantum optics that have been presented in the previous chapter.

During the time of my PhD, all this work has culminated with the demonstration of a quantum current analyzer which I have helped to develop both from the experimental and theoretical point of views, while not being the leading researcher on these topics. I will go into much more details in the corresponding section, but let me stress how crucial the experimental and theoretical contributions done respectively by A. Marguerite and B. Roussel have been in the development of the quantum current analyzer.

The first part of this chapter will mainly be devoted to first order coherence measurements. Then, we will turn to more prospective exper-

iments, still in the development stage, which aim at probing two-electron coherence.

2.1 Experimental challenges

As mentioned in the introduction, electron quantum optics experiments require overcoming several experimental challenges. This has been possible by using cutting edge materials, as well as cryogenic and radio-frequency technologies which we shall now describe briefly.

The first challenge is, of course, the manufacturing of a high-quality bi-dimensional electron gas. This step is performed by Y. Jin and A. Cavanella at the Laboratoire de Photonique et Nanostructure, in Marcoussis. They are also responsible for all lithography processes, a crucial step for the success of all subsequent experiments. Not being the most familiar with material and sample fabrication, I will not go into further detail and simply stress that this first step is what makes everything else possible.

Within the group at Laboratoire Pierre Aigrain, the challenges concern the embedding of samples into the experimental setup and collecting the experimental signals. Reaching the integer quantum Hall regime requires putting the sample inside a dilution fridge in order to be cooled down to about 70 mK in the presence of a high magnetic field (typically of the order of 4 T) generated by a superconducting coil. Maintaining such low temperatures also requires specific protections around all the coaxial lines used to control or drive the sample [53] since external radiation can heat up the electron gas. Once the experimental setup is operational, the real challenge is to collect the experimental signals and to process them in order to extract all relevant physical information. These are the steps we will focus on in the following.

Cryogenic amplification and measurement time

In electronics, the experimentally accessible quantities are electrical currents or voltages. However, the typical order of magnitude of these quantities in our experiments ($V \simeq 10\,\mathrm{nV}$) makes such a measurement quite difficult. Moreover, quantum Hall samples are characterized by their high impedances (of the order of $R_K \simeq 25\,\mathrm{k}\Omega$) and experimentalists have to confront severe impedance matching problems when collecting AC signals.

In order to measure such low voltages, a two-step amplification chain is used, wich involves cryogenic amplifiers allowing a small amplification factor with very low added noise followed by room temperature amplifiers at the end of the measurement chain. Let us stress that, as of now, on-chip quantum-limited superconducting amplifiers[1] are not an option because of the high magnetic field required for entering the quantum Hall regime. The interested reader is advised to take a look at V. Freulon's PhD thesis [52][2], in which a full chapter is devoted to cryogenic amplification and the experimental techniques he has developed in order to reach the present level of sensitivity. The generation of experiments I have been working on is based on his work.

Once the signal is recovered, it can be analyzed using several experimental techniques depending on the quantity we want to measure. However, even with our state-of-the-art amplifying chain, measurement over a large number of periods is still required for the acquired signal to be greater than the noise accumulated from thermic fluctuations and amplifiers. This puts strong constrains on the repetition rate as well as on the acquisition time. To give an idea of numbers, we need to measure for approximately 1 min with a repetition rate around 1 GHz to get a signal-to-noise ratio around 30. This means that we cannot gain access to time-resolved quantities at the scale of a single period in the current state of experimental techniques. The situation is completely different from photonics where time-resolved single photon detection is routinely performed with a high efficiency. In our experiments, it is completely impossible to perform a single shot time-resolved detection of a single electron. Consequently, the quantities we are measuring are averaged over many periods. These include the average time dependent current $\langle i(t)\rangle$ (up to time resolution restrictions), the average finite-frequency current, $\langle i(\omega)\rangle$, or the low-frequency noise which will be defined in equation (2.5). Let us now discuss more precisely these quantities.

Current measurements

Using an ultrafast acquisition card, it is possible to measure the current with a 500 ps resolution to get the average current $\langle i(t)\rangle$, where the average is typically done over 10^8 periods in order to get enough signal. This technique has been used, for example, to extract some parameters of the single-electron source from section 1.1.2 such as the typical dwelling

[1] See [139] for a review on parametric amplification using superconducting circuits.
[2] Unfortunately only in french.

time [108]. As we have seen in equation (1.27a), measuring the average time dependent electrical current gives access to the diagonal part of the excess coherence in the time domain, $\Delta\mathcal{G}^{(e)}(t|t)$:

$$\langle i(t)\rangle_\rho = -ev_{\mathrm{F}}\Delta\mathcal{G}^{(e)}_\rho(t|t)\,. \tag{2.1}$$

However, even if they can prove useful in specific situation, average current measurements in the time domain are not the bread and butter of our experimental setup. The time resolution is limited and, most of the time, it is more convenient to switch to finite-frequency current measurements. To this end, we use a custom homodyne detection setup, enabling the recovery of the finite frequency current in a wide frequency range, from 0.7 GHz to 11 GHz. Since homodyne detection works by mixing a signal with some reference signal in order to measure only DC quantities, it requires specific radio-frequency components such as mixers and amplifiers in the frequency range we want to cover. Of course, it is unrealistic up to now to expect components working on such a large scale. In practice, different combinations of components have been used to cover the 0.5 to 15 GHz frequency range. In particular, such a setup has allowed the measurement of the finite frequency admittance of a $\nu = 2$ quantum Hall edge channels system up to 15 GHz [14]. As will be discussed in detail in chapter 3, and particularly in section 3.2, this particular measurement has been of great use to clarify our understanding of effective Coulomb interactions within the $\nu = 2$ edge channel system.

Noise measurements

Although current measurements are very useful, they are still not the full story of interest for us, due to their fundamental limit with respect to coherences: they only give access to the diagonal part of first order coherence functions (time resolved average current). As we shall see, current noise measurements will be the tool of choice in our experimental investigation of electronic coherence. Let us then take some time to give a more precise account of how we define current noise, how it is measured in an experiment, and how it is linked to electronic coherences. First of all, the definition of current noise is simply

$$\mathcal{S}(t,t') = \langle i(t')i(t)\rangle - \langle i(t')\rangle\langle i(t)\rangle\,. \tag{2.2}$$

Expressed in terms of electronic coherences, it is equal to

$$\mathcal{S}(t,t') = \tag{2.3}$$
$$(ev_{\mathrm{F}})^2 \left[\frac{\delta(t-t')}{v_{\mathrm{F}}} \mathcal{G}^{(e)}(t'|t) + \mathcal{G}^{(2e)}(t,t'|t,t') - \mathcal{G}^{(e)}(t|t)\mathcal{G}^{(e)}(t'|t') \right]$$

where one recognizes the full first and second order electronic coherences, which are known to be highly singular. This is not surprising since this quantity depends on the full coherence, and therefore contains contributions arising from the Fermi sea in which the quantum current noise is non vanishing, even at non zero temperature [56]. Consequently, we shall focus on the quantity $\Delta\mathcal{S}(t,t')$ corresponding to the excess current noise, defined as the difference between this quantity when sources are "on", to the same when sources are "off". The excess current noise can then be expressed in terms of the excess electronic coherences as

$$\Delta\mathcal{S}(t,t') = (ev_{\mathrm{F}})^2 \left[\frac{\delta(t-t')}{v_{\mathrm{F}}} \Delta\mathcal{G}_\rho^{(e)}(t|t') \right. \tag{2.4a}$$
$$- \mathcal{G}_{\mathrm{F}}^{(e)}(t|t')\Delta\mathcal{G}_\rho^{(e)}(t'|t) - \mathcal{G}_{\mathrm{F}}^{(e)}(t'|t)\Delta\mathcal{G}_\rho^{(e)}(t|t') \tag{2.4b}$$
$$\left. + \Delta\mathcal{G}_\rho^{(2e)}(t,t'|t,t') - \Delta\mathcal{G}_\rho^{(e)}(t|t)\Delta\mathcal{G}_\rho^{(e)}(t'|t') \right]. \tag{2.4c}$$

Let us now discuss the physical interpretation of this equation. The first term (2.4a) is directly proportional to the current, and thus corresponds to the standard Poissonian noise associated with the granular nature of electrons. The second term (2.4b) corresponds to noise coming from quantum exchanges between electrons from the source and electrons from the Fermi sea (see equation (1.78)). Finally, term (2.4c) corresponds to the real excess noise contribution of the source itself. Not surprisingly, it involves the intrinsic second order coherence of the source which characterizes electron or equivalently electron/hole pair emissions by the source itself.

From an experimental point of view, we are limited by the acquisition setup and cannot have access to any time-resolved quantity. Instead, what is measured is the low-frequency current noise averaged over a long acquisition time. This corresponds to

$$\mathcal{S} = \lim_{T\to\infty} \frac{1}{T} \int_{-T/2}^{+T/2} \mathrm{d}\bar{t} \int_{-\infty}^{+\infty} \mathrm{d}\delta t\, \mathcal{S}\left(\bar{t} + \frac{\delta t}{2}, \bar{t} - \frac{\delta t}{2}\right). \tag{2.5}$$

Note that equation (2.4) already gives us an order of magnitude for the expected noise signal in electron quantum optics. A single electron source with repetition rate f emits an average current of order $-ef$ and therefore, one should expect a current noise of the order of $e^2 f \simeq 10^{-29}\,\mathrm{A}^2/\mathrm{Hz}$. Since we are often looking for small variations of such a signal, a sensitivity level of 10^{-30} or even better 10^{-31} is often required.

In order to reach such sensitivity levels for current noise measurements, clever solutions have been worked out. The current collected with an Ohmic contact in the sample is sent into two parallel amplification lines, both of them containing cryogenic and room temperature amplifiers adding some noise[3] to the measured signal. A spectrum analyzer is then used to compute the noise spectral density of cross-correlations between the two amplifying lines. This has the advantage that voltage noise added by the amplifiers[4] is no more important, since noises of the two amplifiers are independent from each other. Finally, this power spectral density is integrated over a range corresponding to the width of a resonant LC circuit placed inside the setup, giving access to the quantity we want to measure.

Looking back at the relation between measured noise and coherences from equation (2.4), it becomes clear that the averaging process used in the real measurement will make it difficult to gain access to any other quantity than time averaged electronic coherences. However, the same problem also exists in optics and in standard classical electronics and a solution called homodyning has been devised to circumvent it. As we shall see in the forthcoming section, a variant of this idea can be devised in electronic interferometry experiments to capture the time dependence of the signals we want to access to.

2.2 Interferometry experiments for first order coherences

The history of interferometry experiments in electron quantum optics begun as soon as 1990 with the demonstration of what was essentially an electronic Fabry-Pérot interferometer [149], but really took off when the group of M. Heiblum demonstrated first the electronic equivalent

[3] Real noise in the sense of the "unwanted added part to the signal", not the noise that we wish to measure, which is the real signal we are interested in. Not so easy to follow, is it?

[4] This is the dominant contribution to noise in our setup.

to Young's slit experiment [146] in 1997, and then an electronic Mach-Zehnder interferometer [88]. This sparked quite an interest in the development of electron quantum optics, leading, as we discussed in chapter 1, to the development of single electron sources, and some years later to the demonstration of another optically-inspired interferometer: the Hong-Ou-Mandel experiment [13]. In the present section, we will give an overview of these two interferometers and discuss how, and to what extent, they can be used to access the electronic single electron coherence.

2.2.1 Mach-Zehnder interferometry

The first electronic interferometer of interest is the Mach-Zehnder interferometer (MZI) which was first demonstrated in 2003 [88] and has since been studied by several experimental groups [12, 106, 136]. In particular, these experiments have proved that propagation in the edge channels of the quantum Hall effect is indeed phase coherent with a typical coherence length of 20 µm at an electronic temperature of 20 mK [137]. A pictorial representation of the interferometer is drawn in figure 2.1. Two quantum point contacts (QPCs) with tunable transmission are used to define two propagation paths of different lengths and a source is placed before the separation of paths. The average electrical current is then measured at the output of the interferometer. In a realistic quantum Hall experiment, creating the two paths is challenging because of the chirality of edge channels. This has been achieved through careful lithography techniques and the use of air bridges as shown on the top right part of figure 2.2. Varying the length difference between the two paths is achieved by polarizing a side gate to repel the edge channel. A modulation of the outgoing current is then observed, as shown on the bottom panel of figure 2.2.

Can we understand this electrical current modulation in terms of (electronic) coherences just as in optics? As explained in equation (2.1), the measured quantity is simply $\Delta\mathcal{G}^{(e)}_{1,\mathrm{out}}(t|t)$. Using notations from figure 2.1, this outgoing coherence can be linked to the coherence just before QPC B, using:

$$\begin{pmatrix}\psi_1(t)\\ \psi_2(t)\end{pmatrix}_{\mathrm{out}} = \begin{pmatrix}\sqrt{R_B} & \mathrm{i}\sqrt{T_B}\\ \mathrm{i}\sqrt{T_B} & \sqrt{R_B}\end{pmatrix}\begin{pmatrix}\psi_1(t)\\ \psi_2(t)\end{pmatrix}_{\mathrm{MZI,out}} \tag{2.6}$$

R_B and T_B being respectively the current reflexion and transmission coefficients for QPC B, which can be tuned by the experimentalist. In the

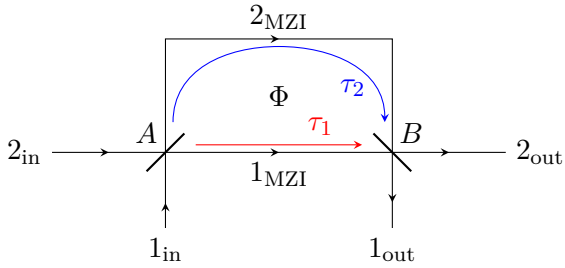

Figure 2.1: Schematic drawing of a Mach-Zehnder interferometer: Two incoming channels are fed to a first beamsplitter whose outputs correspond to two paths of different lengths enclosing some mangnetic flux Φ. These paths are recombined at a second beamsplitter, and the average electrical outgoing current is measured.

absence of interactions, electronic propagation along quantum Hall edge channels is chiral and ballistic. Consequently, these fermionic operators right before QPC B can be derived from the ones just after QPC A with a time delay and a phase:

$$\psi_{1,\mathrm{MZI,out}}(t) = \mathrm{e}^{\mathrm{i}\phi_{\mathrm{AB}}/2}\psi_{1,\mathrm{MZI,in}}(t-\tau_1)\,, \tag{2.7a}$$

$$\psi_{2,\mathrm{MZI,out}}(t) = \mathrm{e}^{-\mathrm{i}\phi_{\mathrm{AB}}/2}\psi_{2,\mathrm{MZI,in}}(t-\tau_2)\,. \tag{2.7b}$$

Here ϕ_{AB} denotes the Aharonov-Bohm phase that needs to be taken into account since the Mach-Zehnder loop encloses some magnetic flux Φ: $\phi_{\mathrm{AB}} = e\Phi/\hbar$. It is then easy to express these operators at the beginning of the interferometer in terms of the incoming ones, using the matrix given by QPC A. Finally, assuming that the source is located on the incoming channel 1 and that the incoming channel 2 is simply fed with the reference Fermi sea, we obtain the outgoing excess single electron coherence as a linear function of the incoming one

$$\begin{aligned}\Delta\mathcal{G}^{(e)}_{1,\mathrm{out}}(t|t') = {} & R_A R_B \Delta\mathcal{G}^{(e)}_{1,\mathrm{in}}(t-\tau_1|t'-\tau_1) \\ & + T_A T_B \Delta\mathcal{G}^{(e)}_{1,\mathrm{in}}(t-\tau_2|t'-\tau_2) \qquad (2.8a) \\ & - \sqrt{R_A R_B T_A T_B}\,\mathrm{e}^{\mathrm{i}\phi_{\mathrm{AB}}}\Delta\mathcal{G}^{(e)}_{1,\mathrm{in}}(t-\tau_1|t'-\tau_2) \\ & - \sqrt{R_A R_B T_A T_B}\,\mathrm{e}^{-\mathrm{i}\phi_{\mathrm{AB}}}\Delta\mathcal{G}^{(e)}_{1,\mathrm{in}}(t-\tau_2|t'-\tau_1)\,. \qquad (2.8b)\end{aligned}$$

In this equation, we can recognize two contributions with distinct origins. The first two terms (2.8a) are the classical terms associated with

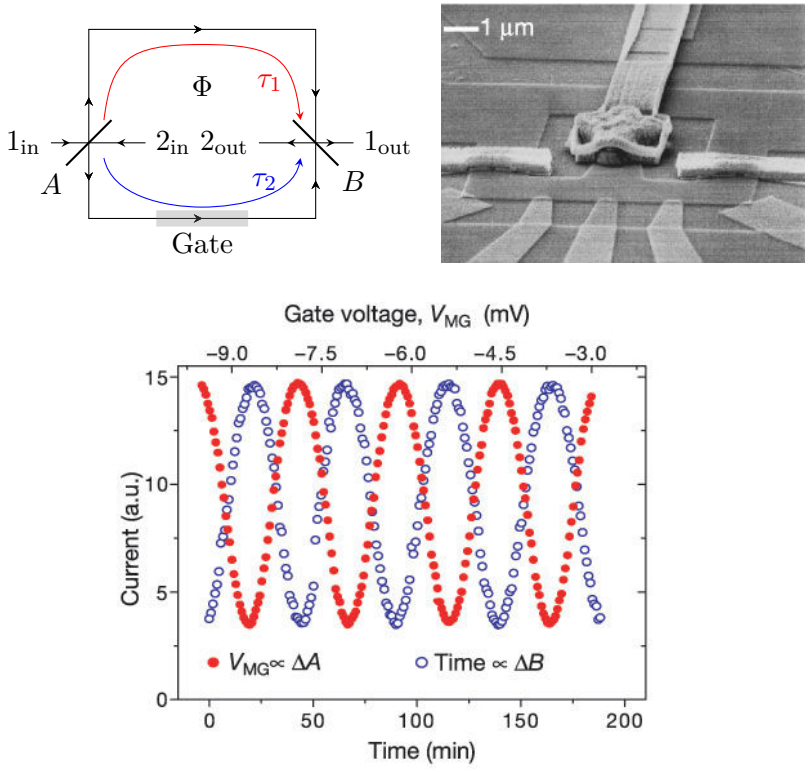

Figure 2.2: *Top*: Visualization of a realistic implementation of a Mach-Zehnder interferometer. It needs to take into account the chirality of channels in the Quantum Hall effect, and would look more like the scheme on the left of this figure. We therefore need to have contacts inside the loop to inject and recover the current. This can be done experimentally through careful lithography, in which we can create some metallic bridges over the 2DEG without touching it, as can be seen on the scanning electron microscopy picture displayed on the right here. *Bottom*: Experimental measurement of the outgoing current when we vary the voltage applied to the side gate. We see clear oscillations of the current. These results and the SEM picture are extracted from [88].

electronic propagation along one branch of the MZI or the other, while the last two terms (2.8b) describe the quantum interferences between these two possible paths. Of course, only the interfering terms depend on ϕ_{AB}, since they are the only ones that are sensitive to the presence of the magnetic flux inside the loop.

The average outgoing current depends on both contributions. But the classical parts only correspond to the time delayed incoming currents. It thus only probes the diagonal of the excess single electron coherence in the time domain. On the contrary, the quantum terms depends directly on the off-diagonal excess single electron coherence $\Delta\mathcal{G}^{(e)}(t-\tau_1|t-\tau_2)$. By extracting these terms from the outgoing time dependent average current, one thus gains an access to the excess single electron coherence. This is the idea behind a protocol proposed by Haack et al. [73]: measuring the outgoing current for different values of the magnetic flux allows, with a suitable Fourier transform, the determination of both the modulus and the phase of $\Delta\mathcal{G}^{(e)}_{1,\mathrm{in}}(t-\tau_1|t'-\tau_2)$. By varying the times of flight τ_1 and τ_2 with side gates, we could then in principle measure the full incoming electronic coherence.

In practice, this reconstruction protocol suffers from one major drawback. Since it requires extended propagation channels, electrons propagating in the interferometer will experience Coulomb interaction, and therefore electronic decoherence. This will be discussed in more detail in the next chapter, but let us stress here that the effect of Coulomb interaction is in fact quite drastic and completely prevents the use of this setup for the direct measurement of an unknown coherence. Decoherence effects within the measurement apparatus itself are so strong that measuring the average time dependent current will not give any usable information on the incoming quantities. However, it gives information on decoherence within the MZI, as was studied for example by Roulleau et al. [134].

2.2.2 Intensity interferometry

Is there a way to overcome this apparatus problem? The answer is yes, and once again comes from the realms of optics. A similar problem had indeed been met in a totally different context, during the first part of the 20th century, when astronomers started to build really huge telescopes. In these old times, random phase shifts, accumulated as light went through the Earth's atmosphere, blurred images to the point that making measurements of stars' diameters was pretty much impossible

even if, in principle, one could have built larger telescopes[5]. In order to circumvent this problem, Hanbury Brown and Twiss (denoted from now on by HBT) had the idea of using intensity correlations [75], since intensity is insentitive to phase blurring. This technique, implemented using two relatively small optical telescopes in the Australian desert allowed them to successfully measure the angular diameter of Sirius. This achievement was met with skepticism at first, since it was expected that visible light arriving from Sirius would only lead to a small number of photons detected during the measurement time, so that intensity correlations would not necessarily give access to the same information as standard optical interferometric measurements. But another experiment by the same authors [76] helped prove that this measurement scheme was indeed valid, and that correlations between photons could be observed when using an incoherent light beam as a source.

This experiment sparked a huge interest in the use and development of intensity interferometry in several domains [5], and also lead to spectacular new experiments in quantum optics. In particular, the one that is of particular interest to us has been demonstrated for the first time in 1987 by Hong, Ou, and Mandel [82] (denoted from now on by HOM). Its idea, represented on the left of figure 2.3, is quite simple: two independent sources are used to feed a beamsplitter and detectors are placed in the outgoing branches. We then count the number of coincidental detections. Since the two sources emit identical single photons, which are indistinguishable from a quantum point of view, two particle interferences are expected to lead to spectacular effects.

By changing the time delay between the two sources, we recover the typical curve displayed on the right of figure 2.3. When the two photons, prepared in the same wavepacket collide at the same time on the beamsplitter, two particle interferences associated with bosonic statistics lead to a phenomenon called *bunching*: both photons regroup in the same outgoing branch. Consequently, one of the detectors does not detect any signal: the coincidence count drops down to 0. By contrast, when they are sufficiently separated from each other (more separated than the typical time-width of their wavefunction), they partition classically reflecting the fact that they have been prepared in distinguishable single particle states. Between the two regimes, a smooth drop of the rate

[5]It took more than a century of development for adaptative optics to reach the point where optical telescopes with mirror diameters above 10 meters could be built and even combined in giant interferometers.

of coincidences is observed when increasing the overlap of the incoming excitations.

Let us now turn directly to the analogue of these experiments in electron quantum optics.

Creating HOM experiments in electronics

The first Hanbury Brown and Twiss experiments have been demonstrated at the end of the previous century [79, 120] in a 2DEG in a quantum Hall regime. Being performed before the advent of single-electron sources, these experiments relied on stationary beams of electrons. The main outcome of these experiments is the following: the excess of correlations between the two outputs is the opposite of the excess noise measured on any of them:

$$\langle \Delta i_1 \Delta i_2 \rangle_{\text{out}} = -\langle \Delta i_1^2 \rangle_{\text{out}} \,. \tag{2.9}$$

Howoever, this result only tells us that charge is conserved in the partitionning at the beamsplitter but does not really give more insight on the details of the quantum partitionning process.

The first electron quantum optics results on electron partitionning was the implementation within the experimental group of G. Fève of both the HBT [123, 15] and of the HOM experiment [13, 16]. These two experiments have opened the way to discussing quantum partitionning at a beamsplitter down to the single electron level.

Electrons being fermions, the results were quite opposite to the ones obtained with photons: two indistinguishable electrons arriving at the same time on the beamsplitter are forbidden to scatter into the same exit channel by the Pauli principle. This leads to the *antibunching* of electrons, and consequently to a rise of coincidence counts as presented in figure 2.3. In the real experiment shown in figure 2.4 however, we do not measure the correlations between the two outputs, but rather the current noise on one of the exiting channels. From equation (2.11), we expect this quantity to have a dip at zero time-delay between the two independent and identical sources. This is indeed what has been observed in the experiment, as can be seen on the right of figure 2.5.

Now, let us be more quantitative and find the physical quantities to which such an experiment gives access to. In particular, as a first step, let us ask ourselves how we can express the outgoing noise in terms of electronic coherences.

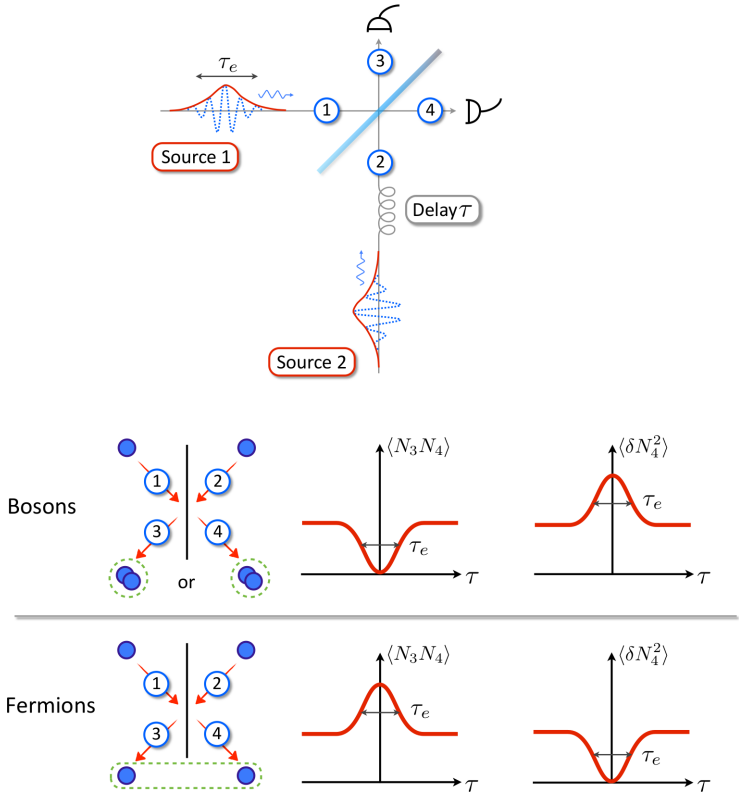

Figure 2.3: A schematic view of the HOM experiment (*Top*) and of its usual results (*Bottom*), adapted from [16]. Two identical wavepackets are sent, with some time-delay, on the two inputs of a beamsplitter. We then measure either correlations between the two outputs of the beamsplitter, or variance in one of the outputs. Quantum statistics lead to spectacular results: for bosons, a bunching phenomenon occurs, leading identical bosons to go out of the experiment in the same output. On the contrary, identical fermions are forbidden to be in the same output, which leads to an antibunching. In electron quantum optics, we are going to measure the current noise in one output, and therefore expect to find curves such as the one displayed in the right graph for fermions.

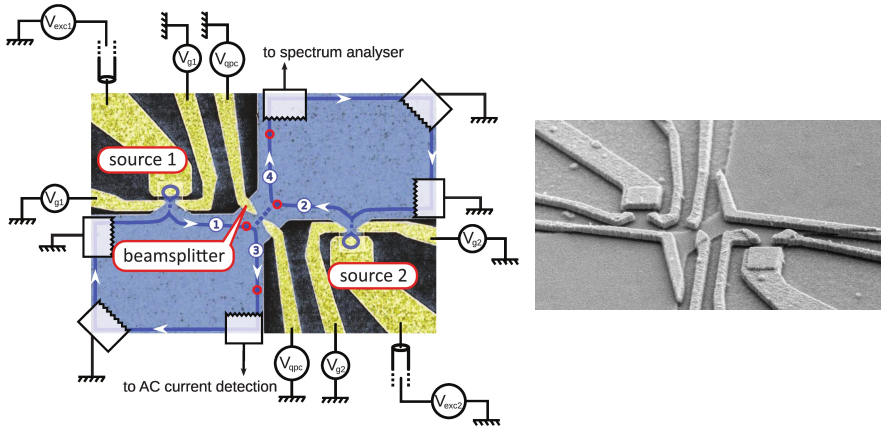

Figure 2.4: *Left*: A false color SEM picture taken from [16] of a real HOM setup. The 2DEG is in blue, and gates are in yellow. We clearly see the two quantum dots that are used as sources, as well as the central QPC. *Right*: A closer look at the sources and the QPC region. This picture, which I took during my stay at Laboratoire Pierre Aigrain, corresponds to a sample with some additional gates.

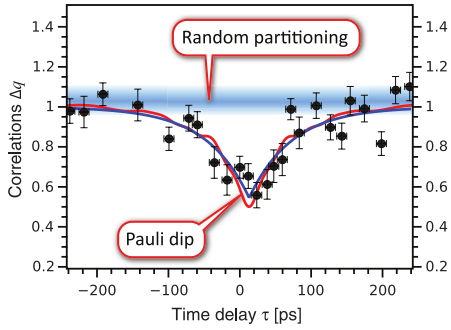

Figure 2.5: Results of an electronic HOM experiment, taken from [16]: we clearly recover the expected dip in the current noise for a low time-delay between the two sources. Its exact depth will be the key subject of section 3.2.

The "on minus off" process gives access to the low-frequency excess noise obtained from equation (2.4). This quantity is indeed independent from any process happening between the QPC and the Ohmic contact that recovers the current, since it is the total power inside the outgoing channel. In particular, this will mean that any interactions happening after the QPC will not have any impact on the result, as will be made clearer in the next chapter.

We therefore need to compute the excess single and two-electron coherences in the output branch, just after the QPC. Let us remember first that outgoing and incoming fermionic operators are related to each other through equation (2.6). Furthermore, the two sources being independent, there are no electronic coherences between the two incoming channels. This leads to

$$\Delta\mathcal{G}^{(e)}_{1\mathrm{out}}(t|t') = R\Delta\mathcal{G}^{(e)}_{1\mathrm{in}}(t|t') + T\Delta\mathcal{G}^{(e)}_{2\mathrm{in}}(t|t') \tag{2.10a}$$

$$\begin{aligned}\Delta\mathcal{G}^{(2e)}_{1\mathrm{out}}(t_1,t_2|t_1',t_2') = {} & R^2\Delta\mathcal{G}^{(2e)}_{1\mathrm{in}}(t_1,t_2|t_1',t_2') + T^2\Delta\mathcal{G}^{(2e)}_{2\mathrm{in}}(t_1,t_2|t_1',t_2') \\ & + RT\Delta\mathcal{G}^{(e)}_{1\mathrm{in}}(t_1|t_1')\Delta\mathcal{G}^{(e)}_{2\mathrm{in}}(t_2|t_2') \\ & + RT\Delta\mathcal{G}^{(e)}_{1\mathrm{in}}(t_2|t_2')\Delta\mathcal{G}^{(e)}_{2\mathrm{in}}(t_1|t_1') \\ & - RT\Delta\mathcal{G}^{(e)}_{1\mathrm{in}}(t_1|t_2')\Delta\mathcal{G}^{(e)}_{2\mathrm{in}}(t_2|t_1') \\ & - RT\Delta\mathcal{G}^{(e)}_{1\mathrm{in}}(t_2|t_1')\Delta\mathcal{G}^{(e)}_{2\mathrm{in}}(t_1|t_2')\,.\end{aligned} \tag{2.10b}$$

Substituting these expressions into equation (2.4) gives us an expression for the excess noise that can be decomposed into three parts:

$$\Delta\mathcal{S}_{1\mathrm{out}}(t,t') = R^2\Delta\mathcal{S}_{1\mathrm{in}}(t,t') + T^2\Delta\mathcal{S}_{2\mathrm{in}}(t,t') + RT\mathcal{Q}(t,t')\,. \tag{2.11}$$

The first two terms correspond to the incoming excess noise within each incoming channel transmitted through the electronic beam splitter. The additionnal part $Q(t,t')$ contains all the effects of two particle interferences between the two incoming channels. It can be decomposed in three contributions

$$\mathcal{Q}(t,t') = \mathcal{Q}_{\mathrm{HBT},1}(t,t') + \mathcal{Q}_{\mathrm{HBT},2}(t,t') + \mathcal{Q}_{\mathrm{HOM}}(t,t') \tag{2.12}$$

in which $\mathcal{Q}_{\mathrm{HBT},i}$ is an additionnal part to the noise that appears due to the partition of current from channel i on the QPC, that would also appear when only one of the source is switched on, whereas $\mathcal{Q}_{\mathrm{HOM}}$ only appears when both sources are switched on[6].

[6]Of course, their names were not chosen at random! $\mathcal{Q}_{\mathrm{HBT}}$ corresponds to the contribution appearing in a Hanbury Brown and Twiss experiment, $\mathcal{Q}_{\mathrm{HOM}}$ to the one appearing on top of it in a Hong, Ou and Mandel one.

Their expressions in terms of coherence is given by

$$\mathcal{Q}_{\mathrm{HBT},i}(t,t') = \tag{2.13a}$$
$$(ev_{\mathrm{F}})^2\left[\frac{\delta(t-t')}{v_{\mathrm{F}}}\Delta\mathcal{G}^{(e)}_{i,\mathrm{in}}(t|t') - \mathcal{G}^{(e)}_{\mathrm{F}}(t|t')\Delta\mathcal{G}^{(e)}_{i,\mathrm{in}}(t'|t) - \mathcal{G}^{(e)}_{\mathrm{F}}(t'|t)\Delta\mathcal{G}^{(e)}_{i,\mathrm{in}}(t|t')\right]$$
$$\mathcal{Q}_{\mathrm{HOM}}(t,t') = \tag{2.13b}$$
$$-(ev_{\mathrm{F}})^2\left[\Delta\mathcal{G}^{(e)}_{1\mathrm{in}}(t|t')\Delta\mathcal{G}^{(e)}_{2\mathrm{in}}(t'|t) + \Delta\mathcal{G}^{(e)}_{1\mathrm{in}}(t'|t)\Delta\mathcal{G}^{(e)}_{2\mathrm{in}}(t|t')\right].$$

The first contribution, $\mathcal{Q}_{\mathrm{HBT}}$ depends only on products between the excess coherence of a source and the Fermi sea coherence[7]. In the real experiment, we are not measuring this quantity directly, but rather a time averaged low frequency excess noise, and we will therefore obtain the following overlap[8]:

$$\mathcal{Q}_{\mathrm{HBT},i} = e^2\int \mathrm{d}t \int \frac{\mathrm{d}\omega}{2\pi}\Delta\mathcal{W}^{(e)}_{i,\mathrm{in}}(t,\omega)(1-2f_{\mathrm{F}}(\omega))\,. \tag{2.14}$$

This equation makes the physical meaning of the excess noise quite easy to understand: at zero temperature $\mathcal{Q}_{\mathrm{HBT},i}$ directly counts the total number of excitations (electrons and holes) emitted by the source.

Let us now focus on the $\mathcal{Q}_{\mathrm{HOM}}$ term. The first relevant question is simply: how to access this quantity? To do so, we will have to run the experiments three times: once with both sources on, once with only source 1 on, and once with source 2 only. For each of these runs, we measure the excess current noise obtained by subtracting the noise signal with all sources off. Finally, we simply subtract the excess noise measured when only one source is on and the other one is turned off. This directly leads to $\mathcal{Q}_{\mathrm{HOM}}$ and, we obtain the full overlap of the coherences functions from both sources:

$$\mathcal{Q}_{\mathrm{HOM}} = -2e^2\int \mathrm{d}t \int \frac{\mathrm{d}\omega}{2\pi}\Delta\mathcal{W}^{(e)}_{1,\mathrm{in}}(t,\omega)\Delta\mathcal{W}^{(e)}_{2,\mathrm{in}}(t,\omega)\,. \tag{2.15}$$

This contains exactly what we are searching for in our quest for the equivalent of homodyne detection: since this probes the overlap between two sources, we may be able to use one of the source in a controlled

[7] We can absorb back the $\delta(t-t')$ term from equation (2.13a) if we write the product of an electronic coherence $\mathcal{G}^{(e)}$ with a hole one $\mathcal{G}^{(h)}$, rather than using only electronic coherences.

[8] Equations (2.14) and (2.15) use the Wigner representation of coherence as it will be the most useful for us in the next sections of this manuscript, but it could also be written in terms of time or frequency representations of single electron coherences.

manner to gain more information on the other one. This will be discussed mostly in section 2.3, but it all comes down to this overlap problem. As of now, let us concentrate on "standard" HOM experiments, and look at the expected results when the two sources are the same.

A simple example

To get a better understanding of $\mathcal{Q}_{\mathrm{HOM}}$, lets us consider a simple case in which source 1 emits a single-excitation state described by a wavepacket φ_1, whereas source 2 emits φ_2. In this case, we have $\Delta\mathcal{G}_i^{(e)}(t|t') = \varphi_i^*(t')\varphi_i(t)$, leading to

$$\mathcal{Q}_{\mathrm{HOM}} = -2(ev_{\mathrm{F}})^2|\langle\varphi_1|\varphi_2\rangle|^2\,. \tag{2.16}$$

In order to normalize this quantity, we define

$$\Delta q = \frac{\mathcal{Q}}{\mathcal{Q}_{\mathrm{HBT},1} + \mathcal{Q}_{\mathrm{HBT},2}} \tag{2.17}$$

which, in the simple case considered here, gives

$$\Delta q = 1 - |\langle\varphi_1|\varphi_2\rangle|^2 \tag{2.18}$$

since we just saw that $\mathcal{Q}_{\mathrm{HBT},i}$ is simply e^2 times the number of excitations emitted by source i, which is equal to 1 here.

The quantity Δq is the one displayed in experimental results, just as in figure 2.5. This is due to the fact that in the specific case of our experiment, it is as simple to measure this specific quantity as it is to measure $\mathcal{Q}_{\mathrm{HOM}}$. Indeed, it can be shown that the excess low-frequency current noise of single electron sources operated in an AC regime at high-frequency is zero: $\Delta\mathcal{S}_{1\mathrm{in}} = \Delta\mathcal{S}_{2\mathrm{in}} = 0$. This can be understood simply through the fact that this quantity measures the fluctuation of the number of charges emitted at each period by our sources. In the single electron regime, we should emit exactly one electron at every period, and the fluctuation is therefore null. This was confirmed up to our experimental resolution [16], and is in fact a way to test whether the source is really in the single electron regime or not.

The three measurement steps to get Δq are then:

- both sources switched on minus both sources turned off to measure $\mathcal{Q}$,
- source 1 switched on minus both sources turned off to get $\mathcal{Q}_{\mathrm{HBT},1}$,

- same measurement for source 2.

These three measurements together give us one point of the Δq curve. In order to have relevant averages and errors, each point corresponds to approximately 5 to 10 minutes of data acquisition. We then change the time-delay between sources for the next point and iterate until the whole curve is recovered. The full process therefore takes a few hours for each Hong-Ou-Mandel curve[9].

When looking at the results in figure 2.5, the attentive reader will see that the HOM dip represented on that figure does not go all the way down to zero. Yet, as we just said, the depth should be directly linked to the overlap between the incoming states. If both of our sources emit indistinguishable single particle excitations in the system, an overlap equal to 1 is expected when they collide at the same time on the QPC. The HOM dip should then go to zero. Could the observed non-zero HOM dip be related to differences between the two sources such that they emit sufficiently different wavepackets ?

In order to test this hypothesis, we have tuned the sources' parameters over a broad range in order to see if we could detect differences in the resulting HOM curves [OP3]. The result of these investigations is depitected in figure 2.6. We have tested two types of differences on the sources. First, we have changed the escape time of one of the source, keeping the injection energies equal. A clear asymmetry of the two parts of the HOM curve has been observed. This feature was not present when both sources have expected escape times close to one another.

Next, we have changed the emission energy of one source, either by detuning the potential applied to the source or by applying some large random fluctuations to the voltage applied to one of them (leading to a varation of the order of 400 mK on the initial emission energy, which is of 700 mK). In both cases, the recovered HOM curve shows no differences with the one obtained when both sources are operated with identical parameters.

These two results are a convincing proof that the smaller than one dip cannot be explained by differences at the source level, but has a different physical origin. Indeed, as we shall see, the explanation for this phenomenon is electronic decoherence induced by Coulomb interaction, which takes place along propagation between the source and the QPC.

[9]Let me stress here how thankful I am to V. Freulon, whose work allowed such small measurement times, as compared to approximately one week for a single curve such as the one presented in Bocquillon et al. [13].

This will be discussed extensively in chapter 3, and more specifically in section 3.2.

2.3 Reconstruction of an unknown coherence

The theoretical discussion of the HOM experiment suggests that one should be able to recover the value of the overlap between two excess single electron coherences. As was hinted before, it is then natural to ask wether or not we can go beyond this result and reconstruct an unknown coherence, with several measurements. Such a process is generically called tomography, a name that encompasses all techniques aiming at reconstructing full properties of a system from measurements giving access only to partial results. For example, in the medical domain, tomography allows the visualization of the internal structure of the human body from measurement of secondary properties such as X-ray transmission, radioactive counting rates or radio-frequency signals (in MRI) depending on the internal structure. In a simplistic manner, tomography is exactly like solving the inner part of a "magic square", knowing the sums of each lines and columns as well as the rules applying to the square itself.

In our case, what we want to reconstruct is directly the Wigner function of an unknown source. This exact idea and experiment has already been demonstrated and greatly used in other domains of quantum physics, and tomography experiments aiming at reconstructing the Wigner function of an unknown state have been demonstrated in the case of trapped ions [103], vibration modes of molecular systems [39], and of a field in a cavity [9]. These experiments are among the main reasons for the attribution of the 2012 Nobel prize to S. Haroche and D. Wineland, "for ground-breaking experimental methods that enable measuring and manipulation of individual quantum systems". Indeed, during the past 25 years, this type of tomography experiments have made their way from their demonstration on simple cases to being used as an everyday tool in order to prepare complex quantum states [129, 145] or characterize their evolution [19]. However, in the case of quantum electronics, such a protocol allowing the reconstruction of an unknown quantum state has long been out of reach, and has only been demonstrated during my PhD, more than 20 years after its optics counterpart.

In this section, I will try to give a detailed account of its birth and describe how we achieved the realization of a fully-working tomography

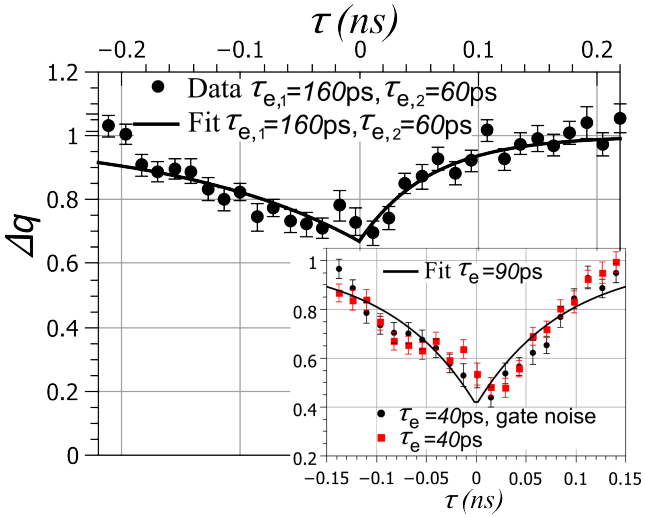

Figure 2.6: Results of Hong-Ou-Mandel measurements, taken from [OP3], for two different sources. *Main panel*: sources with different escape times. We see a clear asymmetry between the two halves of the curve, a fact which was not visible before. The sources used in the previous experiment thus had escape times close to one another. *Inset*: sources with different energies. We compare the standard case (in red) with a case in which the energy of the source is changed randomly through an added noise (in black). As we can see, the energy change has no effect on the measured HOM curve, meaning that the smaller than one size of the dip cannot be explained by a difference in energy between the two sources. Both results indicate that there is another process at play to explain the fact that we do not get the expected size of the dip, and that this process erases all information on the emission energy of the sources. The answer to that problem will be developed in section 3.2.

protocol for quantum currents. This will be done first from a theoretical standpoint, by describing how a generic protocol for reconstructing single electron coherence from HOM-like measurements can be obtained. Then, I will describe its experimental implementation at the Laboratoire Pierre Aigrain, on which I had the chance to work during my stay there. Finally, I will describe a recently invented signal processing step added to this protocol which enables us to extract the individual electronic wavefunctions present in quantum electrical current propagating along a quantum Hall edge channel.

2.3.1 Single electron tomography protocol: the idea

The main ingredient of our tomography protocol is the HOM experiment presented in the previous section. Because it computes the overlap between two coherences, the idea is to probe the unknown coherence arriving on a QPC via a suitable family of reference coherences on the other source. We thus have to find which clever family of probes provides enough information for reconstructing the unknown electronic coherence.

A first answer to this question has been given by Grenier et al. [66] to reconstruct the Wigner function of a periodically driven electronic source. In this case, the full Wigner function of the source can be expanded in a Fourier series with respect to t, using equation (1.53):

$$\mathcal{W}_S^{(e)}(t,\omega) = \sum_{n=-\infty}^{+\infty} \mathcal{W}_{S,n}^{(e)}(\omega) \mathrm{e}^{2\mathrm{i}\pi n f t}\,. \tag{2.19}$$

Our protocol allows to recover the harmonics $\mathcal{W}_{S,n}^{(e)}(\omega)$. This is achieved by using a family of probe that has in fact already been presented in section 1.2.4: sinusoidal drives applied to an Ohmic contact. Indeed, a drive of the form $V_{P_n}(t) = V_{P_n}\cos(2\pi n f t + \phi)$ applied to a Fermi sea at chemical potential μ and temperature T_{el} has a Wigner function given by equation (1.49) in the "quantum regime" $k_{\mathrm{B}}T_{\mathrm{el}} \ll eV_0 \ll hf$. As we shall see, its oscillating time dependance at low drive amplitude can be used to reconstruct the unknown Wigner function.

Spectroscopy of the source

Let us start with the $n = 0$ harmonic, which is probed using a simple DC drive applied on the incoming channel 2, for which the Wigner function

$\mathcal{W}^{(e)}_{\mu_2,T_{\mathrm{el}}}$ is directly the one of the Fermi sea at chemical potential μ_2. The chemical potential can be controlled experimentally and thus be different from the one of our unknown source μ_1. To simplify notations, we will take $\mu_1 = 0$ and $\mu_2 = \mu$ in the following. At zero temperature, the excess Wigner function in channel 2 with respect to the equilibrium situation at $\mu = 0$ is therefore a function equal to 1 in the range $[0, \mu]$ and to 0 everywhere else. This means that the HOM noise that can be measured is, using equation (2.13):

$$\mathcal{Q}^{(0)}_{\mathrm{HOM}}(\mu) = -2e^2 \lim_{T\to\infty} \frac{1}{T} \int_{-T/2}^{T/2} \mathrm{d}t \int_0^{\mu} \frac{\mathrm{d}\omega}{2\pi} \Delta\mathcal{W}^{(e)}_S(t,\omega) \tag{2.20}$$

where the subscript S is used to denote the (unknown) Wigner function of the source. The average over time leads to a vanishing of all harmonics of the Wigner function except for the stationary one $\Delta\mathcal{W}^{(e)}_{S,0}$. Moreover, when starting from a point where the excess coherence of the source vanishes, increasing μ only adds a small quantity related to $\Delta\mathcal{W}^{(e)}_{S,0}(\mu)$. Taking the derivative of $\mathcal{Q}^{(0)}_{\mathrm{HOM}}(\mu)$ with respect to μ leads directly to the recovery of $\Delta\mathcal{W}^{(e)}_{S,0}(\mu)$, which is simply equal to the excess occupation number $\delta f_e(\omega = \mu/\hbar)$ at the corresponding frequency.

This first step of the protocol therefore realizes a spectroscopy of the source and measures its excess occupation number. From a physical point of view, this expresses that a DC bias directly probes whether or not there are electrons present up to a certain energy, as is schematically depicted in figure 2.7. From an experimental point of view, spectroscopy measurements have been accessible for a few years now, but often use another protocol based on quantum dots to recover the excess occupation number emitted by the source [1]. The real advantage of our protocol thus comes from the fact that the same setup can also be used to get higher harmonics of the Wigner function, as we will see now.

Getting the harmonics

Measuring the harmonics $\Delta\mathcal{W}^{(e)}_{S,n}$ is quite simple from a theoretical point of view once we understand which drive to use. Indeed, using one of the drives $V_{P_n}(t)$ in the quantum regime leads, for low enough voltage

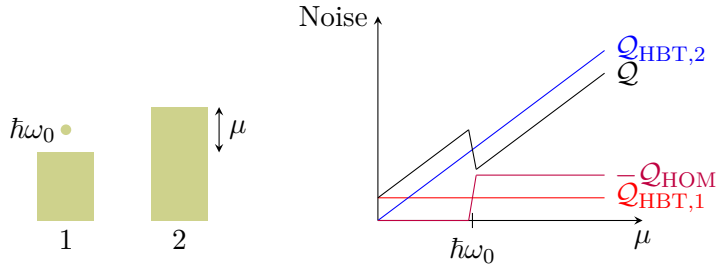

Figure 2.7: A schematic representation of the principle behind our spectroscopy protocol. An unknown source, for example with an excitation around energy $\hbar\omega_0$ above the Fermi sea, is sent into channel 1, while we use a Fermi sea with chemical potential μ as the source in channel 2. The HBT contributions to noise, with respect to μ, are: a constant for channel 1, and a line for channel 2, since we send more and more excitations on the beamsplitter. However, if $\mu > \hbar\omega_0$, an antibunching effect can occur between the electron in channel 1 and the corresponding one in channel 2. This leads to a reduction of the total noise, or equivalently to the apparition of a non-zero HOM contribution. The derivative of this contribution with respect to μ will grant us an access to the energy distribution of excitations emitted by source 1.

amplitude and at zero temperature, to a measured noise of the form

$$\begin{aligned}
&\mathcal{Q}^{(n)}_{\mathrm{HOM}}(\mu,\phi)\\
&= -2e^2 \lim_{T\to\infty} \frac{1}{T}\int_{-T/2}^{T/2} \mathrm{d}t \int_{\mu-n\pi f}^{\mu+n\pi f} \frac{\mathrm{d}\omega}{2\pi} \Delta\mathcal{W}^{(e)}_{S}(t,\omega) \frac{eV_{P_n}}{hnf} \cos(2\pi n f t+\phi)\\
&= -\frac{e^3 V_{P_n}}{hnf} \int_{\mu-n\pi f}^{\mu+n\pi f} \frac{\mathrm{d}\omega}{2\pi} \left(\Delta\mathcal{W}^{(e)}_{S,n}(\omega)\mathrm{e}^{\mathrm{i}\phi} + \Delta\mathcal{W}^{(e)}_{S,-n}(\omega)\mathrm{e}^{-\mathrm{i}\phi}\right) . \qquad (2.21)
\end{aligned}$$

Reality of the Wigner function implies that $\Delta\mathcal{W}^{(e)}_{S,n}$ and $\Delta\mathcal{W}^{(e)}_{S,-n}$ are complex conjugated. Changing the phase ϕ thus allows to recover both the real and imaginary part of $\Delta\mathcal{W}^{(e)}_{S,n}$ [10]. The full energy dependence of $\Delta\mathcal{W}^{(e)}_{S,n}(\omega)$ can finally be recovered by varying the chemical potential with an added DC part to the drive, starting from μ such that $\mathcal{Q}^{(n)}_{\mathrm{HOM}}(\mu,0)=0$.

2.3.2 Experimental results

The first tomography experiment realized in the context of electron quantum optics was performed in 2014 by D.C. Glattli's group in Saclay, and demonstrated the successful reconstruction of a Leviton's wave function [90]. However, the method used was not the generic tomography protocol presented in the previous section. It was a clever adaptation of its idea based on the fact that a periodic driving of an Ohmic contact can be described entirely through the photo-assisted transitions amplitude α_n defined in equation (1.57). This enabled getting the necessary information for reconstructing the Leviton's wavefunction at a reasonable measurement cost, but the demonstration relied on strong hypotheses. Nevertheless, this work showed that the necessary requirements in terms of excess noise measurement sensitivity had been achieved, and that tomography was no more a theoretical idea only.

The first demonstration of the generic tomography protocol we discussed was performed just a bit later within the group of G. Fève at the Laboratoire Pierre Aigrain, during the PhD of A. Marguerite [112], in the case of a sinusoidal source. This specific source has been chosen for a proof of concept since it is mostly unaffected by interactions. On the contrary, most other electronic sources will experience drastic changes in their Wigner distribution function during their propagation within quantum Hall edge channels, as will be discussed in chapter 3 (see page

[10] Of course, the imaginary part should be equal to 0!

152). The physical interpretation of the equations presented there is that the system is in a linear response regime with respect to sinusoidal drives. The specific case of a sinusoidal drive thus enables an easy comparison between the experimental results and the theoretically expected Wigner function without any parameter arising from the modelling of screened effective Coulomb interactions. Here, the expected single electron coherence can be computed using Floquet theory, providing a way to benchmark the tomography experiment. We shall therefore focus on this specific case and present the results published in [OP4].

In order to test the validity of our tomography protocol, we have used two sinusoidal drives with different frequencies. The first one is a low-frequency drive at 10 MHz, which satisfies the condition $hf \ll k_{\mathrm{B}}T_{\mathrm{el}}$, thus allowing the investigation of the quasi-classical regime expected for adiabatic driving (see section 1.2.4, figure 1.10). For this very low frequency driving, we expect the recovered Wigner function to be given by a Fermi sea with a time-dependent chemical potential following the time dependent drive voltage.

By contrast, our second drive at a frequency of 9 GHz is expected to be in the quantum regime. It is applied both at $T_{\mathrm{el}} = 100$ mK and 60 mK which, in both cases, satisfy $k_B T_{\mathrm{el}} \lesssim hf$. The drive's amplitude, is kept almost constant over all experiments ranging from 31 µV to 33 µV, so that we are always in the $k_B T_{\mathrm{el}} \lesssim eV$ regime. Deviations from classicality are then expected, in particular values of the Wigner function outside of the $[0, 1]$ range. Such deviations from classicality should moreover be stronger at the lowest electronic temperature.

On the probing side of the experiment, we need to be able to use sources with frequencies that are multiples of the drive's frequency. This is quite simple in the case of the low-frequency drive, as we can easily use sources with frequencies equal to several times 10 MHz. Howevever, in the 9 GHz case, we are limited by the radiofrequency sources and cables and will therefore only be able to reconstruct the first three harmonics of the Wigner function, which already involves a 27 GHz probe. Knowing the phase relationship between the $n = 1$, $n = 2$ and $n = 3$ probes is also quite difficult, since for such high frequencies, the phase accumulated along the transmission lines can depend on the frequency. A careful calibration was required, and performed using the fact that the imaginary part of the Wigner function should be zero. This has allowed us to easily find the points where $\phi = \pi/2$ or $3\pi/2$ (see equation (2.21)). Since we could never know for sure whether the one we get with this

calibration is $\pi/2$ or $3\pi/2$, we have taken the average between pairs of points with phases separated by π, and chosen for reference the pair of points that minimizes the noise. Doing so implies that the real part of $\Delta\mathcal{W}^{(e)}_{S,n}$ has been obtained through $\mathcal{Q}^{(n)}_{\mathrm{HOM}}(\mu,0)+\mathcal{Q}^{(n)}_{\mathrm{HOM}}(\mu,\pi)$.

This problem of phase calibration is not the only one present in the experiment. The effect of a non-zero electronic temperature has indeed been overlooked so far in our pedagogical presentation of the protocol. Hence, although equation (2.21) is completely valid at zero temperature, the energy limits in the integral are less stringent in a non-zero temperature case. To be more specific, our protocol does not directly recover the harmonics of the Wigner function, but a convolution of them with a thermal broadening function. A deconvolution process called Wiener filtering of the acquired signal has to be performed, and only requires a sufficiently good knowledge of the electronic temperature. We will not go into more detail on the filtering technique here, but a reader interested in this technique will find the reading of A. Marguerite PhD [112] particularly useful.

Without further discussion, let us describe the results obtained with this setup, shown in figure 2.8. First of all, we can see a clear agreement between measured points and Floquet scattering theory which allows us to confirm that our setup indeed works as intended and performs single electron tomography in a controlled way for this specific source. Looking at the Wigner distribution functions reconstructed from the measurements using

$$\mathcal{W}^{(e)}_S(t,\omega) = \tag{2.22}$$
$$f_{T_{\mathrm{el}}}(\omega)+\Delta\mathcal{W}^{(e)}_{S,0}(\omega)+2\sum_{n=1}^{3}\mathrm{Re}\left(\Delta\mathcal{W}^{(e)}_{S,n}(\omega)\right)\cos(2\pi nft)\,,$$

we immediately see the difference between classical and quantum regimes: apart from small discrepancies related to the deconvolution process, the classical source at 10 MHz corresponds to values of the Wigner function within 0 and 1. On the contrary, the high-frequency drives display clear negative and greater than 1 values, which are more visible at the lowest electronic temperature.

This groundbreaking experimental work is a first proof of concept showing that the generic tomography protocol devised a few years ago can indeed be used experimentally. As explained in this manuscript, this has been made possible by improving drastically the degree of control and the precision of excess current noise measurements in Hong-

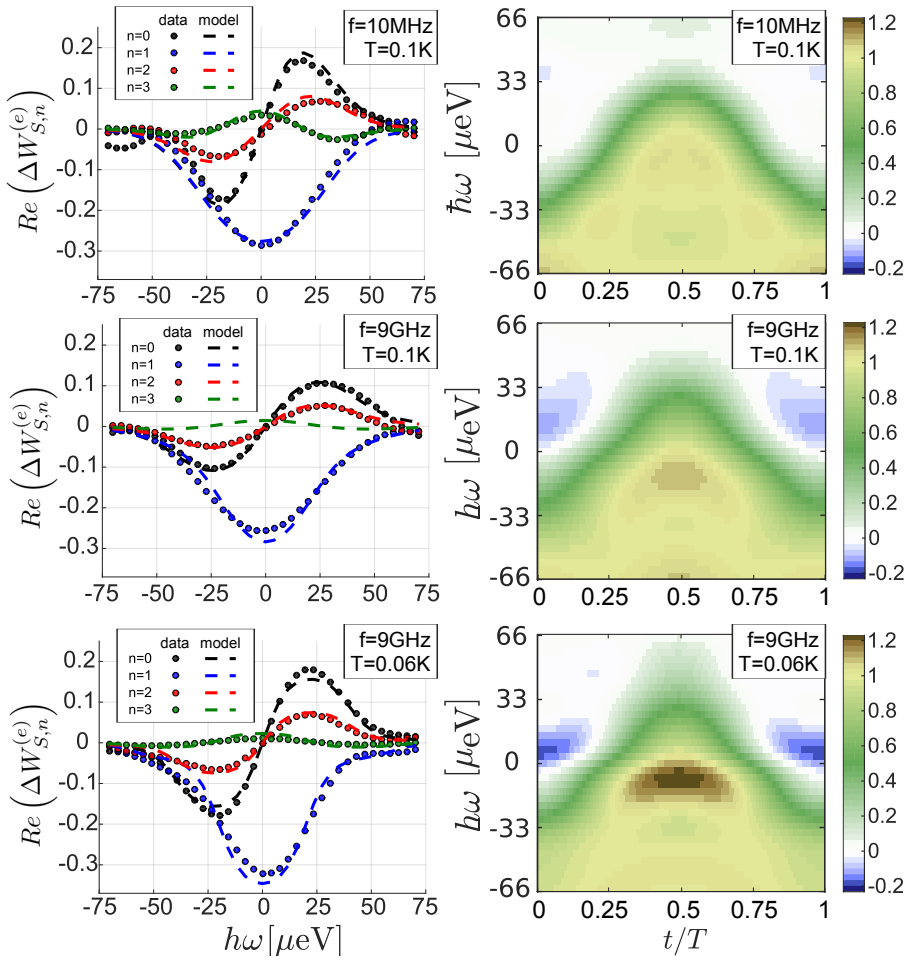

Figure 2.8: Results of measurements for the tomography protocol presented in section 2.3.2, taken from [OP4]. From top to bottom, we use three type of sources: $f = 10\,\mathrm{MHz}$ drive at $T_{\mathrm{el}} = 100\,\mathrm{mK}$, 9 GHz at 100 mK and finally 9 GHz at 60 mK. *Left*: $\Delta\mathcal{W}^{(e)}_{S,n}$ obtained from measured noise in the experiment (points), compared to the theoretical prediction (dashed lines), for harmonics $n = 0$ to $n = 3$. *Right*: Reconstructed Wigner function using the experimentally measured harmonics.

Ou-Mandel experiments. However, in the meantime, theorists have not stood idle, and important developments have been made in order to extract as much information as possible from reconstructed – or computed – electronic Wigner functions. Indeed, up to now, we had mostly predicted and discussed Wigner functions associated with specific many body quantum states such as the ones supposedly generated by the electronic sources. But, with the advent of tomographic reconstructions of a priori unknown Wigner functions, the opposite question finally becomes relevant: given a Wigner function, can we extract the single-electronic wavefunctions present in the many-body electronic state ? What can we say about their emission probabilities? How coherent is the electronic source that generates such a Wigner function ? These questions will now be addressed.

2.3.3 Extracting electronic wavefunctions from the coherence

The problem of extracting information from coherence functions has been adressed mostly by B. Roussel during his PhD [138]. His manuscript is partly devoted to a new approach to the analysis of quantum coherent beams of particles which we have dubbed "Quantum Signal Processing". A full chapter is devoted to the mathematics and usages of a method for analyzing quantum electrical currents at the single particle level, which as we shall see, provides an answer to the question we have just formulated. This section will only serve as a brief summary of the more than 60 pages devoted to this theme in his manuscript, which I advise any reader interested in a more mathematically sound formulation to consult. The present discussion could be seen as my own retro-engineering of the method invented by B. Roussel in a tone more fitting the present manuscript.

The main question is to find the single electron and hole wavefunctions that build a full electronic coherence. In a way, we want to extend the results obtained in equation (1.34) to the case where, for example, several electron-hole pair superpositions are present, without knowing a priori which single particle wavefunctions appear in the coherence. How can we achieve this?

First of all, we restrict ourselves to periodic sources, which implies that the wavefunctions appearing in the coherence at some specific time should also appear a period later. Then, inspired by M. Devoret's discussions of photons propagating in a transmission line [36], we imagine that

the quantum electrical current can be described in terms of *electronic atoms of signal* which form a family of single-electron wavefunctions $\varphi^{(e)}_{a,l}$ with the following properties:

$$\varphi^{(e)}_{a,l}(t) = \varphi^{(e)}_{a,0}(t - lT) \tag{2.23a}$$

$$\langle \varphi^{(e)}_{a,l} | \varphi^{(e)}_{a',l'} \rangle = \delta_{aa'}\delta_{ll'} \, . \tag{2.23b}$$

For a periodic source, this is quite natural: all electronic and hole wavefunctions should be deduced from the set of single particle wavefunctions associated with a given time period. The a subscript accounts for the fact that several electrons may be emitted in a given period. The orthogonality condition means that single particle excitations emitted at one period are perfectly distinguishable from the ones emitted during other periods. Of course, we also need to define in exactly the same way single-hole wavefunctions, denoted by $\varphi^{(h)}_{b,l}$. Our problem is then to find a way to extract these atoms of signal from the coherence function itself.

A first specific case in which this had indeed been done is the case of a Leviton excitation train. An analytical approach has allowed Moskalets [116] to find a representation of the emitted coherence under the form

$$\mathcal{G}^{(e)}_{\text{Lev. train}}(t|t') = \sum_{l=-\infty}^{l=\infty} \varphi^{(e)}_{l}(t')^{*} \varphi^{(e)}_{l}(t) \tag{2.24}$$

with wavefunctions given by

$$\varphi^{(e)}_{l}(t) = \sqrt{\frac{\tau_0}{\pi v_{\mathrm{F}}}} \frac{1}{t - lT + \mathrm{i}\tau_0} \prod_{k=l}^{\infty} \frac{t - kT + \mathrm{i}\tau_0}{t - kT - \mathrm{i}\tau_0} \tag{2.25}$$

We can show that the $\varphi^{(e)}_{l}$ satisfy all properties from equation (2.23), and are indeed a case in which it has been possible to find an analytic expression for the electronic atoms of signal[11]. Moreover, in the case of well-separated Levitons ($\tau_0 \ll T$), we directly see that each electronic atom of signal becomes closer to the standard Leviton wavefunction from equation (1.63) shifted in time, as we would expect from a source emitting Levitons pretty much one by one.

Yet, as of today, no analytical approach has lead to the corresponding family of wavefunctions appearing for n-Levitons obtained with a

[11] Here, since there is only one family of wavefunctions, we have no need for the a subscript that appeared in our general definition.

Lorentzian voltage pulse of charge $-ne$. Even more importantly, in a completely generic case, this family also remained pretty much unknowned, as well as the generic form of a single electron excess coherence. This is where our approach comes into play: it is a systematic procedure allowing to extract numerically the wavefunctions appearing in any coherence. Let us now present how this procedure works, before showing its results for the coherence that was experimentally measured, which we presented in figure 2.8.

Numerically extracting single particle wavefunctions

Let us assume for a moment that we have families of wavefunctions describing electrons and holes present in the system, satisfying the conditions given in equation (2.23). If this is the case, the most natural and general ansatz for the excess coherence with respect to a zero-temperature Fermi sea, which we denote by $\Delta_0\mathcal{G}$, can be written as:

$$\Delta_0\mathcal{G}_S^{(e)}(t|t') = \sum_{(l,l')\in\mathbb{Z}^2} \Bigg[\sum_a g_a^{(e)}(l-l')\varphi_{a,l}^{(e)}(t)\varphi_{a,l'}^{(e)}(t')^* \tag{2.26a}$$

$$- \sum_b g_b^{(h)}(l-l')\varphi_{b,l}^{(h)}(t)\varphi_{b,l'}^{(h)}(t')^* \tag{2.26b}$$

$$+2\sum_{a,b} \mathrm{Re}\left(g_{ab}^{(eh)}(l-l')\varphi_{a,l}^{(e)}(t)\varphi_{b,l'}^{(h)}(t')^* \right) \Bigg]. \tag{2.26c}$$

First of all, this result is sesquilinear in all the electronic and hole atoms of signal at our disposal, and displays both the electrons and holes atoms of signal that are supposed to be present in our coherence, as well as three coefficients $g_a^{(e)}$, $g_b^{(h)}$ and $g_{ab}^{(eh)}$. These complex numbers are easy to interpret. First, when $l-l'=0$, $g^{(e)}(0)$ is real and between 0 and 1. It simply represents the probability to emit an electron in the wavepacket $\varphi_a^{(e)}$ at each period. Obviously, $g^{(h)}(0)$ represents the probability to emit a hole in $\varphi_b^{(h)}$ at each period. Then, whenever $l \neq l'$, they represent coherences between wavepackets emitted at different periods. The last coefficient $g_{ab}^{(eh)}(l-l')$ represents, as expected, the electron/hole coherences between the associated electrons and holes. Such electron/hole coherences can only occur when the probabilities to emit electrons or holes excitations differ from 1, such that a coherent superposition between the equilibrium and the creation of an electron/hole pair is generated. Of course, the $l-l'$ dependence on the period indices reflects

the time periodicity of the source. The only non trivial feature in this expression is the fact that it is diagonal in the a index for the electronic part, and in the b index for the hole part. We will explain in a few lines why this is not restrictive, and show that there are always electronic and hole atoms of signal such that equation (2.26) is satisfied.

Our objective here is simply to find these atoms of signal and the value of all coherence coefficients, in order to understand in the best way possible the building bricks of our coherence. Remembering the quadrant decomposition from figure 1.8, it is easy to show that the three terms from equation (2.26) live respectively in the electron quadrant, the hole quadrant, and the two electron-hole quadrants.

We focus first on the electronic wavefunctions $\varphi_a^{(e)}$, or equivalently restrict ourselves to the electronic quadrants of coherence, denoted by $\mathcal{G}_+^{(e)}$. We are then facing a problem that closely looks like solid state physics, with some localized wavefunctions coupled through amplitudes depending only on the separation $l-l'$ between them. We can draw some inspiration from Bloch's theorem, and search whether the coherence can be written in terms of functions that would be the equivalent of Bloch waves in the time domain. From this perspective, electronic atoms of signal would be the time-domain equivalent of Wannier functions in standard solid state physics. We thus have the following relations between them:

$$\psi_{a,\nu}(t) = \frac{1}{\sqrt{f}} \sum_l \mathrm{e}^{\mathrm{i}l\nu T} \varphi_{a,l}(t) \tag{2.27a}$$

$$\psi_{a,\nu}(t+T) = \mathrm{e}^{-\mathrm{i}\nu T} \psi_{a,\nu}(t) \tag{2.27b}$$

$$\psi_{a,\nu}(t) = \mathrm{e}^{\mathrm{i}\nu t} u_{a,\nu}(t) \tag{2.27c}$$

where we have dropped the (e) subscript for brevity, and the $u_{a,\nu}$ functions are T-periodic. The quasipulsation index ν is chosen in $[0, 2\pi f[$, which plays the role of a 1D Brillouin zone in the pulsation domain. What happens when we try to rewrite coherence in those variables? First of all, we will use the fact that the functions $u_{a,\nu}$ are periodic, and can therefore be written using a Fourier series. This leads to

$$\Delta_0 \mathcal{G}_+^{(e)}(t|t') = \tag{2.28}$$
$$\sum_{n,p} \int_0^{2\pi f} \frac{\mathrm{d}\nu}{2\pi f} \tilde{g}_a(\nu) u_{a,\nu,n} u_{a,\nu,p}^* \mathrm{e}^{2\mathrm{i}\pi f(p-n)\bar{t}} \mathrm{e}^{\mathrm{i}(\nu+\pi f(p+n))\tau}$$

where $u_{a,\nu,n}$ is the n-th coefficient in the Fourier series of $u_{a,\nu}(t)$, and we have defined

$$\tilde{g}_a(\nu) = \sum_l g_a(l) \mathrm{e}^{-\mathrm{i}\nu l T} \,. \tag{2.29}$$

Using the fact that coherences for periodic sources can be decomposed as a sum of harmonics, with equation (1.53), we finally get

$$\sum_{n,p} v_\mathrm{F} \Delta_0 \widetilde{\mathcal{G}}^{(e)}_{+,n-p}(\nu + \pi(n+p)f) - \tilde{g}_a(\nu) u_{a,\nu,n} u^*_{a,\nu,p} = 0 \,. \tag{2.30}$$

This equation gives us what we need in order to obtain the functions $\tilde{u}_{a,\nu}$ as well as the $\tilde{g}_a(\nu)$. Indeed, it can be interpreted as a simple diagonalization problem for each quasipulsation ν! Diagonalizing the matrix M defined by

$$M_{np} = v_\mathrm{F} \Delta_0 \widetilde{\mathcal{G}}^{(e)}_{+,n-p}(\nu + \pi(n+p)f) \tag{2.31}$$

directly gives access to good eigenvectors $\tilde{u}_{a,\nu}$ and associated eigenvalues $\tilde{g}_a(\nu)$ appearing in the simplest possible representation of coherence. Using the inverse transformation of the one from equation (2.27), we can then get back the Wannier functions $\varphi_{a,l}$ and the coefficients $g_a(l - l')$.

To summarize, our procedure contains five main steps:

- Using a tomography experiment, or from numerical results, get some coherence $\mathcal{G}^{(e)}(t|t')$. Restrain yourself to the electronic quadrant.

- Diagonalize the matrix M defined by equation (2.31) from the resulting projection of the excess single electron coherence to the electronic quandrants.

- Build Wannier functions $\varphi_{a,l}(t)$ and inter-period coherences $g_a(l - l')$ from the eigenvectors and eigenvalues of M. These constitute the building blocks of the total coherence, and may be interpreted on their own.

- Perform the first three steps for the hole part of the electronic excess coherence.

- Compute from the electronic and hole eigenvectors the interband matrix elements of the excess single electron coherence.

Testing it on the experiment

Now that we have explained the full protocol for extracting wavefunctions from a coherence, let us test it on the experiment. As a first example, figure 2.9 presents the result of this protocol on the drive at a 9 GHz frequency and a 60 mK electronic temperature (bottom Wigner function from figure 2.8).

In this case, we find that coherence is completely dominated by one electronic $\varphi^{(e)}$ and one hole $\varphi^{(h)}$ atoms of signal[12]. We therefore do not need to keep the a and b subscripts. The Wigner functions associated with these wavepackets, displayed on the top of the figure, show that the hole excitation is shifted by half a period with respect to the electron. In the energy domain, they are almost perfectly upside-down versions of each other, a fact that was expected since we are using a symmetric drive with respect to the Fermi level. Moreover, the energy distribution of these wavepackets presents almost flat plateaus of width hf, as can be seen on the left of each Wigner. In the case of a sinusoidal drive, all energy exchanges should be multiples of hf, so that this behaviour is also expected. The deviation from flatness arises from the finite temperature of the system.

However, the Wigner function depicted in figure 2.8 does not seem to be simply given by one electron in $\varphi^{(e)}$ and one hole in $\varphi^{(h)}$ at each period. This is because finding the wavefunctions is only one half of the problem of reconstruction: we also need to study the $g^{(e/h/eh)}$ coherences! Their moduli are depicted on the bottom of figure 2.9, both for the experimental data (circles) and for the expected coherence simulated through Floquet theory (bars). We can obviously see quite a good agreement between them, which will allow us to compare results with the not experimentally available situation of zero temperature. On all these graphs, we first remark that the probability to emit these wavepackets is far less than 1, which is completely coherent with the fact that a sinusoidal drive should not be in the single electron regime. This was also expected since the ratio $\alpha = eV/hf$, equal to 0.8 in this case, is directly linked to the average number q of electron/hole pairs emitted per period: $q = \alpha/\pi$. Since both $g^{(e)}(0)$ and $g^{(h)}(0)$ are less than 1, we also observe non-zero electron/hole coherence.

Now, the evolution of coherences with temperature also has quite an interesting story to tell. At zero temperature, as was said before, the

[12]This means that the eigenvalues found in the diagonalization of equation (2.31) are roughly all equal to 0, except one.

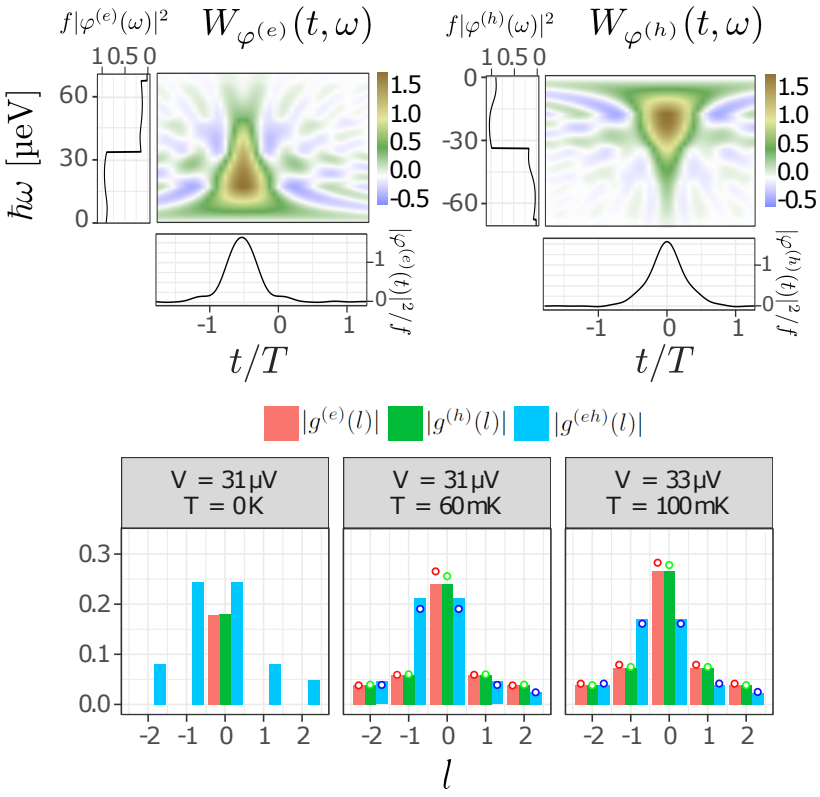

Figure 2.9: Results of the extraction protocol for a sinusoidal drive at $f = 9\,\mathrm{GHz}$, taken from [OP4]. *Top*: Wigner function associated with the dominant electronic (*left*) and holes (*right*) Wannier functions extracted from the coherence. Once we get these functions from our numerical protocol, we simply use $\mathcal{G}_{\varphi^{(e/h)}}(t|t') = \varphi^{(e/h)}(t)\varphi^{(e/h)}(t')^*$ and plot the associated Wigner function. *Bottom*: Moduli of the interperiod coherences $|g^{(e)}(l)|$, $|g^{(h)}(l)|$ and $|g^{(eh)}(l)|$. Colored bars correspond to numerical simulations from Floquet theory, and points to the ones extracted from the experimental data. A complete interpretation of these results is given in the main text, but let us strees that the good agreement between them allows us to believe that our experiment has passed our benchmarking test.

state of the system is a quantum superposition for each period between the emission of an electron/hole pair and the equilibrium [166]. We can thus recover some coherences between the electrons at one period and the holes at some other. Remarkably, though, no interperiod coherence can appear for the electrons or the holes alone in that case. This fact can be understood in another way by noting that a source described by Floquet theory cannot mix wavepackets from different periods (see for example the appendix of [37]).

Then, as we can see, the occupation probability $g^{(e)}(0) \simeq g^{(h)}(0)$ increases with temperature, from 0.17 at 0 mK to 0.26 (60 mK) and 0.28 (100 mK). This reflects the fact that at finite temperature, the available states have a finite probability to be occupied by thermal excitations. This additional thermal population has coherence over a typical timescale given by $h/k_{\mathrm{B}}T_{\mathrm{el}}$, thus leading to the apparition of interperiod coherences $g^{(e)}(l-l')$ and $g^{(h)}(l-l')$ over such a scale. On the contrary, the electron-hole coherences which where quite strong at zero temperature are suppressed when temperature increases. This is a direct reflection of the fact that there is a transition from a pure quantum state at zero temperature to a statistical mixture at higher ones.

Our quantum signal processor, as we dubbed it, therefore already proved its usefulness in terms of extracting physically relevant quantities from a given coherence, allowing an interpretation in terms of simple, single-excitation packets. Moreover, this first example also serves as a benchmark of the experiment itself, since we can compute the expected coherence through Floquet theory, and compare the extraction results on that numerical simulation. And the least we can say is that this benchmarking test has been passed by the experiment: the fidelity between the extracted wavefunctions obtained for the data and the ones obtained for a simulation was greater than 0.99 for all wavefunctions and temperatures, and we already discussed the good agreement for the extracted g coefficient between both cases.

To further prove that our process was indeed working in the general case, we also tested it on a case where more than one excitation is expected to be emitted in the system. We chose a drive with a 4 GHz frequency, 60 µV amplitude, at $T_{\mathrm{el}} = 55$ mK. In this case, we have $\alpha \simeq 3.6$, leading to an average number of electron/hole pairs per period just above 1, $q \simeq 1.1$. Once again, our analyzer passed the test with no problem, unambiguously showing that the quantum electrical current in this case was built from two electronic wavepackets ($\varphi_1^{(e)}$ and

$\varphi_2^{(e)}$) and two holes ($\varphi_1^{(h)}$ and $\varphi_2^{(h)}$), which are emitted with probabilities $g_1^{(e)}(0) = g_1^{(h)}(0) = 0.85$ and $g_2^{(e)}(0) = g_2^{(h)}(0) = 0.25$. The experimental tomography results, reconstructed Wigner function, and the extracted atoms of signal are displayed in figure 2.10. As could be expected from the fact that it appears for higher amplitude drives, the second wavepacket is at a higher energy than the first one. Both of them are emitted within the first half-period.

This second example also proves that our quantum signal processor is perfectly able to distinguish between a regime where a single electron/hole state is generated and one with several states, and we hope to be able to use it next to fully characterize the extent to which single-electron sources really emit a single excitation in the system.

To conclude this part, let me stress once again that this full experiment, from the tomography step to the atoms of signal extraction, allows a full characterization of any quantum electrical current. This is done with only minimal assumptions on the electronic state, as the only requirement of our protocol is the periodicity of the source. Therefore, we expect that it may one day be used on a frequent basis as a characterization tool for electronic quantum states, in the same way as tomography made its way to a daily usage in quantum optics.

2.4 Interferometry experiments for second order coherences

Up to now, we have only studied experiments giving access to first order coherence. Even when second order coherence appeared in our measurements, such as in the excess noise from equation (2.4c), it was through its diagonal part $\mathcal{G}^{(2e)}(t, t'|t, t')$. It then seems natural to ask if we can imagine interferometry experiments allowing the measurements of second order coherence completely or even just partially, and maybe even find a kind a tomography protocol allowing the reconstruction of any unknown second order coherence.

In this section, I will discuss experimental setups which are mostly inspired by the ones we have seen before: Franson interferometers, and Samuelsson-Büttiker interferometers. We will discuss to what extent they give access to the intrinsic second order coherence $\Delta\mathcal{G}^{(2e)}$ introduced in section 1.3.1. As we shall see, our discussion will go pretty much along the same lines as our discussion of single electron coherence which will, in the end, enable us to clarify our view of electron quantum

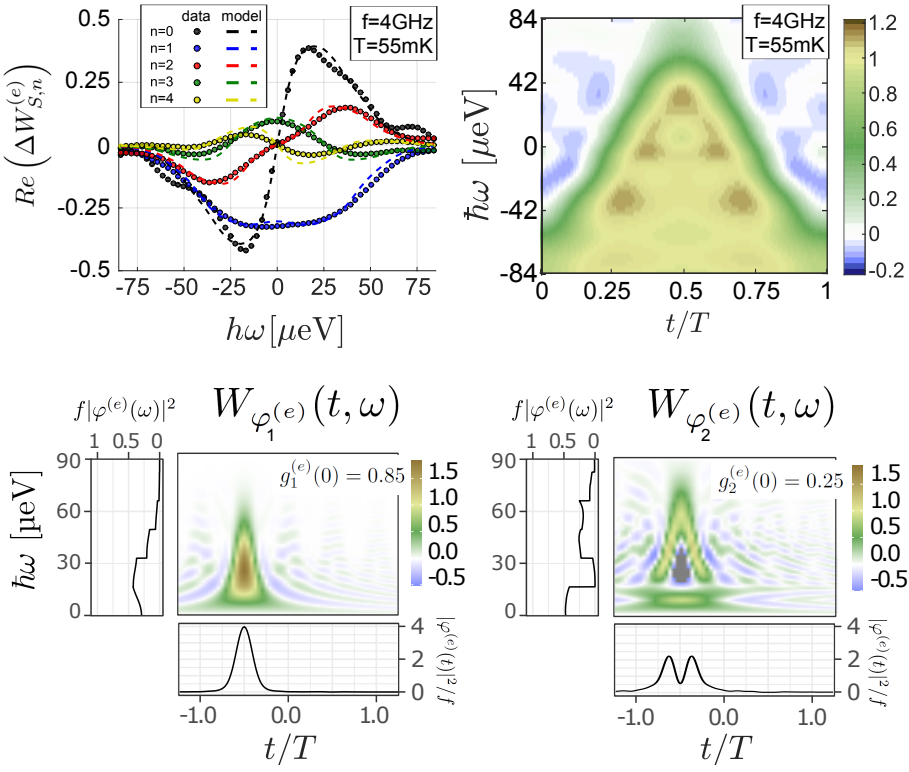

Figure 2.10: Figure taken from [OP4]. *Top*: Results of a tomography experiment performed with our usual protocol, for a sinusoidal drive with 4 GHz frequency, 60 µV amplitude, at $T_{\text{el}} = 55$ mK. Note that, in this case, we can obtain one more harmonic of the Wigner function. The reconstructed Wigner function is given on the right. *Bottom*: Extracted wavefunctions using our quantum signal processing step on the reconstructed Wigner function. In this case, the amplitude of the drive is such that more than one electron is emitted on average during each period. This leads to the extraction of two atoms of signal, the second one being at a higher energy and its emission less probable. The associated holes wavepackets (not shown here) are symmetric with respect to 0 in the energy domain, and emitted half a period later.

optics as quantum signal processing [OP5].

Of course, the problematic of second order coherence measurement is still far from the every day agenda of experimentalists, due to the technical challenges it rises. Yet, I firmly believe that designing and studying protocols even years before their implementation can be very useful. This is an important lesson we can draw from the development of single electron tomography: the protocol proposed by Ch. Grenier in 2011 [66] was at least seen as extremely challenging by all experimentalists in the field. Nevertheless, it lead to exremely fruitful discussions on the perspective opened by this technique as well as on the underlying experimental challenges. This has motivated the experimental groups to express their talent and improve their setups so that the goal has finally been achieved. On the theory side, this dialog has allowed to improve our ideas and develop new concepts such as the Wigner function representation of single electron coherence [41] before the experiment was performed. The whole process, which indeed took almost a decade, has been extremely fruitful and has produced a radically new way to look at quantum electrical currents [OP4]. I think that designing proposals for the measurement of second order intrinsic electronic coherence can also lead to exremely fruitful developments both on the experimental and theoretical side, in particular for gaining access to the notion of entanglement in the many-body electron fluid.

2.4.1 Franson interferometry

General idea

The first type of interferometers we want to present is a two electron interfermeter which is in some sense the generalization of the Mach-Zehnder interferometer. However, for practical reasons, it has to combine the ideas behind both Mach-Zehnder and Hanbury Brown and Twiss interferometers.

As shown by equation (2.8b), the main idea behind an MZI is to make a diagonal quantity, such as the average electrical current, dependent on the off-diagonal part of the unknown excess single coherence we want to access to. In a completely general manner, and using a signal processing inspired terminology, we can say that the experimental signal (an average time dependent electrical current) is obtained from the quantum signal of interest (the unknown excess first order coherence)

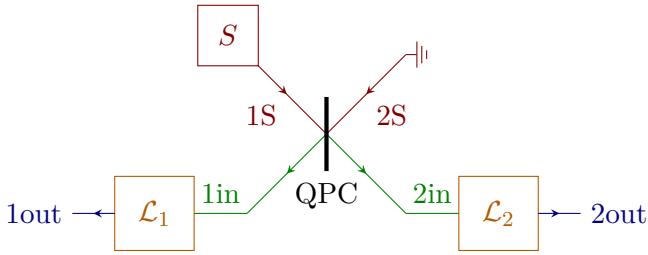

Figure 2.11: A first general idea of interferometer probing the intrinsic second order coherence of the source $\Delta\mathcal{G}_S^{(2e)}$. Correlations between the outcoming currents $i_{1\text{out}}$ and $i_{2\text{out}}$ are related to the incoming intrinsic second order coherence of the source through equation (2.34). By using appropriate linear filters $\mathcal{L}_{1/2}$, the incoming intrinsic second order coherence may be fully recovered.

by a linear filtering [OP5]:

$$\langle i \rangle = \mathcal{L}\left[\Delta\mathcal{G}^{(e)}\right] . \tag{2.32}$$

Concurringly, HBT interferometers are designed in such a way that the currents correlation between the two outputs of a beam splitter directly depends on the diagonal part of the incoming second order coherence on channel 1 when the other is fed with a reference Fermi sea:

$$\langle i_{1\text{out}}(t_1) i_{2\text{out}}(t_2)\rangle \propto \Delta\mathcal{G}_{1\text{in}}^{(2e)}(t_1,t_2|t_1,t_2) . \tag{2.33}$$

The main idea is then to combine the two setups by adding two (possibly different) linear filters for first order electronic coherence on the outcoming channels of a quantum point contact, as depicted in figure 2.11. The outcoming current correlation will then be a linear filtering of the intrinsic second order coherence of the source (S). This can be summarized by the following simple formula:

$$\langle i_{1\text{out}} i_{2\text{out}}\rangle = RT\,(\mathcal{L}_1 \otimes \mathcal{L}_2)\left[\Delta\mathcal{G}_{1\text{S}}^{(2e)}\right] . \tag{2.34}$$

As explained before, Mach-Zehnder interferometers are natural candidates for the linear filtering part. This leads to the setup schematically displayed in figure 2.12, which is completely analogous to the interferometer devised and demonstrated by Franson to study photon entanglement [49, 50]. This setup has been used extensively in the domain of

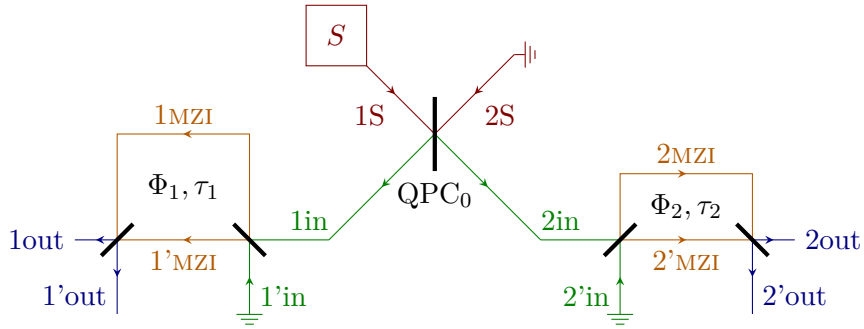

Figure 2.12: A schematic view of a Franson interferometer: the two linear filters from figure 2.11 are Mach-Zehnder interferometers with different Aharonov-Bohm fluxes Φ_i and time-of-flight delays between the long path and the short one, τ_i.

quantum optics to study time-bin entanglement [18, 109] about which we will talk in just a few pages. In the electronic transport domain, it has also been proposed to use such an interferometer to probe a two-particle non-local Aharonov-Bohm effect and use it to entangle electrons coming from two sources [152]. In our case, we use it as a two-particle interferometer that performs a linear filtering of the excess second order coherence into current correlations that are measured experimentally.

Quantitative analysis

Let us now analyze in detail the relation between the measured current correlation $\langle i_{1\text{out}}(t_1) i_{2\text{out}}(t_2)\rangle$ and $\Delta\mathcal{G}_S^{(2e)}$. A simple combinatoric argument shows that the outgoing current correlation involves a total of 16 terms, since each outgoing fermionic operator is a linear combination of two incoming ones. Let us break these terms down.

The first type of terms corresponds to classical contributions to the correlations. As before for the Mach-Zehnder interferometer, these are terms in which electrons propagate along a single branch of the interferometer, so that no interferences between the paths appear. These terms do not depend on the Aharonov-Bohm fluxes applied to the MZIs, and we will therefore denote this contribution to the full coherence with a subscript 0AB. In order to simplify notations, we will assume that both QPCs in each Mach-Zehnder are identical and that the times of flight from the source to any detector along the shortest branch of any of

the two interferometer are equal. This time of flight will not appear in subsequent equations, as it simply corresponds to taking different time origins for the detectors and the source. For the classical terms, this finally leads to[13]

$$\begin{aligned}
&\Delta\mathcal{G}^{(2e)}_{\mathrm{out},0\mathrm{AB}}(1t_1,2t_2|1t'_1,2t'_2) = \\
&\qquad R_0T_0T_1^2T_2^2\Delta\mathcal{G}^{(2e)}_S(t_1,t_2|t'_1,t'_2) && \text{(2.35a)}\\
&\quad + R_0T_0R_1^2T_2^2\Delta\mathcal{G}^{(2e)}_S(t_1-\tau_1,t_2|t'_1-\tau_1,t'_2) && \text{(2.35b)}\\
&\quad + R_0T_0T_1^2R_2^2\Delta\mathcal{G}^{(2e)}_S(t_1,t_2-\tau_2|t'_1,t'_2-\tau_2) && \text{(2.35c)}\\
&\quad + R_0T_0R_1^2T_2^2\Delta\mathcal{G}^{(2e)}_S(t_1-\tau_1,t_2-\tau_2|t'_1-\tau_1,t'_2-\tau_2)\,. && \text{(2.35d)}
\end{aligned}$$

As expected from classical terms, these terms only probe the diagonal part of $\Delta\mathcal{G}^{(2e)}_S$.

The second type of terms corresponds to terms involving single particle quantum interferences in only one of the two Mach-Zehnder interferometers. These terms therefore only depend on one Aharonov-Bohm flux and are denoted by the subscript 1AB. They transform an off-diagonal coherence for one of the variable pairs (t_1 and t'_1, or t_2 and t'_2) into the current correlation that can be accessed by the experiment.

$$\begin{aligned}
&\Delta\mathcal{G}^{(2e)}_{\mathrm{out},1\mathrm{AB}}(1t_1,2t_2|1t'_1,2t'_2) = \\
&- R_0T_0R_1T_1T_2^2\mathrm{e}^{\mathrm{i}\phi_1}\Delta\mathcal{G}^{(2e)}_S(t_1-\tau_1,t_2|t'_1,t'_2) && \text{(2.36a)}\\
&- R_0T_0R_1T_1T_2^2\mathrm{e}^{-\mathrm{i}\phi_1}\Delta\mathcal{G}^{(2e)}_S(t_1,t_2|t'_1-\tau_1,t'_2) && \text{(2.36b)}\\
&- R_0T_0T_1^2R_2T_2\mathrm{e}^{\mathrm{i}\phi_2}\Delta\mathcal{G}^{(2e)}_S(t_1,t_2-\tau_2|t'_1,t'_2) && \text{(2.36c)}\\
&- R_0T_0T_1^2R_2T_2\mathrm{e}^{-\mathrm{i}\phi_2}\Delta\mathcal{G}^{(2e)}_S(t_1,t_2|t'_1,t'_2-\tau_2) && \text{(2.36d)}\\
&- R_0T_0R_1T_1R_2^2\mathrm{e}^{\mathrm{i}\phi_1}\Delta\mathcal{G}^{(2e)}_S(t_1-\tau_1,t_2-\tau_2|t'_1,t'_2-\tau_2) && \text{(2.36e)}\\
&- R_0T_0R_1T_1R_2^2\mathrm{e}^{-\mathrm{i}\phi_1}\Delta\mathcal{G}^{(2e)}_S(t_1,t_2-\tau_2|t'_1-\tau_1,t'_2-\tau_2) && \text{(2.36f)}\\
&- R_0T_0R_1^2R_2T_2\mathrm{e}^{\mathrm{i}\phi_2}\Delta\mathcal{G}^{(2e)}_S(t_1-\tau_1,t_2-\tau_2|t'_1-\tau_1,t'_2) && \text{(2.36g)}\\
&- R_0T_0R_1^2R_2T_2\mathrm{e}^{-\mathrm{i}\phi_2}\Delta\mathcal{G}^{(2e)}_S(t_1-\tau_1,t_2|t'_1-\tau_1,t'_2-\tau_2)\,. && \text{(2.36h)}
\end{aligned}$$

Finally, the third and last type of terms is the one for which both detected electronic excitations get delocalized over the two branches while propagating within each Mach-Zehnder interferometer. These terms are

[13] Here, we use the notation $\mathcal{G}(it|jt')$ to define delocalized coherence over the channels. It must be understood, as previously, as $\langle\psi_i(t)\psi_j^\dagger(t')\rangle$.

dependent on both Aharonov-Bohm phases and offer a possibility to access to fully off-diagonal second order coherence. They are the terms we are mostly interested in and are denoted with the subscript 2AB. More precisely

$$\Delta\mathcal{G}^{(2e)}_{\mathrm{out,2AB}}(1t_1,2t_2|1t'_1,2t'_2) =$$
$$R_0T_0R_1T_1R_2T_2\mathrm{e}^{\mathrm{i}(\phi_1+\phi_2)}\Delta\mathcal{G}^{(2e)}_S(t_1-\tau_1,t_2-\tau_2|t'_1,t'_2) \quad (2.37a)$$
$$+\,R_0T_0R_1T_1R_2T_2\mathrm{e}^{-\mathrm{i}(\phi_1+\phi_2)}\Delta\mathcal{G}^{(2e)}_S(t_1,t_2|t'_1-\tau_1,t'_2-\tau_2) \quad (2.37b)$$
$$+\,R_0T_0R_1T_1R_2T_2\mathrm{e}^{\mathrm{i}(-\phi_1+\phi_2)}\Delta\mathcal{G}^{(2e)}_S(t_1,t_2-\tau_2|t'_1-\tau_1,t'_2) \quad (2.37c)$$
$$-\,R_0T_0R_1T_1R_2T_2\mathrm{e}^{\mathrm{i}(\phi_1-\phi_2)}\Delta\mathcal{G}^{(2e)}_S(t_1-\tau_1,t_2|t'_1,t'_2-\tau_2)\,. \quad (2.37d)$$

Generalizing the proposal by Haack et al. [73] for a standard Mach-Zehnder interferometer, we have proposed [OP6] to measure the outgoing current correlations between the two outputs of the interferometers for several values of the magnetic fluxes going through each MZI. Extracting the part depending only on $\phi_1+\phi_2$ allows us to get $\Delta\mathcal{G}^{(2e)}_S(t_1-\tau_1,t_2-\tau_2|t_1,t_2)$. By varying the time-delays τ_1 and τ_2, one could in principle recover the whole intrinsic second order coherence emitted by the source.

Of course, this time domain measurement protocol through Franson interferometry suffers from the same problems as its MZI based first order counterpart: current and noise measurements in the time domain are quite hard to realize and the spatial extension of the interferometer makes it really sensitive to Coulomb interaction induced decoherence. Howevever, even in its idealized form, this example is interesting since it enables us to capture aspects of two-electron interferences and second order coherence. Let us take a little more time to study an example on which ideal Franson interferometry can yield interesting results.

Using Franson interferometry on time-bin entangled pairs

As mentioned before, Franson interferometry has been used in quantum optics to test a specific type of two-photon entanglement called time-bin entanglement which was motivated by quantum communication protocols. Time-bin entanglement consists in creating a superposition between a given two-particle state and a time-shifted copy of it. In standard quantum mechanical notations, this corresponds to a state of the form

$$|\Psi_2\rangle = \alpha\,|\phi_1(t)\rangle\otimes|\phi_2(t)\rangle + \beta\,|\phi_1(t-\tau)\rangle\otimes|\phi_2(t-\tau)\rangle\ . \quad (2.38)$$

In this state, three time scales appear: the typical time-scale over which wavefunction ϕ_1 is non-zero, its equivalent for ϕ_2, and the time shift τ between pairs. Of course, the most interesting case to study is when the time shift between pairs is greater than the typical time-scale of each wavefunction. Indeed, each pair taken alone will already display some second order coherence on the off-diagonal. For example, $\Delta\mathcal{G}^{(2e)}(t_1, t_2|t_1 + \tau_1, t_2 + \tau_2)$ will be non-zero if each τ_i is smaller than the typical time-scale of wavefunction φ_i. However, the time-bin superposition leads to coherence much further away from the diagonal, since we can have $\Delta\mathcal{G}^{(2e)}(t_1, t_2|t_1 + \tau, t_2 + \tau)$ non-zero, where τ is the time shift. This is why we will mostly be interested in superpositions with a large time shift τ in the following.

How can we create such superpositions? In quantum optics, a source of such time-bin entangled pairs can be realized using two steps. First, a photon is injected into an unbalanced Mach-Zehnder interferometer with a time delay difference τ between its two branches. This creates the time delocalized single photon state $|\Psi\rangle = \alpha\,|\phi(t)\rangle + \beta\,|\phi(t-\tau)\rangle$. It is then sent into a non-linear crystal, in which parametric downconversion converts it into twin photons of lower energy. This leads to the creation of the time-bin entangled two-photon state from equation (2.38), which may then be used for quantum communication [18]. Experimentally, several groups have reported the creation of such time-bin entangled states, and shown that they could be distributed over large distances [110] or stored for later use [71].

In the domain of electron quantum optics, such a source has not been demonstrated yet, but some theoretical proposals have already been made. One of them [25] proposes to use a quantum dot operated with a period smaller than the typical escape time of the source, so that the electron and hole emitted during the standard operation procedure of the source (see figure 1.5) will not always be emitted in the same period. This leads to some kind of entanglement between the state where they are emitted in the same period, and the one where they are not, which could lead to interesting effects even if it is not exactly the one we discussed before. Another proposal [80] has been made in the context of quantum Hall spin effect (QSHE), in which the edge channels have an additionnal property of helicality, *i.e.* different spin channels propagates in different directions. Since this feature is also present in topological insulators, proposals for time-bin entangled pairs generation have also been made in this context [85].

In the present case, we will not try to model such an experimentally feasible source but rather assume that we have it at our disposal. Our starting point will thus be a pair of Landau excitations with typical time width τ_0, separated by a time δt. In second quantization notation, we have the state

$$|\Psi_2\rangle = \psi^\dagger[\varphi_1]\,\psi^\dagger[\varphi_2]\,|F\rangle \tag{2.39}$$

where $\varphi_1(t) = \varphi_{\text{Landau}}(t)$ and $\varphi_2(t) = \varphi_1(t-\delta t)$. Using equation (1.75), we remember that the excess coherence is given in a simple way in terms of the two-electron pair wavefunction Φ_{12} corresponding to the Slater determinant of φ_1 and φ_2:

$$\Delta\mathcal{G}^{(2e)}_{|\Psi_2\rangle}(t_1,t_2|t_1',t_2') = \Phi_{12}(t_1,t_2)\Phi^*_{12}(t_1',t_2')\,. \tag{2.40}$$

Denoting by subscripts 3 and 4 the vavefunctions equivalent to 1 and 2, but emitted after some time τ, a time-bin entangled two-excitations state is then

$$|\Psi_{\text{time bin}}\rangle = \frac{1}{\sqrt{2}}\Big(\psi^\dagger[\varphi_1]\,\psi^\dagger[\varphi_2] + \psi^\dagger[\varphi_3]\,\psi^\dagger[\varphi_4]\Big)\,|F\rangle\ . \tag{2.41}$$

On the other hand, a 50-50 statistical mixture state would be either $\psi^\dagger[\varphi_1]\,\psi^\dagger[\varphi_2]\,|F\rangle$ or $\psi^\dagger[\varphi_3]\,\psi^\dagger[\varphi_4]\,|F\rangle$.

We would like to show that Franson interferometry enables us to distinguish between these two physically different cases of a time-bin entangled equal superposition of two Landau pairs, and a 50-50 statistical mixture of pairs emitted at different times. The intrinsic second order coherences for each case are given by:

$$\Delta\mathcal{G}^{(2e)}_{\text{mixture}}(t_1,t_2|t_1',t_2') = \tag{2.42a}$$
$$\frac{1}{2}\Big(\Phi_{12}(t_1,t_2)\Phi^*_{12}(t_1',t_2') + \Phi_{34}(t_1,t_2)\Phi^*_{34}(t_1',t_2')\Big)$$
$$\Delta\mathcal{G}^{(2e)}_{\text{time-bin}}(t_1,t_2|t_1',t_2') = \tag{2.42b}$$
$$\frac{1}{2}\Big(\Phi_{12}(t_1,t_2) + \Phi_{34}(t_1,t_2)\Big)\Big(\Phi^*_{12}(t_1',t_2') + \Phi^*_{34}(t_1',t_2')\Big)\,.$$

The difference between these two cases is flagrant! Whereas the mixture case only shows coherences within each pair, the time-bin entangled state contains terms involving the 12 and 34 Landau pairs. The main question is therefore whether or not this difference can be detected in a Franson interferometry experiment.

Using the setup described, low frequency current correlations between the two outputs of the Mach-Zehnder interferometers are proportional to the integral over both t_1 and t_2 of $\Delta\mathcal{G}_S^{(2e)}(t_1-\tau_1, t_2-\tau_2|t_1,t_2)$. Figure 2.13 displays both the real and imaginary part of this integral, respectively for the mixture and for the entangled case, with parameters $\delta t = 3\tau_0$ and $\tau = 7\tau_0$.

Three types of contributions to coherence appear on these figures:

- First of all, we get a central peak when $\tau_1 \simeq \tau_2 \simeq 0$. This peak corresponds to interferences between any excitation and itself: any of the emitted wavepackets, delocalized over the 4 possible paths in the interferometer, will lead to second order coherence on a time-scale related to the typical time-width of the wavepacket.

- The second type of contribution corresponds to points where the delay on both interferometers is such that an electron within a pair can interfere with the other electron emitted in the same pair. This corresponds to $\tau_1 = -\tau_2 = \pm\delta t$, and leads to a contribution with the opposite sign and half the amplitude of the one at the center of the figure.

Those two first contributions are classical contributions to coherence coming from single particle interferences between the electrons present inside each two-particle state $\psi^\dagger[\varphi_1]\psi^\dagger[\varphi_2]\,|F\rangle$ and $\psi^\dagger[\varphi_3]\psi^\dagger[\varphi_4]\,|F\rangle$. Interestingly, having removed all information on the time reference of the emitted states with the integration over t_1 and t_2, any pair emitted with a separation δt contributes in the same way to the experimental time-averaged current correlation signal. In particular, this means that they are exactly identical for both a unique pair emitted around some time t_0 and for the statistical mixture of several pairs of interest for us!

- Finally, a third contribution to coherence appears for the entangled pair. It takes the form of a copy of the classical part discussed before for a single pair, shifted around the position $\tau_1 = \tau_2 = \pm\tau$. Of course, this is the signature of the entangled nature of our state, and corresponds to quantum interferences involving the two pairs of electrons present in the superposition: the first pair can take the long path of the MZI, and arrive at the end beamsplitter at the same time as the second pair taking the short path, leading to non-zero correlations.

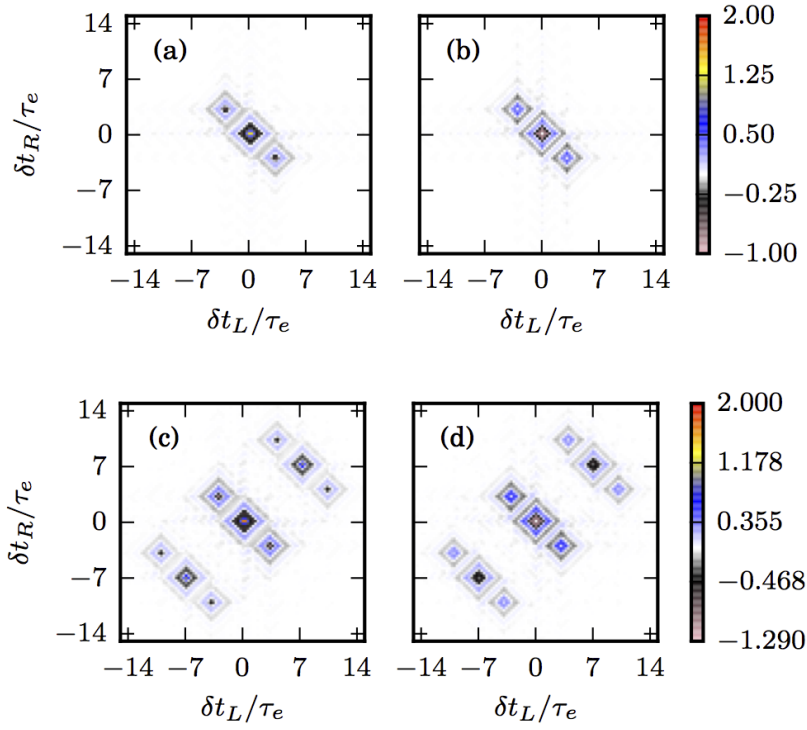

Figure 2.13: Figure taken from [OP6]. Numerical simulation of the real (*left*) and imaginary (*right*) parts of $\int \mathrm{d}t_1\mathrm{d}t_2\Delta\mathcal{G}_S^{(2e)}(t_1-\tau_1,t_2-\tau_2|t_1,t_2)$, as could be extracted using a Franson interferometer, for two types of sources. *Top*: Pair of Landau excitations with typical time scale τ_0 and an energy $\omega_0 = 3/\tau_0$, separated by a time $\delta_t = 3\tau_0$. Note that statistical mixture between several such pairs would give the exact same result. *Bottom*: Time-bin entangled state built from a superposition of two pairs with a time shift $\tau = 7\tau_0$. We see new contributions appearing, signature of the fact that coherence can appear between the pairs in this superposition. (See main text for a more detailed approach).

To summarize the conclusions from this simple example, we can read the presence of off-diagonal $\Delta\mathcal{G}^{(2e)}$ in the experimental Franson interferometry correlation signal. All contributions associated with semi-classical two-particle paths are located close to the anti-diagonal zone $\tau_1 = -\tau_2$ of the Franson interferometer parameter space whereas, by contrast, the signature of off diagonal two electron coherence emitted by the source will manifest itself close to the diagonal zone $\tau_1 = \tau_2$. These two zones are sufficiently separated from each other and this is why the Franson interferometry experiment can distinguish between the time-bin entangled state versus the statistical mixture of two time-shifted two-excitation states.

Generalization of the Franson interferometer

As we have said at the beginning of this section, using Mach-Zehnder interferometers at the outputs of the first beamsplitter is not the only way to transform off-diagonal parts of the coherence into measurable quantities, and other linear filters could be used. For example, we could imagine a situation in which one would simply measure correlations between two different finite-frequency currents at the output of the beamsplitter. This would require doing an homodyning of the measured signal at each output with a reference wave, and using different references with pulsations ω_{r1} and ω_{r2} for the two outputs. Then, by measuring the power density of their cross-correlation, one could recover a quantity proportional to $\int \mathrm{d}\omega_1 \mathrm{d}\omega_2 \Delta\widetilde{\mathcal{G}}^{(2e)}(\omega_1 - \omega_{r1}, \omega_2 - \omega_{r2}|\omega_1, \omega_2)$. Such an experiment could thus certainly distinguish between a state formed as the superposition of pairs of excitations with different energies and the mixture of such pairs. However, this would be a challenging experiment. Therefore, in the same way that noise measurements took over for first order coherence experiments with the advent of Hong-Ou-Mandel experiments, we can ask ourselves if the same type of setup can be imagined for second order coherence. This is what we are going to do now.

2.4.2 The double Hong-Ou-Mandel interferometer

As we have seen, Franson interferometry is a two-particle interference experiment, giving access to information on the intrinsic second order coherence of the source S through currents correlation measurements. It assumes we have two linear filters located right after a first electronic beam splitter. However, since it relies on Mach-Zehnder interferometers,

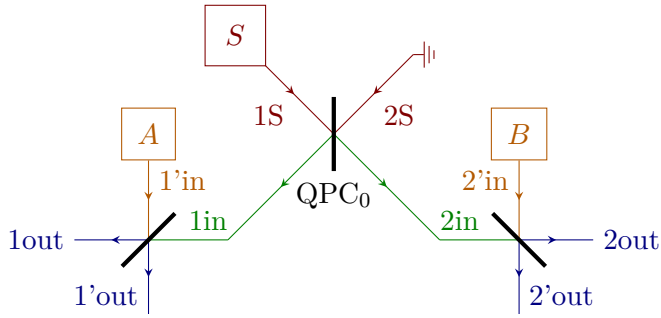

Figure 2.14: A schematic representation of a 2-HOM setup, where we want to probe the second order electronic coherence from source S using two probe sources A and B, with Hong-Ou-Mander interferometry.

the original Franson interferometer device will be plagued by strong decoherence effects exactly as the MZI was for measuring single electron coherence. This decoherence issue is controlled only for specific cases of the generalized Franson interferometers, for example when looking at finite frequency current correlations, as was discussed just before. However such a device is only able to recover partial information on the intrinsic second order coherence $\Delta\mathcal{G}_S^{(2e)}$. This allows the determination of some properties of the source, but will prevent us from performing a full tomography of $\Delta\mathcal{G}_S^{(2e)}$.

Therefore, it is natural to ask ourselves whether we could create some kind of interferometry experiment inspired from Hong-Ou-Mandel interferometry, that would encode the overlap between two second order coherences into some measurable quantity. Such a device would be the second order equivalent of the quantum signal analyzer we have already demonstrated for reconstrucing $\Delta\mathcal{G}_S^{(e)}$.

The simplest idea to achieve this goal consists in using Hong-Ou-Mandel interferometers instead of fixed linear filters such as the Mach-Zehnder interferometer. This amounts to using highly parametrizable linear filters in figure 2.11, and leads to the setup depicted on figure 2.14, in which two sources A and B will be used to probe second order coherence coming from the source S. Even if this setup still has some spatial extension and may be sensitive to decoherence between the first QPC and any of the two other ones, we hope that it may be possible to build it on much smaller sizes than Mach-Zehnder interferometers, so that the influence of decoherence may at least be smaller.

Now, what is the quantity of choice to measure in order to obtain what we are searching for? In the case of HOM interferometry we measured the excess current correlations between the two outputs of the interferometer to obtain information on the overlap between two single electron coherences. In the present case, one has to look at 4-current correlators between all possible outgoing channels of the interferometer. Let us consider the connected current correlator

$$\begin{aligned} C_4(t_1,t_1',t_2,t_2') = &\langle i_1(t_1) i_{1'}(t_1') i_2(t_2) i_{2'}(t_2')\rangle_{\text{out}} \\ &- \langle i_1(t_1) i_{1'}(t_1')\rangle_{\text{out}} \langle i_2(t_2) i_{2'}(t_2')\rangle_{\text{out}} \\ &- \langle i_1(t_1) i_2(t_2)\rangle_{\text{out}} \langle i_{1'}(t_1') i_{2'}(t_2')\rangle_{\text{out}} \\ &- \langle i_1(t_1) i_{2'}(t_2')\rangle_{\text{out}} \langle i_{1'}(t_1') i_2(t_2)\rangle_{\text{out}} \end{aligned} \tag{2.43}$$

which corresponds to the fourth cumulant of currents in the case where all average outgoing currents are zero.

In a realistic experiment, what we may be able to measure is the integrated version of this quantity over all times. Indeed, measurements of this integrated quantity, or rather of its equivalent frequency formulation, have already been done experimentally by Forgues et al. [46] to show that the photo-assisted shot noise of tunnel junction was non-Gaussian, and could be accessible in our usual setup of choice.

Let us now explain how this quantity relates to electronic coherences. Using the standard relations between outgoing and incoming electronic operators for each beamsplitter, $C_4(t_1,t_1',t_2,t_2')$ can be recasted into a sum of four parts: one only depending on properties of the source S, one depending on S and A, one depending on S and B, and finally one that depends on all the three sources S, A and B. This last contribution is the one of interest for us. To extract it, we once again combine on/off measurements in a clever way. The linear combination

$$\begin{aligned} C_4^{\text{on/off}} = &\, C_4(A \text{ on}, B \text{ on}) + C_4(A \text{ off}, B \text{ off}) \\ &- C_4(A \text{ on}, B \text{ off}) - C_4(A \text{ off}, B \text{ on}) \end{aligned} \tag{2.44}$$

removes all contributions that do not depend on the properties of all three sources. Straightforward but tedious computations, using only the canonical anticommutation relations between the various ψ and $\psi^\dagger$ operators allow to rewrite all correlators as products of electron and hole

coherences, leading to the following result:

$$\int C_4^{\text{on/off}}(t_1,t_1',t_2,t_2')\mathrm{d}t_1\mathrm{d}t_1'\mathrm{d}t_2\mathrm{d}t_2' = 4e^4R_0T_0R_AT_AR_BT_B\times$$
$$\int \Delta\mathcal{W}_A^{(e)}(t,\omega)\Delta\mathcal{W}_B^{(e)}(t',\omega')\Delta\mathcal{W}_S^{(2e)}(t,\omega;t',\omega')\frac{\mathrm{d}t\mathrm{d}\omega}{2\pi}\frac{\mathrm{d}t'\mathrm{d}\omega'}{2\pi} \quad (2.45a)$$
$$-\int \Delta\mathcal{W}_A^{(e)}(t,\omega)\Delta\mathcal{W}_S^{(e)}(t,\omega)\frac{\mathrm{d}t\mathrm{d}\omega}{2\pi}\Delta\mathcal{W}_B^{(e)}(t',\omega')\Delta\mathcal{W}_S^{(e)}(t',\omega')\frac{\mathrm{d}t'\mathrm{d}\omega'}{2\pi}\,. \quad (2.45b)$$

The first term (2.45a) contains the overlap between the first order Wigner function of sources A and B and the intrinsic second order Wigner function of source S. This contribution is of central interest for us as it is the only one involving the intrinsic second order coherence $\Delta\mathcal{G}_S^{(2e)}$. The second term (2.45b) corresponds to the product of two HOM overlaps probing first order coherence. Consequently it can be accessed by measuring each of the corresponding HOM current noise independently. This can be achieved using the same procedure as before for HOM interferometry, once using current correlation measurements on outputs 1 and $1'$, and once doing the same with outputs 2 and $2'$. Once we have done all measurements of both C_4 and the different HOM parts, we gain an access to the quantity

$$\mathcal{Q}_4 = 4e^4\int \Delta\mathcal{W}_A^{(e)}(t,\omega)\Delta\mathcal{W}_B^{(e)}(t',\omega')\Delta\mathcal{W}_S^{(2e)}(t,\omega;t',\omega')\frac{\mathrm{d}t\mathrm{d}\omega}{2\pi}\frac{\mathrm{d}t'\mathrm{d}\omega'}{2\pi} \quad (2.46)$$

in a direct manner. This quantity is then the equivalent, for this interferometer, of the Hong-Ou-Mandel noise Q_{HOM} for first order coherence.

Tomography of second order coherence

Can we use this last result to do some tomography of unknown sources? A first, simple idea is to use the same probes as before: sinusoidal drives with low amplitudes. Let us denote by $\mathcal{Q}_4^{(n_A,n_B)}(\mu_A,\phi_A,\mu_B,\phi_B)$ the measured $\mathcal{Q}_4$ when using two sinusoidal drives in the quantum regime as probes, one for source A and one for source B. In full generality, we

get in the zero temperature case

$$\mathcal{Q}_4^{(n_A,n_B)}(\mu_A,\phi_A,\mu_B,\phi_B) = \tag{2.47}$$
$$\lim_{T\to\infty}\frac{1}{T}\int_{-T/2}^{T/2}\mathrm{d}t\lim_{T'\to\infty}\frac{1}{T'}\int_{-T'/2}^{T'/2}\mathrm{d}t'\int_{\mu_A-n_A\pi f}^{\mu_A+n_A\pi f}\frac{\mathrm{d}\omega}{2\pi}\int_{\mu_B-n_B\pi f}^{\mu_B+n_B\pi f}\frac{\mathrm{d}\omega'}{2\pi}$$
$$4e^4\Delta\mathcal{W}_S^{(2e)}(t,\omega;t',\omega')\frac{eV_{P_{n_A}}}{hn_Af}\cos(2\pi ft+\phi_A)\frac{eV_{P_{n_B}}}{hn_Bf}\cos(2\pi ft+\phi_B)\,.$$

In the case of a periodic source, the excess second order coherence function can be decomposed as

$$\Delta\mathcal{W}_S^{(2e)}(t,\omega;t',\omega') = \sum_n \Delta\mathcal{W}_{S,n}^{(2e)}(t-t',\omega,\omega')\mathrm{e}^{2\mathrm{i}\pi nf\frac{t+t'}{2}} \tag{2.48}$$

leading to

$$\mathcal{Q}_4^{(n_A,n_B)}(\mu_A,\phi_A,\mu_B,\phi_B) = \tag{2.49}$$
$$\frac{e^6V_{P_{n_A}}V_{P_{n_B}}}{h^2f^2n_An_B}\int_{\mu_A-n_A\pi f}^{\mu_A+n_A\pi f}\frac{\mathrm{d}\omega}{2\pi}\int_{\mu_B-n_B\pi f}^{\mu_B+n_B\pi f}\frac{\mathrm{d}\omega'}{2\pi}\int\mathrm{d}\tau$$
$$\Bigg[2\mathrm{Re}\left(\Delta\mathcal{W}_{S,n_A+n_B}^{(2e)}(\tau,\omega,\omega')\mathrm{e}^{-\mathrm{i}(\phi_A+\phi_B)}\mathrm{e}^{-\mathrm{i}\pi f\tau(n_A-n_B)}\right)$$
$$+\,2\mathrm{Re}\left(\Delta\mathcal{W}_{S,n_A-n_B}^{(2e)}(\tau,\omega,\omega')\mathrm{e}^{-\mathrm{i}(\phi_A-\phi_B)}\mathrm{e}^{-\mathrm{i}\pi f\tau(n_A+n_B)}\right)\Bigg]\,.$$

There are several analogies between this equation and equation (2.21) for first order coherence. Once again, chosing good phases ϕ_A and ϕ_B allows a direct access to one specific harmonic of the second order Wigner function. Then, using the chemical potential will allow the full reconstruction of its energy dependence, in exactly the same way as we did before, by starting from a point where $\Delta\mathcal{W}_{S,n}^{(2e)}$ vanishes. The only problem with this setup is that we do not gain a full access to the time dependence of each harmonic, but only to specific point of its Fourier transform. This could have been expected, since we tried to probe a signal which was not periodic in one of its time variables using only periodic signals. Nevertheless, this signal reconstruction is still an interesting result, and the protocol can still be used to realize a partial tomography of the excess second order coherence for periodic sources.

In a completely generic case, I have not been able during my PhD to find a family of wavefunctions allowing the reconstruction of the excess

second order coherence from its overlap with two first order ones. I think that it should be possible to do so with another family of signals, which may even already exist in the signal processing community, however I did not have the time to study this problem any further. My personal feeling is that we would need to use the standard periodic sinusoidal drive with low energy extension for one of the sources, in order to capture the harmonics of the Wigner function and their behaviour in at least one energy variable. For the other source, we would maybe need to use a source that would be mostly the opposite, i.e. a very localized excitation with high energy extension. Indeed, another type of time-frequency representation called Gabor transform exists in signal processing [54], and is defined as

$$G_x(t,f) = \int \mathrm{e}^{-\pi(\tau-t)^2}\mathrm{e}^{-2\mathrm{i}\pi f\tau}x(\tau)\mathrm{d}\tau \tag{2.50}$$

for the signal $x(t)$. In this equation, we recognize some sort of time-resolved kernel in the Gaussian function. In our case, maybe an equivalent expression using Lorentzian wavepackets such as the Levitons could also give us some good insight on the properties of our source.

2.4.3 Samuelsson-Büttiker interferometry

In the same family of interferometers based on the HOM interferometer, our first idea when trying to develop a second order tomography protocol was to try to find an interferometer that could compute the overlap between two second order coherences, and would therefore be the direct equivalent of HOM interferometry for second order.

This can be done by adapting a setup that was first proposed by Samuelsson, Sukhorukov, and Büttiker [144] as a way to create two-particle interference effects in mesoscopic capacitors. The same authors then understood that properties of the source could be measured with this setup, and that it could be used to perform a quantum state tomography of a DC source [142]. We therefore call this setup a Samuelsson-Büttiker interferometer, and have represented it in figure 2.15. Its idea is indeed quite simple: using quantum point contacts, we split the incoming current from two sources of interest in two, and then recombine currents from both sources together with a second layer of QPCs. The main idea is then to measure current correlations between the different outputs of this second layer.

Based on what we saw before for Mach-Zehnder interferometers, we know that enclosing some magnetic flux will lead to an Aharonov-Bohm

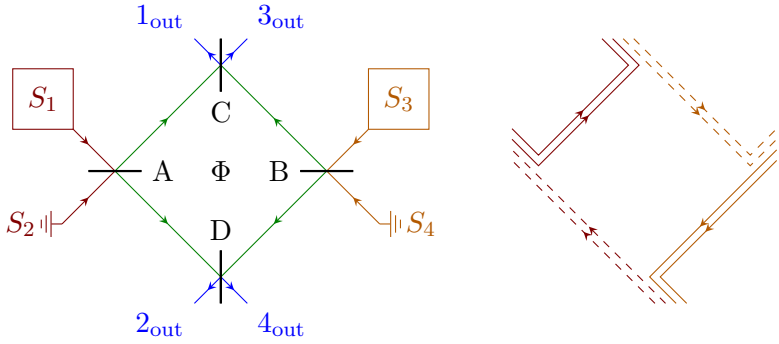

Figure 2.15: *Left*: A schematic representation of a Samuelsson-Büttiker interferometer. Two sources are used as inputs of two beamsplitters, whose outputs are then combined using two other beamsplitters. We will recover correlation between the two outputs 1 and 4. *Right*: A visualization of the type of terms we hope to recover with correlators of the form $\langle i_1^2 i_4^2 \rangle$. Solid lines represent ψ operators while dashed lines represent $\psi^\dagger$ ones. We think that these terms where each detected electron cannot be attributed to one of the source should be associated with the overlap of second order excess coherences of both sources.

phase ϕ_{AB}. In the spirit of what we did for equation (2.7a), we attribute some phase ϕ_i to each of the paths inside the interferometer, with $\sum_i \phi_i = \phi_{\mathrm{AB}}$. Using notations from figure 2.15, the full relation between outgoing operators and incoming ones is given by:

$$\begin{pmatrix} \psi_1 \\ \psi_2 \\ \psi_3 \\ \psi_4 \end{pmatrix}_{\mathrm{out}} = M \begin{pmatrix} \psi_1 \\ \psi_2 \\ \psi_3 \\ \psi_4 \end{pmatrix}_{\mathrm{in}} \tag{2.51}$$

with

$$M = \begin{pmatrix} \mathrm{e}^{\mathrm{i}\phi_1}\sqrt{R_A R_C} & \mathrm{i}\mathrm{e}^{\mathrm{i}\phi_1}\sqrt{T_A R_C} & \mathrm{i}\mathrm{e}^{-\mathrm{i}\phi_3}\sqrt{R_B T_C} & -\mathrm{e}^{-\mathrm{i}\phi_3}\sqrt{T_B T_C} \\ \mathrm{i}\mathrm{e}^{-\mathrm{i}\phi_2}\sqrt{T_A R_D} & \mathrm{e}^{-\mathrm{i}\phi_2}\sqrt{R_A R_D} & -\mathrm{e}^{\mathrm{i}\phi_4}\sqrt{T_B T_D} & \mathrm{i}\mathrm{e}^{\mathrm{i}\phi_4}\sqrt{R_B T_D} \\ \mathrm{i}\mathrm{e}^{\mathrm{i}\phi_1}\sqrt{R_A T_C} & -\mathrm{e}^{\mathrm{i}\phi_1}\sqrt{T_A T_C} & \mathrm{e}^{-\mathrm{i}\phi_3}\sqrt{R_B R_C} & \mathrm{i}\mathrm{e}^{-\mathrm{i}\phi_3}\sqrt{T_B R_C} \\ -\mathrm{e}^{-\mathrm{i}\phi_2}\sqrt{T_A T_D} & \mathrm{i}\mathrm{e}^{-\mathrm{i}\phi_2}\sqrt{R_A T_D} & \mathrm{i}\mathrm{e}^{\mathrm{i}\phi_4}\sqrt{T_B R_D} & \mathrm{e}^{\mathrm{i}\phi_4}\sqrt{R_B R_D} \end{pmatrix}$$

In order to keep everything quite compact, we will suppose that all QPCs are controlled in such a way that all R_α and T_α are equal to $1/2$. This

leads to

$$M = \frac{1}{2}\begin{pmatrix} e^{i\phi_1} & ie^{i\phi_1} & ie^{-i\phi_3} & -e^{-i\phi_3} \\ ie^{-i\phi_2} & e^{-i\phi_2} & -e^{i\phi_4} & ie^{i\phi_4} \\ ie^{i\phi_1} & -e^{i\phi_1} & e^{-i\phi_3} & ie^{-i\phi_3} \\ -e^{-i\phi_2} & ie^{-i\phi_2} & ie^{i\phi_4} & e^{i\phi_4} \end{pmatrix}. \tag{2.52}$$

As was the case for standard HOM interferometry, outgoing currents from the same beam splitter (either 1out and 3out or 2out and 4out) contain pretty much the same information on the incoming coherences. For symmetry reasons, we will therefore only look at correlations between channels 1out and 4out. In terms of sources, since we do not want to overcomplicate things, we will put sources S_1 and S_4 on the input channels 1in and 4in, and connect 2in and 3in to the ground, as drawn on the scheme of the experiment in figure 2.15. We will also, as before, suppose that all paths have the same total length, so as not to take propagation inside the interferometer into account.

Now, what might be the quantity to look at in order to recover the overlap between both sources second order coherences? Since we want at least 4 creation and 4 destruction operators overall, we need to look at 4-currents correlators, such as for example $\langle i_1^2 i_4^2 \rangle$. Yet, it is obvious that this contains far too many terms ($4^8 = 65536$ ones to be precise). Of course, several properties may be used to simplify this. Since all sources are completely independent, we need to chose paths having the same numbers of creation and destruction operators for each source, which puts the number of terms down to $4! \times 4^4 = 1536$. This is still far too much, as it contains mostly terms where the sources do not interact with each other or terms that correspond to standard classical correlations, as well as terms that can be expressed using lower-order coherences that do not interest us. In order to get what we want, we would like terms such as the one depicted on the right of figure 2.15: current detected at the outputs comes from both sources, and no electron can be safely attributed as coming from one of the source or the other. What this schematic representation shows is that this term corresponds to enclosing twice the magnetic flux that pierces the center region. Therefore, our first idea to recover it is to select, within all the terms appearing in the 4-currents correlator, the ones that have a $2\phi_{AB}$ dependence of their phase. This can be done through a careful Fourier transform of the signal acquired for several fluxes, in the same way as what was done for Franson interferometry before. This allows us to reduce the problem to only 36 terms!

So, what exactly is contained in those terms? The full result is expressed as the product of two quantities, one relative to the sources 1 and 2, the other to sources 3 and 4:

$$\langle i_1(t_1)i_1(t_2)i_4(t_3)i_4(t_4)\rangle_{2\phi_{\mathrm{AB}}} = \frac{\mathrm{e}^{2\mathrm{i}\phi_{\mathrm{AB}}}}{2^4}\times$$

$$\Big(\mathcal{G}^{(2h)}_{S_1}(t_3,t_4|t_1,t_2) + \mathcal{G}^{(2h)}_{\mathrm{F}_2}(t_3,t_4|t_1,t_2) \tag{2.53a}$$

$$- \sum_{\sigma,\sigma'\in\mathfrak{S}_2} \mathcal{G}^{(h)}_{S_1}(t_{\sigma'(3)}|t_{\sigma(1)})\mathcal{G}^{(h)}_{\mathrm{F}_2}(t_{\sigma'(4)}|t_{\sigma(2)})\Big)\times \tag{2.53b}$$

$$\Big(\mathcal{G}^{(2e)}_{S_4}(t_3,t_4|t_1,t_2) + \mathcal{G}^{(2e)}_{\mathrm{F}_3}(t_3,t_4|t_1,t_2) \tag{2.53c}$$

$$- \sum_{\sigma,\sigma'\in\mathfrak{S}_2} \mathcal{G}^{(e)}_{S_4}(t_{\sigma'(3)}|t_{\sigma(1)})\mathcal{G}^{(e)}_{\mathrm{F}_3}(t_{\sigma'(4)}|t_{\sigma(2)})\,.\Big) \tag{2.53d}$$

This corresponds to the overlap between hole coherences for sources 1 and 2, and electron ones for sources 3 and 4. However, there are still some parasitic terms (b and d) that do not depend on second order coherence. Is there some clever way to decompose the result from equation (2.53)? Taking the cumulant rather than the simple correlator may simplify the product of all first order coherences together, but since this lower order correlators cannot create a non-diagonal second order coherence, all terms where second order coherences are multiplied by first order ones will still exist.

Thus far, we are therefore still blocked with this partial result. I firmly believe that there are clever ways to measure such quantities that would allow us to measure the overlap between two excess second order coherences, but have not yet found how to achieve it. Moreover, as was the case for the interferometer using two HOM experiments, I do not know which family of sources might be used as probes in this specific case, leaving me a bit in the dark at the time of writing this manuscript about how exactly to tackle the problem of second order coherence tomography. I am convinced that conversations with signal processing specialists could lighten the path for us, but as far as this manuscript goes, I am forced to leave this question in the middle of a foggy road.

Chapter 3

Interactions

> Every empire, every nation,
> every tribe, thought it would
> end in a bit more decent way
>
> Mgła
> *Exercices in Futility IV*

As mentioned before, the main obstacle to controlled manipulation and propagation of electronic excitations compared to what can be done in photon quantum optics is Coulomb interactions. Because of them, electrons experience strong decoherence effects, the consequences of which are observed both in Mach-Zehnder and Hong-Ou-Mandel interferometry (see sections 2.2.1 and 2.2.2 of previous chapter).

In this chapter, we present an approach to effective screened Coulomb interactions within finite regions of space based on edge magnetoplasmon scattering. We show that it enables us to compute electronic coherences after propagation in the sample from the one that are emitted by our sources in a non-perturbative way. This will be the focus of section 3.1. In section 3.2, we will then turn ourselves to practical applications of these computations, making predictions of experimental results for Hong-Ou-Mandel interferometry experiments. This experimental test is indeed the first experimental study of the celebrated quasi-particle decay thought experiment imagined by Landau to introduce its theory of the Landau-Fermi liquid. In the present case, we shall see that the experimental results are in agreement with our theoretical predictions and that we are really observing signatures of the total decay of a Landau quasi-particle excitation in the presence of strong interchannel Coulomb

interactions.

We will then turn to the problem of decoherence control which we will explore along two tracks. In section 3.3, we will present theoretical predictions on electronic decoherence for specific sample designs that are indeed envisioned for blocking electronic decoherence. Then, in section 3.4, we will discuss electronic decoherence in an ideal $\nu = 1$ quantum Hall edge channel, an interesting problem in itself that will lead us to suggest that exfoliated graphene and GaAs are very different materials from the point of view of electronic decoherence because of their difference in bare Fermi velocities.

Finally, the last section of this chapter will be devoted to the effects of Coulomb interactions on higher order decoherence. Besides a general analytical solution to this problem, we will mostly discuss the second order electronic coherence generated by an incoming single electron coherence and discuss how it encodes signatures of the generation of coherent plasmonic excitations. Then we will explore the relaxation of a pure two-electron excitation in the specific regime in which Coulomb interactions do not smash it down to the Fermi level. As we shall see, the general formalism is considerably simplified and a relatively simple but neverthless subtle image of the underlying physics emerges.

3.1 Computing interactions effects

This section will review how bosonization enables us to compute the effect of effective screened Coulomb interactions on electronic coherences. Most of those ideas have been unraveled several years ago, during the PhD of C. Grenier [67] under the direction of P. Degiovanni. Yet, at the time, they had only been able to apply the method to the case of fixed-energy single-electron excitations, and not to obtain results in other physically relevant situations such as arbitrary single electron wavepackets. As we will see, it was quite a big step to solve the full problem and the computation of the full coherence function was quite a challenging problem in many ways. This is indeed the problem on which I started my work in the field of electron quantum optics. Together with B. Roussel and D. Ferraro, we managed to devise a method allowing to solve this problem of interactions and decoherence for an arbitrary single-electron wavepacket [OP2]. This was an important step in the field since, as should already be clear to the reader, this is essential to produce predictions for HOM experiments performed with single

electron sources.

Most of what I present in this section comes directly from this work. It will allow us to familiarize ourselves with the effect of screened Coulomb interactions on single electron excitations. In the remaining of this chapter, we will then use and extend this framework, in order to use it to its full extent and discuss various problems related to Coulomb interaction effects on various electronic excitations.

3.1.1 Interactions as a beamsplitter

Let us consider a chiral relativistic edge channel, coupled to an external environment within a finite length region. This environment can be another edge channel in the case where there are several of them, or the bulk of the sample, or nearby conductors and even transmission lines. The only assumption we make here is that all conductors involved should be in the linear response regime. This prevents us from studying the influence of a non-linear conductor such as a double quantum dot capacitively coupled to the edge channel under consideration but, as we shall see, these assumptions already describe a large number of physically relevant situations.

Under this hypothesis, Coulomb interactions between electrons couple charge densities that, as discussed in section 1.4, are linear in terms of free bosonic fields[1]. In particular, the excess charge density $n(x,t)$ within the edge channel at position x and time t, which corresponds to $:\psi^\dagger\psi:(x,t)$, can be linked to a bosonic field $\phi(x,t)$ via

$$\phi(x,t) = \frac{1}{\sqrt{\pi}} \int_x^\infty n(y,t)\mathrm{d}y\,. \tag{3.1}$$

The equation of motion obeyed by the field ϕ is then

$$\left(\partial_t + v_\mathrm{F}\partial_x\right)\phi(x,t) = \frac{e\sqrt{\pi}}{h} V(x,t) \tag{3.2}$$

where $V(x,t)$ denotes the electric potential along the edge channel of interest. In the linear regime, $V(x,t)$ is linear in all the free bosonic variables describing the conductors to which our channel is coupled. Since the charge density and the electrical current are linearly related, this construction is in fact equivalent, in a free propagation regime, to

[1] This is where the linear response hypothesis comes in.

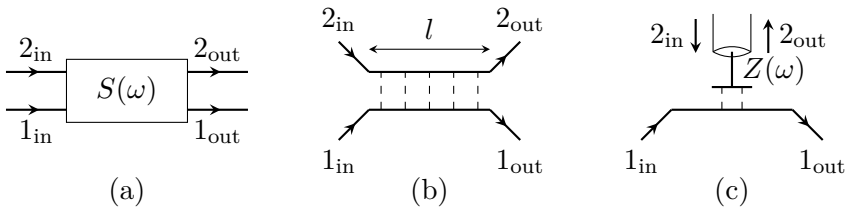

Figure 3.1: (a) A schematic representation of plasmon scattering. The incoming and outgoing modes of several systems are linked to one-another by a frequency dependent scattering matrix $S(\omega)$. This can be used to describe several different physical situations such as, for example, (b) two copropagating edge channels coupled over a distance l, or (c) an edge channel coupled to some linear external circuit described by some frequency-dependent impedance $Z(\omega)$.

the one of chapter 1, provided that

$$\phi(x,t) = -\frac{\mathrm{i}}{\sqrt{4\pi}} \int_0^\infty \left(b(\omega) \mathrm{e}^{\mathrm{i}\omega(x/v-t)} - b^\dagger(\omega) \mathrm{e}^{-\mathrm{i}\omega(x/v-t)} \right) \frac{\mathrm{d}\omega}{\sqrt{\omega}} \tag{3.3}$$

where v is the chiral velocity along the edge of interest, and is generally speaking edge-dependent.

A finite-length interaction region can then be described using the input/output formalism that connects, for each of the interacting elements, the incoming field $\phi^{(\mathrm{in})}$ to the outgoing one $\phi^{(\mathrm{out})}$. Both of these fields propagate freely respectively before and after the interaction region. We thus have incoming and outgoing bosonic modes $b^{(\mathrm{in})}$ and $b^{(\mathrm{out})}$ which are related by input/output relations. In our case, under the assumption of linearity, and since we have time-translation invariant dynamics, the whole interaction region is described by an energy dependent elastic scattering matrix $S(\omega)$ between the incoming and outgoing modes

$$b_\alpha^{(\mathrm{out})}(\omega) = \sum_\beta S_{\alpha\beta}(\omega) b_\beta^{(\mathrm{in})}(\omega) \tag{3.4}$$

where α and β denote the different conductors we are describing. This situation is schematically depicted in figure 3.1 for the case of two conductors, along with two examples of such situations.

A special case is obtained when there are no interactions between different edge channels. Then, we have

$$S_{\alpha\beta}(\omega) = \delta_{\alpha\beta} \mathrm{e}^{\mathrm{i}\omega l/v_\alpha} \tag{3.5}$$

with v_α the velocity in the corresponding edge channel. In the presence of inter-channel interactions, the scattering matrix couples them. Because the dynamics is time translation invariant, and the interaction region is not subjected to any external driving, energy conservation is satisfied and, in the present case, this implies that $S(\omega)$ is unitary for any $\omega > 0$. To summarize, the finite size interaction region is an edge magnetoplasmon frequency-dependent beamsplitter, exactly similar to a directional coupler in the microwave domain.

The two main questions that must be answered once we have this bosonic scattering approach to interactions are

- What are the specific forms of the scattering matrix $S(\omega)$ for (semi-)realistic effective screeened Coulomb interaction models or in the presence of a capacitive coupling to the channel's electromagnetic environment?

- Can we use this to compute fermionic correlators after an interaction region? As we shall see, a positive and clever answer to this question contains the key to understanding the effect of Coulomb interactions on electronic coherences.

In the rest of this chapter, we will thus discuss some specific models of interactions and derive their scattering matrix, before using it to compute outgoing electronic coherences in the case where specific wavepackets are sent into the edge channel. But before this, let us connect the edge magnetoplasmon scattering matrix to some physical quantities: finite-frequency admittances.

Relation between $S(\omega)$ and admittance

The edge magnetoplasmon scattering matrix S determines the outgoing current in any channel from the incoming one. If the incoming channel is fed from an AC generator, this suggests that the scattering matrix encodes AC transport properties of the interaction region seen as a quantum conductor. To make this intuition more quantitative, let us remember that a voltage drive applied to the reservoir feeding the channel β corresponds to the injection of a coherent plasmonic state into the edge channel. Its functional parameter only depends on the Fourier transform of the voltage in said channel (see equation (1.121)).

Because the interaction region is a simple beam-splitter for the edge magnetoplasmon modes, a tensor product of incoming coherent states is

scattered into a tensor product of outgoing coherent states. This is well known for electromagnetic waves in optics: linear optical components cannot generate non-classical quantum states of light, and therefore in particular entanglement. The parameter of the outgoing state in channel α is, at fixed ω, simply given by the sum over β of the product of $S_{\alpha\beta}(\omega)$ with the parameter of the coherent state in channel β at the same frequency. We can associate some voltage to this parameter in channel α and determine the average current associated with this state by reversing what we did in equation (1.121). If we send in a time-resolved excitation at $t = 0$, associated with the percussional voltage $V(t) = -\frac{h}{e}\delta(t)$, we find that the expected outgoing voltage in channel α is directly given by the inverse Fourier transform of $-\frac{h}{e}S_{\alpha\beta}(\omega)$. In other words, the finite frequency admittance of the interaction region is nothing but

$$G_{\alpha\beta}(\omega) = \frac{\partial\langle i_\alpha(\omega)\rangle}{\partial V_\beta(\omega)} = \frac{e^2}{h}\left(1 - S_{\alpha\beta}(\omega)\right) . \tag{3.6}$$

Such a relation had indeed been found before in the context of quantum wires, which are non-chiral 1D conductors, as explained for example in [140]. Here we have obtained the analogous relation in the case of chiral 1D edge channels where it takes a particularily simple form.

This link between the finite-frequency admittance and edge magneto-plasmon scattering is of particular interest for us. On the one hand, it will allow us to derive a scattering matrix from considerations based on the expected admittance of some circuits, or even from real measurements. On the other hand, it will also allow us to discuss possible representations of the interaction region in terms of a simple discrete electrical elements representation.

General properties of $S(\omega)$

The direct interpretation of the single-edge transmission coefficient $\mathrm{T}(\omega) = S_{11}(\omega)$ as a finite-frequency admittance has strong implications which we will discuss now.

First of all, since the analytic continuation to negative frequencies of finite-frequency admittance $G_{11}(\omega)$ obeys the reality condition $G_{11}(-\omega) = G_{11}^*(\omega)$, we have the same analytic extension for $\mathrm{T}(\omega)$

$$\mathrm{T}(-\omega) = \mathrm{T}^*(\omega) . \tag{3.7}$$

Next, the dimensionless finite-frequency admittance $g(\omega) = 1 - \mathrm{T}(\omega)$ is the one of a passive circuit. As such, it obeys the general property first proposed by Cauer [24] and then proven by Brune [21] of being positive real. With our convention, this means that for $z = \sigma + \mathrm{i}\omega$, $z \mapsto g(z)$ is analytic in the half plane $\mathrm{Re}\,((z)) < 0$ and

$$\mathrm{Re}\,((g(z))) > 0 \quad \text{when } \sigma < 0\,, \tag{3.8a}$$
$$\mathrm{Im}\,((g(z))) = 0 \quad \text{when } z \in \mathbb{R}^-\,. \tag{3.8b}$$

The analyticity condition ensures that the current response is causal, while the two other conditions express that, when driven by a time-dependent voltage, the corresponding effective dipole dissipates energy and does not produce it.

3.1.2 Theoretical elements

To explain how to compute the coherence after the interaction region from the one before in a way that is both quite general and not too tedious, I will focus here on the particular example of a $\nu = 2$ system without dissipation. As will be clear, this discussion is however still valid for different situations such as $\nu = 1$ (which will be extensively discussed in section 3.4) or an edge channel coupled to a general linear environment. The model for $\nu = 2$ is of particular interest when trying to explain what happens in real experiments, as we will see in section 3.2.

I shall also focus here on the situation in which a single electron wavepacket is present above the Fermi sea and only compute the first order electronic coherence for the moment. Of course, they are not the full story of interactions, but most of what we will present later can be directly understood as a generalization of what we present here. In particular, a more general case with p electrons and the n-th order coherence will be discussed in section 3.5.

Incoming and outgoing states

The situation of interest for us is simply a two-channel interaction region of length l, which is described by the unitary two-by-two scattering matrix

$$S(\omega) = \begin{pmatrix} \mathrm{T}(\omega) & \mathrm{R}_E(\omega) \\ \mathrm{R}(\omega) & \mathrm{T}_E(\omega) \end{pmatrix}\,. \tag{3.9}$$

The incoming state is simply an electron in a wavepacket φ_e injected in edge channel 1, while edge channel 2, playing the role of the environment, is assumed to be at zero temperature. Since the interaction region is simply a beamsplitter for plasmonic modes, we know that coherent states are also simply scattered into other coherent states: an incoming coherent plasmonic state of the form $|[\Lambda_1]\rangle \otimes |[\Lambda_2]\rangle$ is transformed into the state $|[\Lambda_1']\rangle \otimes |[\Lambda_2']\rangle$, with

$$\Lambda_\alpha'(\omega) = \sum_\beta S_{\alpha\beta}(\omega)\Lambda_\beta(\omega)\,. \tag{3.10}$$

From a physical point of view, this means that all states created by classical voltage pulses can, after an interaction region, still be understood as being created by classical voltage pulses. We only need to use equation (1.121) in one direction to express the incoming state as a bosonic coherent state, and then in the other direction to describe the outgoing coherent state in terms of a classical voltage pulse.

This relation is of a particular interest for us in the case of sinusoidal driving. Indeed, if the incoming state in channel α is a sinusoidal drive with pulsation ω_0, the corresponding coherent state has a parameter of the form $-e\delta(\omega-\omega_0)/h\sqrt{\omega_0}$. When its environment β is at equilibrium (or, equivalently, in a vacuum of bosons), the outgoing state will simply be the coherent state of parameter $-eS_{\alpha\alpha}(\omega_0)\delta(\omega-\omega_0)/h\sqrt{\omega_0}$. Obviously, this state still describes a sinusoidal drive of pulsation ω_0, but the amplitude and the phase of that drive may have changed. In a way, equation (3.10) simply describes that our model corresponds to a linear response regime with respect to sinusoidal drives. This is why we could say in section 2.3.2 that sinusoidal drives were mostly unaffected by interactions.

Now, if we want a result that is valid in a completely general case, all we need to do is to express any incoming state using the bosonization framework of section 1.4 in the form of coherent states. Our state of interest is thus

$$|\varphi_e\rangle_1 \otimes |F\rangle_2 = \int \varphi_e(t)\frac{\mathcal{U}_1^\dagger}{\sqrt{2\pi a}}\,|[-\Lambda_t]\rangle_1 \otimes |[0]\rangle_2\,\mathrm{d}t \tag{3.11a}$$

$$= \int \varphi_e(t)\frac{\mathcal{U}_1^\dagger}{\sqrt{2\pi a}}\bigotimes_{\omega>0}\left(|-\Lambda_t(\omega)\rangle_1 \otimes |0_\omega\rangle_2\right)\mathrm{d}t \tag{3.11b}$$

where $|0_\omega\rangle$ denotes the vacuum of bosons in mode ω. The outgoing state

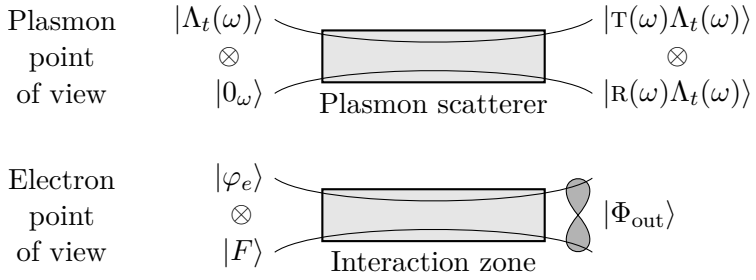

Figure 3.2: A representation of an interaction zone and its effect on plasmons and electrons. *Top*: Interactions seen as a plasmonic scatterer. For mode ω, the incoming state is a coherent state with parameter $\Lambda_t(\omega)$ in one channel, and the vacuum in the other. The outgoing state is still factorized between two coherent states, one corresponding to the transmitted part and the other to the reflected part. *Bottom*: For the full electronic picture, things are different. Since it is a superposition of plasmons, the outgoing state is a superposition of factorized states, or equivalently an entangled state.

is then simply

$$\begin{aligned}|\Phi_{\mathrm{out}}\rangle &= \int \varphi_e(t)\frac{\mathcal{U}_1^\dagger}{\sqrt{2\pi a}}\bigotimes_{\omega>0}\left(|-\mathrm{T}(\omega)\Lambda_t(\omega)\rangle_1 \otimes |-\mathrm{R}(\omega)\Lambda_t(\omega)\rangle_2\right)\mathrm{d}t \\ &= \int \varphi_e(t)\frac{\mathcal{U}_1^\dagger}{\sqrt{2\pi a}}\,|[-\mathrm{T}\Lambda_t]\rangle_1 \otimes |[-\mathrm{R}\Lambda_t]\rangle_2\,\mathrm{d}t\,. \end{aligned} \tag{3.12}$$

As could be expected, interactions have turned a factorized state between the system and the environment into an entangled state, as depicted in figure 3.2.

Computing electronic coherences in either of the two edge channels requires computing the outgoing reduced density matrices in the two channels. Let us start with the reduced density matrix in the injection edge channel, ρ_1.

$$\begin{aligned}\rho_1 &= \mathrm{Tr}\left[|\Phi_{\mathrm{out}}\rangle\langle\Phi_{\mathrm{out}}|\right]_2 \\ &= \int \varphi_e(t_+)\varphi_e^*(t_-)\langle[-\mathrm{R}\Lambda_{t_-}]|[-\mathrm{R}\Lambda_{t_+}]\rangle\psi^\dagger(t_+)\,|[g_{t_+}]\rangle\langle[g_{t_-}]|\,\psi(t_-)\mathrm{d}t_+\mathrm{d}t_-\end{aligned} \tag{3.13}$$

where we have defined the coherent plasmonic state $|[g_t]\rangle$ as

$$|[g_t]\rangle = |[(1-\mathrm{T})\Lambda_t]\rangle = \bigotimes_{\omega>0}|(1-\mathrm{T}(\omega))\Lambda_t(\omega)\rangle \tag{3.14}$$

so that we could re-introduce the ψ and $\psi^\dagger$ operators to reabsorb the Klein operators. This coherent state corresponds to the cloud of electron/hole pairs generated by Coulomb interaction when a localized excitation of the form $\psi^\dagger(t)\,|F\rangle$ is sent into the system. Of course, its complete form depends on the scattering matrix under study. Yet, the reduced density matrix is not directly given by the pure state corresponding to superpositions of such $|[g_t]\rangle$. The imprint these states leave in the environment leads to decoherence between the different parts of the superposition. The corresponding many-body decoherence coefficient is given by

$$\begin{aligned} D_{\text{ext}}(t_+ - t_-) &= \langle [-\mathrm{R}\Lambda_{t_-}] | [-\mathrm{R}\Lambda_{t_+}] \rangle \\ &= \exp\left(\int_0^{+\infty} |\mathrm{R}(\omega)|^2 \left(\mathrm{e}^{\mathrm{i}\omega(t_+ - t_-)} - 1 \right) \frac{\mathrm{d}\omega}{\omega} \right) \end{aligned} \tag{3.15}$$

where the second line can be obtained using equation (1.115).

In the same way, the reduced density matrix for the other edge channel is given by

$$\begin{aligned} \rho_2 &= \mathrm{Tr}\left[|\Phi_{\text{out}}\rangle \langle \Phi_{\text{out}}| \right]_1 \\ &= \int \varphi_e(t_+) \varphi_e^*(t_-) D_{\text{inj}}(t_+ - t_-)\, |[-\mathrm{R}\Lambda_{t_+}]\rangle \langle [-\mathrm{R}\Lambda_{t_-}]|\, \mathrm{d}t_+ \mathrm{d}t_- \end{aligned} \tag{3.16}$$

where

$$\begin{aligned} D_{\text{inj}}(t_+ - t_-) &= \langle [-\mathrm{T}\Lambda_{t_-}] | [-\mathrm{T}\Lambda_{t_+}] \rangle \\ &= \exp\left(\int_0^{+\infty} |\mathrm{T}(\omega)|^2 \left(\mathrm{e}^{\mathrm{i}\omega(t_+ - t_-)} - 1 \right) \frac{\mathrm{d}\omega}{\omega} \right) \end{aligned} \tag{3.17}$$

is the decoherence associated with the imprints left in the injection channel for different environmental states. From these two reduced density matrices, all electronic coherence functions after the interaction region can be computed, as we will show now.

Generalized Wick theorem

To continue our calculations, we will be interested in computing coherence functions of the states defined above. This next step involves correlators of the form

$$\langle [\alpha] | \psi^\dagger(t_1) \psi^\dagger(t_2) \psi(t_3) \psi(t_4) | [\beta] \rangle \tag{3.18}$$

which are reminiscent of correlators we could compute using Wick's theorem (see section 1.2.2). Although these are matrix elements between two edge magnetoplasmon coherent states – and not expectation values in the Fermi sea – these correlators still have a surprisingly simple form arising from the properties of displacement operators displayed by equations (1.114) to (1.116). Since all electronic creation operators can be written as plasmonic displacement operators, we have to compute a product of displacement operators, sandwiched between two coherent states. Yet, we know that a product of displacement operators can always be expressed as a single one, whose parameter is the sum of all initial parameters, times some number depending on the parameters. In the same way, this final operator can always be expressed as a normal ordered one up to a multiplicative factor. This means that we can rewrite the product of fermonic operators as

$$\begin{aligned}&\psi^\dagger(t_1)\psi^\dagger(t_2)\psi(t_3)\psi(t_4) \\ &\quad = \mathcal{A}(t_1,t_2,t_3,t_4)\times :\mathcal{D}\left[-\Lambda_{t_1}-\Lambda_{t_2}+\Lambda_{t_3}+\Lambda_{t_4}\right]:\end{aligned} \tag{3.19}$$

with $\mathcal{A}$ some number to determine. The definition of normal order makes finding out this number quite easy: because $\langle F| :\mathcal{D}: |F\rangle = 1$, it has to be given by

$$\mathcal{A}(t_1,t_2,t_3,t_4) = \langle\psi^\dagger(t_1)\psi^\dagger(t_2)\psi(t_3)\psi(t_4)\rangle_{\mathrm{F}}\,. \tag{3.20}$$

Therefore, these equations mean that all the matrix elements we have to compute can be decomposed into the Fermi correlator multiplied by some exponential that depends on the specific times and states we are looking at, given by equation (1.116). Since the Fermi sea is a state for which Wick's theorem is valid, we can then decompose any correlator into two-points ones on the Fermi sea, which may be easier to compute. Putting everything together, we can get a generalized version of Wick's theorem that reads, for the case under consideration here

$$\begin{aligned}&\frac{\langle[\alpha]|\psi^\dagger(t_1)\psi^\dagger(t_2)\psi(t_3)\psi(t_4)|[\beta]\rangle}{\langle[\alpha]|[\beta]\rangle} \\ &\quad = \frac{\langle[\alpha]|\psi^\dagger(t_1)\psi(t_4)|[\beta]\rangle}{\langle[\alpha]|[\beta]\rangle}\frac{\langle[\alpha]|\psi^\dagger(t_2)\psi(t_3)|[\beta]\rangle}{\langle[\alpha]|[\beta]\rangle} \\ &\qquad - \frac{\langle[\alpha]|\psi^\dagger(t_1)\psi(t_3)|[\beta]\rangle}{\langle[\alpha]|[\beta]\rangle}\frac{\langle[\alpha]|\psi^\dagger(t_2)\psi(t_4)|[\beta]\rangle}{\langle[\alpha]|[\beta]\rangle}\,.\end{aligned} \tag{3.21}$$

Similar results can be obtained for higher order correlators. Most of the time we will directly compute coherences using equation (3.19) as it

will lead to simpler calculations, but this generalized version of Wick's theorem may still be useful.

Outgoing coherence in the injection channel

Let us complete the full calculation of the outgoing coherence in the injection channel, *i.e.* the one associated to the reduced density matrix ρ_1:

$$\mathcal{G}^{(e)}_{\rho_1}(t|t') = \int \varphi_e(t_+)\varphi_e^*(t_-)D_{\text{ext}}(t-t') \\ \langle [g_{t_-}]|\, \psi(t_-)\psi^\dagger(t')\psi(t)\psi^\dagger(t_+)\, |[g_{t_+}]\rangle \, \mathrm{d}t_+\mathrm{d}t_- \,. \tag{3.22}$$

From the above discussion, the main component we need to compute is

$$\langle [g_{t_-}]| :\mathcal{D}\left[\Lambda_{t_-} - \Lambda_{t'} + \Lambda_t - \Lambda_{t_+}\right]: |[g_{t_+}]\rangle \tag{3.23}$$

using equation (1.116). Without going into more detail, we find that this last quantity times $D_{\text{ext}}(t-t')$ is equal to some full decoherence coefficient $D(t,t',t_+,t_-)$ given by

$$D(t,t',t_+,t_-) = \gamma_+(t_+-t')\gamma_-(t_+-t)\gamma_+^*(t_--t)\gamma_-^*(t_--t') \tag{3.24}$$

where we introduce

$$\gamma_\pm(t) = \exp\left(\pm\int_0^{+\infty}\frac{\mathrm{d}\omega}{\omega}(1-\mathrm{T}(\omega))(\mathrm{e}^{\mathrm{i}\omega t}-1)\right) . \tag{3.25}$$

Finally, the outgoing coherence in this channel can be rewritten under a rather compact form

$$\mathcal{G}^{(e)}_{\rho_1}(t|t') = \int \varphi_e(t_+)\varphi_e^*(t_-)D(t,t',t_+,t_-) \\ \langle \psi(t_-)\psi^\dagger(t')\psi(t)\psi^\dagger(t_+)\rangle_{\mathrm{F}} \, \mathrm{d}t_+\mathrm{d}t_- \,. \tag{3.26}$$

Using Wick's theorem on the Fermi correlator, we can decompose the outgoing coherence as a sum of two terms. The first one corresponds to a modification of the Fermi sea which can be seen, under the right conditions, as the contribution of electron/hole pairs generated by Coulomb interaction in the vacuum state. We call it the *modified vacuum* part, and we denote it with an MV subscript. The second contribution corresponds, also under proper conditions, to the coherence of the incoming

excitation after interaction-induced relaxation. It is called the *wavepacket* contribution and will be denoted with a WP subscript. These two contributions can be written as

$$\mathcal{G}^{(e)}_{\mathrm{MV},1}(t|t') = \int \varphi_e(t_+)\varphi_e^*(t_-)D(t,t',t_+,t_-) \langle\psi^\dagger(t')\psi(t)\rangle_{\mathrm{F}}\langle\psi(t_-)\psi^\dagger(t_+)\rangle_{\mathrm{F}}\,\mathrm{d}t_+\mathrm{d}t_- \,, \tag{3.27a}$$

$$\mathcal{G}^{(e)}_{\mathrm{WP},1}(t|t') = \int \varphi_e(t_+)\varphi_e^*(t_-)D(t,t',t_+,t_-) \langle\psi(t)\psi^\dagger(t_+)\rangle_{\mathrm{F}}\langle\psi(t_-)\psi^\dagger(t')\rangle_{\mathrm{F}}\,\mathrm{d}t_+\mathrm{d}t_- \,. \tag{3.27b}$$

Outgoing coherence in the other channel

The same line of reasoning for the other reduced density matrix, ρ_2, corresponding to the environment in our simple system can be followed. At the end of the day, a strikingly simple result is obtained: the outgoing coherence $\mathcal{G}^{(e)}_{\rho_2}(t|t')$ is given by a modified vacuum term of the same form as $\mathcal{G}^{(e)}_{\mathrm{WP},1}(t|t')$, but using function $\mathrm{R}(\omega)$ rather than $1-\mathrm{T}(\omega)$ in the decoherence coefficient. The fact that there is no wavepacket term emphasizes that no electron has been injected in that channel, so that only electron/hole pairs can be created. Therefore, we obtain:

$$\mathcal{G}^{(e)}_{\rho_2}(t|t') = \int \varphi_e(t_+)\varphi_e^*(t_-)D^{(-\mathrm{R})}(t,t',t_+,t_-) \langle\psi(t)\psi^\dagger(t_+)\rangle_{\mathrm{F}}\langle\psi(t_-)\psi^\dagger(t')\rangle_{\mathrm{F}}\,\mathrm{d}t_+\mathrm{d}t_- \tag{3.28}$$

where $D^{(-\mathrm{R})}$ is defined in the same way as D, but using $-\mathrm{R}(\omega)$ instead of $1-\mathrm{T}(\omega)$. This notation, and the corresponding one for $\gamma_\pm$ functions, will be reused later in this manuscript. Of course, if no subscript is given, it must be understood as $\gamma_\pm^{(1-\mathrm{T})}$ as defined in equation (3.25).

3.1.3 Numerical implementation

After this rather theoretical approach to computing coherence, we need to find a way to calculate the result for some specific form of interaction or wavepacket. To do so, B. Roussel has implemented a clever numerical implementation to evaluate the result. This section will therefore be devoted to a rapid explanation of this numerical approach, as well as of the analytic tools which I have developed used to simplify this problem.

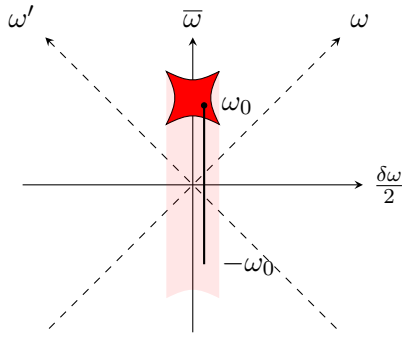

Figure 3.3: A visual representation of the propagation of coherence in the $\omega, \delta\omega$ space. Any point of the incoming coherence leads to coherence in the same $\delta\omega$ line, down to $-\omega$. Therefore, interactions lead to hole coherences as well as electron/hole ones.

Going to the frequency space

Using time translation invariance, we know that the decoherence coefficient $D(t, t', t_+, t_-)$ from equation (3.24) and all Fermi correlators appearing in equation (3.27) are independent in the variable corresponding to the sum of all times. Translating this property to the frequency domain shows that the outgoing electronic coherence is of the form

$$\widetilde{\mathcal{G}}^{(e)}_{\rho_1}\left(\omega + \frac{\delta\omega}{2} \,\middle|\, \omega - \frac{\delta\omega}{2}\right) = \int_{-\infty}^{+\infty} \varphi_e\left(\omega' + \frac{\delta\omega}{2}\right) \varphi_e^*\left(\omega' - \frac{\delta\omega}{2}\right) K(\omega, \omega'; \delta\omega) \mathrm{d}\omega' \tag{3.29}$$

where the propagator K depends on the product of two points correlators on the Fermi sea in the energy domain and of the Fourier transforms of the $\gamma_\pm$ functions defined by equation (3.25), which we will denote by $\Gamma_\pm$.

Let me stress the physical interpretation of equation (3.29): it shows that ω and $\delta\omega$ are decoupled variables, in the sense that the incoming coherence at $(\omega' + \delta\omega/2, \omega' - \delta\omega/2)$ only leads to coherence at points with the same value of $\delta\omega$. This is depicted in figure 3.3. As shown in this figure, this same points can only create coherences down to $-\omega'$ but not lower by energy conservation. The numerical challenge is to compute this propagator in the most efficient way.

Identifying potential difficulties

Expressions (3.27a) and (3.27b) show that the computation of each of the terms contributing to single electron coherence involves two point correlators of free fermion operators in the Fermi sea as well as decoherence coefficients, which are all built from building blocks defined by equation (3.25).

As is well known, the two-point correlator of free fermion operators at equilibrium spreads over the thermal coherence time $\tau_{\rm th}(T_{\rm el}) = \hbar/k_B T_{\rm el}$ which diverges at zero temperature. It also has an ultraviolet (UV) divergence. Moreover, for the simplest interaction model at $\nu = 2$ [105], the building blocks $\gamma_\pm(\tau)$ also present algebraic singularities both in the infrared (IR) and UV. Consequently, a direct time domain evaluation of these expression is certainly likely to encounter serious difficulties. This is the track followed by our partner of the 1SHOT ANR project [171] and their approach is limited to a specific model for effective screened Coulomb interactions. It also experiences IR divergences at low temperatures.

Our approach is to bypass all these difficulties by tracking down all singularities in the reciprocal (frequency) domain so that they could be kept under control. The equilibrium fermionic correlator has no singularity in the energy domain: it is the equilibrium occupation number which is at most discontinuous at zero temperature. More importantly, the key point here is that the $\Gamma_\pm$ functions[2] which encode the effect of effective screened Coulomb interactions have a simple singularity structure whatever effective model we consider. More precisely, we always have a delta function singularity and a regular part

$$\Gamma_\pm(\omega) = 2\pi\kappa_\pm \left(\delta(\omega) + B_\pm(-\omega)\right) \tag{3.30}$$

with constants $\kappa_\pm$ such that $\kappa_+\kappa_- = 1$, and $B_\pm$ regular functions such that $B_\pm(\omega < 0) = 0$. The regular part can be found as the solution of

$$\omega B_\pm(\omega) = \pm\left[1 - \mathrm{T}(\omega) + \int_0^\omega B_\pm(\omega')(1 - \mathrm{T}(\omega - \omega'))\mathrm{d}\omega'\right] \tag{3.31}$$

with the condition

$$B_\pm(0^+) = \pm \lim_{\omega\to 0^+} \frac{1 - \mathrm{T}(\omega)}{\omega}\,. \tag{3.32}$$

[2] They are the Fourier transforms of $\gamma_\pm(t)$.

How can this help us compute the outgoing coherences? The idea is to find a propagator K with the simplest possible expression in terms of computational cost. What I have done was therefore to expand all possible combination of δ and $B_\pm$ for both terms of equation (3.27), so that all δ singularities could be taken out by evaluating them. In full generality, this leads to 16 possible terms for the wavepacket part and 16 more for the modified vacuum part of coherence. The corresponding expansions are given in appendix B. In principle, the last step is to numerically compute all these 31 terms[3] but, as we shall explain now, a brute force approach is not the best way to obtain the results we are longing for.

Computational complexity

In order to estimate the complexity of the numerical evaluation of all these terms, the first thing to do is to organize them according to the number of integrals that would be needed in order to compute the value of the propagator.

The worst term for K, appearing in the modified vacuum contribution when all regular functions are present, corresponds to a triple integration. In terms of computation, this means that we would need a quadruple integral for each point of the outgoing coherence. If we want to evaluate it on n^2 points, computing the full coherence would therefore scale as $\mathcal{O}(n^6)$. Even if it is polynomial and thus an easy problem from a computer scientist point a view, this is a very bad scaling in practice: doubling the number of points multiplies the computation time by 64. Obtaining accurate results may thus prove impossible by a brute force apprach.

Luckily, a whole part of the propagator, including the dominating term, is of the form $\int_\omega^\infty F(k)\mathrm{d}k$ which means that by starting at large ω and going downwards, saving the previous value at each time, we only have to evaluate F once, thus lowering the complexity to $\mathcal{O}(n^5)$. Moreover, the two variables ω and $\delta\omega$ encode different things, and need not be discretized in the same manner in the general case. Indeed, $\delta\omega$ is conjugated to the average time, and therefore encodes the temporal evolution of the wavepacket. But the precision needed to recover it is mostly fixed by the duration and shape of the incoming wavepacket. It can therefore be fixed in a clever way at the beginning and does not

[3] One of them is trivially recognized as the Fermi sea first order coherence.

need to be changed even if we want to refine the calculation to capture the dependence of K in the other variables. As a matter of fact, the number of points in the ω direction controls the precision of all integrals we have to compute in order to reconstruct the energy dependence of the propagator.

This suggest to use an anisotropic discretization with n points in the ω direction and m in the $\delta\omega$ one. Our full numerical computation then scales as $\mathcal{O}(m \times n^4)$, a scaling that can be confirmed by real measurements of the CPU time for different numbers of points. The last tool we use in order to decrease computation time is the parallel OpenMP framework that allows the computation of most of the 32 terms on their own, leading to a running time of about 5 minutes on the best computer available in our lab[4] for parameters $n = 512, m = 256$.

Let us finally mention that specific indicators are used to test the accuracy of the code: they are based on sum rules, such as total charge conservation which had been used previously in the study of the relaxation of an electronic excitation with perfectly defined energy [32]. In time-dependent situations considered here, this sum rule is generalized into sum rules involving the time-dependent average electric current.

More precisely, due to the relation between the Fourier components of the electrical current and the edge magnetoplasmon modes [65], the average outgoing electric current can be computed straightforwardly from the incoming current and the edge magnetoplasmon transmission amplitude $\mathrm{T}(\omega)$. It can then be compared to the average electrical current directly obtained from the result of our computation, that is the outgoing excess single electron Wigner function. These numerical indicators are precisely what is used to specify the discretization for obtaining our final results (see supplementary information of [OP2]).

3.2 The fate of an electron : an experimental autopsy

Having a way to predict the outgoing first order coherence after a single-electron excitation has propagated across an interaction region, it is time to confront the theoretical predictions with expreriments. The purpose of this section is to present the results obtained on single electron decoherence in the $\nu = 2$ quantum Hall edge channel system. These results

[4]Dell Poweredge R920 with 4 Intel Xeon E7-4870v2 15 core 2.3 GHz CPUs.

have been published in several papers: the decoherence scenario for single-electron excitations being presented in [OP2] and the first (and successful) comparison between theory and experiments for HOM experiments being done in [OP3].

Nevertheless, the latter paper is not the end of the story. As will be discussed in the forthcoming section, finite frequency admittance measurements performed a sample at $\nu = 2$ have shown explicitely that the simplest model for effective screened Coulomb interactions is only valid at low enough energies [14]. This rises the question of the influence of differences between effective models on the relaxation and decoherence of single electron excitations. In our recent work [OP1], we discuss how single electron relaxation differs between different models for effective screened Coulomb interactions in the $\nu = 2$ edge channel system, but this will be the central point of further sections.

3.2.1 Spin-charge separation

Let us start by discussing which model could describe screened Coulomb interactions in our typical experiments. Based on admittance measurements performed by Bocquillon et al. [14] and time-domain measurements by Hashisaka et al. [78], we know that the low energy behaviour is given by a so-called spin-charge separation model.

The spin-charge model is based on short-range capacitive coupling between the two edge channels of interest, inspired by Luttinger liquid treatments [57] and developed first and extensively by Levkivskyi and Sukhorukov [105]. The basic assumption is that, in the presence of metallic side gates, Coulomb interactions are screened and the charge density in one channel gets capacitively coupled to the charge density at the same point in the other channel, as schematically depicted on the left of figure 3.4. In terms of electric potentials, charge densities are coupled to potentials through distributed capacitances, $n_\alpha(x,\omega) = \sum_\beta C_{\alpha,\beta} V_\beta(x,\omega)$. Looking back at equation (3.2), this implies that a 2 by 2 velocity matrix describes the motion of the bosonic fields in the interaction region. Within this region, the eigenmodes of this matrix are delocalized over the two channels, and propagate at different velocities.

This leads to the following edge magnetoplasmon scattering matrix[5]:

$$S(\omega) = \begin{pmatrix} p_+ e^{i\omega\tau_+} + p_- e^{i\omega\tau_-} & q\left(e^{i\omega\tau_-} - e^{i\omega\tau_+}\right) \\ q\left(e^{i\omega\tau_-} - e^{i\omega\tau_+}\right) & p_+ e^{i\omega\tau_-} + p_- e^{i\omega\tau_+} \end{pmatrix} \tag{3.33}$$

where

$$p_\pm = \frac{1 \pm \cos(\theta)}{2}, \qquad q = \frac{\sin(\theta)}{2}, \tag{3.34a}$$

$$\tau_+ = \frac{l}{v_+}, \qquad \tau_- = \frac{l}{v_-}. \tag{3.34b}$$

In these equations, θ corresponds to the coupling strength, v_+ to the velocity of the slowest mode and v_- to the one of the fastest mode. In the strong coupling regime, $\theta = \frac{\pi}{2}$, the corresponding modes are a fast charge mode symmetric over the two channels, and a slow neutral mode which is antisymmetric, schematically depicted in the right of figure 3.4.

To understand this behaviour directly from the scattering matrix, one has to refer to the discussion of section 3.1.1 on the properties of the scattering matrix: the inverse Fourier transform of $S_{\alpha\beta}$ correspond to the expected outgoing voltage in channel α if the incoming state is simply an electron emitted at $t = 0$ in channel β. At $\theta = \frac{\pi}{2}$, if we inject such an electron in channel 1, the corresponding voltages are $-\frac{h}{2e}(\delta(t-\tau_+) + \delta(t-\tau_-))$ in channel 1 and $-\frac{h}{2e}(\delta(t-\tau_-) - \delta(t-\tau_+))$ in channel 2. This corresponds to percussional current pulses of charge $-e/2$ arriving at times τ_+ and τ_- in channel 1, and pulses of charges $e/2$ and $-e/2$ at the same times in channel 2. The initial current pulse is splitted in two and we recover the idea of a symmetric mode and an antisymmetric one over the two channels. This separation is often called the spin-charge separation as the two edge channels are of opposite spins. The fast mode (arriving at τ_-) bears all the charge of the incoming excitation whereas the slow one bears the initial spin. Howoever, do not forget that this view is valid only for the average electrical current, which only contains a small part of the information on single electron coherence. As we shall see, this point will be crucial to understand the rich physics of single electron decoherence.

Before we move on to discussing results for single electron decoherence, the reader should be aware that the spin charge separation model is not the end of the story. The admittance measurements performed

[5]See for example Degiovanni et al. [33], specifically its supplementary material for the complete derivation from the equations of motion.

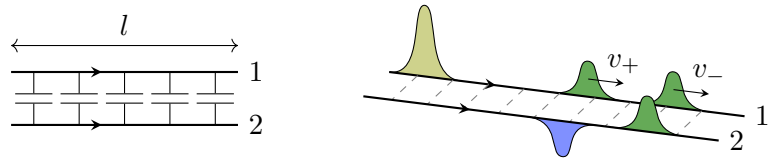

Figure 3.4: *Left*: A schematic of the short-range capacitive coupling model under study in this section. *Right*: Representation of the separation into two modes propagating at different velocities in the system.

by Bocquillon et al. [14] as well as the time-domain measurements by Hashisaka et al. [78] clearly show that the eigenmodes we are discussing exhibit dispersion as well as dissipation at high enough energies, which will be discussed later.

Results for Leviton excitations

To begin our discussion of single electron decoherence in the short-range interaction model, let us start with a unit charge Leviton excitation propagating over larger and larger distances. The nice feature of this example is that the case of a train of Leviton excitation can be treated within the framework of Floquet theory [65] and thus, this simple example can be used as a testbench for our general method.

The results are visible in figure 3.5. Since the Leviton is generated by a classical voltage pulse, it is a coherent state of plasmons, and therefore does not entangle with its environment in the bosonic point of view. The incoming coherent state associated with a Levitonic excitation, $|[-e\tilde{V}(\omega)/h\sqrt{\omega}]\rangle$ is simply changed into $|[-\mathrm{T}(\omega)e\tilde{V}(\omega)/h\sqrt{\omega}]\rangle$. There is no many-body decoherence in this case: ρ_1 and ρ_2 are pure many body states. Of course, there is no reason for this new coherent state to correspond to a perfectly electronic state. It contains electron/hole pairs which can be seen in the Wigner function. Yet, the Wigner function exhibits all features we expected from the spin-charge separation: the incoming Leviton splits into two Lorentzian pulses, each carrying half an electric charge and called half-Levitons. They propagate at different speeds. In the "environmental" channel, we recover a half-Leviton propagating at the fast speed and an anti-half-Leviton propagating at the slow speed. The typical timescale over which this spin charge separation takes place is nothing but the temporal width of the leviton:

To gain an understanding about what will happen in the general case, let us consider a superposition of two Levitons emitted at different times. The corresponding results are depicted on figure 3.6, with the same interaction parameters as before, for the superposition $(|\mathrm{Lev}_{-\delta t}\rangle + |\mathrm{Lev}_{\delta t}\rangle)/\sqrt{2}$, with $\delta t = 12\tau_0$. As we can see, each part of the superposition undergoes the same type of spin-charge separation as a single Leviton, creating a fast symmetric mode and a slow antisymmetric one over the two channels. More interesting is what happens to the interference pattern between these two parts, which is clearly visible at $t = 0$ on the incoming Wigner function. As spin/charge separation occurs, this pattern is washed out, a sign that the outgoing state is no more the quantum superposition of the two parts but rather a mixture of them. We cannot detect this effect by looking only at the current, since the current is not sensitive to the energy content in our system. Its manifestation is much stronger on the electron distribution function, as can be seen in figure 3.7.

Death of the Landau excitation

The previous discussion makes it clear that a generic electronic state will undergo a totally different decoherence scenario when propagating across the interaction region. This comes from the fact that such a generic state is indeed a quantum superposition of an infinite number of time-localized states, each of them experiencing the effects of spin-charge separation. The superposition will thus be subject to decoherence. Note that the only case in which this argument does not work is for the Levitons considered in the previous paragraph. As explained before, this is because Levitons are also edge magnetoplasmon coherent states, but are the only single electron excitations for which this is the case [138].

Without further discussion, let us therefore look at the evolution of an energy-resolved excitation, shown in figures 3.8 and 3.9. We clearly see that the situation is radically different from the Leviton state. A fast relaxation in energy happens, arising from the washing out of all interferences between the parts forming the quantum superposition. This comes from the many-body decoherence experienced by the edge channel in which the excitation is injected under the influence of the second edge channel.

It is only after this initial relaxation that the separation into two main parts propagating at different velocities becomes visible. This reflects the fact that we end up in a statistical mixture of coherent

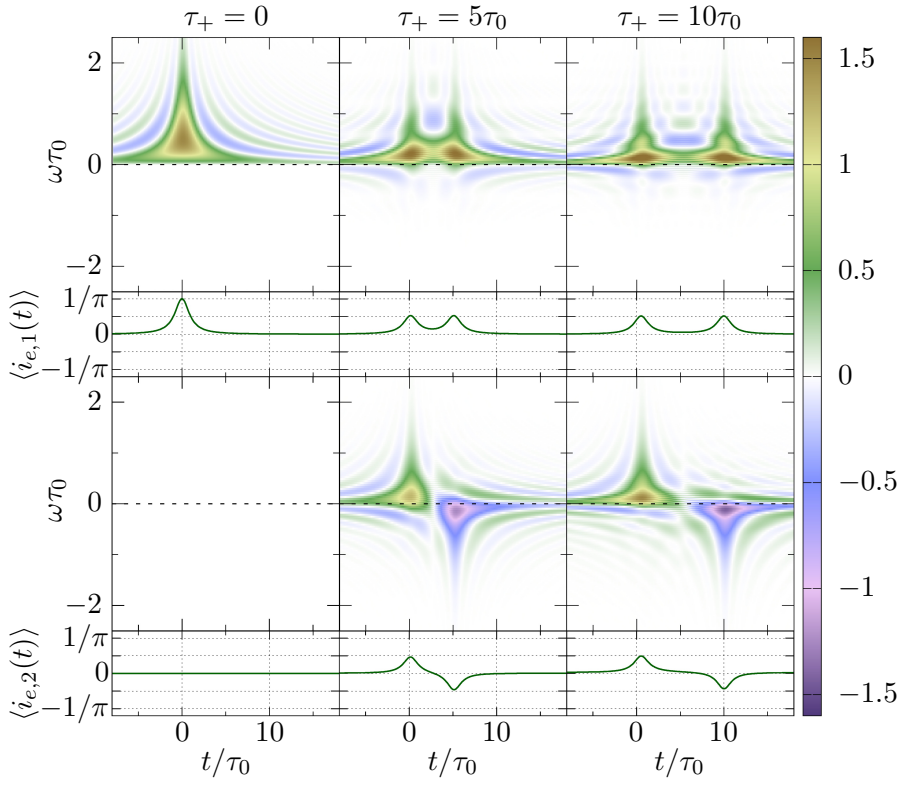

Figure 3.5: Excess Wigner function of a Leviton excitation sent in channel 1 at $t = 0$, going through a short range interaction region with parameters $\theta = \pi/2$ and $\tau_- = \tau_+/20$. From top to bottom, we show $\Delta\mathcal{W}^{(e)}_{\rho_1}(t,\omega)$,$\langle i_{e,1}\rangle$, $\Delta\mathcal{W}^{(e)}_{\rho_2}$ and $\langle i_{e,2}\rangle$. From left to right, the interaction region gets longer and longer. We clearly see a separation of the incoming excitation into two halves propagating at different speeds, that spread further apart from each other with interacting length. As expected from the previous discussion, the fastest part corresponds to a symmetric mode over the two channels, whereas the slow one is antisymmetric and corresponds to hole excitations in the inner channel. The current in both channels shows the same results.

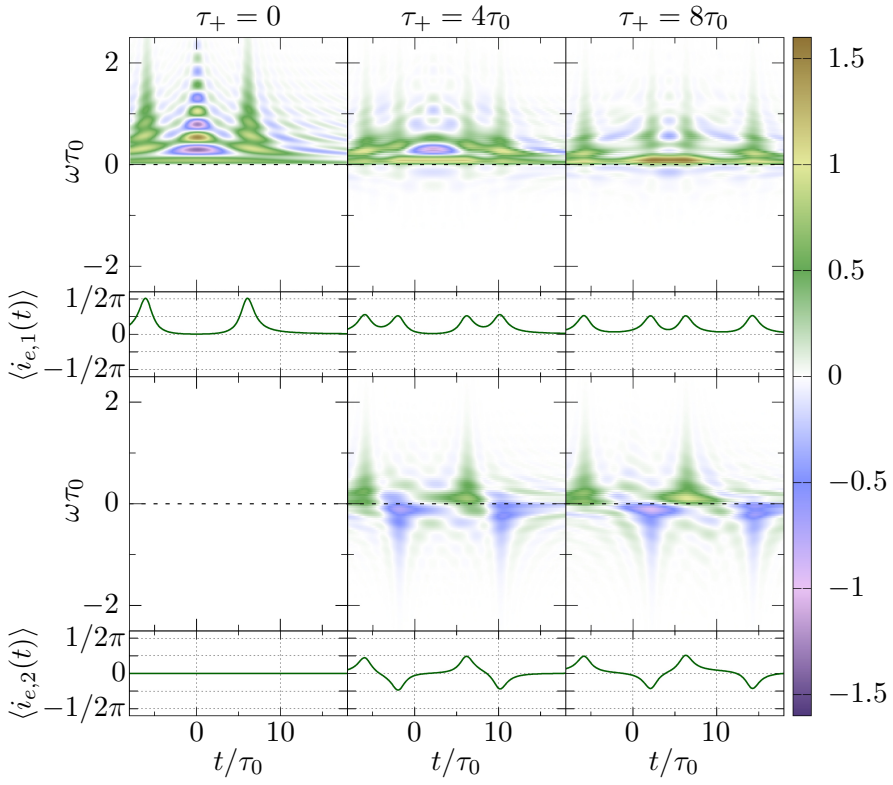

Figure 3.6: Excess Wigner function of a superposition of Levitons, with separation $\delta t = 12\tau_0$ going through a short range interaction region with parameters $\theta = \pi/2$ and $\tau_- = \tau_+/20$. As before we have from top to bottome $\Delta\mathcal{W}^{(e)}_{\rho_1}$, $\langle i_{e,1}\rangle$, $\Delta\mathcal{W}^{(e)}_{\rho_2}$ and $\langle i_{e,2}\rangle$, and interaction time rises from left to right. Each part of the superposition undergoes a separation into two halves, but the interference pattern between them vanishes with longer interaction time, a sign of decoherence. This is not visible on the currents, since they are not sensitive to the energy content of the system.

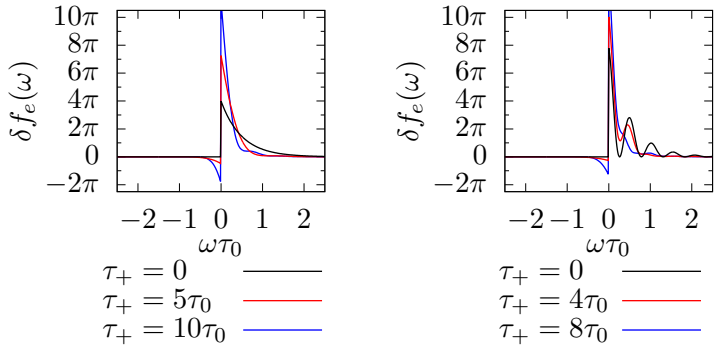

Figure 3.7: Energy distribution for the outer edge channel in the cases displayed on figure 3.5 (*left*) and on figure 3.6 (*right*). When a Leviton goes through an interaction region, it leads to excitations closer to the Fermi sea, and in particular creates hole excitations. For a superposition of two Levitons, however, the interference fringes seen on the Wigner function lead to oscillations in the energy distribution. After the effect of interaction, these oscillations are washed out, reflecting the fact that the state of the system goes from a pure state to a statistical mixture.

plasmonic states, and each of those states undergoes the standard spin-charge separation, leading to the apparition of two mixtures of states involving the two propagation velocities v_- and v_+. Of course, looking at the average current enables us to recover the standard image of symmetric and antisymmetric pulses spread over the two channels. By looking only at the current, we see no difference at all between the Leviton and Landau case. But the full Wigner function tells us a completely different story: the Landau excitation undergoes a fast relaxation even before the current pulses become separated.

To summarize, the decoherence scenario of the Landau quasi-particle involves two tim scales. For an energy resolved excitation ($\gamma \ll \omega_0$), the single electron coherence relaxes close to the Fermi level after a time of flight proportional to ω_0^{-1}. Then, after a time of flight proportional to the wave packet duration $\gamma_0^{-1} \gg \omega_0^{-1}$, $\Delta\mathcal{W}^{(e)}_{\rm out}(t,\omega)$ splits into two parts progressing at the velocities of the two edge magneto-plasmon eigenmodes, thus giving birth to collective excitations close to the Fermi sea. The first phenomenon is associated with energy relaxation probed by Sueur et al. [155], whereas the second one corresponds

to the expected fractionalization arising from the charged/neutral mode separation probed by Bocquillon et al. [14]. This is to be contrasted with the Leviton decoherence scenario for which the only time scale appearing is the time needed to fractionalize a Leviton [65]. The full picture of coherence is therefore necessary to really understand the physics at play here!

The important message here is that the rapid electronic relaxation is simply the electronic analogue of a recent cavity QED experiment [34] which probed the decay of interference fringes in the Wigner function of a superposition of two coherent states. Here, electronic relaxation arises from the decoherence of a mesoscopic superposition of quasi-classical charge density waves. This process takes place over a shorter time than the evolution of each of these quasi-classical states, which corresponds to spin-charge separation. Once extrinsic decoherence has taken place, the outgoing many-body state is an incoherent mixture of fractionalized localized electronic excitations. We confirm this scenario by computing both the current pulse and the electron distribution function corresponding to the outgoing Wigner functions: as shown in Fig. 4 of [OP2], the decay of the quasi-particle peak takes place at short times while the current pulses are almost unseparated and no hole excitations are created, thus confirming that it is a purely extrinsic decoherence effect. It is only when the two half-charge current pulses split that hole excitations are created.

3.2.2 Experimental confirmation

In order to probe the decoherence scenario we just discussed, a tool of choice will be Hong-Ou-Mandel interferometry. Indeed, as discussed in section 2.2.2, the measured quantity for HOM experiments is directly proportional to the time-shifted overlap between the Wigner functions of interest. In our case, we will thus probe the time-shifted overlap between the outgoing Wigner functions arising from two Landau excitations whose injection energy and width of the wavepacket can be tuned by the experimentalist. Note that the length of propagation between the source and the central QPC, which is nothing but the interaction region length, is fixed by the sample geometry. This setup also gives access to the speed of the slow mode [14], which can be compared with an estimation of the speed of the fast one [97]. This leads to a 1/20 factor between τ_+ and τ_-, as was used before.

From these information, we can numerically compute the electronic

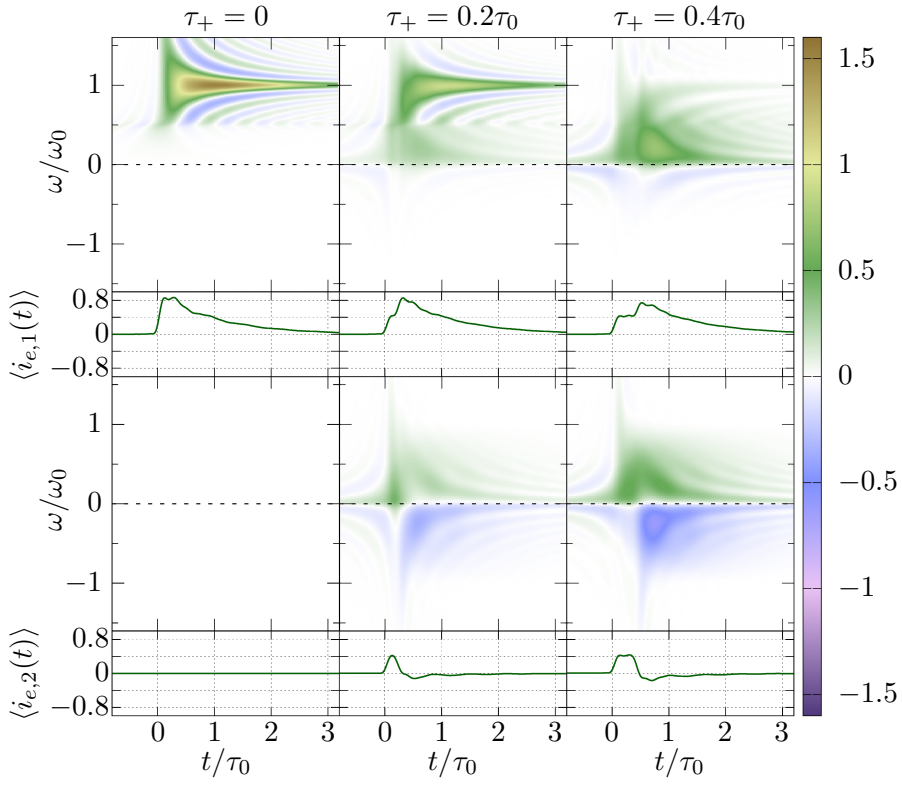

Figure 3.8: Excess Wigner function of a Landau excitation such that $\omega_0\tau_0 = 10$, going through an interaction region with parameters $\theta = \pi/2$, $\tau_- = \tau_+/20$ and varying τ_+. As for Levitons, we present from top to bottome $\Delta\mathcal{W}^{(e)}_{\rho_1}$, $\langle i_{e,1}\rangle$, $\Delta\mathcal{W}^{(e)}_{\rho_2}$ and $\langle i_{e,2}\rangle$. The situation is quite different from the Leviton case: after a very short time, coherence between the different magnetoplasmon coherent states constituting the Landau excitation is lost, leading to a rapid energy relaxation. This is similar to the decay of interference fringes seen for the superposition of two Levitons. Of course, this is not visible on the current, which only exhibits a separation of the incoming exponential into two parts.

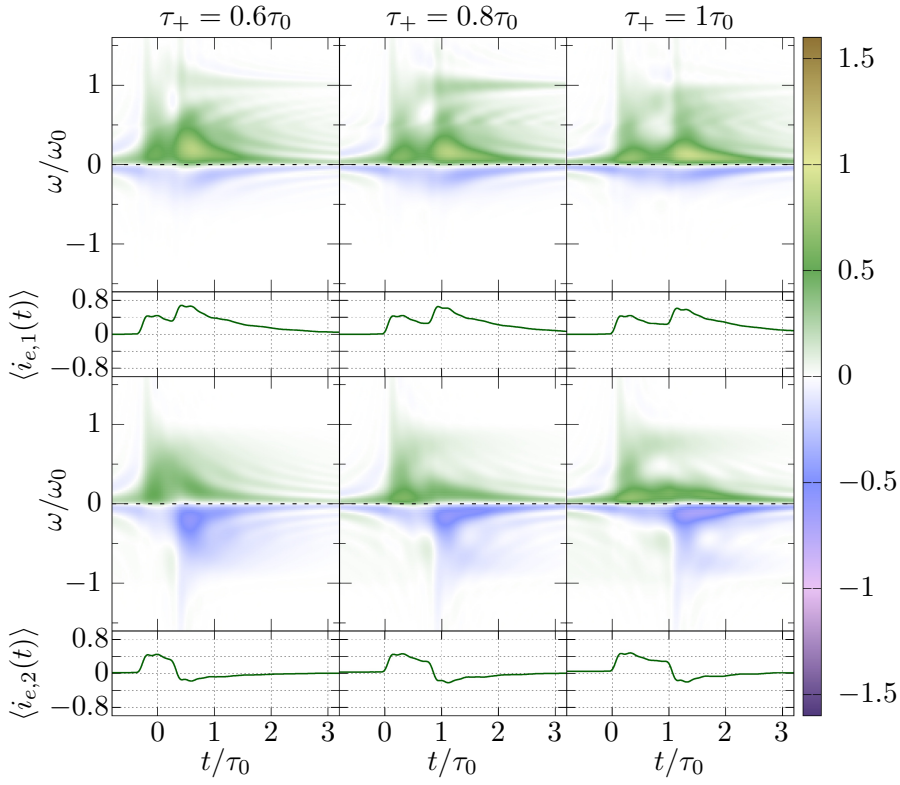

Figure 3.9: Follow-up to figure 3.8 for longer interaction times. We see that after the initial loss of coherence and energy relaxation, the state ends up in a mixture of coherent plasmonic states, each of them undergoing the natural spin-charge separation. This leads to a separation of the resulting state into two parts, and to symmetric and antisymmetric situations over the two channels. In the current, we recover the separation of the initial exponential into two halves.

Wigner functions at the QPC location, and predict from these the HOM noise as a function of the time delay between the two single electron sources. The main result of these computation is shown in figure 3.10 for excitations of the same energy, but with different temporal width. This figure also depicts the experimental results measured in the experimental group of G. Fève as well as a theoretical prediction at $T_{\mathrm{el}} = 100\,\mathrm{mK}$ from the group of Th. Martin[6]

As can be deduced directly from figure 3.10, the results predicted by both theoretical approaches have a strikingly good agreement with experiments. It is a first hint that our decoherence scenario for Landau excitations is correct, or at least not totally wrong. It also shows that the experiment is performed at a low enough temperature for our zero temperature computation to be quite in agreement with the experimental results. Most importantly, the main effect showed here is that the more energy-resolved the incoming excitation is, the more drastic interaction effects become, leading to smaller and smaller dips in the HOM curves.

Before moving on, let us take a moment to adress the disagreement between the value of τ_0 used for the fits and the one given for the experimental data. For that, let us take a look at how the electronic escape time from the source is measured in the experiment and how it is chosen for the numerical computation. In the experimental setup, the electronic escape time is extracted from the phase of the first harmonic in the AC current generated by the source. Unfortunately, this simple method has several limitations: first of all, the measurement precision can lead to significative error bars[7]. Next, the rise time of the excitation pulse is not taken into account, and neither is the widening of current pulses under the effect of interactions. This is the most important caveat since correcting it would require using an interaction model, which is precisely what we are testing. The fact is that the value extracted from the experiment using this method is therefore expected to be somehow different from the real escape time describing the wavepacket injected into the system by the single electron source. Knowing that, how can we choose

[6]The main differences between Th. Martin's group predictions, developed more specifically in Wahl et al. [171], and ours is that their approach relies on the specific model of interaction but is performed at non-zero electronic temperature. As for us, we have not yet implemented the non-zero temperature, but our approach is valid for any effective screened Coulomb interaction model.

[7]For the data presented here, measured escape times are $\tau_0 = 30 \pm 5$, 100 ± 18 and $180 \pm 50\,\mathrm{ps}$.

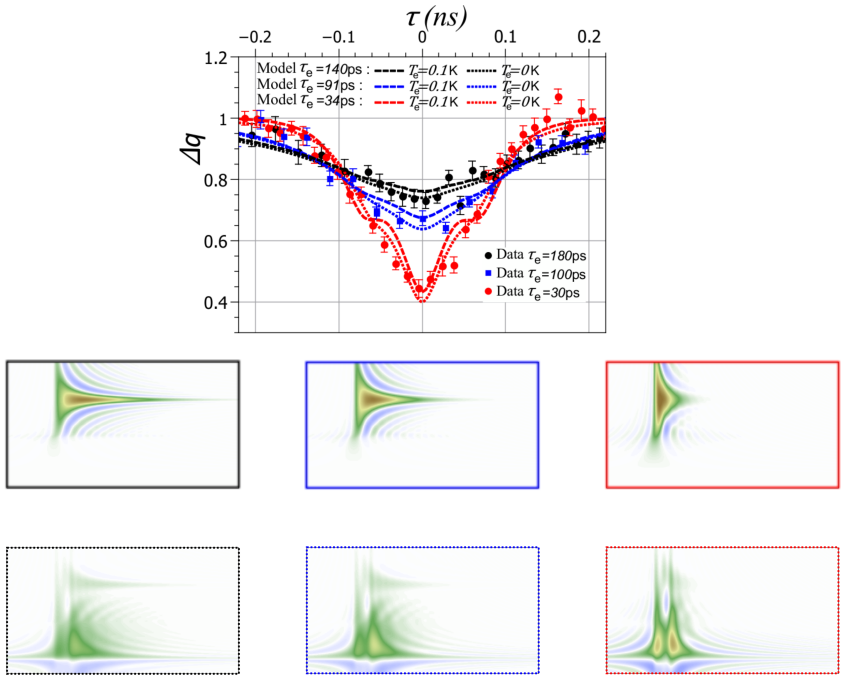

Figure 3.10: Comparison between experimental results and theoretical predictions for electrons emitted at the same energy ω_0, with various time resolutions. *Top*: Results extracted from Marguerite et al. [OP3], showing experimental data points and theoretical predictions both from our zero-temperature computation (dotted curves) and finite temperature computation at $T_{\mathrm{el}} = 100\,\mathrm{mK}$ from Th. Martin's group (dashed curves). *Middle*: Excess Wigner function of the incoming excitations in the ideal single-electron regime. We have $2\pi\omega_0 = 15\,\mathrm{GHz}$ (see section 1.1.2) and τ_0 values are 140 ps (black), 91 ps (blue), and 34 ps (red). *Bottom*: Outgoing excess Wigner function for each of the three injected wavepackets. The HOM theoretical curves are obtained using the overlaps of these Wigner functions with themselves, using a varying time shift. As can be seen on the top part of the figure, theoretical predictions are in great agreement with experimental results, but the effect of temperature is not visible with our experimental resolution.

the value to obtain numerical predictions? To answer this question, we have chosen the escape time in such way that the HOM prediction would have the same width as the data, since this width is a direct result of temporal width of the incoming excitation. All other parameters (energy of the source, interaction length) were directly extracted from the experiment since we had a better resolution on them. The advantage of this approach is that, once the width of the dip had been fixed to match the experimental data, its depth would also fit with the data! Moreover, the value we get for τ_0 in this approach are indeed within experimental error bars. This allows us to be confident in the fact that our theoretical approach does indeed provide a quantitative explanation of interaction effects on single electron coherence in this experiment. However, we would like a more direct and explicit proof of the many body decoherence effect that is responsible for the spectacular difference between the decoherence scenario of Levitons and Landau excitations.

3.2.3 A revival of indiscernability ?

Having a closer look at our decoherence scenario clearly emphasizes the role of energy relaxation in the difference between Leviton and Landau excitations. In the absence of interaction, two Landau excitations with different energies and high quality factor would be quite easy to distinguish from one another. These wavepackets would only have a small overlap, and the expected HOM curve would only have some small dip down to one minus the value of that overlap. On the other hand, in the absence of interactions, two identical Landau excitation depict an HOM dip that goes down to zero.

By contrast, our theoretical approach to interactions shows that any wavepacket not created from a classical current experiences many-body decoherence whose fingerprint on single electron coherence is fast energy relaxation. This suggests that the information on the injection energy might be partially absorbed by the environment and, in contrast with the non-interacting case, this should have visible consequences on the HOM curves.

Let us confirm this intuition by looking more precisely into our analysis: many body decoherence tends to kill all the contributions to the outgoing coherence which would come from coherences of the form $\varphi_e(t)\varphi_e^*(t')$ with $t \neq t'$. This implies that the outgoing single electron coherence, or equivalently the Wigner function, should only depend on $|\varphi_e(t)|^2$. This has the striking consequence that all injected wavepackets

with the same escape time τ_0 but different injection energies should lead, in the limit of an infinite interaction region, to the same HOM curve! This prediction is indeed supported by our numerical computations, and can therefore be tested experimentally. The results of this study are presented in figure 3.11. In this figure, we can see that experimental results confirm, up to our resolution, that the HOM curves for excitations with the same temporal form but different energy contents are indeed the same.

This is the smoking gun we were looking for: at the single electron coherence level, the quantum states after the interaction region are less distinguishable than the ones that have been injected by the single electron sources. Through the looking glass of single electron coherence, the interaction region acts as an eraser for the injection energy, thus restoring indistinguishability of the quantum electrical currents within each incoming channel of the HOM interferometer. This kind of indiscernability revival can be confirmed by looking at the expected Wigner functions after the interaction region, presented on that same figure. Indeed, the Wigner function displays a low-energy state with two main parts, and looks quite identical for both incoming states. Of course, the outgoing states are not pure quantum states, so the contrast of the HOM experiment cannot go all the way down to zero.

As will be clear later, this effect is due to the strong coupling between the injection (outer) edge channel and the second (inner) one. A weaker coupling may lead to an energy relaxation scenario that could be described by a non-zero probability for the electron to propagate across the interaction region without experiencing any inelastic process. We would therefore still have a quasi-particle peak at the injection energy, even in the limit of a very long interaction region. Because these remnants would retain information about the initial injection energy, we would not observe such an indiscernability revival and such an independance of the HOM curves from the incoming initial energy.

Another way to present the environment induced erasure of the injected initial energy is by refering to the famous quasi-particle decay problem originally considered by Landau to motivate his theory of the Fermi liquid. It is a signature that no significant quasi-particle peak survives propagation over a distance which is inversely proportional to the injection energy of the quasi-particle. By contrast, for an electronic quasi-particle created above the Fermi level in a Fermi liquid, the typical energy relaxation time decays as the inverse of the square of the injec-

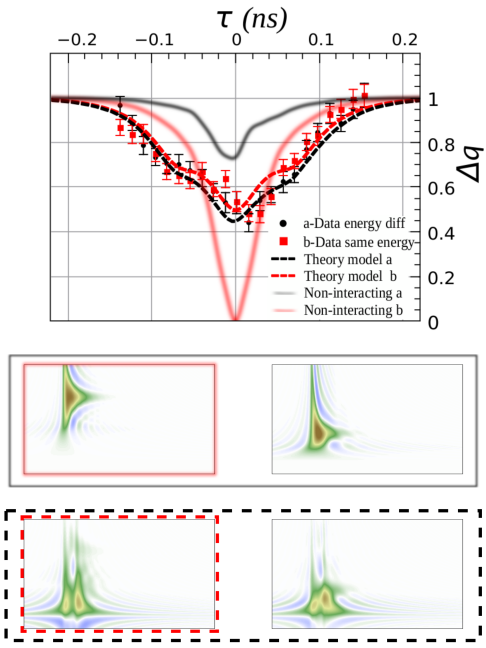

Figure 3.11: Comparison between experimental results and theoretical predictions for electrons emitted with the same temporal width $\tau_0 = 40\,\mathrm{ps}$, with two possible injection energies. *Top*: Results extracted from Marguerite et al. [OP3], showing experimental data points and theoretical predictions from our zero-temperature computation (dashed curves) for two separated cases: both injected wavepacket have the same energy (red) or different energies (black). Blurred lines correspond to the expected HOM signal in the absence of interaction: identical wavepackets lead to a complete dip down to 0, while different ones lead to a smaller dip. We see that the experimental data is pretty much the same for both situations, indicating that we have more indiscernability after interaction than before! *Middle*: Excess Wigner function of the incoming excitations in the ideal single-electron regime. Energies are $\hbar\omega_0/k_\mathrm{B} = 0.7\,\mathrm{K}$ (left) and $0.3\,\mathrm{K}$ (right) *Bottom*: Outgoing excess Wigner function for each of the two injected wavepackets. The HOM theoretical curves are obtained using the overlaps of these Wigner functions with themselves, using a varying time shift. These Wigner functions clearly exhibit less differences than the incoming ones, explaining why the theoretical curves are much closer to each other for the outgoing wavepackets. As before, the agreement between theory and experiment is quite good.

tion energy, thus ensuring that the quasi-particle peak does not broaden towards vanishing injection energy. This is clearly not the case here! The fact that the electronic quasi-particle does not survive propagation in a quantum Hall edge channel at $\nu = 2$ has first been noticed by the group of F. Pierre during their study of the relaxation of a non equilibrium electronic distribution [155]. Here, we are confirming it by a direct study of the fate of a single energy-resolved electronic excitation.

3.2.4 Comparison to another model at $\nu = 2$: long-range interaction

As teased before, we know from Bocquillon et al. [14] that even if the short-range interaction model is valid at low energies, the effect of the finite range of effective screened Coulomb interactions reveals itself at higher energies, typically 10 GHz in the sample studied in this publication. Since this is comparable to the frequencies associated with the injection energy by the single electron source, it is important to discuss the influence of long range interaction effects on electronic decoherence.

Derivation of the transmission matrix

The model we are interested in is a simple case of two co-propagating channels in which Coulomb interactions are not screened locally. The interaction region is thus seen as a capacitor, which amounts to saying that local potentials U seen by electrons are uniform on the whole length of the interaction region. In that case, the interaction region can be discussed in the spirit of the discrete element circuit models introduced by Büttiker and his collaborators for quantum conductors [128] and quantum Hall edge channels [26]. This approach leads to the following edge magnetoplasmon scattering matrix [65]:

$$S(\omega) = \begin{pmatrix} p_+\mathcal{T}_+(\omega) + p_-\mathcal{T}_-(\omega) & q\left(\mathcal{T}_-(\omega) - \mathcal{T}_+(\omega)\right) \\ q\left(\mathcal{T}_-(\omega) - \mathcal{T}_+(\omega)\right) & p_+\mathcal{T}_-(\omega) + p_-\mathcal{T}_+(\omega) \end{pmatrix} \tag{3.35}$$

where $p_\pm$ and q are given by equation (3.34) and other parameters are given in terms of the dimensionless parameter $x = \omega l/v_\mathrm{F}$ by

$$\mathcal{T}_\pm(\omega) = \frac{\mathrm{e}^{\mathrm{i}x} - 1 + \mathrm{i}\alpha_\pm x\mathrm{e}^{\mathrm{i}x}}{\mathrm{e}^{\mathrm{i}x} - 1 + \mathrm{i}\alpha_\pm x} \tag{3.36}$$

$\alpha_\pm$ being related to the eigenvalues of the capacitance matrix $C_\pm$ by $\alpha_\pm = R_\mathrm{K}C_\pm v_\mathrm{F}/l$.

Before using this expression to compute outgoing Wigner functions, let us estimate the typical values of these $\alpha_\pm$. The first thing we know is that the low-energy limit of this long-range case gives back the short-range case introduced before. The low energy limit is given by $\mathcal{T}_\pm = \mathrm{e}^{\mathrm{i}\omega\tau_\pm^{\mathrm{lr}}}$, where the long-range times $\tau_\pm^{\mathrm{lr}}$ are given by

$$\tau_\pm^{\mathrm{lr}} = \frac{\omega l}{v_{\mathrm{F}}} \frac{\alpha_\pm}{1+\alpha_\pm} \,. \tag{3.37}$$

Since we want these times to be equal to their short-range counterparts, and in particular since we want to have $\tau_-^{\mathrm{lr}} = \tau_+^{\mathrm{lr}}/20$, we get a first relation between α_+ and α_-. Moreover, measurements from Bocquillon et al. [14] tell us that the velocity of the slow mode should be $v_+ \simeq 4\times10^5\,\mathrm{m\,s^{-1}}$, whereas the Fermi sea velocity is $v_{\mathrm{F}} \simeq 1\times10^5\,\mathrm{m\,s^{-1}}$. Equivalently, this leads to $\tau_+ v_{\mathrm{F}}/\omega l = 4$. All this together leads us to chose, for the remainder of this section,

$$\alpha_+ = \frac{1}{3} \quad \alpha_- = \frac{1}{79} \,. \tag{3.38}$$

The outgoing Wigner functions for excitations crossing a long-range interaction region can then be computed using the approach described in the present chapter. The results are shown in figure 3.12 for Landau excitations. Several qualitative changes can be noticed compared to the short-range case. First, non-vanishing coherence and current appear at times smaller than the time taken for a free excitation to cross the interaction region. This is due to the long range character of Coulomb interactions: as soon as the incoming excitation enters the interaction region, it excites low-energy electron/hole pairs in the whole interaction region. This explains that a first current peak should begin at a time $\tau = l/v_{\mathrm{F}}$ before the arrival of the "real" excitation, as can be seen in the figure. Of course, this is not a violation of causality: the electromagnetic disturbance does propagate within the space around the conductor at the speed of light since it is not screened by any nearby gate. Speaking of the electrical current, the bottom panel shows that the outgoing average current has three main peaks, compared to the two obtained in a short-range setting. Finally, as expected from the long-range nature of interactions, the outgoing coherence has a bigger spreading in the time domain.

It is then natural to ask whether or not these differences can be detected by an HOM experiment. To answer this question, figure 3.13

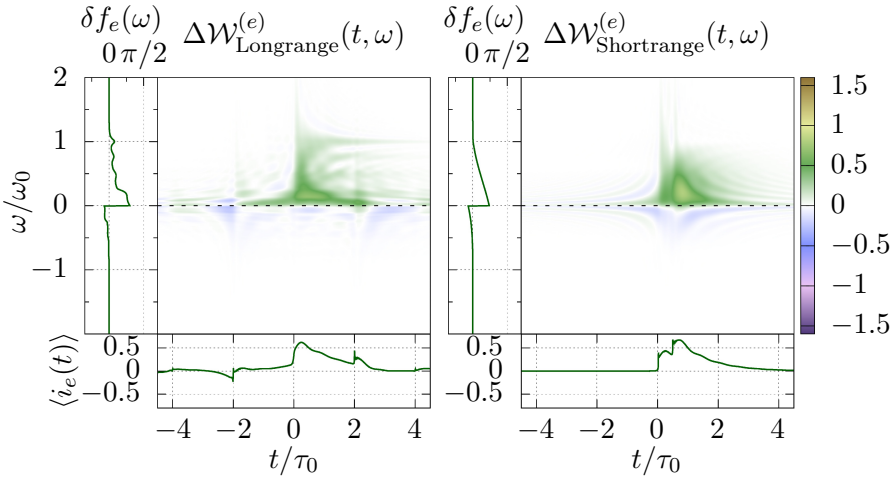

Figure 3.12: Comparison between short- and long-range interactions, for Landau excitations with $\omega_0\tau_0 = 10$. *Left*: Wigner function of the outer channel for an excitation going out of a long-range interaction zone. *Right* : Wigner function for the same incoming excitation, with a short-range interaction region of the same length. Parameters are $\tau_+ = \tau_0/2$, $\tau_- = \tau_+/20$. In both cases, the region length is the same, and we are in the strong interaction regime ($\theta = \pi/2$). The finite frequency admittance of both interaction regions has the same low energy limit when using values given by equation (3.38), as discussed in the text. Time spreading of coherence is different in the two models, and lon-range interaction leads to the apparition of excitations at earlier times, three main peaks in the current instead of two, and a more complex pattern in the energy domain.

displays our prediction for HOM curves for both the short and long range interaction models assuming interaction regions of the same length and the same incoming excitations. As seen from this figure, these two interaction models lead to qualitatively different HOM curves: the long range one shows a wider dip, as expected of the wider time spreading of the outgoing excitation and more "secondary dips" than the short range case. This last feature can be traced back to the three main peaks in the outgoing Wigner function of the long range case compared to the two peaks of short range interaction.

To comment on the experimental state of the art [OP3, 51, 52, 112], we have plotted on the right panel of figure 3.13 the HOM predictions for parameters corresponding to the recently published experimental results in [OP3]. Unfortunately the side lobes that would enable us to differentiate between the two interaction models occur for a time shift comparable or greater than 300 ps. However, probing time shifts larger than 200 ps brings us to values too close to the half-period of the drive, which is typically 1 ns. In such situations, it is not possible anymore to ignore the excitation emitted in the other half period: we cannot rely on a single-electron decoherence computation for a quantitative theory/experiment comparison. Probing such large time shifts while comparing to our present theoretical predictions would therefore require lowering the drive frequency f, thus deteriorating the signal to noise ratio of the low-frequency current noise measurements. This calls for complementary investigations and/or experimental developments in order to determine which interaction model for the $\nu = 2$ edge channel system would be the best at reproducing the full HOM curves in detail.

3.3 Protection from decoherence

We have seen in the previous section that decoherence effects are particularly strong in the $\nu = 2$ quantum Hall edge channel system. This has been confirmed experimentally several times, as we already discussed, putting to a stop the retrospectively naive idea that these systems could be used to process quantum information carried by single electron excitations. Using edge channels as rails for some kind of "flying qubit" system would be severely limited, to say the least, by the effects of electron-electron interactions.

Of course, this has sparked a line of research aiming for the protection of electronic wavepackets against decoherence in these systems. This

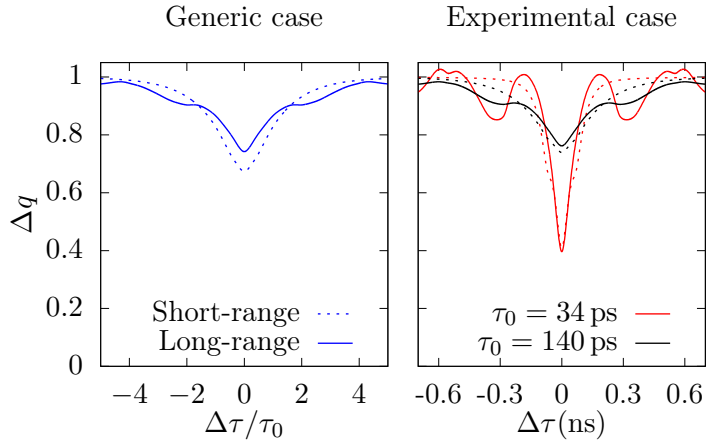

Figure 3.13: Predicted results of an Hong-Ou-Mandel experiment after an interaction region in the short-range (dashed lines) and long-range (solid lines) cases, at $\nu = 2$. *Left*: Interaction parameters are the ones given in the caption of figure 3.12, excitation is a Landau excitation with $\omega_0\tau_0 = 10$. The two HOM curves are quite different, the most striking features being the depth of the HOM dip at $\Delta\tau = 0$, and the secondary dips at $\Delta\tau = \pm 2\tau_0$ in the long range case, associated with the excitations at those same times that can be seen directly on the Wigner function or the current on figure 3.12. The wider time spreading of the outgoing coherence also leads to a wider HOM dip. *Right*: Interaction parameters are realistic experimental ones, with $\tau_+ = 70\,\mathrm{ps}$ and $\tau_- = \tau_+/20$ for the short-range case and a long-range case giving the same low-energy limit. Incoming excitation is a Landau wavepacket with $\hbar\omega_0/k_\mathrm{B} = 0.7\,\mathrm{K}$ and $\tau_0 = 34\,\mathrm{ps}$ (red) or $\tau_0 = 140\,\mathrm{ps}$ (black), as in figure 3.10. Long-range interaction would lead to different HOM curves from the short-range case, specifically in terms of secondary dips.

is the main topic of this section: how can we engineer our setup in order to protect electronic excitations from decoherence? What can we realistically achieve in an experiment? To what extend can some sort of "flying qubit" behaviour be recovered ?

3.3.1 A closed environment

The main idea that has indeed been explored in the last few years at $\nu = 2$ is passive decoherence control using a clever design of the sample allowing to close the inner edge channel on itself. The idea is simple: a closed loop is associated with some energy scale, so that a blocking of energy transfers below that typical energy should happen. Moreover, if the two channels stay close enough, interactions between them should be sufficiently strong to screen all other possible sources of interaction with the edge channel of interest.

This idea has been implemented in two experiments in the DC regime. In the experimental group of F. Pierre at LPN, in Marcoussis, interaction effects indeed lead to energy relaxation along the edge channels in their setup [155] which can be partially blocked by letting the outer channel propagate on longer paths, but along a closed inner edge channel [2]. In the nanoelectronic group at CEA Saclay (SPEC), P. Roche and his collaborators have focused on probing decoherence and limiting its effect in Mach-Zehnder interferometers [134, 135, 83, 157]. The most relevant article for this section is the one of Huynh et al. [83], in which electronic decoherence was partially blocked by bordering the propagating edge channel by closed loops.

Theoretical model

There are two possible ways to interact with a closed inner channel, depending on the geometry of the experiment. In the paper by le Sueur et al. [155], the outer edge channel propagates along the inner edge channel on the whole length of the loop, thus corresponding to what we will call type (a) loops. By contrast, in the paper by Huynh et al. [83], the outer channel only follows the loop on a small part of its length, a feature which we will call type (b) loops. Both are drawn in figure 3.14. We shall now compute the edge magnetoplasmon scattering matrix associated with such an environment.

The main idea is that both geometries impose a periodicity condition

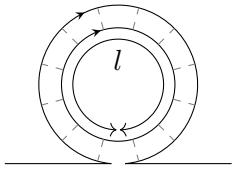

Closed inner channel (a)

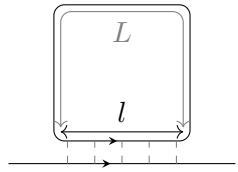

Closed inner channel (b)

Figure 3.14: Schematic representation of the two types of closed environments we are interested in. Either the outer edge channel follows the loop along its whole length (type (a), see [155]), or it only interacts with it on a small part of the loop (type (b), see [83]). For both types, the interaction length is called l, and the interaction type can be chosen from any $\nu = 2$ interaction.

on the field for the inner channel:

$$\phi_2(0,\omega) = \phi_2(l,\omega)\mathrm{e}^{\mathrm{i}\omega\tau_L} \tag{3.39}$$

where $\tau_L = \frac{L}{v_+}$ is the time it takes for an excitation to cover the non-interacting length L of the loop, and l is the size of the region where the two-channels interact. The transmission coefficient for the complete model is then obtained in full generality as

$$\mathrm{T}(\omega) = S_{11}(\omega) + \frac{S_{12}(\omega)S_{21}(\omega)}{\mathrm{e}^{-\mathrm{i}\omega\tau_L} - S_{22}(\omega)} \tag{3.40}$$

with S the scattering matrix describing the interaction region of size l between the two channels in the general case. For short-range interaction, this specializes to

$$\mathrm{T}(\omega) = -\mathrm{e}^{\mathrm{i}\omega(\tau_+ + \tau_- - \tau_L)}\left(\frac{\mathrm{e}^{\mathrm{i}\omega\tau_L} - p_+\mathrm{e}^{-\mathrm{i}\omega\tau_+} - p_-\mathrm{e}^{-\mathrm{i}\omega\tau_-}}{\mathrm{e}^{-\mathrm{i}\omega\tau_L} - p_+\mathrm{e}^{\mathrm{i}\omega\tau_+} - p_-\mathrm{e}^{\mathrm{i}\omega\tau_-}}\right). \tag{3.41}$$

As expected, this transmission coefficient has a unit modulus since no dissipation is present here and the unitary scattering matrix thus reduces to a simple complex number. Of course, the special case (a) is recovered for $\tau_L = 0$.

Time-domain interpretation

To get a better understanding of this transmission coefficient, let us take a look at its interpretation in the time domain, by computing the inverse

Fourier transform of $\mathrm{T}(\omega)$ as we did before for short-range interaction. First, we can rewrite the transmission coefficient as

$$\mathrm{T}(\omega) = S_{11}(\omega) + \mathrm{e}^{\mathrm{i}\omega\tau_L} S_{12}(\omega) S_{21}(\omega) \sum_{n=0}^{\infty} \mathrm{e}^{\mathrm{i}n\omega\tau_L} S_{22}(\omega)^n \,. \tag{3.42}$$

This expression has a clear physical meaning. Indeed, all excitations recovered in channel 1 after the interaction region of size l correspond to one of the following paths :

- Either incoming excitations cross directly the region in channel 1 (S_{11});
- Or incoming excitations create excitations in channel 2 (S_{21}) which go round the closed loop and create excitations back in channel 1 (S_{12}). This can either happen after one lap around the loop ($\mathrm{e}^{\mathrm{i}\omega\tau_L}$) or after $n+1$ laps, in which case we need to take into account the fact that excitations in channel 2 crossed the interaction region in channel 2 n times (S_{22}^n) and made n more laps ($\mathrm{e}^{\mathrm{i}n\omega\tau_L}$). This corresponds to the sum in equation (3.42) .

In the case of short range interaction, $\mathrm{T}(\omega)$ can be rewritten as a sum of complex exponentials

$$\begin{aligned} \mathrm{T}(\omega) = {} & p_+ \mathrm{e}^{\mathrm{i}\omega\tau_+} + p_- \mathrm{e}^{\mathrm{i}\omega\tau_-} \\ & + \sum_{n=0}^{\infty} \sum_{k=0}^{n+2} w_{n,k} \mathrm{e}^{\mathrm{i}\omega((n+1)\tau_L + k\tau_+ + (n+2-k)\tau_-)} \end{aligned} \tag{3.43}$$

where the weights $w_{n,k}$ are given by[8]

$$\begin{aligned} & w_{n,k} = \\ & q^2 \left[\binom{n}{k} p_+^{n-k} p_-^k + \binom{n}{k-2} p_+^{n+2-k} p_-^{k-2} - 2 \binom{n}{k-1} p_+^{n+1-k} p_-^{k-1} \right] \end{aligned} \tag{3.44}$$

This equation shows that the outgoing voltage for a localized excitation of charge $-e$ created at time t_0 corresponds to the generation of a percussional current pulse with charge $-p_+ e$ emitted at time $t_0 + \tau_+$, another one with charge $-p_- e$ at time $t_0 + \tau_-$, and an infinity of others at times $t_0 + (n+1)\tau_L + k\tau_+ + (n+2-k)\tau_-$ with charges $-w_{n,k} e$. Total current is conserved, since $p_+ + p_- = 1$ and $\forall n, \sum_{k=0}^{n+2} w_{n,k} = 0$.

[8] In this equation, we adopt the convention that $\binom{n}{k} = 0$ if $k > n$ or $k < 0$.

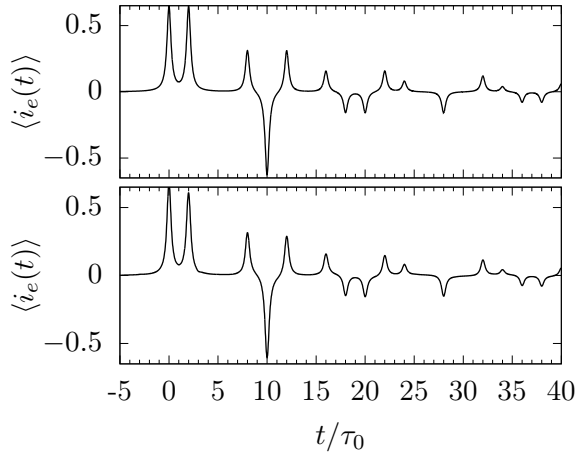

Figure 3.15: Outgoing current for an incoming Leviton excitation of width $\tau_0/4$ after an interaction with a closed loop. Parameters are $\tau_- = \tau_0$, $\tau_+ = 3\tau_0$ and $\tau_L = 7\tau_0$. Such parameters, while not experimentally reasonable, allow a good visualization of the physical properties of the current. Going from left to right, we indeed see first the two peaks corresponding to standard fractionalization when crossing the interaction region, followed by a series of three peaks corresponding to excitations having crossed twice the interaction region and going around the loop once (first corresponds to two crossings in the symmetric mode, then one antisymmetric and one symmetric, third one is two crossings in antisymmetric mode), and so on. *Top*: as given by the analytical computation from equation (3.43). *Bottom*: as recovered when integrating the numerically obtained outgoing Wigner function over all energies.

For the Leviton source, with the exact same reasoning, the outgoing current is a sum of time-shifted Lorentzian currents with suitable charges. Figure 3.15 shows the outgoing current for this type of environment computed in two different ways. The top panel corresponds to an analytical computation of the expected current in the way we just exposed. The bottom panel is obtained from our numerical code used to compute the outgoing single-electron coherence by integrating the resulting excess Wigner distribution function over the energy. The very good agreement between the two results illustrates the validity of our numerical approach.

Frequency domain interpretation

Let us now turn to the transmission coefficient as a function of energy. Since $|\mathrm{T}(\omega)|^2 = 1$, this system behaves as an effective $\nu = 1$ system, with a transmission of the form $\mathrm{T}(\omega) = \mathrm{e}^{\mathrm{i}\omega\tau(\omega)}$, $\tau(\omega)$ being an effective frequency-dependent plasmon velocity.

First of all, let us consider short-range interactions at weak coupling. In that case, the closed inner channel can be seen as a Fabry-Pérot interferometer with low transparency on one side and total reflection on the other side. The interaction region can then be viewed as a cavity connected to a transmission line. As in optics, the phase of its reflexion coefficient, which is here the edge magnetoplasmon transmission $\mathrm{T}(\omega)$, exhibits sharp resonances. To characterize these resonances, let us look at the Wigner-Smith time delay

$$\tau_{\mathrm{WS}}(\omega) = \frac{1}{2\pi\mathrm{i}} \frac{\mathrm{d}\log\left(\mathrm{T}(\omega)\right)}{\mathrm{d}\omega} \tag{3.45}$$

which represents the dwelling time within the cavity for plasmons at ω. Resonances in the phase will lead to peaks in τ_{WS}, corresponding to the fact that quasi-bound scattering states are available within the interaction region seen as a cavity. These resonances are sharply visible in the weak-coupling regime, as can be seen in figure 3.16. The left panel depicts the phase of $\mathrm{T}_{\mathrm{eff}}(\omega) = \mathrm{e}^{-\mathrm{i}\omega\tau_-}\mathrm{T}(\omega)$, and displays strong jumps of 2π every time $\omega(\tau_+ + \tau_L) \simeq 2n\pi$. These jumps lead to strong resonances in the Wigner Smith time delay as seen on the right panel. At low coupling, we therefore expect that all plasmon states with an energy lower than $2\hbar\pi/(\tau_+ + \tau_L)$ will not be affected by the interaction region at all, since there are no available bound states in the cavity at such energies.

Of course, we already presented strong experimental evidence that the coupling between quantum Hall edge channels is strong ($\theta \simeq \pi/2$). It is then natural to ask ourselves how the results obtained for the low-coupling case are modified. As can be expected from the comparison with a Fabry-Pérot interferometer with higher transparency, higher coupling leads to an energy broadening of the quasi bound states inside the loop, as can be seen in figure 3.17. Equivalently, the phase does not display the same plateaus separated with strong jumps, but still exhibits some kind of washed-out version of that behaviour.

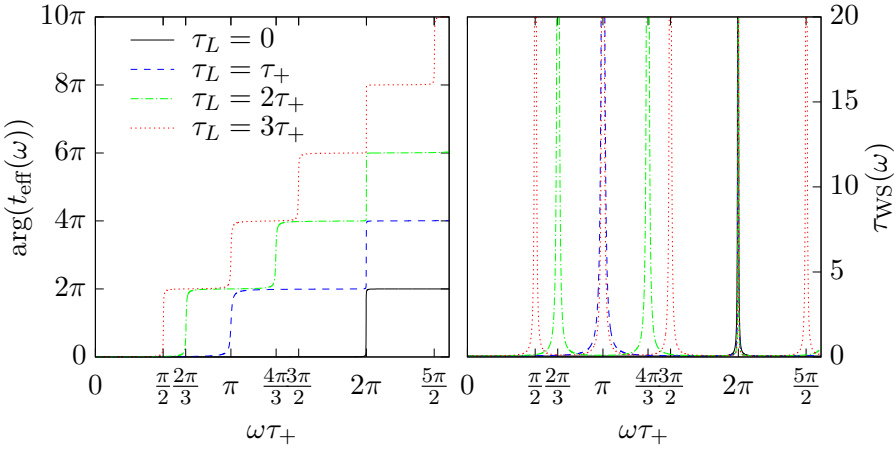

Figure 3.16: Phase of the transmission coefficient (*Left*) and the associated dwelling time $\tau_{\rm WS}(\omega)$ (*Right*) for a short-range interaction with weak coupling ($\theta = \pi/10$) and parameters $\tau_- = \tau_+/20$, for 4 different geometries of the loop. We see that the phase jumps each time $\omega(\tau_+ + \tau_L) \simeq 2n\pi$, with a stronger jump when $\omega\tau_+ = 2\pi$. These jumps are the signature of a quasi bound state (scattering resonance) at corresponding energy inside the loop.

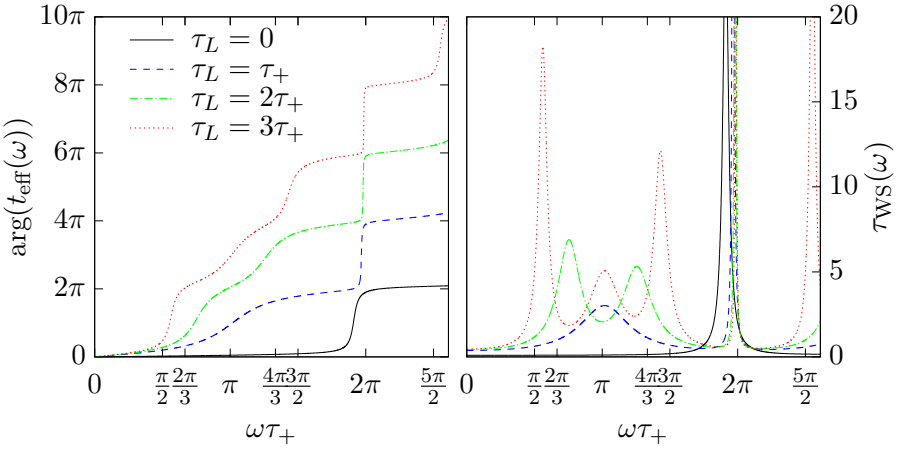

Figure 3.17: Phase of the transmission coefficient (*Left*) and associated dwelling time in the closed inner channel (*Right*) for a short-range interaction with strong coupling ($\theta = \pi/2$) and the same 4 different geometries for the loop as for the low-coupling case. We see that the phase does not go from one plateau to another, but still exhibits jumps at values close to the ones seen before, the jump at $\omega\tau_+ = 2\pi$ being once again the strongest. The corresponding quasi bound states inside the loop are therefore broadened in energy.

3.3.2 Experimental predictions and Wigner functions

Comparison to an open channel

Now that we have a better understanding of the expected behaviour of our transmission coefficient, we hope that any excitation whose energy content is completely below the first resonance will be protected against decoherence. To test this assertion, we have computed numerically the Wigner functions of an electron emitted in an energy-resolved wavepacket centered around $\omega_0 = \pi/\tau_+$, propagating across an interaction region of length l. The results are displayed in figure 3.18 both for a closed environment of type (a) ($\tau_L = 0$) and for a standard, open, co-propagating short-range interaction region. In this situation, electron/hole pair generation is inhibited in the first case, because the electronic energy is off resonance with the cavity. In other words, relaxation is blocked and almost no decoherence happens: the single electron excitation leaves the interaction region pretty much unchanged. This is in complete opposition with the result for standard spin-charge separation, where the usual decoherence takes place.

Of course, we are also interested in the evolution of excitations emitted above the cavity resonances. Figure 3.19 depicts such a case, with an incoming excitation centered around $\omega_0 = 5\pi/(2\tau_+)$. In this case, the Landau excitation relaxes by emitting electron/hole pairs precisely at the energy given by the first resonance. This relaxation leads to a peak in the electronic distribution at the final energy of the electron, which is its injection energy minus the resonance energy. In the temporal domain, the characteristic features of the interaction-generated electron/hole pairs cloud are the oscillations of $\Delta\mathcal{W}^{(e)}$ at energies below the resonance energy.

To be more precise, we expect that the state generated by this system is simply a plasmon emitted with the energy of the loop. The two decoherence processes are completely different: on the one hand, in the closed environment case, the quasiparticle peak stays quite strong, and relaxation involves a typical energy scale. On the other hand, for an open environment, decoherence leads to a proliferation of low energy excitations close to the Fermi level, and the incoming quasiparticle is washed out. The result of this process is far more complicated than a simple energy-loss of the excitation. Of course, saying that closing the environment leads to a completely controlled decoherence scenario is an overstatement, but we can safely say that it leads to *more* control on

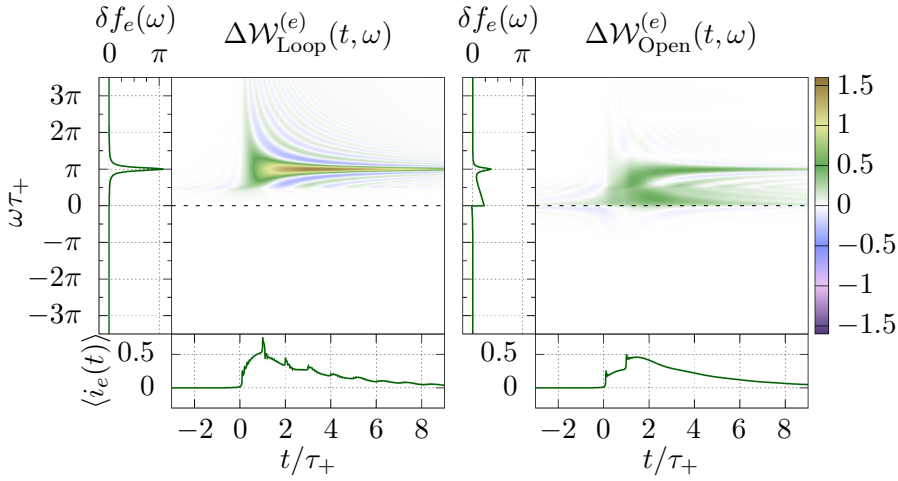

Figure 3.18: Outgoing Wigner function for an incoming Landau excitation of duration $\tau_0 = 0.8\tau_+$. Interaction parameters are $\theta = \pi/2$ and $\tau_- = \tau_+/10$. *Left*: short-range interaction with a closed environment of type (a) ($\tau_L = 0$). *Right*: copropagation along an open channel on the same distance with same interaction parameters. For both graphs, the incoming excitation is at an energy $\omega_0\tau_+ = \pi$, below the energy resonances of the loop. When interacting with a closed channel, relaxation is highly suppressed compared to copropagation along an open channel. Because the injection energy is below closed channel resonances, the outgoing occupation number remains close to the incoming one. Electron/hole pair creation is responsible of the spikes that appear on the average electric current which are characteristic of the closed channel geometry.

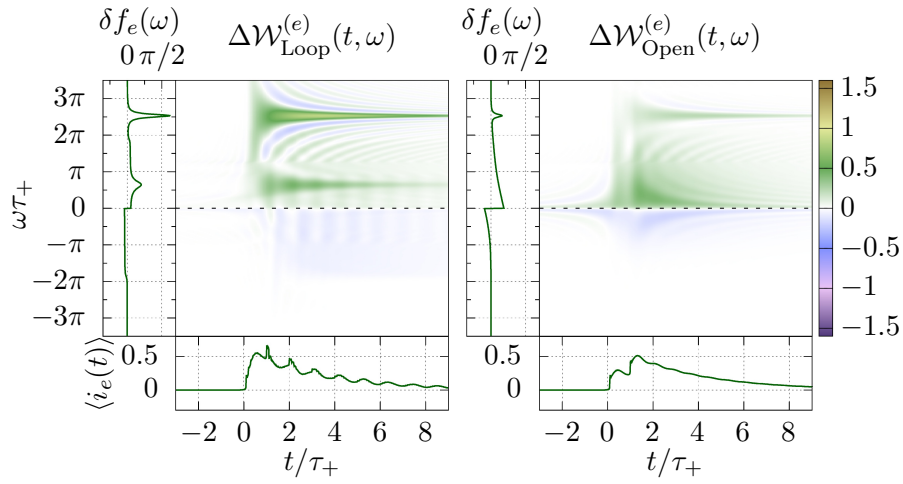

Figure 3.19: Same as figure 3.18 for an incoming excitation above the resonance energy, $\omega_0\tau_+ = 5\pi/2$. Energy relaxation involves the emission of electron/hole pairs at the resonance energy, leading to a second peak in the energy distribution. We have a clear difference in the two decoherence scenarii.

decoherence than in the presence of an open second channel.

To be a bit more quantitative on these discussions, we can of course look at the expected HOM signals for all these excitations, and check whether or not we are protected against decoherence. This is what is displayed on figure 3.20. We clearly see that the HOM dips for wavepackets propagating along a closed inner channel are deeper than their opened environment counterparts, meaning that less decoherence has occured during their propagation. In the specific case of the low-energy wavepacket emitted below the first resonance, we even recover a dip going down close to 0, denoting a quasi-complete protection from decoherence. In theory, the setups we are interested in should therefore be good candidates for decoherence protection. Yet, we need to ask ourselves whether they can be built in a real experiment, specifically in terms of loop sizes.

Can we imagine a possible geometry in which Landau excitations such as the one emitted by a single-electron source would be protected against decoherence? This is what we are going to discuss in the forthcoming section.

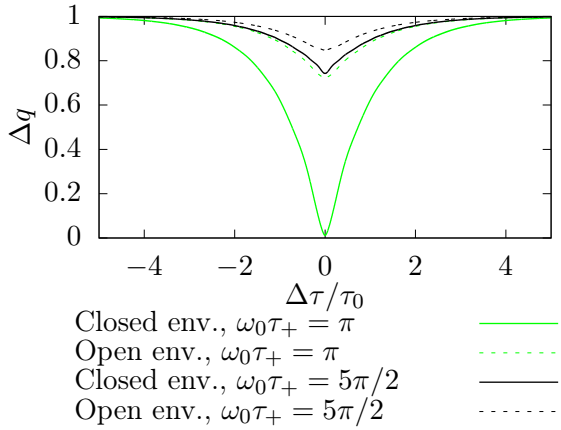

Figure 3.20: Results of an Hong-Ou-Mandel experiment for the 4 Wigner distributions presented in figures 3.18 and 3.19 . The greater depth of the HOM dip for the loop environment proves that closing the environment on itself provides a net advantage compared to the open case. Specifically, in the case where the excitation is emitted below the first level in the loop ($\omega\tau_+ = \pi$), we see a dip going nearly all the way down to 0, which denotes a quasi-complete protection from decoherence.

A realistic sample proposal

One may naively think that loops smaller than the size of dots used to emit the excitation would be needed, which seems unreasonable experimentally. Luckily, previous experimental studies [156] have shown that the speed of electronic excitations in top-gated regions of the electron gas are smaller than the "free" velocity, a fact that can be checked using available experimental data on the energies of the quantum dot. The energy $\hbar\omega_0$ of Landau particles emitted by the dot used in [OP3] is around 60 µeV, the size of the dot being 2 µm, leading to a relevant velocity in gated region of the 2DEG $v^{\text{gate}} \sim 5.8 \times 10^4\,\text{m}\,\text{s}^{-1}$, whereas the velocity in chemically defined edge channels, $v^{\text{chem.}}$ is around $1 \times 10^5\,\text{m}\,\text{s}^{-1}$. The dwelling time of excitations in the dot is $\tau_0 \simeq 100\,\text{ps}$, leading to a typical width in energy of about 1/10th of the injection energy. Consequently, a safe limit for blocking decoherence would be to have a loop such that $\omega_0(\tau_+ + \tau_L) < 3\pi/2$. The edge magnetoplasmon modes populated within the incoming electronic excitations would then have their energies below the resonance, even when considering the resonance width.

A sample design with a loop of total size 4 µm is sketched in figure 3.21. Such a size may be available experimentally, and we predict that this design leads to protection against decoherence for the single-electron excitations we are interested in. Of course, by tuning the dot parameters for emitting excitations at two times lower energies, decoherence protection would still be possible even with two times larger loops.

The design presented here would allow a test of decoherence protection for single-electron excitations emitted by the mesoscopic capacitor driven by square pulses. Electronic decoherence and relaxation of energy resolved single-electron excitations being stronger than for an out of equilibrium distribution generated by a biased QPC, such an experiment would provide a stronger test of the potential of sample design for decoherence protection.

3.4 Interaction without an environment : the $\nu = 1$ case

One of the commonly asked question when discussing electronic decoherence within quantum Hall edge channels is "Why don't you work at $\nu = 1$? Surely, without the second channel acting as an environment,

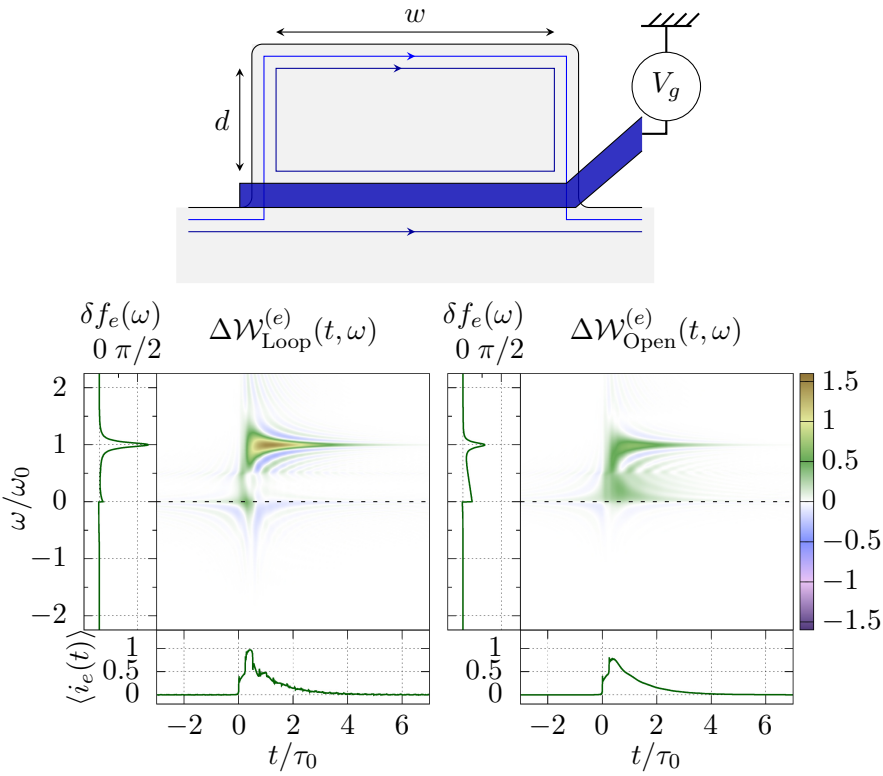

Figure 3.21: *Top*: a possible experimental design for testing decoherence control on a Landau excitation. Here, the 2DEG defines a cavity delimited by a top gate shifting the electron density so that only the outer edge channel can pass through. This creates a region with a closed inner channel. The single-electron source as well as the QPC of the HOM probe should be located close to the loop. The loop corresponds to $\tau_+ = (w+2d)/v_+^{\mathrm{chem.}}$ and $\tau_L = w/v_F^{\mathrm{gate}}$, where $v_+^{\mathrm{chem.}}$ denotes the speed of the slow mode in chemically defined edge channels, whereas v_F^{gate} is the Fermi velocity in an edge channel propagating along a metallic gate. *Bottom*: outgoing Wigner functions when $w = 1.5\,\mu\mathrm{m}, d = 0.5\,\mu\mathrm{m}$ for an incoming excitation with parameters $\omega_0\tau_0 = 10$ and $\tau_0 = 100\,\mathrm{ps}$. The velocities are $v_+^{\mathrm{chem.}} = 1\times10^5\,\mathrm{m\,s^{-1}}$ and $v_F^{\mathrm{gate}} = 5.8\times10^4\,\mathrm{m\,s^{-1}}$. *Left*: Case where the gates let the outer channel through, making it interact with a cavity. *Right*: Case where the gate closing the loop is used to either let both channels through or none (times of flight are equivalent in those two cases). Decoherence would be far more important in such cases where the inner channel is not closed on itself.

decoherence should be much less important, right?"

There are several answers to this important and natural question. In a real experiment, having two channels close to each other leads to a strong coupling between them that effectively screens other sources of decoherence, allowing a better understanding of decoherence mechanisms compared to an experiment in which uncontrolled capacitive couplings to nearby conductors, metallic gates or even bulk degrees of freedom would occur. In particular, the $\nu = 1$ case is often dissipative precisely because bulk degrees of freedom carry some energy away.

But, even leaving dissipation aside, discussing systems for which the scattering matrix is a simple transmission coefficient $\mathrm{T}(\omega)$ with modulus equal to one has its own interest. In such a case, the many body state does not decohere and electronic decoherence is due to the influence of all other electrons on the one injected by the single electron source. But in this situation, because electrons are identical quantum particles, we cannot separate the system and the environment. Therefore, this situation is a case study for understanding how quantum information initially stored within a single particle state spreads into many body correlations. The objective of the current section is therefore to study this interesting problem using a semi-realistic model for $\nu = 1$ systems. As we shall see, this will also shed some light on the role of the material used to perform electron quantum optics experiments.

3.4.1 Long-range interaction in a single channel

Let us first derive an exact expression for the edge magnetoplasmon transmission coefficient in the $\nu = 1$ case in a simple model. We describe the effective unscreened long-range intrachannel interaction within a finite length region of size l by assuming that electrons within the interaction region feel an electric potential $U(x,t)$ given by a capacitive coupling inside the whole region:

$$U(x,t) = \begin{cases} 0 & \text{if } x \notin \left[-\frac{l}{2}, \frac{l}{2}\right] \\ \frac{1}{C}\int_{-\frac{l}{2}}^{\frac{l}{2}} n(y,t)\mathrm{d}y & \text{else} \end{cases} \tag{3.46}$$

where the excess density of charges n is itself expressed in terms of the bosonic field ϕ through equation (3.1). Equation (3.2) can then be recasted as a closed equation on ϕ expressed in the frequency domain as

$$\left(-\mathrm{i}\omega + v_\mathrm{F}\partial_x\right)\phi(x,\omega) = \frac{e^2}{hC}\left(\phi\left(-\frac{l}{2},\omega\right) - \phi\left(\frac{l}{2},\omega\right)\right). \tag{3.47}$$

Expressing $\phi(x,\omega)$ as $\mathrm{e}^{\mathrm{i}\omega x/v_\mathrm{F}}\varphi_\omega(x)$ leads to

$$\partial_x\varphi_\omega(x) = \frac{e^2}{v_\mathrm{F}hC}\mathrm{e}^{-\mathrm{i}\omega x/v_\mathrm{F}} \left(\mathrm{e}^{-\mathrm{i}\omega l/(2v_\mathrm{F})}\varphi_\omega\left(-\frac{l}{2}\right) - \mathrm{e}^{\mathrm{i}\omega l/(2v_\mathrm{F})}\varphi_\omega\left(\frac{l}{2}\right)\right) \tag{3.48}$$

which can be integrated over the whole interaction region to give us a relation between $\varphi_\omega\left(-\frac{l}{2}\right)$ and $\varphi_\omega\left(\frac{l}{2}\right)$. Finally, the solution reads

$$\phi\left(\frac{l}{2},\omega\right) = \mathrm{T}(\omega)\phi\left(-\frac{l}{2},\omega\right) \tag{3.49}$$

where

$$\mathrm{T}(\omega) = \mathrm{e}^{\mathrm{i}\omega l/v_\mathrm{F}}\frac{1+A(\omega,l)\mathrm{e}^{-\mathrm{i}\omega l/(2v_\mathrm{F})}}{1+A(\omega,l)\mathrm{e}^{\mathrm{i}\omega l/(2v_\mathrm{F})}} \tag{3.50a}$$

$$A(\omega,l) = \frac{4e^2/C}{hv_\mathrm{F}/l}\,\mathrm{sinc}\left(\frac{\omega l}{2v_\mathrm{F}}\right). \tag{3.50b}$$

We recognize in $A(\omega,l)$ the kinetic energy scale hv_F/l as well as the dimensionless ratio $\alpha = e^2l/Chv_\mathrm{F}$ between the electrostatic energy e^2/C and this kinetic energy scale. The dimensionless ratio α quantifies the strength of Coulomb interactions in this system. Note that, at least for sufficiently long edge channels, this coupling constant does not depend on the length l since C also scales as l.

As expected, the transmission coefficient $\mathrm{T}(\omega)$ we just recovered is of modulus 1, since no energy can be lost in a $\nu = 1$ setup without any dynamical environment. The quantity of interest is therefore the phase of $\mathrm{T}(\omega)$.

In the limit where Coulomb interaction effects can be neglected ($\alpha \to 0$), $\mathrm{T}(\omega) = \mathrm{e}^{\mathrm{i}\omega l/v_\mathrm{F}}$ showing that the bare Fermi velocity is recovered. The opposite limit of ultrastrong Coulomb interactions ($\alpha \to \infty$) leads to $\mathrm{T}(\omega) = 1$: the edge magnetoplasmon velocity is infinite as expected since the electromagnetic disturbance is then propagated instantaneously (*i.e.* at the speed of light) across the interaction region. At a fixed finite and non-zero value of the coupling α, the edge magnetoplasmon velocity tends to $v_\infty = v_\mathrm{F}$ when $\omega l/v_\mathrm{F} \gg 1$. At low frequency, we find that the time of flight of edge magnetoplasmons is renormalized, thus leading to an increased renormalized plasmon velocity

$$\frac{v_0}{v_\infty} = 1 + \frac{4e^2/C}{hv_\infty/l} \tag{3.51}$$

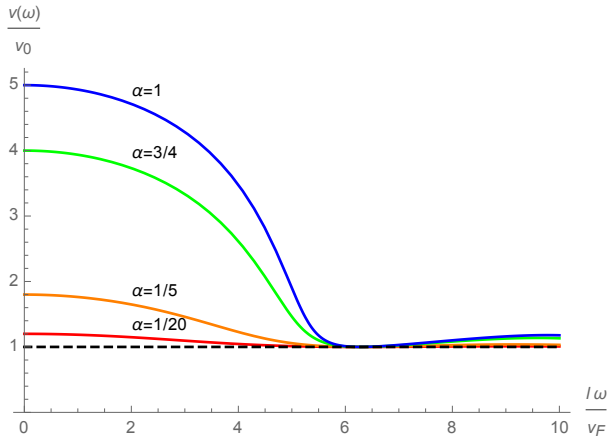

Figure 3.22: Velocity $v(\omega)/v_0$ corresponding to $\mathrm{T}(\omega) = \exp(\mathrm{i}\omega l/v(\omega))$ given by equation (3.50) in terms of $\omega l/v_F$ for $\alpha = 1/20$ (graphene), $\alpha = 1/5$, $\alpha = 3/4$ (GaAs) and $\alpha = 1$.

compared to the high frequency velocity. As can be seen on figure 3.22, the edge magnetoplasmon velocity $v(\omega)$ therefore decreases from $v_0 = (1 + 4\alpha)v_\mathrm{F}$ to its asymptotic value $v_\infty = v_\mathrm{F}$, showing some mild oscillations that arise from the sharp position dependence of the interaction potential at the boundary of the interaction region.

We expect a more realistic model of intra-channel interactions to lead to a qualitatively similar but smoother behavior of $v(\omega)$. Key features are the two different asymptotic velocities v_0 and v_∞ in the limits $\omega \to 0$ and $\omega \to +\infty$. The infrared velocity v_0 is the velocity of low energy edge magnetoplasmon modes and should therefore be called the plasmon velocity. Due to Coulomb interactions, it is expected to be higher than the velocity of high-energy excitations which do not experience interactions for a long time. Reasonable models for $v(\omega)$ should thus interpolate between v_0 and v_∞ with $v_0 > v_\infty$ and we shall denote by ω_c the crossover scale. However, the relation between $\mathrm{T}(\omega)$ and the finite-frequency admittance combined with the positive reality condition (3.8) severely constrains the general form of $\mathrm{T}(\omega)$. As explained in the Appendix E of our recent paper [OP1], it indeed rules out most of the simple phenomenological expressions for the edge magnetoplasmon velocity $v(\omega)$, and that is why we will stick with our long-range model for most of the results presented here: it can indeed be explicitely checked that this model leads to a transmission coefficient that satisfies the phys-

ical constrains.

Estimating α

Motivated by experiments, let us estimate an order of magnitude of the ratio α. First of all, C being the capacitance of an interaction region which is roughly similar to a 1D wire, we have for large l, that is when boundary effects are small, $C \simeq 2\pi\varepsilon_0\varepsilon_r l$ up to a geometrical factor. As annouced before, α does not depend on l but behaves as [65]

$$\alpha \simeq \frac{\alpha_{\text{qed}}}{\pi\varepsilon_r} \times \frac{c}{v_{\text{F}}} \times (\text{Geometrical Factor}) \tag{3.52}$$

where α_{qed} denotes the fine-structure constant, ε_r the relative permittivity of the material and v_{F} the bare Fermi velocity. Therefore, the choice of material could have a big impact on the coupling constant, and consequently on electronic decoherence in $\nu = 1$ systems. We will focus on two types of materials in this manuscript in order to keep things simple: GaAs and graphene.

For GaAs, one usually estimates $v_{\text{F}} \simeq 10^5\,\text{m/s}$ and $\varepsilon_r \simeq 10$, thus leading to

$$\alpha \simeq 0.75 \times (\text{Geometrical Factor}) \tag{3.53}$$

Assuming a geometrical factor of order 1, this gives a velocity for low-energy magnetoplasmons of the order of $v_0 \sim 4 \times 10^5\,\text{m/s}$ which is compatible to what has been observed in $\nu = 2$ edge channel systems by Kamata et al. [91]. However, let us remind that the edge magnetoplasmon velocity depends on the details of the electric potential seen by electrons near the edge of the 2DEG and therefore of the design and manufacturing of the sample. This is precisely what is used in the above reference to modulate it by polarising gates, or what we used in section 3.3.2 for a realistic decoherence protection sample design.

In the case of graphene, a common estimation for the Fermi velocity is of the order of $v_{\text{F}} \simeq 1 \times 10^6\,\text{m/s}$ and $\varepsilon_r \simeq 14$ [126] thus leading to

$$\alpha \simeq 0.054 \tag{3.54}$$

when using a geometrical factor equal to unity. The coupling constant is much lower, leading to $v_0/v_{\text{F}} \simeq 1.2$. Let us stress that, as far as we know, no direct measurement of v_{F} in quantum Hall edge channels of graphene have been performed yet. Nevertheless, if this commonly discussed value is confirmed, this would put graphene in a totally different coupling range than GaAs.

3.4.2 High-energy decoherence and relaxation

To start our discussion of electronic decoherence, we begin by using a very crude physical picture for a single edge channel in which we have a low-frequency ($\omega \lesssim \omega_c$) edge magnetoplasmon velocity v_0 greater than the high frequency ($\omega \gtrsim \omega_c$) velocity v_∞. This is an oversimplification of the model presented before, but it presents the key feature of having distinct high and low energy edge magnetoplasmon velocities.

Since for $\omega \gtrsim \omega_c$, edge magnetoplasmons travel at the velocity v_∞, decoherence only arises from the effective edge magnetoplasmon scattering phase $\widetilde{\mathrm{T}}(\omega) = \mathrm{T}(\omega)\mathrm{e}^{-\mathrm{i}\omega\tau_\infty}$ which is roughly 1 for $\omega \gtrsim \omega_c$ and $\mathrm{e}^{-\mathrm{i}\omega\Delta\tau}$ for $\omega \lesssim \omega_c$, where $\Delta\tau = \tau_\infty - \tau_0$ denotes the difference of time of flights between high and low energy edge magnetoplasmons. As interactions have an effective bandwidth $\sim \omega_c$, creation of electron/hole pair excitations happens close to the Fermi level (within one to a few ω_c). Consequently, for electronic excitations injected at a much higher energy, the corresponding low energy edge magnetoplasmon modes can be viewed as an effective distinct environment for the high-energy electronic excitations [32].

At lower energies, electronic decoherence also arises from the ω-dependence of the edge magnetoplasmon velocities but, at low enough frequency, a perturbative approach in $\omega R_\mathrm{K} C_\mu$ can be used. This will be the point of section 3.4.3. In the following, we shall first explore the high energy limiting regime of electronic decoherence.

Elastic scattering and relaxation tail

For a single-electron excitation injected at high energy, the contribution to electronic coherence $\varphi_e(t)\,\varphi_e^*(t')$ picks up an effective decoherence coefficient $D(t-t')$:

$$\Delta\mathcal{G}^{(e)}_{\mathrm{WP}}(t|t') \simeq \varphi_e(t)\,\varphi_e^*(t')\,D(t-t')\,. \tag{3.55}$$

At $\nu = 1$, this coefficient is equal to the overlap $\langle g(t')|g(t)\rangle$ of the electron/hole pair clouds generated by Coulomb interactions:

$$D(\tau) = \exp\left(\int_0^{+\infty} |1-\widetilde{\mathrm{T}}(\omega)|^2 \left(\mathrm{e}^{\mathrm{i}\omega\tau}-1\right)\frac{\mathrm{d}\omega}{\omega}\right). \tag{3.56}$$

This description is analogous to the one used in the weak-coupling description of dynamical Coulomb blockade across a tunnel junction [84].

The relaxation kernel

$$\widetilde{D}(\omega') = \int_{-\infty}^{+\infty} \mathrm{e}^{-\mathrm{i}\omega\tau} D(\tau)\,\mathrm{d}\tau\,. \tag{3.57}$$

can then be decomposed into an elastic and an inelastic part: $\widetilde{D}(\omega') = 2\pi(Z_\infty\delta(\omega') + d(\omega'))$ where

$$Z_\infty = \exp\left(-\int_0^{+\infty} |1-\widetilde{\mathrm{T}}(\omega)|^2 \frac{\mathrm{d}\omega}{\omega}\right) \tag{3.58}$$

is nothing but the high-energy limit of the elastic scattering probability $|\mathcal{Z}(\omega)|^2$. The inelastic part $d(\omega)$ describes electronic relaxation: it represents the probability that the electron has lost energy ω. It is determined by the integral equation

$$\begin{aligned}\omega\, d(\omega) &= |1-\widetilde{\mathrm{T}}(\omega)|^2 \\ &\quad + \int_0^{\omega} |1-\widetilde{\mathrm{T}}(\omega')|^2 d(\omega-\omega')\,\mathrm{d}\omega'\end{aligned} \tag{3.59}$$

which can readily be solved on a computer using the inital condition that $d(\omega \to 0^+) \to \lim_{\omega\to 0^+}(|1-\widetilde{\mathrm{T}}(\omega)|^2/\omega)$. It can also be expressed as a formal series corresponding to the various processes involving the emission of an increasing number of pairs of electron/hole excitations, exactly the same structure as in the dynamical Coulomb blockade theory. With these notations, the elastic part of the outgoing Wigner function is well separated from the inelastic part:

$$\Delta\mathcal{W}^{(e)}_{\mathrm{WP}}(t,\omega) = Z_\infty \mathcal{W}_{\varphi_e}(t,\omega) \tag{3.60a}$$

$$+ \int_0^{\omega} d(\omega')\mathcal{W}_{\varphi_e}(t,\omega+\omega')\,\mathrm{d}\omega' \tag{3.60b}$$

where $\mathcal{W}_{\varphi_e}(t,\omega)$ denotes the Wigner function associated to the incoming wavepacket φ_e. The incoming electron loses energy through electron/hole pair creation within a few $\hbar\omega_c$ of the Fermi sea.

In order to make this discussion a bit more visual, figure 3.23 displays the elastic scattering probability $|\mathcal{Z}(\omega)|^2$ in the specific long-range model from equation (3.50), as well as its asymptotic high energy limit Z_∞, with respect to coupling strength. As could be expected, stronger coupling leads to a vanishing elastic scattering probability, meaning that high-energy excitation will never go through an interaction region with strong coupling without experiencing some kind of decoherene.

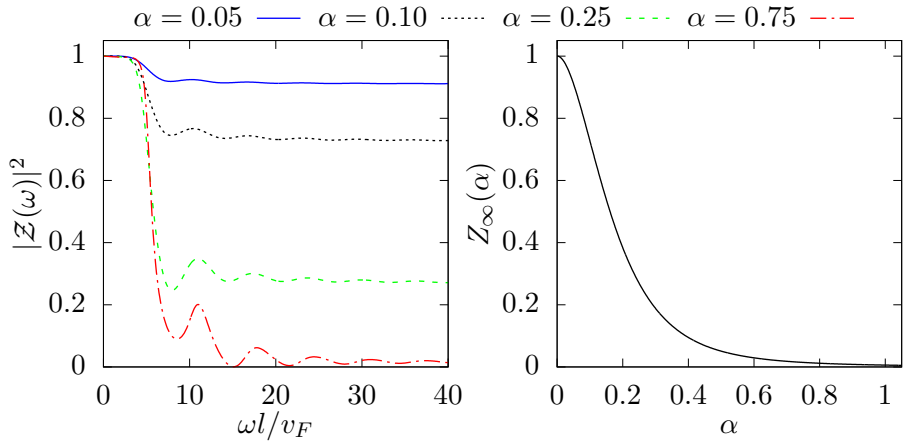

Figure 3.23: *Left*: Elastic scattering probability for a single-electron excitation as a function of $\omega l/v_\mathrm{F}$ for the long-range interaction model given by equation (3.50), for different values of the coupling constant α. *Right*: Asymptotic elastic scattering probability for high energy electrons $Z_\infty(\alpha)$ given by equation (3.58) as a function of the coupling constant α for that same interaction model.

Of course, for our approach to be valid, we need to show that for high-energy electrons the amount of energy dissipated through electron/hole pair creations is small compared to their injection energy. With these first results, we expect it to hold at small coupling only, but we are going to search for a more quantitative vision now.

Dissipated energy

In order to study the validity of our approach, we shall assume that the spectral weight of the incoming electron as well as of the contribution $\mathcal{G}^{(e)}_\mathrm{WP}$ to the outgoing coherence are well above the vicinity of the Fermi level.

The incoming average energy comes from the injected electron and is equal to

$$E_\mathrm{in} = \hbar \int_0^{+\infty} |\varphi_e(\omega)|^2 \, \omega \, \frac{\mathrm{d}\omega}{2\pi v_\mathrm{F}} \,. \tag{3.61}$$

The outgoing average energy then consists of two parts: the energy carried by the injected electron which has flewn across the interaction region either elastically or inelastically, and the energy of electron/hole

excitations created by its passage through the region:

$$E_{\text{out}}^{(e)} = Z_\infty E_{\text{in}} \tag{3.62a}$$

$$+ \hbar \int_{(\mathbb{R}^+)^2} |\varphi_e(\omega)|^2 \, (\omega - \omega') d(\omega') \, \mathrm{d}\omega' \frac{\mathrm{d}\omega}{2\pi v_{\text{F}}} \, . \tag{3.62b}$$

The first line corresponds to elastic scattering and the second line to inelastic processes in which the electron has fallen down from $\hbar\omega$ to $\hbar(\omega - \omega')$. Because of our working hypothesis, we can safely extend the integrals to $+\infty$ safely as the relaxation tail is well above the Fermi level. We then use that $\int_0^{+\infty} d(\omega') \, \mathrm{d}\omega' = 1 - Z_\infty$ and the normalization condition of the wavepacket to rewrite this as

$$E_{\text{out}}^{(e)} = E_{\text{in}} - \hbar \int_0^{+\infty} \omega' d(\omega') \, \mathrm{d}\omega' \, . \tag{3.63}$$

Energy conservation, which is true on average, shows that the dissipated energy in electron/hole pair creation is equal to

$$E_{\text{out}}^{(\text{diss})} = \hbar \int_0^{+\infty} \omega d(\omega) \, \mathrm{d}\omega \, . \tag{3.64}$$

Recognizing that $\int_0^{+\infty} \omega d(\omega) \mathrm{d}\omega$ corresponds to the derivative of the decoherence coefficient $D(\tau)$ when $\tau \to 0^+$ leads to

$$E_{\text{out}}^{(\text{diss})} = \hbar \int_0^{+\infty} |1 - \tilde{\mathrm{T}}(\omega)|^2 \, \mathrm{d}\omega \, . \tag{3.65}$$

In the particular case of the transmission coefficient given by equation (3.50), the dissipated energy is finally given by

$$E_{\text{out}}^{(\text{diss})} = \frac{h v_{\text{F}}}{\pi \, l} \int_0^{+\infty} \frac{64\alpha^2 \sin^4(u) \, \mathrm{d}u}{(u + 2\alpha \sin(2u))^2 + 16\alpha^2 \sin^2(u)} \tag{3.66}$$

which converges both in the UV and the IR.

Figure 3.24 presents the numerical evaluation of the dissipated energy in units of hv_0/l, where $v_0 = (1 + 4\alpha)v_{\text{F}}$ is the low energy edge magnetoplasmon velocity in this model. We observe that it saturates to 1 at large coupling. The finiteness of the dissipated energy validates a posteriori that the high-energy description of electronic decoherence is valid as long as the average energy of the incoming excitation is large compared to $\alpha h v_0/l$.

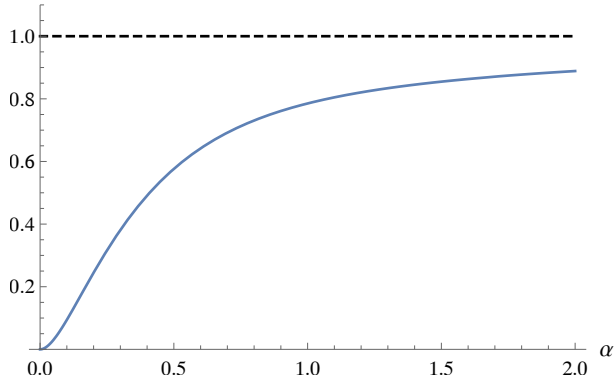

Figure 3.24: Dependence of the average energy dissipated by an incoming high-energy electron, $E_{\rm out}^{\rm (diss)}(\alpha, hv_{\rm F}/l)$, with respect to the coupling constant α, in units of hv_0/l, in the specific case of the long-range model given by equation (3.50). In that case, $E_{\rm out}^{\rm (diss)}$ is given by equation (3.66).

As a final check, one can rederive equation (3.65) by considering the reduced density operator for the low energy electron/hole pair excitations. When assuming that even after relaxation, the wavepacket remains well separated from the Fermi sea, one can use $\langle \psi(t_-)\psi^\dagger(t_+)\rangle_{\rm F} \simeq v_{\rm F}^{-1}\delta(t_+ - t_-)$ in the modified vacuum term from equation (3.27a). This means that $\mathcal{G}_{\rm MV}^{(e)}(t|t')$ can be approximated by an expression which corresponds to the statistical mixture of states $|g(t)\rangle$ ponderated by $|\varphi_e(t)|^2$. This naturally comes from the physical image of the incident electron emerging from the interaction in a quantum superposition of the coherent electron/hole pair clouds $|g(t)\rangle$ attached to the electron being at position $v_{\rm F}t$. Two different positions $v_{\rm F}t$ and $v_{\rm F}t'$ of the electron being perfectly distinguishable, what comes out is the statistical mixture of coherent electron/hole pair clouds for the low energy edge magnetoplasmon modes. Computing the average energy stored in this statistical mixture precisely leads to (3.65) since all the states $|g(t)\rangle$ carry the same average energy.

3.4.3 Low-energy decoherence

Let us now turn ourselves towards the opposite limit, that means to low-energy decoherence. In this limit, we can study the interaction region as an effective electric dipole. Following the tracks of M. Büttiker [128], we can look for a simple description of this linear dipole in terms of discrete

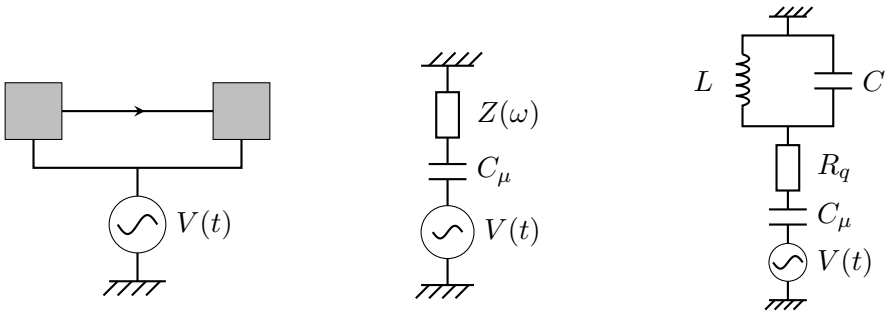

Figure 3.25: *Left*: Effective dipole associated with the interaction region. *Middle*: Equivalent effective ZC-circuit at low-frequency in the generic case. *Right*: The simplest non-dissipative circuit that can be built. The resistive part of $Z(\omega)$ is the relaxation resistance $R_q = R_\mathrm{K}/2$ and its imaginary part comes from an LC circuit.

circuit elements. This simple low frequency description is interesting for the experimentalists since it describes the frequency dependance of the edge magnetoplasmon transmission amplitude by a few parameters which have a simple physical interpretation. Then, we can study single electron decoherence using this effective description which is, per construction, well suited to the low frequency domain[9].

Discrete elements circuit description

At low frequency, the interaction region effective linear electrical dipole does not respond to a DC bias and can thus be described in terms of a frequency dependent admittance $G(\omega)$ in series with a capacitor C_μ as shown in figure 3.25. Using the relation $\mathrm{T}(\omega) = 1 - R_\mathrm{K} G(\omega)$, the transmission amplitude $\mathrm{T}(\omega)$ can be expressed in terms of the impedance $Z(\omega)$ as

$$\mathrm{T}(\omega) = \frac{1 + \omega C_\mu \mathrm{Im}\left(Z(\omega)\right) + \mathrm{i}\omega C_\mu (R_\mathrm{K} - \mathrm{Re}\left(Z(\omega)\right))}{1 + \omega C_\mu \mathrm{Im}\left(Z(\omega)\right) - \mathrm{i}\omega C_\mu \mathrm{Re}\left(Z(\omega)\right)}\,. \tag{3.67}$$

Consequently, $\mathrm{T}(\omega)$ is a pure phase, corresponding to non-dissipative processes, if and only if $\mathrm{Re}\left(Z(\omega)\right) = R_\mathrm{K}/2$ at all frequencies. We can then write

$$\mathrm{T}(\omega) = \frac{1 + \mathrm{i}\alpha(\omega)}{1 - \mathrm{i}\alpha(\omega)} = \exp\left(2\mathrm{i}\arctan\left(\alpha(\omega)\right)\right) \tag{3.68}$$

[9]Here low frequencies can go up to a few gigahertz.

where

$$\alpha(\omega) = \frac{\omega R_{\mathrm{K}} C_\mu}{2} \frac{1}{1 + \omega C_\mu \mathrm{Im}\left(Z(\omega)\right)} . \tag{3.69}$$

With our conventions, the reactance $\mathrm{Im}\left(Z(\omega)\right)$ is a strictly decreasing function of ω [47]. Since, by definition, the electrochemical capacitance C_μ contains the low-frequency divergence of the ZC circuit, it is expected to be regular at low frequency, starting with a zero at $\omega = 0$ and then alternating poles and zeroes. A suitable low-frequency expansion of $\mathrm{T}(\omega)$ can then be obtained using a Cauer form of circuit synthesis [24, 21], which leads to a continuous fraction expansion of the finite-frequency admittance. Starting from any $\mathrm{T}(\omega)$, we could therefore find a circuit representing it up to any order.

What we are going to do is the inverse process. Starting from a simple circuit at low order, we will recover the first orders in the development of $\mathrm{T}(\omega)$ for the specific case of long-range interaction, in order to study its low energy behaviour. This simplest case corresponds to the circuit depicted on the right panel of figure 3.25. It leads to

$$\alpha(\omega) = \frac{\omega R_{\mathrm{K}} C_\mu}{2} \frac{1 - \omega^2 LC}{1 - \omega^2 L(C + C_\mu)} . \tag{3.70}$$

Expanding $2 \arctan\left(\alpha(\omega)\right)$ in powers of $\omega R_{\mathrm{K}} C_\mu$ then leads, up to order $(\omega R_{\mathrm{K}} C_\mu)^5$, to

$$\mathrm{T}(\omega) = 1 + \mathrm{i}\omega R_{\mathrm{K}} C_\mu - \frac{1}{2}(\omega R_{\mathrm{K}} C_\mu)^2 \tag{3.71a}$$

$$+ \mathrm{i}\left[\frac{L/R_{\mathrm{K}}}{R_{\mathrm{K}} C_\mu} - \frac{1}{4}\right](\omega R_{\mathrm{K}} C_\mu)^3 \tag{3.71b}$$

$$- \left[\frac{L/R_{\mathrm{K}}}{R_{\mathrm{K}} C_\mu} - \frac{1}{8}\right](\omega R_{\mathrm{K}} C_\mu)^4 \tag{3.71c}$$

$$+ \mathrm{i}\left[\left(1 + \frac{C}{C_\mu}\right)\left[\frac{L/R_{\mathrm{K}}}{R_{\mathrm{K}} C_\mu}\right]^2 + \frac{1}{16} - \frac{3}{4}\frac{L/R_{\mathrm{K}}}{R_{\mathrm{K}} C_\mu}\right](\omega R_{\mathrm{K}} C_\mu)^5 . \tag{3.71d}$$

Being described by two parameters (L and C) besides C_μ and $R_q = R_{\mathrm{K}}/2$, this circuit provides an expansion of the phase of $\mathrm{T}(\omega)$ up to order $(\omega R_{\mathrm{K}} C_\mu)^5$. In order to capture the low-frequency behavior of the transmission to the next non trivial orders (7 and 9), we would need to go one step further in the Cauer form of the circuit. This would correspond to adding another LC impedance in series with the capacitor C. This process, called circuit synthesis, can then be iterated to reconstruct the full ω dependence of any transmission coefficient.

Perturbative expansion

Let us now discuss electronic decoherence in the low frequency domain, trying to make use of its analytical behavior. Since we are at low energy, the relevant base velocity is v_0 and it is convenient to define the effective transmission amplitude as $\mathring{\mathrm{T}}(\omega) = \mathrm{T}(\omega)\mathrm{e}^{-\mathrm{i}\omega\tau_0}$ so that the deviation from $\mathring{\mathrm{T}}(\omega) = 1$ for $0 < \omega \lesssim \omega_c$ is small.

If we had $\mathring{\mathrm{T}}(\omega) = 1$ for $\omega \lesssim \omega_c$, the electronic excitation would not experience decoherence for the part which is located below ω_c: it would simply move at the plasmon velocity v_0. This is consistent with the high-energy picture discussed in section 3.4.2: although a high-energy electronic excitation moves forward at the velocity v_∞ together with its relaxation tail, the electron/hole pairs created close to the Fermi level move at the plasmon velocity v_0. Therefore, in order to account for the real frequency dependence of $\mathrm{T}(\omega)$, the idea is to perform a perturbative expansion in terms of $\omega\tau_0$ of the rescaled edge magnetoplasmon transmission coefficient $\mathring{\mathrm{T}}(\omega)$.

At low frequency, this coefficient is a pure phase that depends analytically on the frequency. The linear term in the phase being taken out, it is of the form

$$\mathring{\mathrm{T}}(\omega) = \exp\left(\mathrm{i}\sum_{k\geq 2}\alpha_k(\omega\tau_0)^k\right) \tag{3.72}$$

where τ_0 is a typical time scale of the problem and α_k are dimensionless couplings. Note that only odd powers of $\omega\tau_0$ need to be considered because we know from the link between transmission and admittance that $\mathrm{T}(\omega)^* = \mathrm{T}(-\omega)$. Using this form for the expansion of the phase, we can derive the low energy behaviour of several interesting physical quantities. In particular, we will be interested in the inelastic scattering probability $\sigma_{\mathrm{in}}(\omega) = 1 - |\mathcal{Z}(\omega)|^2$. To do this, we are going to expand perturbatively in $\omega\tau_0$ the elastic scattering amplitude

$$\mathcal{Z}(\omega) = 1 + \int_0^\omega B_-(\omega')\,\mathrm{d}\omega' \tag{3.73}$$

where

$$B_-(\omega) = \sum_{n=1}^{\infty}\frac{1}{n!}\left(\frac{\mathrm{T}(\omega)-1}{\omega}\right)^{*n}(\omega) \tag{3.74}$$

is obtained as a series of convolution powers $(\cdot)^{*n}$.

We can show that the expansion of $\mathcal{Z}(\omega)$ up to order $(\omega\tau_0)^8$ only involves the 2nd convolution power of $(1-\mathrm{T}(\omega))/\omega$, which corresponds to two edge magnetoplasmon emission processes. Processes with higher order multi-plasmon emission will only contribute to higher powers in $\mathcal{Z}(\omega)$'s expansion, and can therefore be neglected at low energy. We finally get, using the expansion of $\mathring{\mathrm{T}}(\omega)$ up to this order, the final result for the inelastic scattering probability $\sigma_{\mathrm{in}}(\omega) = 1 - |\mathcal{Z}(\omega)|^2$:

$$\sigma_{\mathrm{in}}(\omega) = \frac{11\alpha_3^2}{180}(\omega\tau_0)^6 + \frac{5\alpha_3\alpha_5}{42}(\omega\tau_0)^8 + \mathcal{O}\left((\omega\tau_0)^9\right). \tag{3.75}$$

Note that keeping only the first convolution power in the expansion would lead to

$$\sigma_{\mathrm{in}}^{(1)}(\omega) = \frac{\alpha_3^2}{18}(\omega\tau_0)^6 - \frac{7\alpha_3\alpha_5}{60}(\omega\tau_0)^8 + \mathcal{O}\left((\omega\tau_0)^9\right) \tag{3.76}$$

which is the inelastic scattering probability arising from single edge magnetoplasmon emission.

Link between the two approachs

As can be seen directly in the result of equation (3.75), in order to obtain the behaviour of the inelastic scattering probability at low energies, we only need to expand the phase of $\mathrm{T}(\omega)$ up to order 5. Yet, as we saw in equation (3.71), the simplest possible circuit – displayed on the right of figure 3.25 – corresponds to such an expansion. We can therefore relate the circuit parameters (L, C) to the family of α_k. In particular, the inductance L is directly related to the α_3 coefficient, and the capacitance C only contributes to the next order:

$$\tau_0 = R_{\mathrm{K}} C_\mu \tag{3.77a}$$

$$\alpha_3 = \frac{L/R_{\mathrm{K}}}{R_{\mathrm{K}}C_\mu} - \frac{1}{12} \tag{3.77b}$$

$$\alpha_5 = \frac{1}{80} - \frac{1}{4}\frac{L/R_{\mathrm{K}}}{R_{\mathrm{K}}C_\mu} + \left(\frac{L/R_{\mathrm{K}}}{R_{\mathrm{K}}C_\mu}\right)^2 \left(1 + \frac{C}{C_\mu}\right) \tag{3.77c}$$

This connects the inelastic scattering probability for an incoming electron to the low-frequency discrete element circuit description for the interaction region.

A complementary understanding can be obtained by relating the finite-frequency admittance to the edge magnetoplasmon's effective velocity $v(\omega)$ within the interaction region, using $\mathrm{T}(\omega) = \exp(\mathrm{i}\omega l/v(\omega))$.

The effective circuit of figure 3.25 corresponds to a low-frequency expansion of $v(\omega)$ of the form

$$\frac{v(\omega)}{v_0} = 1 + \left(\frac{1}{12} - \frac{L/R_\mathrm{K}}{R_\mathrm{K}C_\mu}\right)(R_\mathrm{K}C_\mu\omega)^2 \tag{3.78a}$$

$$- \left[\frac{C}{C_\mu}\left(\frac{L/R_\mathrm{K}}{R_\mathrm{K}C_\mu}\right)^2 - \frac{1}{12}\frac{L/R_\mathrm{K}}{R_\mathrm{K}C_\mu} + \frac{1}{180}\right](R_\mathrm{K}C_\mu\omega)^4 \tag{3.78b}$$

$$+ \mathcal{O}\left((\omega R_\mathrm{K}C_\mu)^6\right) \tag{3.78c}$$

where $R_\mathrm{K}C_\mu$ is the low-frequency time of flight l/v_0. This expansion directly connects the discrete circuit element parameters L and C to the low-frequency behavior of $v(\omega)$. The value $L = C_\mu R_\mathrm{K}^2/12$ (or, equivalently, $\alpha_3 = 0$) corresponds to a frequency dependency of the form $v(\omega) = v_0 + \mathcal{O}\left((R_\mathrm{K}C_\mu\omega)^4\right)$. For $0 \leq L < C_\mu R_\mathrm{K}^2/12$, the velocity of edge magnetoplasmons first increases quadratically at low-frequency, whereas $v(\omega)$ directly starts decreasing for $L > C_\mu R_\mathrm{K}^2/12$. Note that a higher inductance contributes to a stronger slow-down of the edge magnetoplasmons with increasing frequency, as expected for an inductive effect. The order 4 term given by equation (3.78b) describes the behavior of the plasmon velocity beyond this first order and contributes to its decrease with increasing frequency. All of this is coherent with our initial approach stating that low-energy plasmons should, in a realistic model, move faster than their high-energy counterparts.

Coming back to the electronic inelastic scattering probability given by equation (3.75), the case where $L = R_\mathrm{K}^2 C_\mu/12$ minimizes its growth: the first non zero term is at order $(\omega\tau_0)^{10}$. This reflects the fact that for $L = R_\mathrm{K}^2 C_\mu/12$, the distorsion of a percussional current pulse is minimal at low-frequencies.

When $\alpha_3 \neq 0$, the first and second non trivial orders in $\omega\tau_0$ compete as soon as $\alpha_3\alpha_5 < 0$, which means that they also compete in the expansion of the edge magnetoplasmon time of flight as a function of frequency.

Long-range interaction

Now that we have given most general results surrounding the low energy expansion of both $\mathrm{T}(\omega)$ and quantities such as the inelastic scattering probability, let us apply them to our specific long-range intra-channel interaction model from equation (3.50). Expanding the phase of this

model in powers of $\omega\tau_0$ leads to

$$\tau_0 = \frac{l}{v_0} = \frac{l}{(1+4\alpha)v_\mathrm{F}} \tag{3.79a}$$

$$\alpha_3 = \frac{\alpha}{3} \tag{3.79b}$$

$$\alpha_5 = \frac{8\alpha}{90}\left(\alpha^2 + 2\alpha - 1/8\right) \tag{3.79c}$$

with α the coupling strength. Equivalently, the discrete element circuit parameters for this interaction type are

$$R_K C_\mu = \tau_0 = l/v_0 \tag{3.80a}$$

$$\frac{L/R_K}{R_K C_\mu} = \frac{1+4\alpha}{12} \tag{3.80b}$$

$$\frac{C}{C_\mu} = \frac{1+4\alpha}{5} \tag{3.80c}$$

As expected, the low energy time of flight for the edge magnetoplasmon gives the main RC time scale of the circuit: $R_K C_\mu$. Increasing α increases the capacitance C of the first Cauer ladder element. It also increases the inductance reflecting the increase of the low frequency velocity with respect to the bare Fermi velocity: this means that electrons have more inertia than low energy edge magnetoplasmon[10]. Since this effect increases with α, the inductance which encodes kinetic inertia of the electrons has to increase.

Using these parameters, we can comment on the validity of our low energy expansion when compared to the full results plotted in figure 3.23. This is done on figure 3.26, which depicts the ratio of the full inelastic scattering probability to the perturbative expression as a function of ω. It shows that the perturbative result is only valid at very low energies, that is significantly before the drop of the elastic scattering probability, when the inelastic scattering probability is still very close to unity. Understanding the full behavior of the elastic scattering probability indeed requires a full non-perturbative approach even at weak coupling because, at higher injection energies, multiple low energy electron/hole pair emissions coexist with the emission of a single electron/hole pair of higher energy. Properly accounting for all these processes requires the full knowledge of the frequency dependance of $g(\omega)$ for which the simplest discrete element circuit description is not sufficient.

[10] Electrons are slower at equal energy.

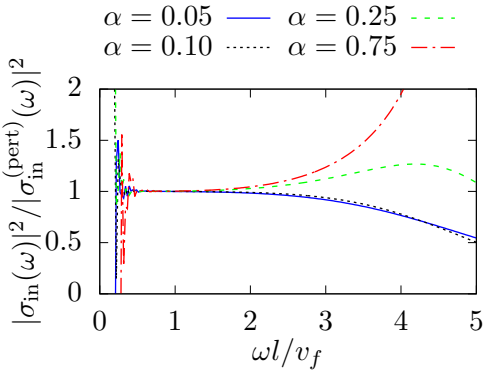

Figure 3.26: Ratio of inelastic scattering probabilities for the full model to its perturbative circuit expansion obtained in equation (3.75) at low energy. Numerical errors at small $\omega l/v_{\rm F}$ are due to the rapid decay of the dominant $(\omega l/v_{\rm F})^6$ asymptotic behavior of the inelastic scattering probability at very low energies. Remember that the full elastic scattering probability was plotted in figure 3.23.

3.4.4 Numerical results at $\nu = 1$

After this extensive discussion of the limiting regimes of decoherence in the $\nu = 1$ case, it is now time to discuss the full result for the outgoing Wigner functions associated with initial Landau excitations.

Let us start with wavepackets injected at a high energy. Figure 3.27 presents the electronic decoherence of an incoming wavepacket injected at energy $\omega_0\tau_0 = 15$, with a temporal width also equal to $l/v_{\rm F}$. In the weak-coupling case, we clearly see the separation in energy between the elastically scattered electronic excitation together with its relaxation tail at high energy, and the resulting electron/hole pairs close to the Fermi level. From the previous discussions, we know that this is expected since the elastic scattering probability is quite high at the injection energy. The temporal separation, which is a result of the difference between the hot-electron velocity v_∞ and the plasmon velocity v_0 is also clearly visible on the average electric current $\langle i_e(t)\rangle$: the sharp rise of the current corresponds to the arrival of the elastically scattered quasi-particle and $t = 0$ corresponds to propagation at the fastest velocity v_0.

By contrast, in the strong-coupling case, electronic decoherence is much stronger. The relaxation tail of the incoming excitation is visible as a sharp rise of the current which arrives later than the beginning of the

neutral electron/hole pairs cloud. As expected, the difference between the plasmon and high-energy electron velocities is also more important than in the weak-coupling case.

These results can be compared to the ones depicted in figure 3.28, which displays the electronic decoherence of an incoming wavepacket injected at $\omega_0 l/v_F = 3$, an energy lower than the previously discussed threshold (see figure 3.22 or figure 3.23: the threshold between the two velocities is around $\omega l/v_F = 2\pi$). Most of its spectral weight is below the threshold and thus, the Landau quasiparticle propagates without experiencing much decoherence in both cases. We also see that it propagates at the low energy edge magnetoplasmon velocity v_0. As expected, the incoming excitation seems less altered at weak coupling ($\alpha = 0.05$) than at strong coupling ($\alpha = 0.75$).

All this discussion confirms the following physical picture: a low energy single electron excitation will indeed propagate at the edge magnetoplasmon low energy velocity which corresponds to the $R_K C_\mu$ time scale. The fate of a high energy excitation will depend on the value of the coupling constant α and thus on the material. For a strong coupling material, the excitation will be torned between two very different velocities and will relax by creating a cloud of low energy electron/hole pair excitations. Only a small part of it will propagate at the high energy Fermi velocity. On the contrary, in a small coupling material, electronic decoherence is much weaker and the propagation of the unscattered single electron excitation will occur at the Fermi velocity.

As explained several times in this manuscript, the main tool that can be used in electron quantum optics to test robustness to decoherence is an Hong-Ou-Mandel experiment. We then expect strong and weak coupling regimes to lead to quantitatively different results in such experiments. In order to answer this question, we have computed the HOM signal in both cases. Results are shown in figure 3.29 for both injection energies and both coupling values. As was discussed when looking at the Wigner functions, theses curves confirm that weak coupling materials would lead to a stronger protection against decoherence.

3.4.5 Low vs strong coupling materials: a comment on GaAs vs Graphene

As discussed above, exfolliated graphene on a silicon oxyde surface may correspond to a weak coupling value of α and thus to much lower electronic decoherence. Moreover, provided velocities in graphene are

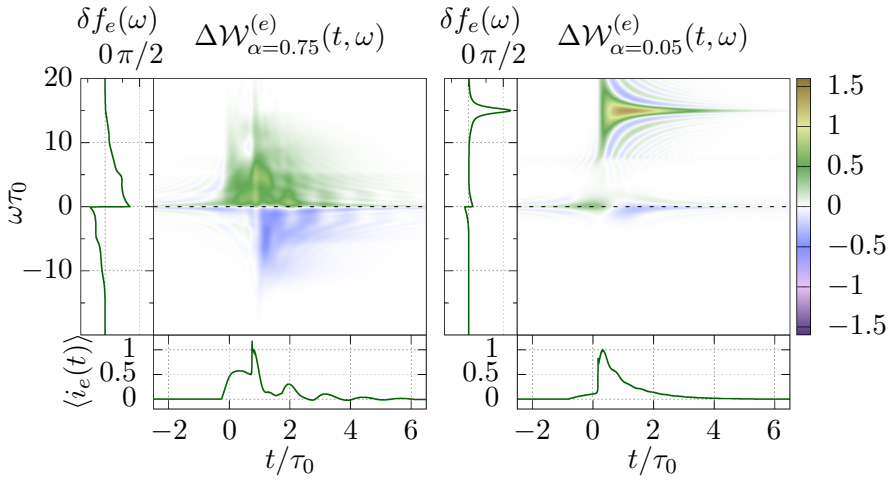

Figure 3.27: Wigner distribution function of an incoming wavepacket injected at energy $\omega_0 l/v_\mathrm{F} = 15$. *Left*: outgoing single-electron coherence for $\alpha = 0.75$. *Right*: outgoing single-electron coherence for $\alpha = 0.05$. $t = 0$ corresponds to the expected time of reception for a free propagation at the low energy velocity v_0. In the weak coupling case, we recover an elastically scattered excitation with its relaxation tail, well separated in energy from the electron/hole pairs it created close to the Fermi level. In the strong coupling case, electronic decoherence is clearly much stronger, and there is no more energy separation between the relaxation tail of the incomng excitation and the electron/hole pairs clouds. In both cases, we see a temporal separation between the arrival of the cloud around $t = 0$ and the sharp rise of current corresponding to the arrival of the relaxation tail: this is a direct signature of the difference between low- and high-energy velocities in our model.

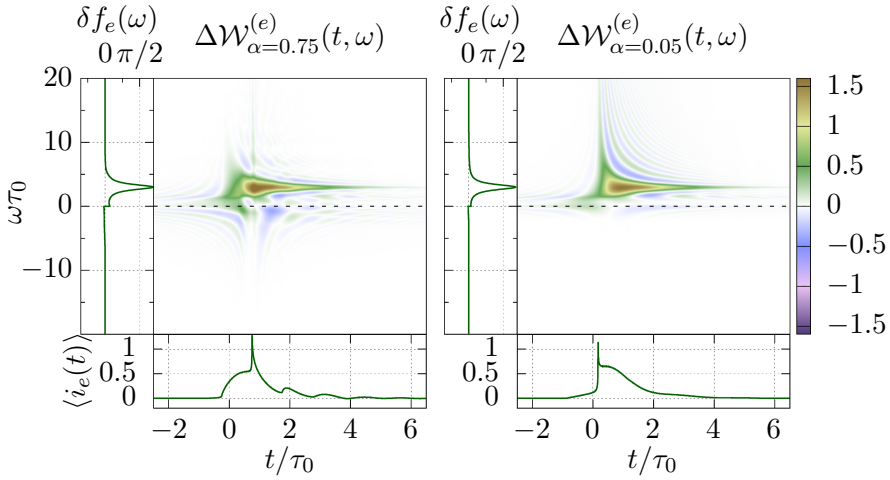

Figure 3.28: Wigner distribution function of an incoming wavepacket injected at energy $\omega_e l/v_F = 3$. *Left*: outgoing single-electron coherence for $\alpha = 0.75$. *Right*: outgoing single-electron coherence for $\alpha = 0.05$. $t = 0$ is the expected time of reception for a free propagation at the low energy velocity v_0. Contrary to figure 3.27, there is not much electronic decoherence happening for low-energy excitations, as everything pretty much moves at the low-energy velocity. Yet, we still get some peak in the current at a later time, coming from the relaxation tail associated with the small part of the incoming wavepacket that lies at high energy.

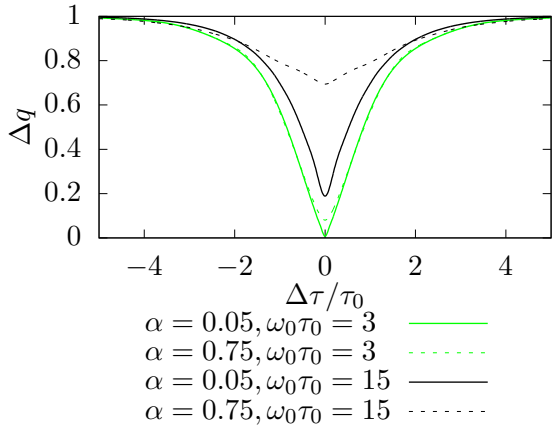

Figure 3.29: Theoretical results of an Hong-Ou-Mandel interferometry experiment obtained from the Wigner functions displayed in figures 3.27 and 3.28. As expected from the Wigner functions themselves, low energy excitations ($\omega_0\tau_0 = 3$) present a high contrast HOM dip. The results for high-energy exitations ($\omega_0\tau_0 = 15$) are clearly different between a weak coupling ($\alpha = 0.05$) and a strong coupling ($\alpha = 0.75$) material, thus providing a clear signature of the protection against decoherence offered by weak coupling materials.

much higher than in GaAs, the crossover energy between the low and high energy regimes should be much higher for fixed device dimensions. For example, a $l = 20\,\mu\text{m}$ propagation distance corresponds to $\omega/2\pi = v_F/l \simeq 500\,\text{GHz}$ for $v_F = 10^6\,\text{m}\,\text{s}^{-1}$ and to 50 GHz for $v_F = 10^5\,\text{m}\,\text{s}^{-1}$.

The single-electron source based on the mesoscopic capacitor that has been developed in GaAs generates electronic excitations at an energy comparable to this crossover scale. With our estimated parameters, strong electronic decoherence is expected for a propagation above 30 µm when injecting at an energy of the order of 40 µeV[11]. Although no single-electron source has been developed yet for graphene in the quantum Hall regime, the ratio of estimated high-energy velocities in the two materials suggests a propagation distance of the order of 200 µm in a $\nu = 1$ ideal channel before any significant step in the inelastic scattering probability manifests itself in graphene. Moreover, as discussed in the previous section, even for such long propagation distances, electronic decoherence would be much lower in a weak coupling material compared to the case of a strong coupling material (see figure 3.23).

Of course, this discussion has been made within the framework of our model for electronic propagation within an ideal $\nu = 1$ edge channel. In practice, it is known that edge magnetoplasmons propagating along quantum Hall edge channels experience dissipation [170, 97, 14, 126, 98]. This is one of the possible causes for missing energy in electronic relaxation experiments [66], but I unfortunately did not have the time to look at it more closely during my PhD. One possible path towards taking into account dissipation problems may be found using the discrete element circuit discussed in section 3.4.3 with dissipative elements. In particular, a first try of such dissipative circuits seemed to give pretty consistent results with the phenomenological dissipative model presented in [14], and I hope that we will be able to go a bit deeper in this study soon.

Nevertheless, the main point stressed in the present paragraph is that the effect of the Fermi velocity difference both on the coupling constant and on the length to time scale conversion may lead to important differences between strong and weak-coupling materials, as far as single-electron decoherence is concerned. As suggested by figure 3.29, HOM

[11] These numbers correspond to the ideal $\nu = 1$ case which is not the case that has been experimentally studied. In the experiments, extrinsic decoherence induced by the second edge channel leads to much shorter coherent propagation distance for such energy resolved excitations.

experiments may offer clear discriminating signatures of weak versus strong coupling materials, but this would require the experimental development of single electron sources for Landau quasi-particles injection in graphene quantum Hall edge channels.

On the experimental side, a Mach-Zehnder interferometer has recently been demonstrated with encapsulated monolayer graphene sheets embedded within hexagonal boron nitride [174]. The beam splitters exploit same-spin intervalley scattering at a p-n junction and the interferometer's geometry is controlled by Coulomb exchange interactions. Surprisingly, a contrast of more than 90 % has been observed at low bias for an arm length[12] of 1.2 µm. Such a high contrast remains up to a bias voltage larger than 200 µV. Although decoherence mechanisms have not yet been studied in great detail for this device, we think that such a surprisingly high contrast as well as our discussion of coupling constant and high energy velocity effects call for intensive studies of single-electron decoherence in a material such as graphene.

3.5 Higher order coherences

After this rather complete study of first order coherence, let us now turn to higher order coherences. As explained in the introduction of this thesis, second order electronic coherence contains all the information on two particle entanglement in the many-body electron fluid. It is also the physical quantity that contains a direct signature of non-trivial correlations through violations of Wick's theorem. In particular, allowing the measurements of second order coherence, a natural question to ask concerns the intrinsic second order coherence generated by a single electron flying across an interaction region. Another question is the determination of how an incoming second order coherence may be modified by the interaction region. These are the two questions that will be adressed in this section. As a starting point of this investigation, we will present the general computation of all outgoing electronic coherences from an interaction region provided a p-electron excitation has been injected into it.

[12] Even more impressive, this setup is such that one arm consists of one carrier edge channel, while the other arm consists of two edge channels.

3.5.1 Computing the most general expression

The ideas presented in section 3.1 can be applied directly to study any coherence of systems with several electrons. However, the calculations involved can become quite tedious, and have therefore been relegated to appendix C. In the appendix, we derive the general expression of the n-th order electronic coherence after an interaction region for an incoming state containing p electrons on top of the Fermi sea, $\prod_{i=1}^{N} \psi^\dagger[\varphi_i]\,|F\rangle$. All wavefunctions appearing in this p-electron state are supposed to be entirely above the Fermi sea. The resulting expression, which will be explained here, is

$$\begin{aligned}
&\mathcal{G}^{(ne)}_{\text{out}}(t_1,\dots,t_n|t'_1,\dots,t'_n) = \\
&\int \prod_{i=1}^{p} \mathrm{d}t_{i+}\mathrm{d}t_{i-}\varphi_i(t_{i+})\varphi_i^*(t_{i-}) \\
&\left\langle \psi(t_{1-})\cdots\psi(t_{p-})\psi^\dagger(t'_1)\cdots\psi^\dagger(t'_n)\psi(t_n)\cdots\psi(t_1)\psi^\dagger(t_{p+})\cdots\psi^\dagger(t_{1+})\right\rangle_{\text{F}} \\
&\prod_{k=1}^{n}\prod_{i=1}^{p} \gamma_+^*(t_{i-}-t_k)\gamma_-^*(t_{i-}-t'_k)\gamma_+(t_{i+}-t'_k)\gamma_-(t_{i+}-t_k) \\
&\exp\left(\int_0^\infty \frac{\mathrm{d}\omega}{\omega}\mathrm{i}\mathrm{Im}\left(\mathrm{T}(\omega)\right)\sum_{i,j=1}^{p}\left(\mathrm{e}^{\mathrm{i}\omega(t_{j-}-t_{i-})}-\mathrm{e}^{\mathrm{i}\omega(t_{j+}-t_{i+})}\right)\right).
\end{aligned} \tag{3.81}$$

In equation (3.81), we may recognize the n-th order equivalents of everything present in equation (3.26). First of all, in the absence of any other terms, the product of all wavepackets and the Fermi sea correlator would give back the incoming n-th order electronic coherence. As expected, the outgoing coherence can thus be seen as a decohered version of the incoming one, the decoherence coefficient being given by two terms. The product of all $\gamma_\pm$ functions is exactly the product of all decoherence coefficient $D(t_k, t'_k, t_{i+}, t_{i-})$ arising from the passage of a single electron in the system (see equation (3.24). It encodes the interaction of an electron with all the excitations it generates in its environment, both in its channel and the other one. Finally, the last exponential function encodes a decoherence coefficient linked to the interaction of the p electrons with each other. Of course, this did not appear in the case $p = 1$ and is specific to the injection of a many-electron excitation.

In order to perform the same analysis as for the $n = 1, p = 1$ case, several steps would have to be taken. First of all, we have to go to the frequency space and rewrite all γ functions as the sum of two parts,

one singular and one regular, as was done in appendix B. Then, we would need to use Wick's theorem in order to divide the Fermi sea correlator into several smaller, well-known parts. This is the best way to control all the singularities arising in the computation. Unfortunately, this expansion generates an exponentially large number of terms to write down and compute:

$$N = (n+p)! \times 2^{4np}\,. \tag{3.82}$$

In the simplest case of $n = 1, p = 1$, we recover the 32 terms we detailed in appendix B. The next interesting cases are either $n = 1, p = 2$ or $n = 2, p = 1$, and both of them contain a total of 1536 terms. Of course, symmetries would help reducing the complexity of the task. Moreover, one should expect some of these terms to lead to contribution that are well understood, as they come from products between lower order ones. But in the end, the remaining number of contributions would still be far too much for us to be written down explicitly, at least by hand. And this is only the first step along the way since, in the end, we have to numerically evaluate a large number of high dimensional multiple integrals, which would certainly be a highly non trivial problem untractable by brute force methods. In the remainder of this section, we will therefore try to simplify this problem by looking for physically relevant information that can be extracted at a reasonable cost from equation (3.81) in some limiting cases. We shall now focus on at most second order electronic coherence since this is probably the best we can expect to access in forthcoming experiments, using for example the measurement protocols described in section 2.4.

3.5.2 Second order coherences from a single excitation

The first case we are interested in is the case of second order electronic coherence created from the propagation of a single electron in the interaction region, $n = 2, p = 1$. In this case, we are interested in some intrinsic excess second order coherence since it would be completely generated by Coulomb interactions. This quantity contains interesting information on the electron/hole pairs that are generated by interactions.

The quantity we are interested in is given by

$$\begin{aligned}\mathcal{G}^{(2e)}_{\text{out}}(t_1,t_2|t'p_1,t'_2) = \int \mathrm{d}t_+\mathrm{d}t_-\varphi_e(t_+)\varphi_e(t_-) \\ \times\langle\psi(t_-)\psi^\dagger(t'_1)\psi^\dagger(t'_2)\psi(t_2)\psi(t_1)\psi^\dagger(t_+)\rangle_{\text{F}} \\ \times\gamma_+(t_+-t'_1)\gamma_-(t_+-t_1)\gamma^*_+(t_--t_1)\gamma^*_-(t_--t'_1) \\ \times\gamma_+(t_+-t'_2)\gamma_-(t_+-t_2)\gamma^*_+(t_--t_2)\gamma^*_-(t_--t'_2)\,.\end{aligned} \tag{3.83}$$

Of course, we need to remember that this can be decomposed, as any second order coherence, into a Fermi sea contribution $\mathcal{G}^{(2e)}_{\text{F}}$, two classical correlations parts of the form $\mathcal{G}^{(e)}_{\text{F}}(t_i|t'_i)\Delta\mathcal{G}^{(e)}_{\rho}(t_j|t'_j)$, two quantum exchange terms $-\mathcal{G}^{(e)}_{\text{F}}(t_i|t'_j)\Delta\mathcal{G}^{(e)}_{\rho}(t_j|t'_i)$ and finally the excess contribution $\Delta\mathcal{G}^{(2e)}_{\rho}$. Here, those terms will appear as specific terms in the decomposition of the full coherence using the properties of γ functions discussed in appendix B.

Let us start by using Wick's theorem to describe the Fermi sea six-points correlators in terms of two-points correlators:

$$\langle\psi(t_-)\psi^\dagger(t'_1)\psi^\dagger(t'_2)\psi(t_2)\psi(t_1)\psi^\dagger(t_+)\rangle_{\text{F}} =$$

$$+\langle\psi(t_-)\psi^\dagger(t_+)\rangle_{\text{F}}\langle\psi^\dagger(t'_1)\psi(t_1)\rangle_{\text{F}}\langle\psi^\dagger(t'_2)\psi(t_2)\rangle_{\text{F}} \tag{3.84a}$$

$$-\langle\psi(t_-)\psi^\dagger(t_+)\rangle_{\text{F}}\langle\psi^\dagger(t'_1)\psi(t_2)\rangle_{\text{F}}\langle\psi^\dagger(t'_2)\psi(t_1)\rangle_{\text{F}} \tag{3.84b}$$

$$+\langle\psi(t_-)\psi^\dagger(t'_1)\rangle_{\text{F}}\langle\psi^\dagger(t'_2)\psi(t_2)\rangle_{\text{F}}\langle\psi(t_1)\psi^\dagger(t_+)\rangle_{\text{F}} \tag{3.84c}$$

$$+\langle\psi(t_-)\psi^\dagger(t'_2)\rangle_{\text{F}}\langle\psi^\dagger(t'_1)\psi(t_1)\rangle_{\text{F}}\langle\psi(t_2)\psi^\dagger(t_+)\rangle_{\text{F}} \tag{3.84d}$$

$$-\langle\psi(t_-)\psi^\dagger(t'_1)\rangle_{\text{F}}\langle\psi^\dagger(t'_2)\psi(t_1)\rangle_{\text{F}}\langle\psi(t_2)\psi^\dagger(t_+)\rangle_{\text{F}} \tag{3.84e}$$

$$-\langle\psi(t_-)\psi^\dagger(t'_2)\rangle_{\text{F}}\langle\psi^\dagger(t'_1)\psi(t_2)\rangle_{\text{F}}\langle\psi(t_1)\psi^\dagger(t_+)\rangle_{\text{F}} \tag{3.84f}$$

We can easily recognize here three types of terms:

- Terms (3.84a) and (3.84b), together, can be recasted as the product of $\mathcal{G}^{(e)}_{\text{F}}(t_+,t_-)$ with $\mathcal{G}^{(2e)}_{\text{F}}(t_1,t_2|t'_1,t'_2)$. Therefore, the corresponding contributions may be called *modified vacuum* terms (MV) for second order electronic coherrence.

- Terms (3.84c) and (3.84d) involve correlators of the form $\mathcal{G}^{(e)}_{\text{F}}(t_i|t'_i)$, and should thus be called *modified correlations* (MC) to electronic second order coherence.

- Finally, the last two terms (3.84e) and (3.84f) involve correlators of the form $\mathcal{G}^{(e)}_{\text{F}}(t_i|t'_j)$, and will then be called *modified exchange* terms (ME).

As the reader may have noticed, we are just organizing the various contributions according to the various contributions given by Wick's theorem, thereby generalizing what we had previously done when computing the outgoing single electron coherence generated by the injection of a single electron excitation into the interaction region. Of course, in the present situation, there is no *modified intrinsic excess* (MΔ) term, since the excess first order coherence of the incoming state is directly equal to 0. This does not mean that there will be no intrinsic excess second order coherence in the outgoing state, but this will come from non-obvious processes.

To make this point more precise, we need to describe the different $\gamma_\pm$ functions themselves. Remember that their Fourier transform can be divided into two parts, as is defined in equation (3.30). In the time domain, this division can be written as $\gamma_\pm = \kappa_\pm(1+b_\pm(t))$, with $\kappa_+\kappa_- = 1$ and $b_\pm$ regular functions obtained as the inverse Fourier transforms of $2\pi B_\pm(\omega)$. The full decoherence coefficient given by

$$\begin{aligned} D_{n=2,p=1}(t_1,t_2,t_1',t_2',t_+,t_-) = \\ \gamma_+(t_+-t_1')\gamma_-(t_+-t_1)\gamma_+^*(t_--t_1)\gamma_-^*(t_--t_1') \\ \times\gamma_+(t_+-t_2')\gamma_-(t_+-t_2)\gamma_+^*(t_--t_2)\gamma_-^*(t_--t_2') \end{aligned} \tag{3.85}$$

therefore can be decomposed into 256 terms, but some of them are more interesting than others. To be a bit more precise, we can get the following decomposition:

$$\begin{aligned} &D_{n=2,p=1}(t_1,t_2,t_1',t_2',t_+,t_-) = \\ &1 && \text{1 term} && \text{(3.86a)} \\ &+D(t_1,t_1',t_+,t_-)+D(t_2,t_2',t_+,t_-)-2 && \text{30 terms} && \text{(3.86b)} \\ &+D(t_1,t_2',t_+,t_-)+D(t_2,t_1',t_+,t_-)-2 && \text{30 terms} && \text{(3.86c)} \\ &+\text{all other possible terms} && \text{195 terms} && \text{(3.86d)} \end{aligned}$$

where $D(t,t',t_+,t_-) = D_{n=1,p=1}(t,t',t_+,t_-)$ is the single particle decoherence coefficient appearing in equation (3.24), consisting of a product of 4 γ functions, and thus containing 16 terms. The -2 are needed in order to avoid double counting the only term corresponding to the product of all the 1s.

Now, let us put together the decompositions from equations (3.84) and (3.86). First of all, using the 1 from equation (3.86a) with correlators from terms (3.84a) and (3.84b) leads to the Fermi sea second order coherence $\mathcal{G}_{\mathrm{F}}^{(2e)}(t_1,t_2|t_1',t_2')$. Then, using $D(t_1,t_1',t_+,t_-)$ with term

(3.84a) leads to $\mathcal{G}_{\mathrm{F}}^{(e)}(t_2|t_2')\mathcal{G}_{\rho,\mathrm{MV}}^{(e)}(t_1|t_1')$, while using it on term (3.84c) leads to $\mathcal{G}_{\mathrm{F}}^{(e)}(t_2|t_2')\mathcal{G}_{\rho,\mathrm{WP}}^{(e)}(t_1|t_1')$. Both terms, together with the -1 that avoids double counting, lead to $\mathcal{G}_{\mathrm{F}}^{(e)}(t_2|t_2')\Delta\mathcal{G}_{\rho}^{(e)}(t_1|t_1')$. In the same way, using the $D(t_2, t_2', t_+, t_-)$ with both terms (3.84a) and (3.84d) leads to $\mathcal{G}_{\mathrm{F}}^{(e)}(t_1|t_1')\Delta\mathcal{G}_{\rho}^{(e)}(t_2|t_2')$. With the exact same idea, it is easy to see that using equation (3.86c) with equation (3.84b) and equations (3.84e) and (3.84f) will give us the exchange terms, $-\mathcal{G}_{\mathrm{F}}^{(e)}(t_1|t_2')\Delta\mathcal{G}_{\rho}^{(e)}(t_2|t_1') - \mathcal{G}_{\mathrm{F}}^{(e)}(t_2|t_1')\Delta\mathcal{G}_{\rho}^{(e)}(t_1|t_2')$.

Using these considerations, out of the 1536 terms that would constitute the full second order electronic coherence function, we can get down to "only" $6 \times 195 + 4 \times 60 = 1410$ terms contributing to the intrinsic excess second order coherence. This is still completely unrealistic to deal with by hand, but it allows us to understand a bit more what needs to be done in order to compute the excess coherence coming from interactions.

Going to the frequency space

Exactly as in section 3.1.3, it is easier to work in the frequency domain to visualize how electronic coherence "leaks down" from one point to another. Remember that in the first order case, we had

$$\widetilde{\mathcal{G}}_{\rho_1}^{(e)}\left(\omega + \frac{\delta\omega}{2}\,\middle|\,\omega - \frac{\delta\omega}{2}\right) = \int_{-\infty}^{+\infty} \varphi_e\left(\omega' + \frac{\delta\omega}{2}\right)\varphi_e^*\left(\omega' - \frac{\delta\omega}{2}\right) K(\omega, \omega'; \delta\omega)\mathrm{d}\omega' \tag{3.87}$$

when using the reduced variables ω and $\delta\omega$. Time translation invariance therefore implies that decoherence only happens along lines of constant $\delta\omega$, since points with different values of $\delta\omega$ do not mix in the integral. A visual representation of this was given in figure 3.3, on page 158. Now, is there a way to do the same type of things in this second order case, with one electron emitted in the system? The answer is yes, and we can recast equation (3.83) in the energy domain under the following form:

$$\widetilde{\mathcal{G}}_{\mathrm{out}}^{(2e)}(\overline{\omega}, \delta\overline{\omega}, \overline{\Omega}, \delta\Omega) = \int \varphi_e\left(\omega' + \overline{\Omega}\right)\varphi_e^*\left(\omega' - \overline{\Omega}\right) K_{n=2,p=1}\left(\omega', \overline{\omega}, \delta\overline{\omega}, \delta\Omega; \overline{\Omega}\right)\mathrm{d}\omega'\,. \tag{3.88}$$

In this equation, we have used the reduced density variables defined in equation (1.84)[13]. Here also, time translation invariance implies that decoherence only happens along subspaces of constant Ω. We shall now try to give a visual representation of where it can be expected to happen on figures 3.30 and 3.31.

Incoming coherence coming from $\varphi_e(\omega_0 + \overline{\Omega}_0)\varphi_e^*(\omega_0 - \overline{\Omega}_0)$ seems to "leak down", within the $\overline{\Omega} = \overline{\Omega}_0$ subspace. A priori, we know that it will be contained inside a cube delimited by the planes $\overline{\omega} = \pm\omega_0/2$, $\delta\overline{\omega} = \pm\omega_0/2$ and $\delta\Omega = \pm\omega_0/2$, displayed in figure 3.30, since total energy needs to be conserved. Yet, we can find more stringent conditions, since we also need $|\omega_1|, |\omega_2|, |\omega_1'|, |\omega_2'|$ to be all inferior to ω_0. This leads to some missing parts in this first cube, as can be seen in figure 3.31. The exact form of the propagator depends on the value of Ω_0 under consideration. In a way, all these conditions are simply there to ensure energy conservation, and it is obvious that having $|\Omega_0|$ too close to ω_0 means that not much energy is available for generating two particle excitations.

It is not easy to understand how exactly things will happen when looking only at this cutout cube. To gain a more intuitive vision of how decoherence actually occurs, we will describe some specific simplified situations and show how they modify second order coherence. In its first part, this discussion may seem a bit academic, but we will attach it to experimentally realistic processes in just a few pages.

Electron/hole pair emission

The simplest process through which an electron relaxes is by emitting an electron/hole pair into in its own propagation channel or by releasing a pair into the other channel. We are therefore interested in the different manners in which such an emission can contribute to the intrinsic excess second order coherence, starting from a system that has no such intrinsic excess second order coherence.

For the remainder of this section, we also suppose that all electrons are perfectly localized in energy, the incoming electron being emitted at an energy ω_0 in the system: $\varphi_e(\omega) = \delta(\omega - \omega_0)$. In such a case, the incoming second order coherence is quite simple, and was discussed in section 1.3.1, on page 73. In particular, since it is located in the $\overline{\Omega} = 0$

[13] In order to understand the current section in the best possible way, it will be useful to remember most of the discussion of second order coherence in the energy domain, starting on page 68.

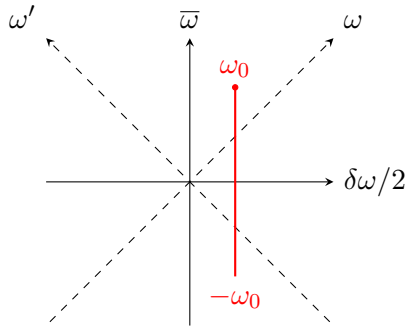

$n = 1, p = 1$

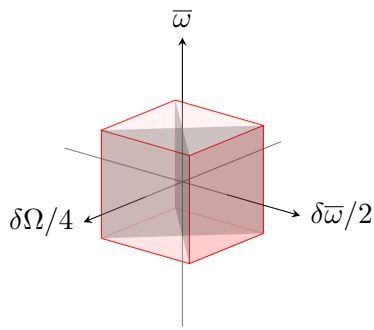

$n = 2, p = 1$
$(\overline{\Omega} = \overline{\Omega}_0)$

Figure 3.30: A visual representation of the way in which coherence appears from a single point under the effect of interactions. *Left*: First order case. The starting point $\varphi_e(\omega_0 + \delta\omega_0/2)\varphi_e^*(\omega_0 - \delta\omega_0/2)$ leads, under the effect of interactions, to the apparition of coherences along the red line, corresponding to constant $\delta\omega = \delta\omega_0$. *Right*: Second order case. The starting point is now $\varphi_e(\omega_0 + \overline{\Omega}_0)\varphi_e^*(\omega_0 - \overline{\Omega}_0)$, and it leads to the creation of coherence within the red cube contained within the $\overline{\Omega} = \overline{\Omega}_0$ subspace displayed here. Of course, we need to have $|\overline{\Omega}_0| < \omega_0/2$, since the incoming point corresponds to coherence of an electron. Each side of the cube crosses the corresponding axis at a value $\pm\omega_0/2$. Note that the two gray planes within the cube are forbidden by Pauli principle, so that the second order coherence will vanish there.

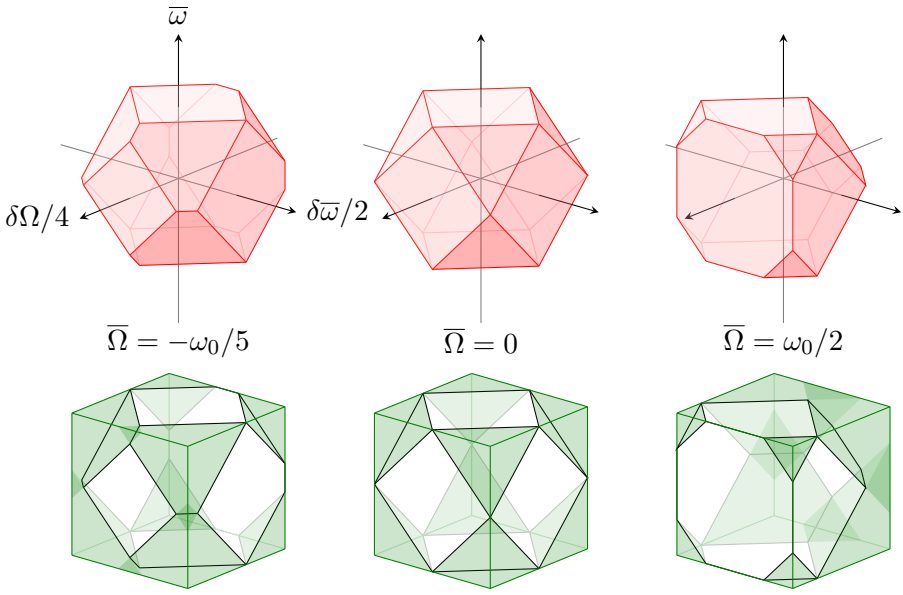

Figure 3.31: Using more stringent conditions on the different energies at play, we can limit even more the space in which coherence will propagate. The exact form of that space will depend on Ω_0, as can be seen in the figure, but will always be a smaller, cutout version of the full cube we discussed before. Here, we represent both the space in which coherence could propagate (*Top row*) and the complementary part that would give the full cube (*Bottom row*), as a way to make things a bit more easy to understand, since 3D representation can be a bit tricky sometimes. The space we are looking for is therefore a cube of which we would have cut the angles. This comes from the fact that the 4 space diagonals of the cube represent the projection in that space of ω_1, ω_2, ω_1', ω_2', which must all be smaller than $\omega_0/2$ in absolute value.

subspace, all outgoing coherence will also be in that same subspace, allowing us to use the 3-dimensional representation which we also studied in section 1.3.1. In particular, the sectors division from figure 1.18 will be of particular help in the remainder of this section.

First of all, let us study one specific process of second order coherence creation from electron/hole pair emission. We are interested in the state displayed on the left of figure 3.32, in which the incoming electron has lost energy ω_l, and an electron/hole pair with that same energy is created, with the electron emitted at ω_e and the hole at $\omega_h = \omega_e - \omega_l$. Once we understand the second order coherence of that state, we will be able to change both ω_e and ω_l. In order to be readable, figure 3.32 only depicts the $\delta\Omega = 0$ plane, which corresponds to a correlation plane in the energy domain between the electrons under consideration. Of course, due to symmetries, the orthogonal plane $\delta\overline{\omega} = 0$ will display coherences in the same places, with a minus sign.

In reality, the state created by Coulomb interactions will not be this specific, but it will rather be a superposition of states such as the one we considered up to now, as well as states in which more electron/hole pairs could be generated. We also know that there must be non-zero overlaps between the relative states in the environment for coherences between two states to appear. However, a really simple physical process such as a superposition between an electron that lost energy ω_l and created a specific e/h pair in its channel and one that created another pair with the same energy, without sending anything in the environment, may lead to second order coherence in other points of the 3-frequencies space than the ones seen up to now[14]. For such a superposition, depicted on the left of figure 3.33, there will be coherences in all the points shown on the right of that same figure. As can easily be seen, these points are no more contained within the 2 planes corresponding to correlations or exchanges. When varying the two e/h pairs within the superposition, we can therefore recover coherences at points that are contained within the cutout cube that represents the propagator in this $\overline{\Omega} = 0$ subspace, as seen in figure 3.31. It is interesting to note that all coherence created by this process is in the electron+hole (e+h) sector, as we are indeed probing both the electron and the hole from the pairs.

The second type of superposition we can be interested in are superpositions between states where the holes generated by the e/h pair

[14]We are still in the $\overline{\Omega} = 0$ subspace, since the incoming coherence is only in that space.

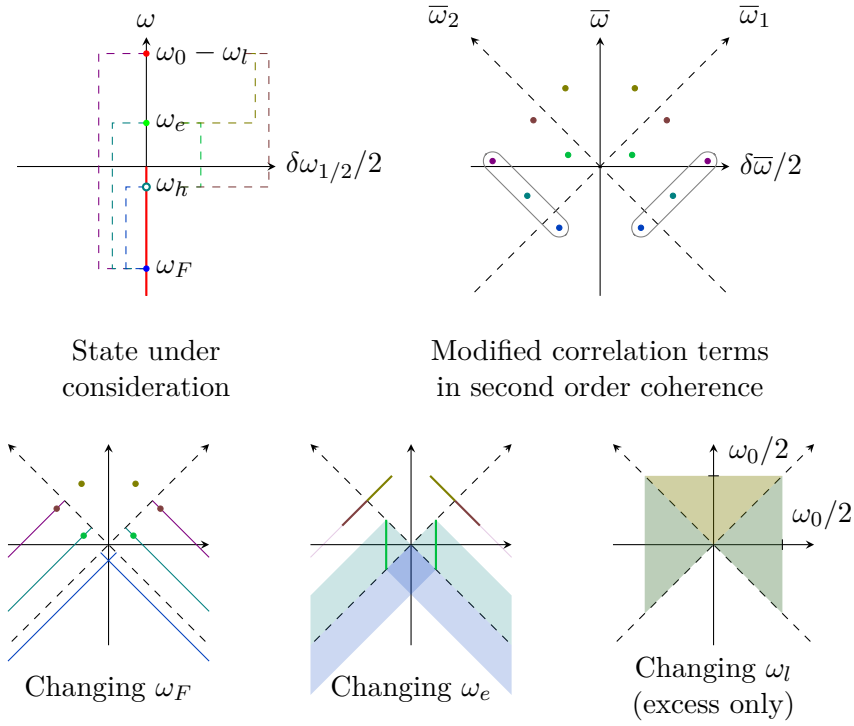

Figure 3.32: A representation of coherences created by a simple process in which an energy-resolved electron loses some energy through the creation of an electron/hole pair. *Top left*: The state under consideration. The e/h pair is such that $\omega_e - \omega_h = \omega_l$. We also show one specific electron of the Fermi sea as representative for correlation contributions. *Top right*: Correlation terms arising from this state in the diagonal subspace $\overline{\Omega} = \delta\Omega = 0$. From the 4 excitations shown on the left, we create 12 points with coherences. 6 of them, within the gray borders, are contained within the correlation terms in the standard sense of second order coherence. The other 6 are excess coherences between the initial electron which has lost energy and the excitations it created. *Bottom left*: We recover the full correlation terms $\Delta\mathcal{G}^{(e)}(\omega_1|\omega_1')\mathcal{G}_{\mathrm{F}}^{(e)}(\omega_2|\omega_2') + 1 \leftrightarrow 2$ by changing ω_F. *Bottom center*: Changing the position of the e/h pair without changing its energy leads to coherences along small lines rather than points. The correlation with Fermi sea electrons leads to greater domains in which coherence can appear. *Bottom right*: Finally, changing the energy lost by the incoming excitation leads to excess coherences within a square region that is the projection of the cube we displayed in figure 3.30 in the subspace displayed here.

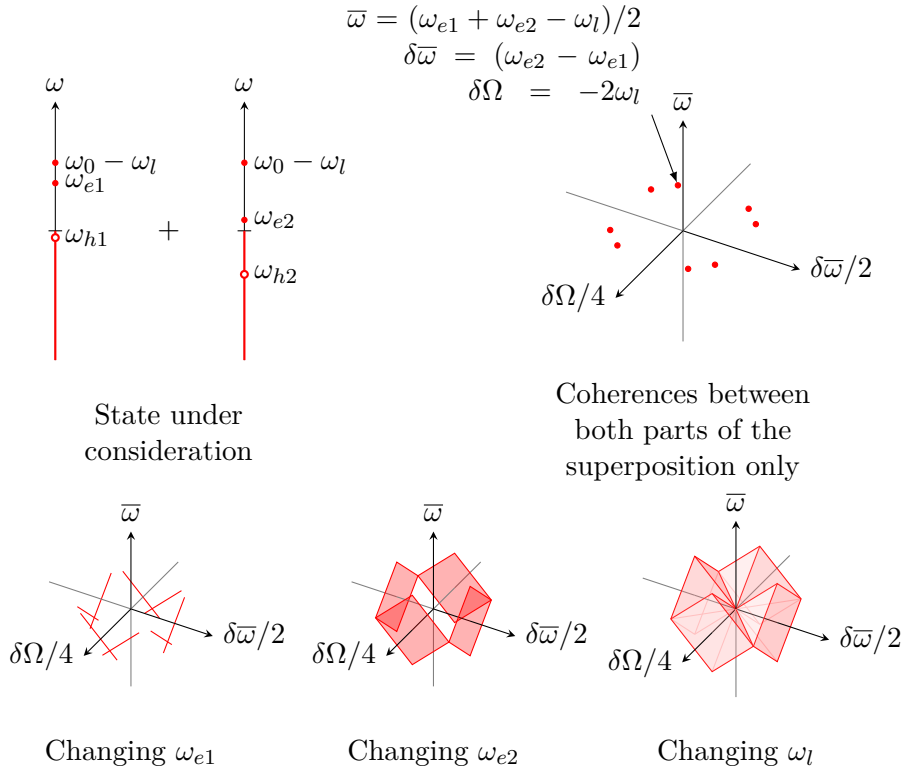

Figure 3.33: A visualization of where coherence can appear when considering a superposition of two states where the electron has lost the same energy but created different pairs. *Top left*: The state under consideration. Correlators of the form $\langle c^\dagger(\omega_{e2})c^\dagger(\omega_{h1})c(\omega_{h2})c(\omega_{e1})\rangle$ on that state should be non-zero. *Top right*: The new excess second order coherence points that appear specifically from the fact that we are looking at a superposition. All points corresponding to any of the two parts taken alone are not represented. Correlations and quantum exchange terms with the Fermi sea are not shown either. *Bottom, from left to right*: All points where such coherence could be recovered when varying the different parameters we have. They all lie within the (e+h) sector of second order coherence. In the last figure, the limiting points are on the surface of a cube with sides of size $\omega_0/2$.

creation are at the same energy, but the incoming electron has undergone different energy losses as displayed on figure 3.34. In this case, we are probing coherences between the two electrons present in the superposition, so that everything happens in the (2e) sector of second order coherence. This type of process therefore allows us to gain access to other parts of the propagator seen before!

Of course, we could also create superpositions between states where it is the electron generated by interaction that always lies at the same energy. However, due to the indiscernability of electrons, this is exactly the same process as the one displayed in figure 3.33, since we only need to intervert which electron is called by which name.

The real last superposition of interest for us is therefore one between an electron that lost some energy in its environment (for example another channel) and the state where the electron emitted the same state in its environment plus some electron/hole pair in its own channel. Such a case is displayed in figure 3.35 and leads to coherences in yet another sector of second order coherence: the (e+e/h) one.

To conclude this brief study, we just explained how simple processes involving only a single electron/hole pair emission can generate excess second order coherence in almost every part of the cutout cube from figure 3.31 that represents a generic propagator. This can be seen simply by summing all the processes seen before. Yet, two sectors are still unattainable with such simple processes: the (2h) and (h+e/h) ones, as they would need the creation of more than one hole. But of course, even at relatively small coupling more than one electron pair will be generated by Coulomb interactions and these processes with electron/hole pairs would contribute to second order electronic coherence in these zones.

A look at some realist processes

Although it does not seem easy to imagine what would happen in a realistic experiment in full generality, there are two cases which we have already discussed for first order coherence that may be enlightening to consider under the prism of second order coherence.

High-energy excitation The first example is when the incoming single electron excitation is injected at some high energy above the Fermi sea and interactions are sufficiently weak and with limited bandwidth so that we are in the so-called dynamical Coulomb blockade-like (DCB-like) regime of electronic decoherence [32]. Remember that in this regime,

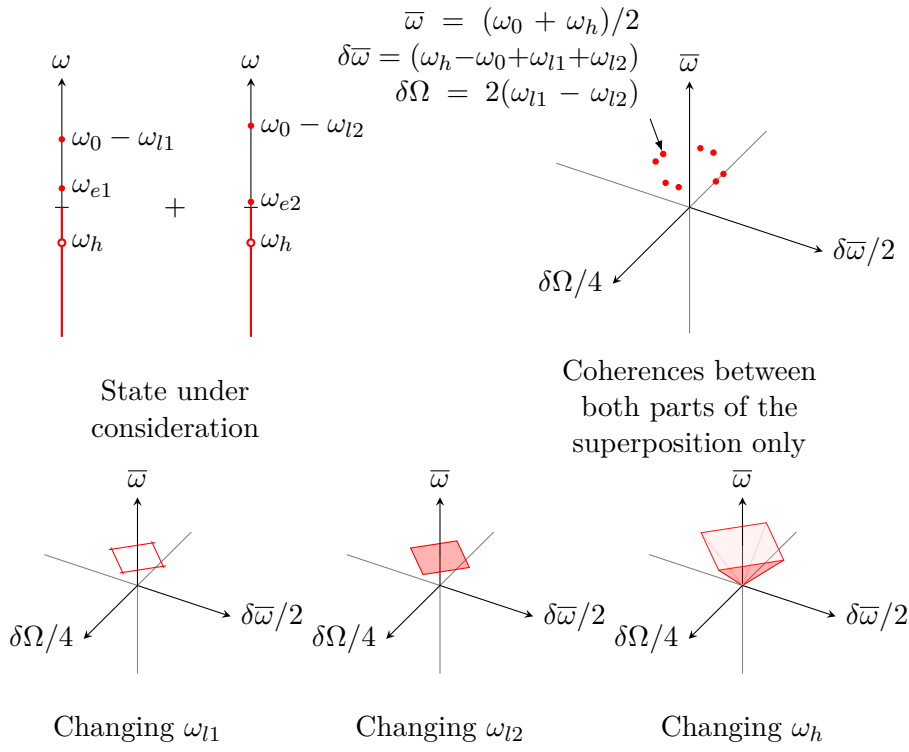

Figure 3.34: A visualization of where coherence can appear when considering a superposition of two states where the electron has lost different energies but created the same hole excitation. *Top left*: The state under consideration. Correlators of the form $\langle c^\dagger(\omega_{e2})c^\dagger(\omega_0 - \omega_{l2})c(\omega_{e1})c(\omega_0 - \omega_{l1})\rangle$ should be non-zero. *Top right*: The new excess second order coherence points that appear specifically from the fact that we are looking at a superposition. All points corresponding to any of the two parts taken alone are not represented. Correlations and quantum exchange terms with the Fermi sea are not shown either. *Bottom, from left to right*: All points where such coherence could be recovered when varying the different parameters we have. They all lie within the (2e) sector of second order coherence. In the last figure, the limiting points are on the surface of a cube with sides of size $\omega_0/2$.

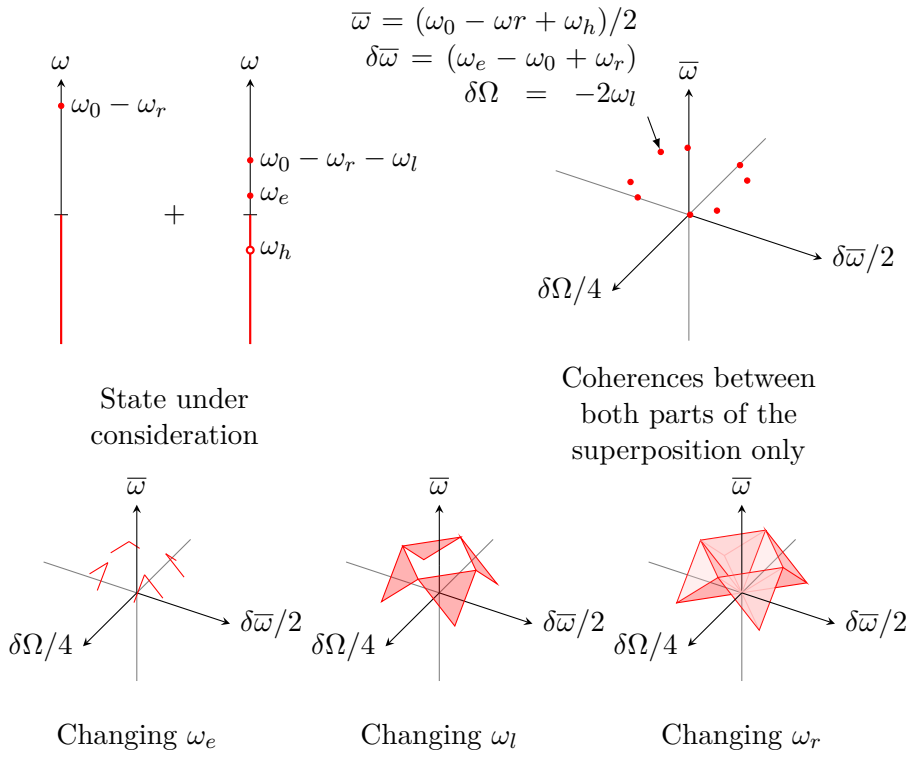

Figure 3.35: A visualization of where coherence can appear when considering a superposition of two states where the electron has lost some energy in an outside environment, and then either created an e/h pair in its channel or not. *Top left*: The state under consideration. Correlators of the form $\langle c^\dagger(\omega_e)c^\dagger(\omega_e - \omega_r - \omega_l)c(\omega_h)c(\omega_0 - \omega_r)\rangle$ should be non-zero. *Top right*: The new excess second order coherence points that appear specifically from the fact that we are looking at a superposition. All points corresponding to any of the two parts taken alone are not represented. Correlations and quantum exchange terms with the Fermi sea are not shown either. *Bottom, from left to right*: All points where such coherence could be recovered when varying the different parameters we have. They all lie within the (e+e/h) sector of second order coherence. In the last figure, the limiting points are on the surface of a cube with sides of size $\omega_0/2$.

considering first order coherence, the wavepacket contribution is given by equation (3.55):

$$\Delta\mathcal{G}^{(e)}_{\mathrm{WP}}(t|t') \simeq \varphi_e(t)\,\varphi_e^*(t')\,D(t-t') \tag{3.89}$$

with[15]

$$D(\tau) = \exp\left(\int_0^{+\infty} 2\mathrm{Re}\left(1-\mathrm{T}(\omega)\right)\left(\mathrm{e}^{\mathrm{i}\omega\tau}-1\right)\frac{\mathrm{d}\omega}{\omega}\right). \tag{3.90}$$

In terms of physical interpretation, $D(t-t')$ corresponds to the product $\langle[\mathrm{R}\Lambda'_t]|[\mathrm{R}\Lambda_t]\rangle\langle[g'_t]|[g_t]\rangle$, *i.e.* to the overlap between states generated in both environmental channels by either an electron located at t or at t'. The key point here is that interactions and the injection energy are such that the electron/hole pairs are well separated from the injected electron's relaxation tail and consequently, excitations close to the Fermi level can be treated as an effective environment for the injected high energy electron. A subsequent study of D then allows us to recover both the inelastic scattering probability of our electron and its high-energy relaxation tail. Our idea is to try to find the same type of effective decoherence coefficients for second order coherence generated by a single excitation under the assumption that we are in the so called DCB-like regime.

The main technical trick used in this approximation scheme is the fact that if $\varphi_e(\omega)$ is completely separated from the Fermi sea, then two points correlators of the form $\langle\psi(a)\psi^\dagger(b)\rangle_{\mathrm{F}}$ with either a or b being equal to $t_\pm$ can be replaced by a Dirac distribution $\delta(a-b)$. This is where the physical assumption is expressed. It allows a rewriting of modified correlations and exchanges terms from equations (3.84c) to (3.84f) under the following form:

$$\begin{aligned}\mathcal{G}^{(2e)}_{\mathrm{MC1}}(t_1,t_2|t'_1,t'_2) = \mathcal{G}^{(e)}_{\mathrm{F}}(t_2|t'_2)\Delta\mathcal{G}^{(e)}_{\mathrm{WP}}(t_1|t'_1) \\ \times\,\gamma_+(t_1-t'_2)\gamma_-(t_1-t_2)\gamma_+^*(t'_1-t_2)\gamma_-^*(t'_1-t'_2)\end{aligned} \tag{3.91}$$

where $\Delta\mathcal{G}^{(e)}_{\mathrm{WP}}(t_1|t'_1)$ is given by equation (3.55). Other correlation and exchange terms are obtained with suitable symmetries, as always. How can we understand this result? As expected, it looks quite like a standard

[15] Note that this is not the definition we have seen before, but an equivalent one in the generic case where an external environment is present. We have studied it in the $\nu = 1$ case where $|\mathrm{T}| = 1$, which leads to $|1-\mathrm{T}|^2 = 2\mathrm{Re}\,(1-T)$. This comes from the fact that there is no external environment at $\nu = 1$.

correlation term, with one part coming from the Fermi sea and one from the injected electron having gone through the interaction region. Yet, the product of γ functions means that these two simple outgoing excitations have interacted with one another, leading to some leaking of coherences around the specific correlation point.

Another way to rewrite the result from equation (3.91) can be obtained by taking a few steps back before introducing the γ functions:

$$\mathcal{G}^{(2e)}_{\mathrm{MC1}}(t_1,t_2|t'_1,t'_2) = \varphi_e(t_1)\varphi_e^*(t'_1)\langle[g_{t'_1}]|\psi^\dagger(t'_2)\psi(t_2)|[g_{t_1}]\rangle D_{\mathrm{ext}}(t_1-t'_1)\,. \tag{3.92}$$

Remember that $|[g_t]\rangle$ corresponds to the electron/hole pairs cloud generated within the channel by an electron localized at time t, and D_{ext} denotes the extrinsic decoherence coefficient defined in equation (3.15). This form makes it a bit easier to understand exactly what is being probed. After an interaction region, coherence was transformed from a simple product between the incoming excitation part and the Fermi sea, $\varphi_e(t_1)\varphi_e^*(t'_1)\langle\psi^\dagger(t'_2)\psi(t_2)\rangle_{\mathrm{F}}$ to something that probes on the one hand the incoming high-energy excitation after it went through some environment-induced decoherence, and on the other hand the coherence of the state it created in its own channel, which replaces the standard Fermi sea. Another way to describe what happens is that the Fermi sea is affected by the quantum fluctuations of the charge density of the incoming particle. The electronic second order coherence picks a contribution from the incoming electron that has possibly (or not) relaxed, as well as the contribution from the partially quantum electron/hole pairs cloud that has been generated (hence the factor $\langle[g_{t'_1}]|\psi^\dagger(t'_2)\psi(t_2)|[g_{t_1}]\rangle$).

Loop environment and plasmon emission The second interesting example that we can study is the one discussed in section 3.3, in which an electron emitted at an energy ω_0 interacts with a closed environment. We have shown that this situation leads to the loss of an energy $\omega_l = \pi/\tau_+$, τ_+ being the time it takes for excitations to go one lap around the loop, and to the emission of a plasmon with that same energy in the channel. We then asked if there was a way to show that the emitted excitation is indeed a single plasmon, *i.e.* a quantum superposition of all electron/hole pairs with a given energy, and not a statistical mixture of them.

To answer this question, our detailed study of all possible single-pair emission processes is perfectly relevant. The processes we are interested

in are the following:

- The electron went through the interaction region and its outgoing state is a mixture of all possible states: those where it lost no energy, or those where it lost ω_l and created any e/h pair with that energy. These shall be called fully incoherent processes.

- The electron's outgoing state is the superposition of having lost no energy and having lost ω_l with creation of any corresponding single e/h pair. There is no superposition between the different e/h pairs, but rather a mixture of all possible ones. We shall call them partially incoherent processes.

- The electron's outgoing state is the full superposition of having lost no energy, having created one specific e/h pair, having creating any other specific pair, and so on. This is the fully coherent emission of plasmonic excitations.

In the first case, since all states in the mixture are independent from one another, we only get second order coherence within each state with an electron plus an e/h pair. This is the process shown on the bottom center panel of figure 3.32, and it leads to excess second order coherence only within specific lines of the $\delta\overline{\omega} = 0$ or $\delta\Omega = 0$ planes[16]. This part of coherence lives within the (2e) and (e+h) subspaces, but is fully contained within these planes.

In the second case, we would of course still have every excess coherence obtained from these processes, but we have new excess second order coherence coming from the superposition. Here, we are exactly in the situation depicted on the bottom left panel of figure 3.35, with $\omega_r = 0$ and ω_l constant: the outgoing state is the superposition of having lost no energy and having created a single pair with the expected energy. The mixture between all different possible pairs allows the reconstruction of all eight lines, all contained within the (e+e/h) sector of second order coherence. We already see a clear difference between a mixture and a superposition in that case, since different sectors cannot be mistaken for one another.

Finally, the last case corresponds to a superposition of states in which an energy-resolved electron loses the same energy ω_l but creates different e/h pairs. We have already seen that this leads to electronic coherences within 4 specific zones of our usual 3-dimensional space (see the bottom

[16] We still do this whole study in the $\overline{\Omega} = 0$ subspace, as before.

center panel from figure 3.33). These zones are the 4 squares defined by

$$\delta\Omega/4 = \pm\frac{\omega_l}{2} \quad \text{and} \quad |\overline{\omega} \pm \delta\overline{\omega}/2| < \frac{\omega_l}{2} \tag{3.93a}$$

$$\delta\overline{\omega}/2 = \pm\frac{\omega_l}{2} \quad \text{and} \quad |\overline{\omega} \pm \delta\Omega/4| < \frac{\omega_l}{2} \tag{3.93b}$$

and all lie within the (e+h) sector of coherence. The important point is that finding coherences in any point of these 4 squares that is not within the planes $\delta\Omega = 0$ or $\delta\overline{\omega} = 0$ is a clear signature of the fact that there is indeed a superposition of states in which different electron/hole pairs are emitted. Therefore, if the process happening when an energy-resolved electron interact with a closed environment is indeed the coherent emission of a single plasmon, we should be able to measure coherence in these specific regions. Hence, second order coherence measurements could provide a clear signature of the fact that we emitted a single plasmonic state.

This simple examples shows that a measurement of two electron coherence, which involves at least a two-electron interference experiment (Franson interferometry) or a double two-electron interference experiment (double HOM) probes in a very specific way the generation of a single plasmon excitation.

3.5.3 Two high-energy excitations

After this walk through the study of the excess second order coherence generated by a single electron going through an interaction region, let us engage in an a priori steeper road which will lead us to understand what happens for the $p = 2$ situation, in which two electrons are sent in the system initially. We will look both at first and second order electronic coherences and try to unravel some similarities with what we have seen before for a single electron. However, due to the increased complexity of the problem compared to the above single electron case, we will only be able to perform the discussion under the assumptions of the last paragraph, that is in the case of high energy excitations and under the hypothesis that relaxation effects do not lead the two electron excitations to relax down to the Fermi sea.

First order coherence

For an incoming state consisting of a pure two-electron excitation injected on top of the Fermi sea, the incoming first order coherence is

given by

$$\mathcal{G}^{(e)}_{\text{in}}(t|t') = \int \mathrm{d}t_{1+}\mathrm{d}t_{2+}\mathrm{d}t_{1-}\mathrm{d}t_{2-}\varphi_1(t_{1+})\varphi_1^*(t_{1-})\varphi_2(t_{2+})\varphi_2^*(t_{2-}) \quad (3.94)$$
$$\langle\psi(t_{1-})\psi(t_{2-})\psi^\dagger(t')\psi(t)\psi^\dagger(t_{2+})\psi^\dagger(t_{1+})\rangle_{\text{F}}$$

where φ_1 and φ_2 are mutually orthogonal normalized single electron wavepackets. We can then use Wick's theorem to compute the Fermi correlator, and in the case of high-energy excitation, we can as before replace correlators of the form $\langle\psi(a)\psi^\dagger(b)\rangle$ by $\delta(a-b)$ when either a or b is one of the integration variables. Doing that here directly leads to

$$\mathcal{G}^{(e)}_{\text{in}}(t|t') = \mathcal{G}^{(e)}_{\text{F}}(t|t') + \varphi_1(t)\varphi_1^*(t') + \varphi_2(t)\varphi_2^*(t')\,. \quad (3.95)$$

For the outgoing state, things are a bit more complicated and we need to use equation (3.81), but the idea is quite the same: we still have our 6-points correlator on the Fermi sea and are going to compute it using Wick's theorem. Remember that, for high-energy excitations, we are mostly interested in the equivalent of the wavepacket term from the standard case. The first two terms in Wick's decomposition that we could think about are the ones where the Fermi sea coherence $\langle\psi^\dagger(t')\psi(t)\rangle_{\text{F}}$ appears. These two terms correspond to some kind of modified vacuum terms and are not the ones we are the most interested in here. Therefore, let us start with another specific term arising from Wick's theorem: the one that leads to $\varphi_1(t)\varphi_1^*(t')$ in the incoming coherence, for which the δ functions are $\delta(t'-t_{1-})\delta(t-t_{1+})\delta(t_{2+}-t_{2-})$. This leads to the following result:

$$\mathcal{G}^{(e)}_{\varphi_1\,\text{term}}(t|t') = \varphi_1(t)\varphi_1^*(t')D(t-t') \quad (3.96)$$
$$\int \mathrm{d}t_2\,\varphi_2(t_2)\varphi_2^*(t_2)\gamma_+^*(t_2-t)\gamma_-^*(t_2-t')\gamma_+(t_2-t')\gamma_-(t_2-t)$$
$$\exp\left(\int_0^\infty \frac{\mathrm{d}\omega}{\omega} 2\mathrm{i}\mathrm{Im}\left(\mathrm{T}(\omega)\right)\left(\cos(\omega(t_2-t')) - \cos(\omega(t_2-t))\right)\right)$$

which can be rewritten as

$$\mathcal{G}^{(e)}_{\varphi_1\,\text{term}}(t|t') = \varphi_1(t)\varphi_1^*(t')D(t-t')\int \mathrm{d}t_2\,\varphi_2(t_2)\varphi_2^*(t_2) \quad (3.97)$$
$$\exp\left(\int \frac{\mathrm{d}\omega}{\omega}\mathrm{Re}\left(1-\mathrm{T}(\omega)\right)\left(\mathrm{e}^{\mathrm{i}\omega(t-t_2)} - \mathrm{e}^{-\mathrm{i}\omega(t-t_2)} + \mathrm{e}^{\mathrm{i}\omega(t_2-t')} - \mathrm{e}^{-\mathrm{i}\omega(t_2-t')}\right)\right)\,.$$

The last part of this equation looks quite like a product of decoherence coefficients D, but this is not exactly the case. To rewrite it more easily,

let us decompose $D(t)$ into its modulus and phase parts:

$$D(t) = |D(t)|\mathrm{e}^{\mathrm{i}\zeta(t)}\,. \tag{3.98}$$

Remember that $D(-t) = D(t)^*$, so that $\zeta(-t) = -\zeta(t)$. Using the definition of $D(t)$, we easily obtain

$$|D(t)| = \exp\left(\int_0^\infty \frac{\mathrm{d}\omega}{\omega} 2\mathrm{Re}\left(1 - \mathrm{T}(\omega)\right)\left(\cos(\omega t) - 1\right)\right) \tag{3.99a}$$

$$\zeta(t) = \int_0^\infty \frac{\mathrm{d}\omega}{\omega} 2\mathrm{Re}\left(1 - \mathrm{T}(\omega)\right)\sin(\omega t)\,. \tag{3.99b}$$

It is therefore straightforward to rewrite

$$\mathcal{G}^{(e)}_{\varphi_1\,\mathrm{term}}(t|t') = \varphi_1(t)\varphi_1^*(t')D(t-t') \tag{3.100a}$$

$$\times \int \mathrm{d}t_2\, \varphi_2(t_2)\varphi_2^*(t_2)\mathrm{e}^{\mathrm{i}(\zeta(t-t_2)-\zeta(t'-t_2))}\,. \tag{3.100b}$$

In this form, we obviously recognize in term (3.100a) the direct decoherence of the incoming wavepacket φ_1 as would be expected if that electron was alone in the system. Yet, the presence of the second electron is encoded in the factor (3.100b). In the incoming coherence, $\varphi_1(t)\varphi_1^*(t')$ was multiplied by $\int \mathrm{d}t_2|\varphi_2(t_2)|^2$, which was equal to 1. But for the outgoing coherence, the multiplicative coefficient given by equation (3.100b) is now the overlap between two distinct states $\varphi_{2,t}$ and $\varphi_{2,t'}$, defined as

$$\varphi_{2,t_0}(t) = \varphi_2(t)\mathrm{e}^{\mathrm{i}\zeta(t_0-t)}\,. \tag{3.101}$$

Under a different form, this can be rewritten as

$$\mathcal{G}^{(e)}_{\varphi_1\,\mathrm{term}}(t|t') = \varphi_1(t)\varphi_1^*(t')D_{\mathrm{ext}}(t-t') \tag{3.102}$$

$$\times \int \mathrm{d}t_2\, \varphi_2(t_2)\varphi_2^*(t_2)\langle[g_{t'}]|\psi(t_2)\psi^\dagger(t_2)|[g_t]\rangle\,.$$

What do these equations mean? Taking them together, we find that the overlap between the states where we created an electron in wavepacket φ_2 above the coherent plasmon states $|[g_t]\rangle$ and $|[g_{t'}]\rangle$ is equivalent to the overlap between states $|\varphi_{2,t}\rangle$ and $|\varphi_{2,t'}\rangle$ times the overlap between $|[g_t]\rangle$ and $|[g_{t'}]\rangle$:

$$\langle[g_{t'}]|\psi[\varphi_2]\psi^\dagger[\varphi_2]|[g_t]\rangle = \langle[g_{t'}]|[g_t]\rangle\langle\varphi_{2,t'}|\varphi_{2,t}\rangle\,. \tag{3.103}$$

In the general case, the overlap $\langle\varphi_{2,t'}|\varphi_{2,t}\rangle$ is always less than or equal to 1, meaning that decoherence can only become stronger in the presence of an additional electron.

In terms of physical interpretation, the states described by wavefunctions φ_{2,t_0} can be seen as describing the excess state present in the system due to the emission of the other electron, with respect to the interaction-generated plasmonic coherent state $|[g_{t_0}]\rangle$. In a way, it probes whether or not the electron/hole pairs generated in the channel under the effect of interaction have an overlap with the other electron present in the system. Indeed, the modification of φ_2 into φ_{2,t_0} is a direct consequence of Coulomb interaction between the two injected electrons. As we said for example in equation (1.56), applying some classical voltage to an Ohmic contact leads to a change in the phase of the emitted excitations. Here, the phase change for φ_2 can be interpreted as coming from the voltage generated by an electron present in the system at time t_0, the amplitude of probability for such an electron to be present being given by $\varphi_1(t_0)$.

The same type of result can be obtained for the term proportional to $\varphi_2(t)\varphi_2^*(t')$ in the incoming coherence, and we get

$$\mathcal{G}^{(e)}_{\varphi_2\ \mathrm{term}}(t|t') = \varphi_2(t)\varphi_2^*(t')D(t-t')\langle\varphi_{1,t'}|\varphi_{1,t}\rangle\,. \tag{3.104}$$

The interesting result is the fact that there are two other terms that become non-zero in the general case: interference terms between the two electrons. Indeed, the incoming coherence could have terms of the form $\varphi_1(t)\varphi_2^*(t')\langle\varphi_1|\varphi_2\rangle$, but the orthogonality of incoming states prevented them from appearing in equation (3.95). Yet, in the outgoing coherence, there is no reason to remove those terms, and we get

$$\begin{aligned}\mathcal{G}^{(e)}_{\mathrm{interference}}(t|t') = &-\varphi_1(t)\varphi_2^*(t')D(t-t')\langle\varphi_{1,t'}|\varphi_{2,t}\rangle &\text{(3.105a)}\\ &-\varphi_2(t)\varphi_1^*(t')D(t-t')\langle\varphi_{2,t'}|\varphi_{1,t}\rangle\,. &\text{(3.105b)}\end{aligned}$$

In a realistic setup, we could expect that wavepackets $\varphi_{1,t}$ and $\varphi_{2,t'}$ would be quite different, so that these interference terms should be pretty small compared to the dominant terms seen before. Still, there is no reason for these terms to be directly equal to 0, thus showing that interactions can lead to a much more complex and interesting coherence picture for the outgoing state when compared to the incoming one.

Second order coherence

To conclude this study of decoherence for a two-electron system, we will finally describe how the intrinsic second order coherence would be

modified for the specific case of two electrons injected at high energies above the Fermi sea. As before, we will use equation (3.81) in the $n = 2, p = 2$ case, with the added result that $\langle \psi(a)\psi^\dagger(b)\rangle_{\mathrm{F}} = \delta(a-b)$ when either a or b is an integration variable. And, exactly as before, we can only give detailed result for cases in which there are no correlators of the form $\langle \psi^\dagger(a)\psi(b)\rangle_{\mathrm{F}}$ left. In our usual terminology, this means that we will not interest ourselves to modified vacuum, modified correlations and modified exchanges terms. The only term we are going to study is the modified excess one, and there are already a few things to say about decoherence in that case.

Remember that the incoming excess term is given directly, using the ideas discussed above, by

$$\begin{aligned}
&\Delta\mathcal{G}^{(2e)}_{\mathrm{in}}(t_1,t_2|t_1',t_2') = \\
&\int \mathrm{d}t_{1+}\mathrm{d}t_{1-}\mathrm{d}t_{2+}\mathrm{d}t_{2-}\varphi_1(t_{1+})\varphi_1^*(t_{1-})\varphi_2(t_{2+})\varphi_2^*(t_{2-}) \\
&\times \det\begin{bmatrix}\delta(t_{1+}-t_1) & \delta(t_{1+}-t_2)\\ \delta(t_{2+}-t_1) & \delta(t_{2+}-t_2)\end{bmatrix}\det\begin{bmatrix}\delta(t_{1-}-t_1') & \delta(t_{1-}-t_2')\\ \delta(t_{2-}-t_1') & \delta(t_{2-}-t_2')\end{bmatrix}
\end{aligned} \tag{3.106}$$

which we usually recast under the more standard form

$$\Delta\mathcal{G}^{(2e)}_{\mathrm{in}}(t_1,t_2|t_1',t_2') = \Phi_{12}(t_1,t_2)\Phi^*_{12}(t_1',t_2') \tag{3.107}$$

with $\Phi_{12}(t_1,t_2)$ the Slater determinant built from wavefunctions φ_1 and φ_2. After the interaction region, the modified excess (MΔ) second order coherence is given by the same type of equation, with added γ functions and phases,

$$\begin{aligned}
&\Delta\mathcal{G}^{(2e)}_{\mathrm{M}\Delta}(t_1,t_2|t_1',t_2') = \\
&\int \mathrm{d}t_{1+}\mathrm{d}t_{1-}\mathrm{d}t_{2+}\mathrm{d}t_{2-}\varphi_1(t_{1+})\varphi_1^*(t_{1-})\varphi_2(t_{2+})\varphi_2^*(t_{2-}) \\
&\times \det\begin{bmatrix}\delta(t_{1+}-t_1) & \delta(t_{1+}-t_2)\\ \delta(t_{2+}-t_1) & \delta(t_{2+}-t_2)\end{bmatrix}\det\begin{bmatrix}\delta(t_{1-}-t_1') & \delta(t_{1-}-t_2')\\ \delta(t_{2-}-t_1') & \delta(t_{2-}-t_2')\end{bmatrix} \\
&\times \gamma_+^*(t_{1-}-t_1)\gamma_-^*(t_{1-}-t_1')\gamma_+(t_{1+}-t_1')\gamma_-(t_{1+}-t_1) \\
&\times \gamma_+^*(t_{2-}-t_1)\gamma_-^*(t_{2-}-t_1')\gamma_+(t_{2+}-t_1')\gamma_-(t_{2+}-t_1) \\
&\times \gamma_+^*(t_{1-}-t_2)\gamma_-^*(t_{1-}-t_2')\gamma_+(t_{1+}-t_2')\gamma_-(t_{1+}-t_2) \\
&\times \gamma_+^*(t_{2-}-t_2)\gamma_-^*(t_{2-}-t_2')\gamma_+(t_{2+}-t_2')\gamma_-(t_{2+}-t_2) \\
&\times \exp\left(\int_0^\infty \frac{\mathrm{d}\omega}{\omega} 2\mathrm{i}\mathrm{Im}\left(\mathrm{T}(\omega)\right)\left(\cos(\omega(t_{2-}-t_{1-}) - \cos(\omega(t_{2+}-t_{1+}))\right)\right).
\end{aligned} \tag{3.108}$$

Now, we simply need to account for the different products of δ functions in order to rewrite this result in a more compact manner. First of all, we see that $|t_{1+} - t_{2+}|$ will always be equal to $t_1 - t_2$, whereas $|t_{1-} - t_{2-}| = t'_1 - t'_2$. This means that the phase from the last line will always be exactly the same. Moreover, it is easy to convince ourselves that the product of all 16 γ functions will also always be the same. Indeed, this allows us to rewrite this coherence in a much more compact manner, under the form

$$\begin{aligned}
&\Delta\mathcal{G}^{(2e)}_{\mathrm{M}\Delta}(t_1, t_2|t'_1, t'_2) = \\
&\Phi_{12}(t_1, t_2)\Phi^*_{12}(t'_1, t'_2) \\
&\times D(t_1 - t'_1)D(t_2 - t'_2)D(t_2 - t'_1)D(t_1 - t'_2) \\
&\times \gamma_-(t_2 - t_1)\gamma_-(t_1 - t_2)\gamma^*_-(t'_2 - t'_1)\gamma^*_-(t'_1 - t'_2) \\
&\times \exp\left(\int_0^\infty \frac{\mathrm{d}\omega}{\omega} 2\mathrm{i}\mathrm{Im}\left(\mathrm{T}(\omega)\right)\left(\cos(\omega(t'_2 - t'_1) - \cos(\omega(t_2 - t_1))\right)\right)
\end{aligned} \tag{3.109}$$

where we used once again the fact that $D(t) = \gamma_+(t)\gamma^*_+(-t)$. Now, we only need to put the last two lines of this equation together to find a compact form of this modified excess term. Doing so leads to the following expression:

$$\begin{aligned}
&\Delta\mathcal{G}^{(2e)}_{\mathrm{M}\Delta}(t_1, t_2|t'_1, t'_2) = \\
&\Phi_{12}(t_1, t_2)\Phi^*_{12}(t'_1, t'_2) \times \frac{D(t_1 - t'_1)D(t_2 - t'_2)D(t_2 - t'_1)D(t_1 - t'_2)}{|D(t_1 - t_2)D(t'_1 - t'_2)|},
\end{aligned} \tag{3.110}$$

which is pretty nice since it only depends on the single electron decoherence coefficient D, making it rather easy to compute and to interpret. In terms of physical interpretation, remember first that for a single electron, the effective decoherence coefficient D corresponds to the overlap of the states that localized excitations would create in both the environment and their channel,

$$D(t - t') = \langle[-\mathrm{R}\Lambda_{t'}]|[-\mathrm{R}\Lambda_t]\rangle\langle[(1 - \mathrm{T})\Lambda_{t'}]|[(1 - \mathrm{T})\Lambda_{t'}]\rangle\,. \tag{3.111}$$

Here, we can show in exactly the same way that the decoherence coefficient for Slater determinants is also given by the overlap of the states created by *a pair* of localized excitations, in their environment and in

their channel:

$$
\begin{aligned}
D^{(2)}&(t_1,t_2,t_1',t_2') \\
&= \frac{D(t_1-t_1')D(t_2-t_2')D(t_2-t_1')D(t_1-t_2')}{|D(t_1-t_2)D(t_1'-t_2')|} && \text{(3.112a)} \\
&= \langle[-\mathrm{R}(\Lambda_{t_1'}+\Lambda_{t_2'})]|[-\mathrm{R}(\Lambda_{t_1}+\Lambda_{t_2})]\rangle \\
&\times \langle[(1-\mathrm{T})(\Lambda_{t_1'}+\Lambda_{t_2'})]|[(1-\mathrm{T})(\Lambda_{t_1'}+\Lambda_{t_2'})]\rangle\,. && \text{(3.112b)}
\end{aligned}
$$

From these arguments, a reasonable guess for a more generic case is that, whenever we send n electrons in a system, we can get that the modified excess term for n-th order coherence after an interaction region is simply given by

$$
\begin{aligned}
&\Delta\mathcal{G}^{(ne)}_{\mathrm{M}\Delta,ne\text{- inj.}}(\mathbf{t}|\mathbf{t}') = \\
&\Phi_{1\cdots n}(\mathbf{t})\Phi^*_{1\cdots n}(\mathbf{t}')\,\langle[R_{\mathbf{t}'}]|[R_{\mathbf{t}}]\rangle\,\langle[1-T_{\mathbf{t}'}]|[1-T_{\mathbf{t}}]\rangle
\end{aligned}
\tag{3.113}
$$

with $|[R_{\mathbf{t}}]\rangle$ and $|[1-T_{\mathbf{t}}]\rangle$ the states generated respectively in the environment and the channel by a n-uplet of localized excitations emitted at times t_i. This n-th order effective decoherence coefficient may certainly be expressed as

$$
D^{(n)}(\mathbf{t},\mathbf{t}') = \frac{\prod_{i=1}^n\prod_{j=1}^n D(t_i-t_j')}{\prod_{i=1}^n\prod_{j=i}^n |D(t_i-t_j)D(t_i'-t_j')|}\,. \tag{3.114}
$$

How could we go further than this result? One thing we know about $D(t)$ is that its Fourier transform can be separated into an elastic and an inelastic part: $\tilde{D}(\omega') = 2\pi(Z_\infty\delta(\omega') + d(\omega'))$. Exactly as before, using this decomposition would be instrumental for numerically evaluating these expressions and thus extracting explicit results.

Unfortunately, I did not have the time to perform this last but very important test. In my opinion, some extra work is also needed to precisely understand the physical content of the expressions obtained before, and even if I have started to work on them, it did not seem mature enough to be explicited in the present manuscript. Nevertheless, the roadmap for completing this work is clear and it will certainly lead to interesting and maybe surprising results.

Conclusion

> La houle est passée, faites place au vide.
>
> D É L U G E
> *Houle*

As we come to the end of this manuscript, it is time to look back at its title – Measurement and control of electronic coherences – under the light of what has been achieved. Starting with the end of this title, I think that it will be clear for any reader that this manuscript was indeed about electronic coherences. We have spent a good part of chapter 1 defining them, both in the first and higher order cases. I have tried to explain their physical meaning and to give a clear vision of the subtleties awaiting us when considering n-th order coherence. In particular, the symmetries and representations of second order coherence in a 4-dimensional space have been extensively discussed.

Chapter 2 is all about the very first word of this title: measurement. After a complete review of the different methods used in electron quantum optics to measure first order coherence through interferometry experiments, this chapter presented two works to which I had the opportunity to contribute. The first of them [OP4] is the development of a new tool to measure and analyze an unknown single electron coherence. In this work done in close collaboration with the Laboratoire Pierre Aigrain in Paris, we have demonstrated the two stages of what we call a quantum signal analyzer. Even if that denomination may sound a bit exotic, it extracts and processes single electron coherence in order to provide us with a simple and easily understandable representation of the single particle content of the quantum electical current under consideration. Indeed, we have demonstrated the first experimental realization of the *generic* tomography protocol proposed a few years ago by C. Grenier [66], and

pipelined it into a signal processing analysis, extracting from it what we call electronic atoms of signal [OP5], their emission probabilities and coherences. This approach has allowed us to discuss quantum electrical currents in a way that is completely new in our community. For the first time, we have extracted the different single-electron wavefunctions that are present in the current created by a sinusoidal drive and obtained from this analysis a better understanding of the role of electronic temperature in the smoothing out of coherence as well as in the change of electronic emission probabilities. We hope that our quantum signal analyzer will become a useful tool in electron quantum optics experiments and will earn its place among all other standard tools of mesoscopic physics as a way to characterize quantum electrical currents.

The second part of my work on the measurement of electronic coherences aims at reconstructing higher order coherences, and more specifically the second order one. Inspired both by what already exists for first order coherence measurement in our domain and for higher order measurements in photon quantum optics, we devised a series of interferometers based on Franson interferometry. The first one, using current correlations between the outputs of the direct equivalent of this interferometer, was discussed at the very beginning of my PhD in a work mainly done by E. Thibierge [OP6]. It aims at reconstructing second order coherence in the time domain, probing in a direct way the existence of quantum coherence between pairs of electrons emitted at different times. This is for example the case of time-bin entangled pairs that was discussed in this manuscript, but could also be the case of other type of sources. However, this proposal suffers from the same problem as the measurement of single electron coherence by a Mach-Zehnder interferometer: the drastic effect of Coulomb interactions within the measurement device itself may obliterate the coherence signal we wish to reconstruct.

I have then explored an alternative path to two electron tomography through its overlap with the two electron coherence signal corresponding to well controlled sources. This is nothing but the quest for a second order equivalent to the HOM tomography protocol devised in the first order case. However, while I have found interferomery experiments that lead to signals related to the overlap of second order coherence functions, we still need to analyze more precisely which known signals are the best for enabling a full and accurate reconstruction of the unknown second order coherence. This project is not fully completed but we can consider that the major steps have already been taken.

The other important word of my title, "Control", might look at first glance as a strange word for anyone not familiar with the field of electron quantum optics or quantum information. Why would we need to control the coherence of single to few electron excitations in a conductor? Is there some external factor, that would precisely be out of our control, acting on electronic coherences and preventing us from using electrons as photons in a quantum optics experiment ?

The answer, stated in chapter 3, is yes. Screened Coulomb interaction between electrons in and outside of the conductor under consideration is a major source of decoherence in our system. It needs to be taken into account quantitatively in order to understand any electron quantum optics experiment. In other words, electron quantum optics is generically non-linear, by contrast with its usual photonic counterpart. The control of electronic decoherence then leads to two interesting questions. Can we characterize the non-linearities of electron quantum optics? Can we limit their effect in real experiments? Interestingly, these questions come from the two possible meanings of the verb "control", as it can be used either in the sense of "supervise" or "regulate". Both meanings were indeed used in my approach to electronic decoherence.

Under the supervision side, I have discussed how a non-perturbative approach can be developed to compute the effect of any effective model for linearily screened Coulomb interactions on any single-electron wavepacket [OP2], using it for several physical cases. This study of first order coherence has allowed us to discuss the extent to which electrons are affected by the presence of other charges in the system, highlighting the crucial difference between pointer states that can be seen as coherent plasmonic states such as Levitons and generic ones that are superpositions of such pointer states such as energy resolved excitations. In this latter case, interactions lead to a loss of coherence between the different parts of the superposition, resulting in a complete destruction of the excitation itself and its energy relaxation towards the Fermi level. This is nothing but the exact analogue of Landau's quasiparticle problem in an unidimensional channel. The HOM experiment performed in G. Fève's group in Paris is indeed the first real-life implementation of this famous thought experiment in quantum Hall edge channels, thus illustrating that even in a complicated condensed matter system, some of the founding fathers' dreams can also be realized. These experimental results have confirmed our predictions and the relevance of the decoherence scenario we have unraveled, stressing the role of many-body decoherence induced

by the edge channel's electromagnetic environement.

The last section of my manuscript explores the few-body physics of electrons within a strongly interacting conductor. This is really the new frontier of electron quantum optics since it may offer us a unique window on the buildup and dynamics of quantum correlations in a many-body interacting quantum fluid. Motivated by this perspective, I have computed the effect of Coulomb interaction on more general electronic excitations, extending it both to higher order coherences and to cases where more than one electron has been injected into the system. Even if we have obtained a full analytical solution to the problem that can be written down as a quite compact formula, a complete numerical implementation avoiding any approximation but discretization seems to be out or reach for the moment, apart from the few cases we have indeed treated. Nevertheless, we have been able to discuss the physical meaning of several key cases, explaining how a single high-energy excitation could create second order coherence under the effect of interaction, as well as how a coherent two-electron high-energy excitation evolves in the presence of effective Coulomb interactions that are not too strong to smash it down to the Fermi level. These preliminary results still require some extra work in order to express their full potential but I think they already correspond to a significant step in our understanding of the dynamics of few electron excitations, a problem that has not really been investigated in depth by the quantum transport community.

Under the regulation side of the word "control", I have discussed in sections 3.3 and 3.4 several ideas on passive ways of limiting electronic decoherence [OP1]. Our study of interaction with a closed region of environment shows that such sample designs could indeed lead to a good protection against decoherence for electrons emitted under some energy given by the specific size of the sample, while our study of the $\nu = 1$ case for interactions highlighted the importance of velocity in the interaction strength, and therefore on decoherence. We suggest that changing the material from AsGa to a higher Fermi velocity one could lead to drastic improvements on the typical time over which decoherence would happen, leading to even more impressive results on the length scale over which an electron could propagate without being much disturbed by its environment. In particular, exfoliated graphene could prove very interesting to study. We hope that electron quantum optics experiments aiming at measuring precisely electronic decoherence in this material will be performed in the forthcoming years.

However, a title is not just a bunch of fancy keywords: these words have not been assembled for poetic reasons and the full title has a meaning. Indeed, a central part of my work has been focused on the experimental confirmation of our electronic decoherence scenario. This work [OP3], which stands at the exact crossing point of measuring electronic coherence and trying to understand what can happen to it, also put me at the crossing point between experimental and theoretical physics. Indeed, I have had the opportunity to contribute to this work both from the experimental point of view under the supervision of G. Fève and from the theoretical side under the supervision of P. Degiovanni. I think that the excellent agreement displayed in this thorough study of electronic decoherence between the measurements and calculations allows us to have some confidence in our predictions, and I hope that future works may confirm that not only our predictions are indeed valid in the case of decoherence control but also that electron quantum optics will now enter a new phase of its development in which various applications will be developped.

Perspectives

As for any research work, even if many questions asked in this manuscript have been given partial to complete answers, nothing is ever carved in stone. It is the logic of the ever-expanding domain of fundamental research that any answer calls for more questions, and this work indeed calls for several questions, which I will divide in two main categories:

- Direct expansion of the work presented throughout this manuscript. These are the most obvious questions and the roadmap towards answering them is pretty clear.
- New areas of research opened by the constant evolution of electron quantum optics as a whole. In these cases, the path to follow is often still foggy, but significant recent progresses have already occured and more might be in sight.

In the first category, we have already dispatched several hints in the manuscript about what remains to be done. Let us review them for a final wrap-up.

First of all, we are still at the very beginning of the use of tomography protocols and quantum analyzers as tools for the characterization of quantum electrical currents. Now that the benchmarking tests have

been passed, it would be of great interest to use these tools on the states emitted by single-electron sources. In particular, it would be interesting to measure and analyze the Wigner function obtained at the output of some interaction region in the real, experimental case.

This directly leads to another interesting development, this time from a theoretical point of view: in order to compare the results obtained in the laboratory with predictions for the full quantum signal processing experiment, two things remain to be done. The first one is the implementation of finite temperature effects in our theoretical apparatus computing the effect of interactions. I have already done some part of the analytical work. But as often, more interesting questions crossed our path and we did not take the time to implement these formula numerically. Yet, we may have such a tool in the next few months, but I think that the results will not be drastically different from the ones obtained at zero temperature when considering the decoherence of a single electron wavefunction. Indeed, thanks to our colleagues in Marseille, we already saw that the effect of temperature was not that strong on the HOM signal predictions for the actual experimental parameters.

The real challenge, which englobes the temperature dependence, resides in the description of Coulomb interaction effects on periodically driven sources. This is the main problem that should be addressed in order to expand the domain of validity of our approach to electronic decoherence: being able to describe not only single-electron wavepackets, but completely generic sources, and in particular time-periodic ones. To do so, we would need to go from the equilibrium bosonization used in this manuscript to the recently developped non-equilibrium bosonization [72]. First steps in this direction have already been made within our group, but some basic issues related to gauge invariance and the chiral anomaly still lie on our way. We know for sure that the numerical implementation step will no longer be possible on a small scale computer such as the one used to obtain the results presented here. High performance supercomputing will almost surely be necessary and therefore, all shadow zones must be cleaned up before moving on. I think that it is not impossible, and I would expect such a research program to move forward in a few years at most.

Still in the list of natural developments in the light of this conclusion, the extension of all the electron quantum optics framework to second and higher order coherences is still in its infancy. Proposing an operationally viable tomography protocol for second order coherence based on the dif-

ferent interferometers that were presented in this manuscript is clearly within reach. We are looking forward to the first proposals and then experimental demonstration of sources displaying non-trivial second order coherence, such as time-bin entangled pairs. Given the difficulty of noise measurements in a real experiment, I am unsure on how long it could take to really implement a protocol relying on the measurement of "noise of the noise", *i.e.* correlations between four currents, within a complex setup using single electron sources and Hong-Ou-Mandel interferometers. However, I think that such measurements of second order coherence could lead to interesting applications. For example, as was discussed at the very end of chapter 3, the emission of a coherent plasmonic excitations could be probed with this type of experiments. More generally, this type of question is related to understanding the relation between electron quantum optics and its photonic counterpart. Studying the light emitted by quantum electrical currents is already the subject of research both from the theoretical [68, 114] and experimental [55, 46, 158] point of views. This question, asked in particular by C. Mora, is under scrutiny in the context of electron quantum optics, between our group and his, and a first step in this direction is presented in the PhD of B. Roussel [138].

Finally, a particularly interesting extension of my work that will be hopefully completed in the next few months is the study of delocalized electronic excitations over several channels and their evolution under the effect of interaction. This is of particular interest for several reasons: first, this is directly related to the physics of the electronic Mach-Zehnder interferometer since the first beamsplitter will create a delocalized excitation over the two branches, which will then interact with their environment. If we want to predict accurately the signal at the output of a Mach-Zehnder interferometer, it is therefore necessary to develop a way to study the evolution of such delocalized excitations. Moreover, if we want to study decoherence protection in the Mach-Zehnder interferometers, we need to adapt the calculations made for loops in this manuscript to the case of delocalized excitations. The second interest comes from the idea of using single electron excitations as flying qubits in a railroad system where being on one channel encodes a classical bit of information. This motivates understanding the dynamics of a single electron excitation delocalized over the two channels of a $\nu = 2$ system. However, we have shown that interactions would lead to a strong loss of coherence, and it is natural to ask ourselves how the state of our flying

qubit would evolve during its propagation along the experimental setup. In the same idea, it would also be quite natural to try to protect this qubit state from decoherence with a suitable choice of either the material or the sample design. New designs may therefore be imagined and their performances estimated using the ideas and methods developed in this work. During my PhD, I have started this study of delocalized excitations propagating across an interaction region. I have made analytical computations of the evolution of coherence for generic cases where channels could interact with several (independent or not) environments and with each other. Everything is ready for numerical implementation but I did not have the time to implement the numerical evaluation of these results, and this study could not make it into the present manuscript. However, I am confident that this study can be finished soon, and that its results could be of great interest in our community.

After this brief overview of the works which I have started but which are not yet finished, let me give some insight on more prospective lines of research for electron quantum optics. Some of them are just only starting, but could potentially grow much bigger in the years to come.

First, the recent demonstration of superconducting correlations in edge channels of the quantum Hall effect [102, 121, 70] asks the question of the interplay between the concepts and ideas behind electron quantum optics and superconductivity. In particular, superconductors could lead to non-zero correlators of the form $\langle\psi\psi\rangle$, completely modifying the way in which coherences behave and evolve in our framework. For me, there is no doubt that this domain is bound to take off.

Second, it will be no surprise to anyone familiar with the quantum Hall effect that I shall mention the fractional quantum Hall effect [164, 100, 154]. This new state of matter manifests itself by new plateaus in the Hall resistance for fractional filling factors of the form p/q, with p and q two co-prime numbers. In these states, since there are indeed many of them, it has been shown that charge carriers where no more electrons but composite fermions [87] that carry a charge $e^* = e/q$. This was demonstrated experimentally for several different values of q [127, 132], and several experiments studying the shot noise of such excitations [141] have been realized to probe the fractional charge of these elementary excitations. From a theoretical point of view, composite fermions are interesting particles, since it has been shown that their statistics could be engineered to create anyons [87], a type of particles such that the state of a pair of two anyons takes a phase which is neither 0 or π

under the braiding of the two particles. The strength of anyons is also in their use in the field of quantum information, where proposals have been made to create fault-tolerant quantum computers based on these excitations [94]. From an electron quantum optics point of view, anyons may lead to completely new physics, but the situation should be much more complex since there is no ideal beamsplitter for anyons. Despite this limitation, attempts have been made for extending the electron quantum optics framework to the case of the fractional quantum Hall regime, with proposals for single quasi-particle emission [42], studies of minimal excitations in the fractional quantum Hall regime [130, 168], discussions of the photoassisted noise [167], and HOM experiments with trains of Levitons excitations in the fractional quantum Hall regime [133].

A personal take on quantum information

As I think will be clear both from the introduction and the conclusion of this work, I have a great interest in quantum information. Indeed, I have spent the last three years not only working on the fate of electrons sent in the edge channels of the quantum Hall effect, but also writing a book on quantum information with P. Degiovanni, N. Portier, A. Feller and B. Roussel. This two volume book should be published in 2018 or 2019 through the Éditions Savoirs Actuels, associated with the CNRS. I think that this manuscript, and more generally all the work I did during my PhD, have been heavily influenced by the research I did for the writing of this book.

To be a bit more precise, our book may seem to be about quantum physics at first sight, but its central topic is relations. It deals first with the relations between three domains that have shaped the 20th century, and have already interacted far more than what can be thought at first glance: quantum physics, information theory and computation theory. These three domains fed one another for more than 50 years now, each of them shedding some light on some specific aspects of the others. This led, of course, to the development of the field known today as quantum information, which aims at using quantum resources as means of communication [7] or computation [148, 69]. I think that the current state of experimental quantum mechanics would be far less advanced if the long term perspective of building a quantum computer was not so appealing. The completely new ideas that this dream has put forward

are unparalleled and could really lead to a huge paradigm shift in many areas of science in the next decades.

But our book is not only a book on the development of a quantum computer or, more generally, on quantum technologies, as this is covered already in quite a large number of textbooks. Of course, we do provide the reader with the necessary background to enter this exciting field. But along writing the book, we have also decided to turn things around, and use information theory and computation theory as a way to learn new things about quantum physics, in the same way that quantum physics has led to new research areas in the other domains. This intellectual journey has taught us that quantum theory, in itself, is a theory about relations. In particular, following the work of Everett [40], we discuss that the state of a system cannot be an objective quantity in the general case, but is always relative to the state of all other systems with which it has interacted. This relational vision of quantum physics, which is of course at the heart of the decoherence theory that was used extensively in this manuscript, has finally allowed us to draw some parallel between quantum physics and general relativity. Both of them are relational theories that do not describe an absolute reality but a net of relations betwteen different descriptions by physical observers, the real predictive power of both theories giving us access to correlations between events recorded by these observers.

Of course, our book does not go further than simply explaining this parallel since a complete theory including both general relativity and quantum theory is not yet available. However, my personal opinion is that such a theory should exist, due to the strong conceptual similarities between its two parts. Whether the answer to this question will be quantum strings, quantum loops, or a completely unthought construction still needs to be discovered. I can only hope that the answer will not elude the physics community for too long, and I would be glad to be able to see it during my lifetime.

Appendices

Appendix A

Conventions

In this manuscript, the following conventions are adopted with respect to wavepackets, operators, and Fourier transforms.

$$\int |\varphi(x)|^2 \mathrm{d}x = 1 \tag{A.1}$$

$$v_\mathrm{F} \int |\varphi(t)|^2 \mathrm{d}t = 1 \tag{A.2}$$

$$\frac{1}{v_\mathrm{F}} \int |\varphi(\omega)|^2 \frac{\mathrm{d}\omega}{2\pi} = 1 \tag{A.3}$$

$$\varphi(\omega) = v_\mathrm{F} \int \varphi(t) \mathrm{e}^{\mathrm{i}\omega t} \mathrm{d}t \tag{A.4}$$

$$\left\{\psi(x), \psi^\dagger(x')\right\} = \delta(x - x') \tag{A.5}$$

$$\left\{\psi(t), \psi^\dagger(t')\right\} = \frac{\delta(t - t')}{v_\mathrm{F}} \tag{A.6}$$

$$\left\{c(\omega), c^\dagger(\omega')\right\} = \delta(\omega - \omega') \tag{A.7}$$

$$c(\omega) = \sqrt{\frac{v_\mathrm{F}}{2\pi}} \int \psi(t) \mathrm{e}^{\mathrm{i}\omega t} \mathrm{d}t \tag{A.8}$$

Appendix B

Computing outgoing coherences

In this appendix, we are going to give all the building blocks that allow us to compute numerically the outgoing first order coherence after an interaction region.

B.1 Basic blocks

Let us briefly recall the main idea of what we are interested in, as was discussed in section 3.1.3.

We are searching the propagators allowing to compute the outgoing coherence from the incoming one. The best strategy, as was explained in the main text, is to evaluate them in the frequency domain. In the interacting case, the real part of interest is the decoherence coefficient $D(t, t', t_+, t_-)$. Its Fourier transform can be obtained as a convolution involving the Fourier transforms:

$$\Gamma_\pm(\omega) = \int_{-\infty}^{+\infty} \mathrm{e}^{\mathrm{i}\omega t} \exp\left(\pm \int_0^{+\infty} (1 - \mathrm{T}(\omega'))(\mathrm{e}^{\mathrm{i}\omega' t} - 1)\frac{\mathrm{d}\omega'}{\omega'}\right) \mathrm{d}t\,. \quad \text{(B.1)}$$

Assuming that

$$\kappa_\pm = \exp\left(\mp \int_0^{+\infty} (1 - \mathrm{T}(\omega))\frac{\mathrm{d}\omega}{\omega}\right)$$

is finite and non zero, which can always be ensured by a suitable ultraviolet regularization since it is known that $\mathrm{T}(\omega) - 1 \simeq \mathcal{O}(\omega)$ at $\omega \to 0^+$,

these Fourier transforms have a δ singularity at $\omega = 0$ and a regular part for $\omega < 0$:

$$\Gamma_{\pm}(\omega) = 2\pi\kappa_{\pm}\left(\delta(\omega) + B_{\pm}(-\omega)\right) \tag{B.2}$$

where $B_{\pm}(\omega)$ are regular functions vanishing for $\omega < 0$. As we shall see, once the functions $B_{\pm}$ are known, the Fourier transform of the decoherence coefficient is known.

More precisely, using the decomposition given by equation (B.2), the Fourier transform of the decoherence coefficient D can be decomposed as a sum of $2^4 = 16$ terms. Therefore, each of the propagators is also a sum of 16 terms. One among the 16 terms of the modified vacuum propagator[1] contains the Fermi sea contribution. This means that the analytic expressions for the full propagator giving the excess outcoming single electron coherence involve 31 terms which will be detailed in the present section. Although quite tedious, these expressions provide a perfect control of all the infrared singularities arising in a direct time domain computation at vanishing temperature [171].

Before detailing these 31 terms, let us mention that both auxiliary functions $B_{\pm}(\omega)$ are evaluated for positive frequencies by solving numerically the following integral equations:

$$\omega B_{\pm}(\omega) = \pm\left[1 - \mathrm{T}(\omega) + \int_0^{\omega} \mathrm{d}\omega' B_{\pm}(\omega')\left(1 - \mathrm{T}(\omega - \omega')\right)\right] \tag{B.3}$$

where the initial value $B_{\pm}(0^+)$ is defined using the derivatives of $\mathrm{T}(\omega)$:

$$B_{\pm}(0^+) = \pm \lim_{\omega \to 0^+} \frac{1 - \mathrm{T}(\omega)}{\omega}\,. \tag{B.4}$$

Expressions in the case of effective short range interactions in the $\nu = 2$ edge channel system are given in appendix section B.3. They have been used to check the validity of the numerical solutions for $B_{\pm}$ in this case.

[1] The one where we take the δ part of each Γ function.

B.2 The wave packet contribution

The wave packet contribution is a sum of two contributions of the following form:

$$\Delta\mathcal{G}^{(e)}_{\mathrm{WP}}\left(\omega+\frac{\delta\omega}{2},\omega-\frac{\delta\omega}{2}\right)$$
$$=\widetilde{\varphi}_e\left(\omega+\frac{\delta\omega}{2}\right)\widetilde{\varphi}^*_e\left(\omega-\frac{\delta\omega}{2}\right)\mathcal{Z}\left(\omega+\frac{\delta\omega}{2}\right)\mathcal{Z}^*\left(\omega-\frac{\delta\omega}{2}\right) \tag{B.5a}$$
$$+\int_{-\infty}^{+\infty}\widetilde{\varphi}_e\left(\omega'+\frac{\delta\omega}{2}\right)\widetilde{\varphi}^*_e\left(\omega'-\frac{\delta\omega}{2}\right)K^{(\mathrm{ne})}_{\mathrm{WP}}\left(\omega,\omega';\delta\omega\right)\,\mathrm{d}\omega'\,. \tag{B.5b}$$

The first contribution, equation (B.5a), contains the purely elastic contribution corresponding to the electronic excitation going through the interaction region without experiencing any inelastic process. The elastic scattering amplitude $\mathcal{Z}(\omega_0)$ for an electron at incoming energy $\hbar\omega_0>0$ is given by [32]:

$$\mathcal{Z}(\omega_0)=1+\int_0^{\omega_0}B_-(\omega')\,\mathrm{d}\omega'\,. \tag{B.6}$$

Let us recall that the inelastic scattering probability for the electron at initial energy $\hbar\omega_0$ is then given by

$$\sigma_{\mathrm{in}}(\omega_0)=1-\left|\mathcal{Z}(\omega_0)\right|^2. \tag{B.7}$$

The second contribution, which contains the inelastic wave packet part $K^{(\mathrm{ne})}_{\mathrm{WP}}$ of the propagator, is given by

$$K^{(\mathrm{ne})}_{\mathrm{WP}}\left(\omega,\omega';\delta\omega\right)$$
$$=B_+(\omega'-\omega)\mathcal{Z}\left(\omega+\frac{\delta\omega}{2}\right)\mathcal{Z}^*\left(\omega'-\frac{\delta\omega}{2}\right)+\ \text{conj.} \tag{B.8a}$$
$$+\int_{-\infty}^{+\infty}B_+(k)B^*_+(\omega'-\omega-k)\mathcal{Z}\left(\omega'+\frac{\delta\omega}{2}-k\right)\mathcal{Z}^*\left(\omega-\frac{\delta\omega}{2}+k\right)\mathrm{d}k \tag{B.8b}$$

where the notation $f(\delta\omega)+\ $conj. should be understood as $f(\delta\omega)+f^*(-\delta\omega)$.

The modified vacuum contribution

The vacuum contribution to the excess single electron coherence K_{MV} is given by:

$$\begin{aligned}
&\Delta\mathcal{G}^{(e)}_{\mathrm{MV}}\left(\omega+\frac{\delta\omega}{2},\omega-\frac{\delta\omega}{2}\right)\\
&=\int_{-\infty}^{+\infty}K_{\mathrm{MV}}(\omega,\omega';\delta\omega)\times\widetilde{\varphi}_e\left(\omega'+\frac{\delta\omega}{2}\right)\widetilde{\varphi}^*_e\left(\omega'-\frac{\delta\omega}{2}\right)\mathrm{d}\omega'\,. \qquad \text{(B.9)}
\end{aligned}$$

The modified vacuum propagator $K_{\mathrm{MV}}(\omega,\omega',\delta\omega)$ can be expressed as a sum of a part arising from singularities and a part which involves no δ distributions, which is called the regular part:

$$K_{\mathrm{MV}}(\omega,\omega';\delta\omega)=K^{(\mathrm{sing})}_{\mathrm{MV}}(\omega,\omega';\delta\omega)+\int_{\omega}^{+\infty}\mathcal{F}^{(\mathrm{reg})}_{\mathrm{MV}}(k,\omega';\delta\omega)\,\mathrm{d}k\,. \quad \text{(B.10)}$$

The singular part is given by

$$\begin{aligned}
&K^{(\mathrm{sing})}_{\mathrm{MV}}(\omega,\omega';\delta\omega)\\
&=B_-(\delta\omega)\,\mathrm{H}\left(-\omega+\frac{\delta\omega}{2}\right)+\ \text{conj.} && \text{(B.11a)}\\
&+B_+(\delta\omega)\,\mathrm{H}\left(-\omega-\frac{\delta\omega}{2}\right)+\ \text{conj.} && \text{(B.11b)}\\
&+\mathrm{H}\left(-\omega+\frac{\delta\omega}{2}\right)\int_0^{\infty}B_-\left(\omega'-k+\frac{\delta\omega}{2}\right)B^*_+\left(\omega'-k-\frac{\delta\omega}{2}\right)\mathrm{d}k\\
&+\ \text{conj.}\,. && \text{(B.11c)}
\end{aligned}$$

The various Heaviside functions H show that $K^{(\mathrm{sing})}_{\mathrm{MV}}(\omega,\omega';\delta\omega)$ corresponds to discontinuities at the boundaries between the (e) and (h) quadrants as well as at the boundaries between the (e/h) and (h) quadrants [41]. Finally, the regular part is the integral over k from ω to

infinity of:

$$
\begin{aligned}
&\mathcal{F}^{(\mathrm{reg})}_{\mathrm{MV}}(k,\omega';\delta\omega) \\
&= B_+\left(-k+\frac{\delta\omega}{2}\right) B_-\left(k+\frac{\delta\omega}{2}\right) + \text{ conj.} && \text{(B.12a)}\\
&+ B_-\left(k+\frac{\delta\omega}{2}\right) B_-^*\left(k-\frac{\delta\omega}{2}\right) \mathrm{H}(\omega'-k) && \text{(B.12b)}\\
&+ B_+\left(-k+\frac{\delta\omega}{2}\right) B_+^*\left(-k-\frac{\delta\omega}{2}\right) \mathrm{H}(\omega'+k) && \text{(B.12c)}\\
&+ \int_0^\infty B_+^*\left(\omega'-q-\frac{\delta\omega}{2}\right) B_-\left(\omega'-q+k\right) B_+\left(-k+\frac{\delta\omega}{2}\right) \mathrm{d}q \\
&+ \text{ conj.} && \text{(B.12d)}\\
&+ \int_0^\infty B_-^*\left(\omega'-q-\frac{\delta\omega}{2}\right) B_+\left(\omega'-q-k\right) B_-\left(k+\frac{\delta\omega}{2}\right) \mathrm{d}q \\
&+ \text{ conj.} && \text{(B.12e)}\\
&+ \int_0^\infty \mathrm{d}q \int_{-\infty}^\infty \mathrm{d}q' && \text{(B.12f)}\\
&\quad B_+\left(q'-\frac{1}{2}\left(q-\omega'-\frac{\delta\omega}{2}+k\right)\right) B_-\left(-q'-\frac{1}{2}\left(k-\omega'-\frac{\delta\omega}{2}-k\right)\right) \\
&\times B_+^*\left(-q'-\frac{1}{2}\left(q-\omega'+\frac{\delta\omega}{2}+k\right)\right) B_-^*\left(q'-\frac{1}{2}\left(q-\omega'+\frac{\delta\omega}{2}-k\right)\right)
\end{aligned}
$$

The most complicated term to compute is, of course, the one involving the most integrals, from equation (B.12f). Section 3.1.3 explains how we can do our best to use the decomposition given above to limit the total computational complexity.

B.3 Analytical results

To test that our numerical approach was valid, we were able to give analytical expressions for functions $B_\pm(\omega)$ and the elastic scattering probability $\mathcal{Z}(\omega)$, in the specific case of short-range interaction in a $\nu = 2$ system. This work was mainly done with D. Ferraro during my M1 internship, and can be used to check that our computation works as

intended. We get

$$B_+(\omega) = -\mathrm{i}\tau_+^{p_+}\tau_-^{p_-}\mathrm{H}(\omega) + \frac{p_+p_-}{2} \tag{B.13a}$$
$$+ \frac{(\tau_- - \tau_+)^2}{\tau_+}\mathrm{e}^{-\mathrm{i}\omega\tau_+}\phi_1\left[\frac{1}{2}+p_+, 1, 3; 1-\frac{\tau_-}{\tau_+}, \mathrm{i}\omega(\tau_- - \tau_+)\right]$$

$$B_-(\omega) = \mathrm{H}(\omega)\Bigg(\mathrm{i}\tau_{+\,1}F_1\left[p_+, 1; \mathrm{i}\omega(\tau_- - \tau_+)\right] \tag{B.13b}$$
$$+ \mathrm{i}(\tau_- - \tau_+)p_{+\,1}F_1\left[\frac{1}{2}+p_+, 2; -\mathrm{i}\omega(\tau_- - \tau_+)\right]\Bigg)$$

$$\mathcal{Z}(\omega) = \mathrm{e}^{\mathrm{i}\omega\tau_+}{}_1F_1\left[p_+, 1; \mathrm{i}\omega(\tau_- - \tau_+)\right] \tag{B.13c}$$

where $p_\pm$ and $\tau_\pm$ are defined in equation (3.33), $\mathrm{H}(\omega)$ denotes the Heaviside function, ${}_1F_1(\alpha, \beta; \gamma)$ is the confluent hypergeometric function and $\phi_1(\alpha, \beta, \gamma; x, y)$ is the Humbert double series. The definition and all useful properties of these complicated functions can be found, for example, in Gradshteyn, Jeffrey, and Ryzhik [64].

Appendix C

Interactions and high-order coherences

In this appendix, we are going to detail how the compact formula from equation (3.81) can be derived from the same type of computations as the one done for first order coherence. What we are interested in is therefore the n-th order coherence of a system where we emit p electrons in wavefunctions $(\varphi_i)_{i=1,;p}$, after going through an interaction region of size l described by the unitary scattering matrix $S(\omega)$. All electrons are emitted in the same channel, which we call channel 1: $|\varphi_{\text{in}}\rangle = \prod_{i=1}^{p} \psi^\dagger[\varphi_i]\,|F\rangle_1 \otimes |F\rangle_2$.

C.1 Computing the outgoing state

The first step to compute coherence is to compute the state itself, which will only be easy in a bosonic point of view since interactions are directly bosonic scattering. Let us use the dictionnary from section 1.4 to write the incoming and outgoing states as bosonic states.

C.1.1 Incoming state expression

The incoming state can be written as

$$|\varphi_{\text{in}}\rangle = \int \prod_{i=1}^{p} \left[\mathrm{d}t_{i,+} \varphi_i(t_{i,+}) \frac{U_1^\dagger}{\sqrt{2\pi a}} \mathcal{D}_1[-\Lambda_{t_{i,+}}(\omega)] \right] |0\rangle_1 \otimes |0\rangle_2 \,. \tag{C.1}$$

Using properties of the displacement operators given in equation (1.114), we can write

$$\mathcal{D}\left[-\Lambda_{t_{1,+}}(\omega)\right]\mathcal{D}\left[-\Lambda_{t_{2,+}}(\omega)\right] = \exp\left(\mathrm{i}\int_0^\infty \frac{\mathrm{d}\omega}{\omega}\mathrm{Im}\left(\mathrm{e}^{\mathrm{i}\omega(t_{1,+}-t_{2,+})}\right)\right)\mathcal{D}\left[-\Lambda_{t_{1,+}}(\omega)-\Lambda_{t_{2,+}}(\omega)\right]. \tag{C.2}$$

Since all subsequent displacement operators will lead to the same types of results, we have

$$\prod_{i=1}^{p}\mathcal{D}\left[-\Lambda_{t_{i,+}}(\omega)\right] = \exp\left(\mathrm{i}\int_0^\infty \frac{\mathrm{d}\omega}{\omega}\sum_{i>j}\mathrm{Im}\left(\mathrm{e}^{\mathrm{i}\omega(t_{i,+}-t_{j,+})}\right)\right)\mathcal{D}\left[\sum_{i=1}^{p}-\Lambda_{t_{i,+}}(\omega)\right] \tag{C.3}$$

and thus

$$|\varphi_{\mathrm{in}}\rangle = \int\prod_{i=1}^{p}\mathrm{d}t_{i,+}\varphi_i(t_{i,+})\exp\left(\mathrm{i}\int_0^\infty\frac{\mathrm{d}\omega}{\omega}\sum_{i>j}\mathrm{Im}\left(\mathrm{e}^{\mathrm{i}\omega(t_{i,+}-t_{j,+})}\right)\right)\left(\frac{U_1^\dagger}{\sqrt{2\pi a}}\right)^p\left|\left[\sum_{i=1}^{p}-\Lambda_{t_{i,+}}(\omega)\right]\right\rangle_1\otimes|0\rangle_2\,. \tag{C.4}$$

C.1.2 Outgoing state

The interaction zone is described by the bosonic scattering matrix

$$S(\omega) = \begin{pmatrix}\mathrm{T}(\omega) & \mathrm{R}_E(\omega)\\ \mathrm{R}(\omega) & \mathrm{T}_E(\omega)\end{pmatrix} \tag{C.5}$$

leading to the entangled outgoing state

$$|\varphi_{\mathrm{out}}\rangle = \int\prod_{i=1}^{p}\mathrm{d}t_{i,+}\varphi_i(t_{i,+})\left(\frac{U_1^\dagger}{\sqrt{2\pi a}}\right)^p\exp\left(\mathrm{i}\int_0^\infty\frac{\mathrm{d}\omega}{\omega}\sum_{i>j}\mathrm{Im}\left(\mathrm{e}^{\mathrm{i}\omega(t_{i,+}-t_{j,+})}\right)\right)\left|\left[\sum_{i=1}^{p}-\mathrm{T}(\omega)\Lambda_{t_{i,+}}(\omega)\right]\right\rangle_1\otimes\left|\left[\sum_{i=1}^{p}-\mathrm{R}(\omega)\Lambda_{t_{i,+}}(\omega)\right]\right\rangle_2. \tag{C.6}$$

The reduced density matrix describing channel 1 is therefore

$$\begin{aligned}\rho_{\text{out},1} = & \\ \int \prod_{i=1}^{p} & \mathrm{d}t_{i,+}\mathrm{d}t_{i,-}\varphi_i(t_{i,+})\varphi_i^*(t_{i,-}) \\ & \left\langle \left[\sum_{i=1}^{p} -\mathrm{R}(\omega)\Lambda_{t_{i,-}}(\omega)\right] \middle| \left[\sum_{i=1}^{p} -\mathrm{R}(\omega)\Lambda_{t_{i,+}}(\omega)\right] \right\rangle_2 \\ & \left(\left(\frac{U_1^\dagger}{\sqrt{2\pi a}} \right)^p \middle| \left[\sum_{i=1}^{p} -\mathrm{T}(\omega)\Lambda_{t_{i,+}}(\omega)\right] \right\rangle \\ & \left\langle \left[\sum_{i=1}^{p} -\mathrm{T}(\omega)\Lambda_{t_{i,-}}(\omega)\right] \middle|_1 \left(\frac{U_1}{\sqrt{2\pi a}} \right)^p \right) \\ & \exp\left(\mathrm{i}\int_0^\infty \frac{\mathrm{d}\omega}{\omega} \sum_{i>j} \mathrm{Im}\left(\mathrm{e}^{\mathrm{i}\omega(t_{i,+}-t_{j,+})} \right) \right) \\ & \exp\left(-\mathrm{i}\int_0^\infty \frac{\mathrm{d}\omega}{\omega} \sum_{i>j} \mathrm{Im}\left(\mathrm{e}^{\mathrm{i}\omega(t_{i,-}-t_{j,-})} \right) \right) . \end{aligned} \tag{C.7}$$

This state is, obviously, not a pure one!

C.2 Computing $\mathcal{G}^{(ne)}$ on the outgoing state

C.2.1 A bit of rewriting

We are trying to compute

$$\begin{aligned}\mathcal{G}^{(ne)}_{\text{out}}(t_1,\ldots,t_n|t'_1,\ldots,t'_n) = & \\ \mathrm{Tr}\left[\psi(t_n)\cdots\psi(t_1)\rho_{\text{out},1}\psi^\dagger(t'_1)\cdots\psi^\dagger(t'_n)\right] . & \end{aligned} \tag{C.8}$$

To rewrite things in a more compact manner, we can write back ψ and $\psi^\dagger$ operators from U and $U^\dagger$ ones. In that way, one operator can be written for each of the $t_{i,\pm}$, and all phases are absorbed by this rewriting. This is completely equivalent to what we did in equation (3.14) for first order

coherence, and leads to

$$\mathcal{G}^{(ne)}_{\text{out}}(t_1,\dots,t_n|t'_1,\dots,t'_n) = \tag{C.9}$$
$$\int\prod_{i=1}^{p}\mathrm{d}t_{i,+}\mathrm{d}t_{i,-}\varphi_i(t_{i,+})\varphi_i^*(t_{i,-})\,\langle[R_-]|[R_+]\rangle_2$$
$$\times\Big\langle[1-T_-]\Big|\Big(\psi(t_{1,-})\cdots\psi(t_{p,-})\psi^\dagger(t'_1)\cdots\psi^\dagger(t'_n)$$
$$\psi(t_n)\cdots\psi(t_1)\psi^\dagger(t_{p,+})\cdots\psi^\dagger(t_{1,+})\Big)\Big|[1-T_+]\Big\rangle_1$$

where we used the compact states

$$|[R_\pm]\rangle = \left|\left[\sum_{i=1}^{p}-\mathrm{R}(\omega)\Lambda_{t_{i,\pm}}(\omega)\right]\right\rangle \tag{C.10a}$$
$$|[1-T_\pm]\rangle = \left|\left[\sum_{i=1}^{p}(1-\mathrm{T}(\omega))\Lambda_{t_{i,\pm}}(\omega)\right]\right\rangle . \tag{C.10b}$$

Just as we did for first order coherence, it is now possible to rewrite the full product of ψ and $\psi^\dagger$ operators as a single normal ordered displacement operator $:\mathcal{D}[\alpha]:$, multiplied by some complex number β. A clever way to find this constant is simply to notice that $\langle:\mathcal{D}[\alpha]:\rangle_{\mathrm{F}} = 1$ for any value of the parameter α. Therefore, we know that the multiplicative constant β is equal to the same correlators of ψ and $\psi^\dagger$ appearing before, taken on the Fermi sea. This leads to

$$\mathcal{G}^{(ne)}_{\text{out}}(t_1,\dots,t_n|t'_1,\dots,t'_n) = \tag{C.11}$$
$$\int\prod_{i=1}^{p}\mathrm{d}t_{i,+}\mathrm{d}t_{i,-}\varphi_i(t_{i,+})\varphi_i^*(t_{i,-})\,\langle[R_-]|[R_+]\rangle_2$$
$$\Big\langle\psi(t_{1,-})\cdots\psi(t_{p,-})\psi^\dagger(t'_1)\cdots\psi^\dagger(t'_n)\psi(t_n)\cdots\psi(t_1)\psi^\dagger(t_{p,+})\cdots\psi^\dagger(t_{1,+})\Big\rangle_{\mathrm{F}}$$
$$\left\langle[1-T_-]\right|:\mathcal{D}\left[\sum_{i=1}^{p}\Lambda_{t_{i,+}}(\omega)-\Lambda_{t_{i,-}}(\omega)+\sum_{k=1}^{n}\Lambda_{t_k}(\omega)-\Lambda_{t'_k}(\omega)\right]:\left|[1-T_+]\right\rangle_1 .$$

C.2.2 Computing the different parts

The Fermi correlator part can be computed using Wick's theorem. What we are interested in is the decoherence coefficient constituted of two parts:

- The extrinsic decoherence coefficient $\langle[R_-]|[R_+]\rangle_2$ coming from the overlap between the states created in the environment channel.

- The intrinsic decoherence coefficient $\langle[1-T_-]|{:}\mathcal{D}\left[\cdot\right]{:}|[1-T_+]\rangle_1$ coming from the overlap between the electron-hole clouds generated inside the injection channel.

Computing $\langle[R_-]|[R_+]\rangle_2$

Using simply the definition of generalized coherent states, we have

$$\langle[R_-]|[R_+]\rangle_2 = \exp\left(\int_0^\infty \mathrm{d}\omega\, R_-^* R_+ - \frac{|R_+|^2}{2} - \frac{|R_-|^2}{2}\right) \tag{C.12}$$

and thus

$$\langle[R_-]|[R_+]\rangle_2 = \tag{C.13}$$
$$\exp\left(\int_0^\infty \frac{\mathrm{d}\omega}{\omega}|\mathrm{R}(\omega)|^2 \sum_{i,j=1}^{p}\left(\mathrm{e}^{\mathrm{i}\omega(t_{i,+}-t_{j,-})} - \frac{\mathrm{e}^{\mathrm{i}\omega(t_{i,+}-t_{j,+})}}{2} - \frac{\mathrm{e}^{\mathrm{i}\omega(t_{i,-}-t_{j,-})}}{2}\right)\right).$$

Computing $\langle[1-T_-]|{:}\mathcal{D}\left[\cdot\right]{:}|[1-T_+]\rangle_1$

There are two parts in this formula, a huge exponential function and the scalar product $\langle[1-T_-]|[1-T_+]\rangle$. This second part is easy to write, since it is exactly the same one as equation (C.13), replacing $|\mathrm{R}(\omega)|^2$ by $|1-\mathrm{T}(\omega)|^2$. The real work that remains to be done is therefore the computation of the exponential part coming from equation (1.116), which we denote by $\mathcal{F}$:

$$\mathcal{F} = \tag{C.14}$$
$$\exp\left(\int_0^\infty \mathrm{d}\omega \left(\sum_{i=1}^{p}\Lambda_{t_{i,-}}(\omega) - \Lambda_{t_{i,+}}(\omega) + \sum_{k=1}^{n}\Lambda_{t_k}(\omega) - \Lambda_{t'_k}(\omega)\right) T_-^* \right.$$
$$\left. - \left(\sum_{i=1}^{p}\Lambda_{t_{i,-}}(\omega) - \Lambda_{t_{i,+}}(\omega) + \sum_{k=1}^{n}\Lambda_{t_k}(\omega) - \Lambda_{t'_k}(\omega)\right)^* T_+\right).$$

We will divide this into two parts. The first one contains all terms where one t_k and one $t_{i,\pm}$ appear, denoted by $\mathcal{F}_1$, while the second one, $\mathcal{F}_2$, takes into account all parts using two $t_{i,\pm}$.

Part with times t_k This factor $\mathcal{F}_1$ is

$$\mathcal{F}_1 = \exp\left(\int_0^\infty \frac{\mathrm{d}\omega}{\omega} \sum_{k=1}^{n}\sum_{j=1}^{p} (1 - \mathrm{T}^*(\omega)) \left(\mathrm{e}^{-\mathrm{i}\omega(t_{j,-} - t_k)} - \mathrm{e}^{-\mathrm{i}\omega(t_{j,-} - t'_k)} \right) \right.$$
$$\left. - \sum_{k=1}^{n}\sum_{j=1}^{p} (1 - \mathrm{T}(\omega)) \left(\mathrm{e}^{\mathrm{i}\omega(t_{j,+} - t_k)} - \mathrm{e}^{\mathrm{i}\omega(t_{j,+} - t'_k)} \right) \right). \tag{C.15}$$

When using the usual functions defined as

$$\gamma_\pm(t) = \exp\left(\pm \int_0^\infty \frac{\mathrm{d}\omega}{\omega} (1 - \mathrm{T}(\omega))(\mathrm{e}^{\mathrm{i}\omega t} - 1) \right) \tag{C.16}$$

we get

$$\mathcal{F}_1 = \prod_{k=1}^{n}\prod_{j=1}^{p} \gamma_+^*(t_{j,-} - t_k)\gamma_-^*(t_{j,-} - t'_k)\gamma_+(t_{j,+} - t'_k)\gamma_-(t_{j,+} - t_k) \tag{C.17}$$

which reminds us of what we saw in the main text for first order coherence, as in equation (3.24) for example.

Part using only times $t_{i,\pm}$ This second part can be deduced quite easily:

$$\mathcal{F}_2 = \exp\left(\int_0^\infty \frac{\mathrm{d}\omega}{\omega} \sum_{i,j=1}^{p} (1 - \mathrm{T}^*(\omega)) \left(\mathrm{e}^{-\mathrm{i}\omega(t_{j,-} - t_{i,-})} - \mathrm{e}^{-\mathrm{i}\omega(t_{j,-} - t_{i,+})} \right) \right.$$
$$\left. - \sum_{i,j=1}^{p} (1 - \mathrm{T}(\omega)) \left(\mathrm{e}^{\mathrm{i}\omega(t_{j,+} - t_{i,-})} - \mathrm{e}^{\mathrm{i}\omega(t_{j,+} - t_{i,+})} \right) \right). \tag{C.18}$$

Product of both factors

The $\mathcal{F}_1$ factor will stay on its own and cannot be simplified any further. However, we can study with a bit more detail the product of the three factors $\mathcal{F}_2 \langle [R_-][R_+] \rangle \langle [1 - T_-][1 - T_+] \rangle$. When using the unitarity of $S(\omega)$, that implies $|\mathrm{R}(\omega)|^2 + |\mathrm{T}(\omega)|^2 = 1$ or equivalently $|\mathrm{R}(\omega)|^2 + |1 -$

$\mathrm{T}(\omega)|^2 = 1 - \mathrm{T}(\omega) + 1 - \mathrm{T}^*(\omega)$, we can rewrite

$$\begin{aligned}
&\mathcal{F}_2 \langle [R_-]|[R_+] \rangle \langle [1-T_-]|[1-T_+] \rangle \qquad \text{(C.19)}\\
&= \exp\left(\int_0^\infty \frac{\mathrm{d}\omega}{\omega} \mathrm{iIm}\left(\mathrm{T}(\omega)\right) \sum_{i,j=1}^{p} \left(\mathrm{e}^{\mathrm{i}\omega(t_{j,-}-t_{i,-})} - \mathrm{e}^{\mathrm{i}\omega(t_{j,+}-t_{i,+})} \right) \right)\\
&= \exp\left(\int_0^\infty \frac{\mathrm{d}\omega}{\omega} 2\mathrm{iIm}\left(\mathrm{T}(\omega)\right) \right.\\
&\qquad\qquad \left. \sum_{i=1}^{p} \sum_{j=i}^{p} \left(\cos(\omega(t_{j,-}-t_{i,-})) - \cos(\omega(t_{j,+}-t_{i,+})) \right) \right).
\end{aligned}$$

C.2.3 Final result

Putting everything back together, we finally get

$$\begin{aligned}
&\mathcal{G}^{(ne)}_{\mathrm{out}}(t_1,\dots,t_n|t'_1,\dots,t'_n) = \qquad \text{(C.20)}\\
&\int \prod_{i=1}^{p} \mathrm{d}t_{i,+}\mathrm{d}t_{i,-} \varphi_i(t_{i,+})\varphi_i^*(t_{i,-})\\
&\left\langle \psi(t_{1,-})\cdots\psi(t_{p,-})\psi^\dagger(t'_1)\cdots\psi^\dagger(t'_n)\psi(t_n)\cdots\psi(t_1)\psi^\dagger(t_{p,+})\cdots\psi^\dagger(t_{1,+}) \right\rangle_F\\
&\prod_{k=1}^{n}\prod_{i=1}^{p} \gamma_+^*(t_{i,-}-t_k)\gamma_-^*(t_{i,-}-t'_k)\gamma_+(t_{i,+}-t'_k)\gamma_-(t_{i,+}-t_k)\\
&\exp\left(\int_0^\infty \frac{\mathrm{d}\omega}{\omega} \mathrm{iIm}\left(\mathrm{T}(\omega)\right) \sum_{i,j=1}^{p} \left(\mathrm{e}^{\mathrm{i}\omega(t_{j,-}-t_{i,-})} - \mathrm{e}^{\mathrm{i}\omega(t_{j,+}-t_{i,+})} \right) \right).
\end{aligned}$$

Of course, we can then use Wick's theorem to divide the Fermi sea correlator into several smaller, computable parts, leading to the equivalent of wavepackets and modified vaccuum terms of this p-electrons, n-th order coherence case. It is also possible to divide each $\gamma_\pm$ function into a singular and regular part in pretty much the same way as we did in appendix B, in order to control all singularities that could appear in this coherence. Doing all this leads to a total number of terms N:

$$N = (n+p)! \times 2^{4np}\,. \qquad \text{(C.21)}$$

This result explains why we could not do a total computation for second order coherence for example, since the second simplest case is $n = 2, p = 1$. Trying to find the excess second order coherence created by a single

electron propagating through an interaction region leads to the computation of 1536 terms for full coherence, which is completely impossible to write down explicitly.

Résumé en français

Durant les quelques pages qui suivent, je vais essayer de résumer en français et de manière succinte le travail présenté dans ce manuscrit. Ce résumé ne fera pas justice à l'ensemble des détails présentés dans la version anglaise, mais s'attachera à faire ressortir les points les plus importants apparaissant dans cette thèse. Il s'agit essentiellement d'une traduction condensée de l'introduction et de la conclusion de ce travail, agrémentée de quelques figures et équations mettant en avant les résultats les plus importants de mon travail de recherche doctoral.

Contexte de cette thèse

Au sens large, cette thèse s'inscrit dans le domaine de l'information quantique. Cette branche de la physique a pour but la préparation, la manipulation et le contrôle de systèmes quantiques, et pourrait offrir de nouvelles possibilités en matière de communication ou de calcul. Cependant, malgré les très importantes avancées effectuées dans ce domaine [77], l'utilisation de la mécanique quantique comme outil quotidien de communication ou de calcul reste limitée par un effet appelé décohérence : lorsque le système que l'on souhaite utiliser peut s'intriquer avec son environnement, son état quantique va évoluer graduellement vers un état dit "relatif" à celui de l'environnement [185, 89, 186]. Cet effet de décohérence est un indice important pour la résolution de l'énigme de l'émergence du monde classique dans lequel nous vivons à partir de son homologue quantique [187]. Depuis les premières expériences sur le sujet [20], tout un pan de la recherche en physique quantique est ainsi dévolu à la compréhension de la décohérence, afin de mieux la contrôler. Comme nous le verrons, c'est l'une des thématiques principales de cette thèse.

Néanmoins, revenons pour le moment au domaine de l'information

quantique en général. Parmi les systèmes utilisables en laboratoire pour effectuer des expériences d'information quantique, les systèmes d'optique quantique partent avec un avantage de taille : à cause de leur nature, les photons n'interagissent pas entre eux et sont en général faiblement couplés à la matière, ce qui les isole de la décohérence. On a ainsi pu démontrer que des paires de photons intriqués pouvaient garder leur cohérence sur des centaines de kilomètres dans des fibres optiques ou dans l'espace [165, 131]. Cependant, cet avantage est aussi un inconvénient, car on veut également que les systèmes que l'on utilise puissent interagir entre eux. Des outils de matière condensée peuvent alors apporter une réponse parfaite à ce problème, car certains d'entre eux permettent de contrôler le couplage entre les degrés de liberté électromagnétique et ceux de la matière. En particulier, les circuits supraconducteurs sont généralement vus comme présentant les meilleurs chances dans la quête d'un ordinateur quantique [178], tout comme les systèmes de spintronique quantique qui restent un challenger prometteur combinant l'isolation d'un spin nucléique ou électronique unique avec la contrôlabilité d'un système mésoscopique, comme proposé par Kane [92]. Dans ce contexte, comprendre et contrôler les courant électriques quantiques jusqu'à l'échelle de l'électron unique paraît extrêmement important.

C'est dans cette perspective qu'un système spécfique est apparu comme très prometteur à la fin du XXe siècle, en particulier grâce aux fortes analogies qu'il présente avec l'optique quantique : les gaz bidimensionnels d'électrons en régime d'effet Hall quantique [96]. Ces systèmes ont une première propriété intéressante : le transport électronique s'y déroule dans des canaux de bords chiraux quasi-unidimensionnels, qui constituent un analogue électronique des fibres optiques [22]. La découverte expérimentale de l'équivalent électronique des lames semi-réfléchissantes [172, 173] a ensuite constitué un pas important, permettant la réalisation d'interféromètres de Mach-Zehnder [88], grâce auxquels on a pu observer que la cohérence des électrons dans ces canaux de Hall pouvait être conservée sur plusieurs micromètres [137]. En parallèle, les techniques permettant de mesurer des fluctuations de courants électriques ont été grandement améliorées, à la fois en sensibilité et en gamme de fréquence accessible [60, 122], permettant l'exploration de la dynamique électronique sur des temps inférieurs à la nanoseconde. Cependant, c'est la fabrication de sources à électrons uniques [44] qui a vraiment lancé le domaine dans lequel cette thèse s'inscrit, celui de l'optique quantique électronique [17]. Depuis cette découverte, le retard

accumulé sur l'optique quantique des photons a été petit à petit comblé, notamment à travers la réalisation de nombreuses expériences d'interférométrie [111] et de nouvelles sources d'électrons uniques [38, 4]. L'optique quantique électronique s'étend désormais également à d'autres systèmes que les canaux de Hall [43], et continue à se développer rapidement, comme l'atteste un récent volume de Physica Status Solidi [151] dédié à l'état de l'art de ce domaine émergent.

Cependant, si l'avantage des photons est leur sensibilité réduite à la décohérence, cela signifie que cette dernière constitue l'inconvénient majeur des systèmes électroniques. En effet, puisque les électrons sont des particules chargées, il vont être sensible à l'interaction Coulombienne lors de leur propagation. Sous l'effet de cette interaction avec tous les autres électrons présents dans le conducteur, les états quantiques électroniques vont perdre leur cohérence sur des distances de l'ordre de la taille typique des expériences. Cet effet va empêcher en général l'utilisation des électrons se propageant dans les canaux de bord de l'effet Hall quantique comme des "qubits volants", même si cela avait constitué une grande part de la motivation initiale pour développer ces systèmes [10, 86, 11, 184].

C'est dans ce contexte que mon travail prend place : puisque l'effet des interactions semblent interdire l'utilisation des systèmes d'optique quantique électronique pour l'information quantique, il semble alors naturel de nous concentrer sur l'étude des interactions elles-mêmes. Un programme de recherche ayant pour but la prédiction de l'effet de l'interaction de Coulomb sur des excitations électroniques dans des cas expérimentalement réalisable a alors été mis en place à Lyon autour de P. Degiovanni [32], tandis que le groupe expérimental dirigé par G. Fève au Laboratoire Pierre Aigrain travaillait sur le test expérimental de ces idées, afin de confimer ou d'infirmer les scénarios théoriques. Cette collaboration a mené à de nombreux développements à la fois expérimentaux et théoriques, qui sont présentés pour la plupart dans ce manuscrit et que je vais m'attacher à résumer dans les prochains paragraphes qui présenteront le contenu global des 3 chapitres de ce manuscrit. Pour chacun de ces chapitres, cette thèse contient à la fois des travaux publiés, qui sont dénotés par les références [OPx], ainsi que des résultats plus préliminaires qui donneront lieu à des publications ultérieures.

Chapitre 1 : Optique quantique électronique

Le premier chapitre de ce manuscrit présente une revue des divers outils et concepts formant le cœur du cadre de l'optique quantique électronique à la fois d'un point de vue expérimental et théorique, tels qu'ils ont été résumés dans le bref contexte ci-dessus. Sa première section est donc dévolue à la "boîte à outils" mise en jeu quotidiennement dans des groupes tels que celui du Laboratoire Pierre Aigrain, et présente en détail comment les gas bidimensionnaux d'électrons sous un fort champ magnétique transverse peuvent permettre de créer des canaux de conduction balistiques. Les contacts ponctuels quantiques, qui constituent pour les électrons un analogue contrôlable par l'expérimentateur des lames semi-réfléchissantes pour les photons, sont également présentés. Enfin, cette première section présente les différentes sources d'électrons qui sont utilisées en optique quantique électronique, en s'attachant particulièrement au fonctionnement de deux d'entre elles : les sources d'électrons uniques résolus en temps et en énergie.

Après cette section de contexte expérimental, la section 1.2 s'intéresse au cadre théorique de l'optique quantique électronique et à l'étude du concept fondamental de ce travail : celui de la fonction de cohérence électronique. Cette quantité, introduite C. Grenier [66, 67], est un équivalent direct pour l'électronique des fonctions de cohérence de Glauber pour les photons [62]. Elle est définie, en deux points et deux instants, comme

$$\mathcal{G}^{(e)}_{\rho}(\mathbf{r},t|\mathbf{r}',t') = \left\langle \psi^{\dagger}(\mathbf{r}',t')\psi(\mathbf{r},t)\right\rangle_{\rho} ,$$

où $\psi(\mathbf{r},t)$ est l'opérateur qui détruit un électron à la position $\mathbf{r}$ et à l'instant t, $\psi^{\dagger}$ son analogue pour la création d'électrons, et ρ est l'opérateur densité de l'état quantique considéré. De nombreuses propriétés de ces fonctions sont discutées dans ce chapitre, et en particulier les liens entre la cohérence électronique et des quantités mesurables expérimentalement. Dans cette thèse, j'utilise également énormément une représentation temps-fréquence de cette fonction de cohérence, appelée fonction de Wigner électronique [41], inspirée des travaux de Wigner [182] et Ville [169], et définie comme :

$$\mathcal{W}^{(e)}(\bar{t},\overline{\omega}) = v_{\mathrm{F}}\int_{-\infty}^{+\infty}\mathcal{G}^{(e)}\left(\bar{t}+\frac{\tau}{2}\middle|\,\bar{t}-\frac{\tau}{2}\right)\mathrm{e}^{\mathrm{i}\overline{\omega}\tau}\mathrm{d}\tau\,.$$

Cette représentation permet un accès direct à deux quantités intéressantes pour nous : le courant moyen à l'instant t, et le nombre d'occu-

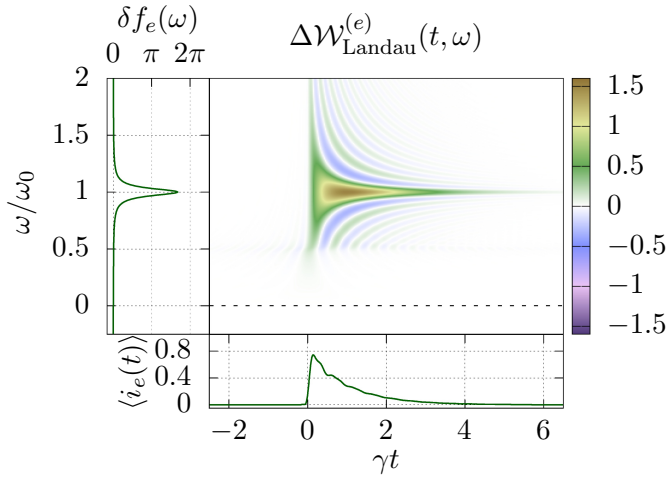

FIGURE F.1 : Fonction de Wigner électronique d'une excitation telle qu'elle est émise dans une expérience, avec les paramètres $\hbar\omega_0 = 0.7\,\text{K}$ et $\tau_0 = 1/\gamma = 140\,\text{ps}$.

pation à l'énergie $\hbar\omega$ sont obtenus comme les distributions marginales de $\mathcal{W}^{(e)}$:

$$\int_{-\infty}^{+\infty} \Delta\mathcal{W}^{(e)}(t,\omega)\frac{\mathrm{d}\omega}{2\pi} = -\frac{\langle i(t)\rangle}{e}$$
$$\lim_{T\to\infty}\left(\frac{1}{T}\int_{-T/2}^{+T/2}\mathcal{W}^{(e)}(t,\omega)\mathrm{d}t\right) = f(\omega)\,.$$

Pour mieux comprendre cette quantité, un grand nombre d'exemples est présenté dans le corps principal du texte. Présentons-en un en particulier : la source d'électons uniques du LPA, que nous utilisons le plus souvent dans les expériences. Sa fonction de Wigner est représentée sur la figure F.1, ainsi que les deux marginales discutées précédemment. Comme on le voit sur cette figure, cette source émet une excitation résolue de manière Lorentzienne en énergie, et le courant associé est exponentiellement décroissant et contient une unique charge électrique.

La section 1.3 de ce premier chapitre continue ce tour d'horizon des fonctions de cohérence et présente les outils permettant d'aller plus loin que les quantités à un électron : les cohérences d'ordre 2 et d'ordre n. Ces fonctions possèdent de nombreuses propriétés de symétrie qui sont étudiées, et peuvent être reliées à plusieurs quantités physiques intéressantes, mais la lourdeur mathématique des expressions correspondantes

m'oblige à ne pas en dire plus dans ce court résumé. Notons cependant que ces outils sont reliés à des concepts centraux d'information quantique, puisqu'ils donnent accès à des indicateurs d'intrication électronique.

Enfin, la dernière section de ce premier chapitre présente un dernier outil théorique d'importance pour mon travail de recherche : la bosonisation à l'équilibre. En effet, on peut montrer qu'il existe une équivalence entre les excitations électroniques de basse énergie dans un conducteur unidimensionnel et des ondes de densité de charge quantifiées, qui sont des degrés de liberté bosoniques. Ces ondes de densité de charge sont appelées magnetoplasmons de bord. Le but de cette section est donc de donner un dictionnaire entre les électrons et les plasmons, afin de permettre de passer d'une représentation à l'autre. En particulier, on peut montrer qu'un plasmon d'énergie $\hbar\omega$ correspond à une superposition cohérente de toutes les paires électron/trou de cette énergie, tandis qu'un électron émis à l'instant t est représenté par un état cohérent de plasmons, le paramètre de cet état cohérent étant dépendant de l'instant considéré. En étudiant un même état quantique sous l'angle des électrons ou des plasmons, différents phénomènes physiques peuvent être modélisés, ce qui forme le cœur du chapitre 3 de ce manuscrit.

Chapitre 2 : Mesure de cohérences

Le deuxième chapitre de ce manuscrit s'intéresse au fonctionnement des expériences que l'on peut effectuer en optique quantique électronique. Avant de pouvoir décrire une expérience, il est nécessaire de se demander quelles quantités peuvent être mesurées pour des problèmes d'électronique aux échelles que nous considérons ici. C'est ce qui est fait dans la première section de ce chapitre, qui présente les deux principales quantités qui seront mesurées dans la suite : le courant moyen et le bruit à fréquence finie. La relation entre ces quantités expérimentales et les fonctions de cohérence définies dans le premier chapitre est présentée, ainsi qu'un bref résumé des difficultés techniques qui sont rencontrées dans une vraie expérience pour obtenir ces quantités. En effet, de nombreuses étapes sont nécessaires pour pouvoir extraire un signal exploitable : basse température, amplification cryogénique, grand nombre de répétitions... Pour donner un ordre de grandeur, la sensibilité que l'on cherche à atteindre pour une mesure de bruit est de l'ordre de $10 \times 10^{-30}\,\mathrm{A}^2/\mathrm{Hz}$. Pour atteindre cette sensibilité en un temps de

mesure raisonnable (quelques minutes), il a fallu de nombreuses avancées expérimentales, qui sont détaillées dans la thèse de V. Freulon [52] et rappelées brièvement dans cette section.

La section 2.2 s'intéresse ensuite aux diverses expériences d'interférométrie qui ont été developées durant les dernières années dans le contexte de l'optique quantique électronique. Deux interféromètres sont discutés en détails : celui de Mach-Zehnder, qui est un interféromètre d'amplitude, et celui de Hong-Ou-Mander qui est un interféromètre d'intensité. En particulier, cette section présente tous les avantages et inconvénients de ces interféromètres, ainsi que les quantités physiques auxquelles ils donnent accès. Ainsi, le courant moyen à l'instant t en sortie d'un Mach-Zehnder permet d'accéder à l'excès de cohérence hors diagonale $\Delta\mathcal{G}^{(e)}(t-\tau_1|t-\tau_2)$, τ_1 et τ_2 étant des paramètres de l'interféromètre. Cependant, l'effet des interactions dans cette expérience est extrêmement élevé, ce qui entraîne dans la plupart des cas la destruction de la cohérence que l'on voudrait mesurer. Ce problème est en partie résolu dans l'interféromètre de Hong-Ou-Mandel, mais cette seconde expérience ne permet d'accès direct à la cohérence émise par une source. À la place, on va accèder à une quantité à deux sources à travers le bruit à fréquence finie :

$$\mathcal{Q}_{\mathrm{HOM}} = -2e^2 \int \mathrm{d}t \int \frac{\mathrm{d}\omega}{2\pi} \Delta\mathcal{W}^{(e)}_{1,\mathrm{in}}(t,\omega)\Delta\mathcal{W}^{(e)}_{2,\mathrm{in}}(t,\omega)\,.$$

Ces deux types d'expériences peuvent également être interprétés d'une manière un peu différente, en utilisant un langage inspiré de celui du traitement du signal [OP5].

En utilisant le résultat de l'équation précédente et cette vision de type traitement du signal, on peut remarquer que l'interférométrie Hong-Ou-Mandel permet d'effectuer un autre type de mesure qui était il y a encore quelques annéees réservé à l'optique quantique des photons : la tomographie d'un état quantique inconnu. L'idée est assez simple : en utilisant pour la source 2 une source dont la fonction de Wigner est bien connue et bien choisie, il est possible de reconstruire complètement la fonction de Wigner de la source 1. Ce protocole est présenté dans la section 2.3, et j'ai participé à son développement à la fois d'un point de vue théorique et expérimental. En particulier, nous avons pu effectuer au cours de ma thèse la première procédure complète de reconstruction d'un état quantique en utilisant ce protocole générique [OP4]. Cette première expérience, dont les résultats sont visibles sur la figure F.2, peut être vue comme l'étalonnage d'un nouvel outil d'analyse des courants quan-

tiques, et nous espérons qu'une telle procédure pourra devenir utilisée de manière plus systématique dans le futur.

Bien que cette reconstruction par tomographie d'une cohérence électronique soit une réussite expérimentale impressionnante, il ne s'agit pas de la seule chose qui est obtenue à l'aide de ce que nous appelons notre analyse de signaux quantiques. En effet, durant la thèse de B. Roussel au sein du groupe de théorie de l'ENS de Lyon [138], il a inventé une méthode d'analyse numérique des cohérences permettant l'extraction des fonctions d'ondes à un électron et à un trou présentes dans un courant électrique quantique périodique. Cette méthode nous permet de décrire tout courant quantique à travers les excitations élémentaires à une particule qui le constituent, que nous appelons les atomes de signaux électroniques [OP5]. Dans ce manuscrit, je présente les résultats principaux, sur lesquels j'ai eu l'opportunité de travailler, de cette analyse de signaux quantiques. Bien entendu, la thèse de B. Roussel contient de plus amples informations sur ce sujet, mais mon manuscrit présente plusieurs éléments de compréhension de cette méthode, ainsi qu'une analyse dans le cas particulier présenté sur la figure F.2 de l'effet de la température sur les cohérences électroniques.

Enfin, ce deuxième chapitre se conclut par une section consacrée aux mesures de cohérences électroniques d'ordre supérieur. En s'inspirant des expériences présentées pour les cohérences du premier ordre ainsi que des expériences qui existent en optique quantique pour mesurer les ordres supérieurs, je m'intéresse à divers interféromètres construits à la manière de l'interféromètre de Franson [49, 50]. En utilisant une méthode proche de celle à l'œuvre pour les expériences de Mach-Zehnder, nous avons ansi pu proposer au tout début de ma thèse, sous l'impulsion d'E. Thibierge [OP6, 159], un interféromètre permettant la reconstruction de cohérences d'ordre 2 directement dans le domaine temporel. Une telle mesure directe de cohérences permet de sonder l'existence de cohérences quantiques entre des paires d'électrons émises à des temps différents, ce que l'on présente dans ce manuscrit à travers l'exemple de l'intrication en fenêtre de temps [18, 109]. Cependant, cette première approche souffre des mêmes problèmes que la mesure de cohérences avec un interféromètre de Mach-Zehnder : l'effet des interactions de Coulomb à l'intérieur du système expérimental rend quasi impossible la survie de la cohérence que l'on cherche à mesurer lors de la propagation électronique.

À la suite de cette première tentative, je me suis naturellement penché sur l'extension au cas à deux électrons du protocole de tomographie

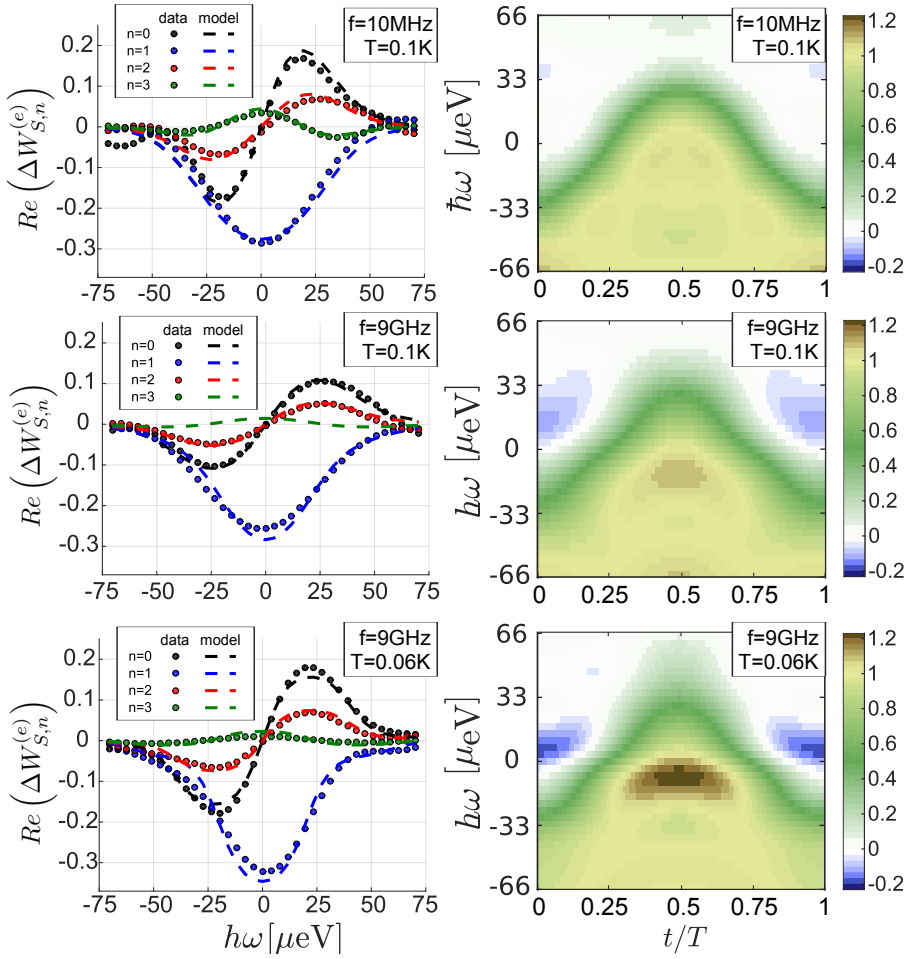

FIGURE F.2 : Résultats de mesures utilisant le protocole de tomographie présenté dans la section 2.3, tirés de [OP4]. De haut en bas, trois types de sources sinusoïdales sont utilisées, qui varient par leur fréquence ou par la température du système : $f = 10\,\mathrm{MHz}$ à $T_{\mathrm{el}} = 100\,\mathrm{mK}$, 9 GHz à 100 mK et enfin 9 GHz à 60 mK. *À gauche* : Les harmoniques de la fonction de Wigner, $\Delta\mathcal{W}^{(e)}_{S,n}$, obtenues à partir de mesures de bruits à fréquence nulle (points) et comparées à des prédictions théoriques (lignes tiretées), pour $n = 0$ à $n = 3$. *À droite* : Fonction de Wigner reconstruite à partir des harmoniques mesurées dans l'expérience.

dont nous avons parlé précédemment. Ce projet n'a pas pu aboutir complètement, mais de nombreuses avancées significatives ont été obtenues. En particulier, j'ai pu proposer plusieurs expériences d'interférométrie dont les signaux de sorties sont reliés au recouvrement de cohérences à deux électrons. La partie qui reste à développer est donc la manière d'utiliser ces signaux, et plus spécifiquement les sources de référence qu'il faudrait utiliser pour permettre une reconstruction complète de la cohérence électronique d'ordre deux. L'implémentation d'un tel protocole dans une expérience réelle reste encore à discuter, notamment du point de vue de la géométrie des échantillons à utiliser ou des mesures à effectuer, qui pourraient nécessiter la mesure d'un "bruit du bruit".

Chapitre 3 : Interactions

Le troisième et dernier chapitre de cette thèse, qui est également le plus conséquent, est dévolu à l'étude des interactions coulombiennes écrantées en optique quantique électronique, que ce soit du point de vue de leur effet sur les électrons présents dans le système, de leur caractérisation ou de leur contrôle.

Dans sa première section, on utilise le dictionnaire développé dans la section 1.4 pour montrer que la bosonisation offre un très bon outil pour le traitement de l'interaction de Coulomb écranté. En particulier, on peut montrer qu'une région d'interaction de taille finie se comporte comme un diffuseur élastique pour les états cohérents, ce qui est représenté schématiquement sur la figure F.3. Cependant, cette vision change complètement lorsque l'on utilise notre dictionnaire dans l'autre sens pour exprimer l'état de sortie sous une forme électronique, car l'état obtenu est alors un état intriqué entre le système et son environnement.

En utilisant la forme exacte de cet état intriqué, on peut alors calculer complètement la cohérence électronique après la région d'interaction. Le résultat final peut être écrit sous une forme assez compacte lorsqu'on injecte un unique électron dans le paquet d'onde φ_e dans le système en entrée :

$$\mathcal{G}^{(e)}_{\text{sortie}}(t|t') = \int \varphi_e(t_+)\varphi_e^*(t_-)D(t,t',t_+,t_-) \\ \langle \psi(t_-)\psi^\dagger(t')\psi(t)\psi^\dagger(t_+)\rangle_{\text{F}}\, \mathrm{d}t_+\mathrm{d}t_- \,.$$

Cependant, le coefficient $D(t,t',t_+,t_-)$ est difficile à évaluer. Pour ce faire, il faut tout d'abord le développer analytiquement sous une forme

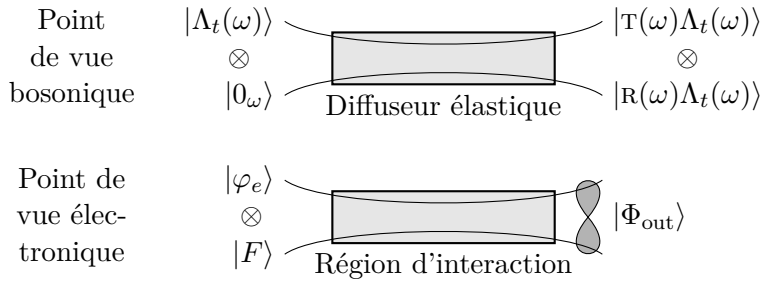

FIGURE F.3 : Représentation schématique d'une région d'interaction et de son effet sur les plasmons ou les électrons. *En haut* : vision plasmonique. La région d'interaction se comporte comme un diffuseur élastique. Pour le mode à ω, l'état d'entrée est un état cohérent de paramètre $\Lambda_t(\omega)$ dans un canal accompagné du vide dans l'environnement. En sortie, on obtient un état factorisé entre les deux canaux, chaque partie étant un état cohérent de plasmons. *En bas* : vision électronique. Les électrons étant des superpositions de plasmons, l'état de sortie est un état intriqué entre les deux canaux.

contrôlant "à la main" les différentes singularités qui peuvent y apparaître, avant d'utiliser une approche numérique pour calculer la valeur de ces termes. Mettre en place ce calcul a été un travail en binôme, la partie numérique étant implémentée par B. Roussel tandis que j'ai effectué la partie analytique dont le résultat est détaillé dans l'annexe B. L'utilisation de cet outil extrêmement puissant, qui permet de calculer la cohérence du premier ordre en prenant en compte l'effet de l'interaction de Coulomb pour de nombreux modèles d'environnements et tout type de paquet d'ondes monoélectronique en entrée a alors constitué l'essentiel de mon travail de thèse. Ainsi, trois grandes situations ont retenu mon attention et sont présentées dans ce manuscrit : la prédiction de résultat expérimentaux, le contrôle de la décohérence, et le cas spécifique d'un système sans environnement extérieur.

La première situtation, décrite dans la section 3.2, cherche à relier directement les prédictions que l'on peut faire en utilisant nos outils numériques aux résultats d'une expérience. Le système considéré est alors un système à deux canaux interagissant par une interaction effective de courte portée, qui a été observée expérimentalement comme étant celle qui intervient à basse énergie. Pour ce modèle spécifique d'interaction, on peut montrer qu'un état cohérent de plasmon va subir une fractio-

nalisation en un mode rapide et un mode lent. C'est en particulier le cas pour les états créés en appliquant une tension classique à un contact ohmique. Cependant, les électrons bien résolus en énergie qui peuvent être émis à l'aide de la source d'électrons uniques du LPA vont montrer un comportement bien différent : une très forte relaxation en énergie a lieu sur des temps très courts, signe de la perte de cohérence entre les différentes parties de la superposition qui constituent cet état, avant que la fractionalisation n'intervienne. Les figures correspondantes (3.5, 3.8, 3.9) sont malheureusement un peu grandes pour être présentées dans ce résumé, mais forment le cœur de cette analyse [OP2].

En utilisant ces résultats théoriques, on peut également prédire des quantités qui sont mesurables dans l'expérience, tel que des signaux de bruit Hong-Ou-Mandel par exemple. C'est ce que nous avons fait lors d'une collaboration entre le groupe de G. Fève à Paris, celui de T. Martin à Marseille et le nôtre [OP3], qui a menée entre autres au résultat présenté sur la figure F.4. Sur cette figure sont représentés à la fois les résultats expérimentaux et les prédictions théoriques correspondantes pour la source d'électron uniques dans trois différents régimes, et on peut remarquer un très fort accord entre la théorie et l'expérience, bien que l'effet de la température sur le signal soit encore en dehors de la résolution expérimentale. D'autre résultats sont présentés dans le manuscrit, tels que la réapparition d'indiscernabilité, sous l'effet des interactions, entre deux états initialement très différents, ou la discussion d'autres modèles d'interaction à plus longue portée et les différences que cela entraînerait sur le signal mesuré. Cette section se conclue ainsi sur une discussion des expériences qui restent à mener pour discriminer définitivement entre divers scénarios de décohérence possibles.

Cette comparaison entre théorie et expérience montre de manière convaincante que nos prédictions peuvent donner des informations pertinentes sur les résultats expérimentaux. L'étape suivante est donc naturellement de se servir de notre outil prédictif pour étudier des situations qui ne sont pas toujours accessibles expérimentalement pour le moment, dans le but de trouver des situations dans lesquelles on peut limiter au maximum le phénomène de décohérence à l'œuvre dans notre système. C'est ce que je présente dans les deux sections suivantes, qui sont essentiellement tirées d'un article long publié en parallèle [OP1].

La première idée, présentée dans la section section 3.3, est d'utiliser des géométries bien spécifiques pour l'environnement de notre canal d'intérêt pour protéger les excitations électroniques de la décohérence.

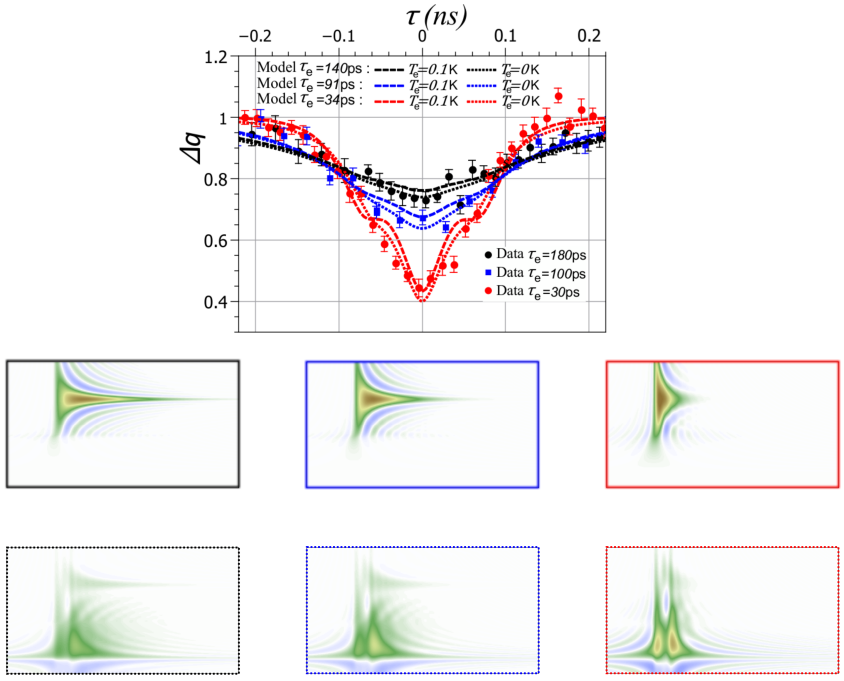

FIGURE F.4 : Comparaison entre les prédictions théoriques et les résultats expérimentaux pour une expérience de Hong-Ou-Mandel effectuée avec des électrons uniques de même énergie $\hbar\omega_0$, pour différentes résolutions temporelles. *En haut* : Résultats tirés de [OP3], contenant les points expérimentaux, les prédictions de notre calcul à température nulle (en pointillés) et celles du groupe de T. Martin à 100 mK (en lignes tiretées). On observe un très bon accord entre mesure et prédictions, bien que l'effet de la température reste inaccessible avec la résolution expérimentale actuelle. *Au milieu* : Fonction de Wigner des différentes excitations émises par la source. *En bas* : Fonction de Wigner après la région d'interaction pour chacune de ces excitations. Les prédictions théoriques sont calculées à partir de ces fonctions de Wigner.

En utilisant notre formalisme et nos outils numériques, nous pouvons revisiter une idée qui a déjà été développée dans le régime DC depuis quelques années [2, 83] : refermer l'environnement sur lui-même. On peut alors s'intéresser à la manière dont de tels systèmes permettent une protection contre la décohérence, mais également à l'état qui est obtenu dans les cas où cette protection ne fonctionne pas. Ainsi, on peut démontrer qu'un environnement bouclé introduit une énergie typique en-dessous de laquelle les processus de relaxation sont bloqués, tandis que des électrons émis à une énergie supérieure vont émettre dans leur environnement un état très proche d'un plasmon unique. Une attention particulière est portée à la possibilité de réaliser ces systèmes expérimentalement, la section 3.3.2 décrivant spécifiquement des échantillons qui permettraient de tester une protection contre la décohérence pour la source d'électrons uniques du LPA.

La seconde idée est apparue de manière indirecte à partir du dernier type de système que j'ai étudié en détail au cours de ma thèse : le cas d'un canal de bord unique, qui n'est couplé à aucun environnement extérieur. Bien que ce cas semble complètement académique, puisqu'il sera impossible en réalité d'obtenir un canal découplé de tout environnement, il met déjà en œuvre une situation qui n'est pas si simple : la décohérence de l'état à un corps dans un système à n-corps en interaction. Comme je le discute dans la section 3.4, ce cas permet également d'étudier la vitesse de propagation des excitations électroniques dans les canaux 1D. En effet, savoir si les courants quantiques associés à un électron unique se propagent à la vitesse de Fermi ou à la vitesse des plasmons, qui sont différentes en présence d'interactions, est une question récurrente dans notre communauté. La réponse à cette question est en réalité assez subtile, et dépend particulièrement du matériau utilisé. Ce point est souvent oublié, car la grande majorité des expériences d'optique quanique électronique sont menées dans des gas bidimensionnels d'AsGa, mais nous montrons que des matériaux avec des vitesses de propagation plus élevés entraînent une bien meilleure protection contre les phénomènes de décohérence. Cela pourrait par exemple être le cas du graphène, si les premières estimations des vitesses mise en jeu dans ce matériau sont confirmées.

De manière plus détaillée, cette section montre que les interactions intra-canal dans les systèmes 1D donnent une vitesse de propagation des plasmons qui dépend de la fréquence. Pour traiter plus facilement ce type de vitesse, on peut alors introduire de manière perturbative un

circuit électrique effectif reproduisant le comportement des interactions à l'ordre que l'on veut. Cela nous permet de discuter quantitativement des modèles dépendant du matériau sous la forme de circuits avec des capacités différentes par exemple. Bien que cela ne soit pas fait dans ce manuscrit, nous pensons également que ce modèle en circuit permet d'introduire assez facilement des possibilités de dissipation dans le système, permettant ainsi de traiter des cas plus complexes et sûrement pertinents pour l'expérience.

Enfin, ce chapitre se termine sur une section un peu plus mathématique de ma thèse, qui vise à calculer le cas complètement général d'une cohérence électronique d'ordre n en sortie d'une zone d'interaction dans le cas où l'on a injecté p électrons en entrée. Puisque les cohérences d'ordre 2 et plus sont la clé pour comprendre et quantifier les phénomènes d'intrication dans le fluide électronique, ce calcul possède un réel intérêt théorique dans le cadre d'une application de l'optique quantique électronique pour l'information quantique. Il permet également de commencer une étude plus complète des effets à n-corps dans les systèmes que nous étudions.

La mauvaise nouvelle que ce calcul a mis en avant est la complexité algorithmique du résultat, qui est complètement impossible à implémenter numériquement en utilisant la même approche que pour la cohérence du premier ordre. Cependant, on peut chercher à extraire de ces équations extrêmement lourdes des cas spécifiques intéressants. C'est ce que je fais dans la section 3.5, où les limites à haute énergie de deux exemples particuliers sont traitées. Dans le cas $n = 2$ et $p = 1$, on peut montrer que la cohérence d'ordre 2 créée par un électron unique se propageant dans le système est très différente selon la manière dont il crée des paires particules-trou dans son environnement, permettant par exemple de faire la différence entre une émission incohérente de telles paires ou l'émission d'un plasmon unique. Dans le cas $n = 1$ et $p = 2$, on s'intéresse à l'effet de l'interaction de Coulomb entre deux électrons injectés en même temps dans le système, et on peut montrer plusieurs résultats intéressants qui permettent de mieux comprendre la manière dont les électrons agissent l'un sur l'autre.

Perspectives

Afin de mieux inscrire cette thèse dans son contexte, il me paraît utile de traduire également les perspectives qui peuvent en être tirées et non

seulement les résultats que j'ai obtenu et qui sont résumés ci-avant. Ces perspectives se divisent naturellement en deux grandes catégories. Tout d'abord, les extensions de ce travail, qui sont souvent visibles de manière assez directe et pour lesquelles nous pouvons d'ores et déjà avoir une bonne vision sur l'avenir. Ensuite, les nouvelles questions qui se posent et les nouveaux domaines qui sont ouverts par l'évolution de l'optique quantique électronique elle-même, qui sont souvent des perspectives un peu plus éloignées ou brumeuses.

Commençons par la première catégorie, pour laquelle plusieurs indices sont disséminés tout au long de ce manuscrit.

Tout d'abord, nous ne sommes qu'au tout début de l'utilisation des protocoles de tomographie pour les courants électriques quantiques. Maintenant que les expériences "d'étalonnage" sont passées, il serait naturellement extrêmement intéressant de se servir de ce système pour mesurer de manière directe la fonction de Wigner correspondant à un électron ayant traversé une région d'interaction dans une vraie expérience.

Ceci m'amène directement à un autre développement intéressant, cette fois du côté théorique : pour pouvoir comparer de manière exacte une telle mesure avec des prédictions théoriques, deux choses restent à faire. La première est l'implémentation des effets thermiques dans notre calcul des cohérences, pour lesquels j'ai déjà fait une bonne partie du travail analytique, mais qui n'a pas encore été ajoutée à notre outil numérique. Cela sera important en particulier pour l'étape d'extraction de fonctions d'onde de notre outil de traitement de signal quantique. La seconde chose qui pourrait être améliorée, et qui est bien plus générale, serait de permettre directement le calcul des effets de l'interaction de Coulomb sur n'importe quel type de sources, en particulier des sources périodiques, et non seulement sur des paquets monoélectroniques. Pour cela, il faudrait passer de la bosonisation à l'équilibre utilisée dans ce manuscrit à sa version hors équilibre qui a été développée très récemment [72]. De premiers pas dans cette direction ont été effectués dans notre groupe, mais plusieurs problèmes rencontrés ont empêchés d'aller très loin dans cette approche. Il paraît également clair qu'une implémentation numérique d'un tel cas complètement générique sera totalement impossible sur un ordinateur "standard", nécessitant potentiellement l'utilisation d'un supercalculateur. Cependant, je pense que ce programme de recherche devrait avancer significativement dans les prochaines années.

Pour continuer cette liste des développements naturels de mon travail, l'extension du cadre de l'optique quantique électronique aux cohérences d'ordre 2 et plus en est encore à ses débuts. Un protocole de tomographie pour la cohérence d'ordre deux qui soit expérimentalement accessible semble complètement possible en utilisant les interféromètres qui sont présentés dans cette thèse. De la même manière, les propositions et les réalisations de sources possédant une cohérence d'ordre deux non triviale, comme des paires intriquées en fenêtre de temps, semblent proches. Cependant, étant donné la difficulté des mesures de bruit, il semble encore bien difficile de prédire le temps nécessaire avant que des protocoles basés sur la mesure du "bruit du bruit" (c'est-à-dire des corrélations à 4 courants) puissent être implémentés dans des systèmes complexes contenant par exemple des sources d'électrons uniques ou des interféromètres de Hong-Ou-Mandel. Cependant, je suis convaincu que de telles expériences pourraient mener à de très intéressantes applications. Par exemple, j'ai pu montrer à la toute fin de la section 3.5 que l'emission de plasmons pourrait être sondée par ce type d'expériences. De manière plus générale, cette question est reliée à celle de la compréhension des relations qui existent entre l'optique quantique électronique et son homologue photonique. Étudier la lumière émise par un courant électrique quantique est déjà le sujet de nombreuses études théoriques [68, 114] et expérimentales [55, 46, 158]. Cette question, posée en particulier par C. Mora dans le contexte de l'optique quantique électronique, est actuellement l'objet d'une collaboration entre notre groupe et le sien. Un premier pas dans cette direction est notamment présenté dans la thèse de B. Roussel [138].

Enfin, une dernière extension particulièrement intéressante de mon travail est l'étude d'excitations électroniques délocalisées sur plusieurs canaux, et en particulier de leur évolution sous l'effet des interactions. Plusieurs raisons nous poussent à nous intéresser à ce problème, qui sera complété je l'espère dans les prochains mois. Tout d'abord, il s'agit d'une situation directement reliée au cas de l'interféromètre de Mach-Zehnder, dans lequel la première lame semi-réfléchissante crée une excitation délocalisée sur les deux branches, qui interagit ensuite avec son environnement. Si l'on veut pouvoir prédire avec précision le signal en sortie d'un Mach-Zehnder, il est donc nécessaire de développer un moyen d'étudier l'évolution de telles excitations. De plus, pour pouvoir étudier les outils de protection contre la décohérence dans ces interféromètres, il faut adapter les calculs menés pour des environnements fermés dans

ce manuscrit à ce cas spécifique. Un deuxième intérêt de cette étude se retrouve dans l'idée d'utiliser des excitations électroniques comme des qubits volants se propageant sur des "rails" bien définis, les deux bits classiques d'information étant encodés par le fait d'être sur un canal ou l'autre. Néanmoins, puisque nous avons montré que les interactions mène à une forte perte de cohérence, il semble naturel de nous demander comment l'état de notre qubit va évoluer lors de sa propagation dans l'échantillon. De la même manière, on voudrait chercher à protéger ce qubit de la décohérence en utilisant des matériaux ou des designs appropriés, qui restent encore à développer. Durant ma thèse, j'ai commencé cette étude et effectué des calculs analytiques dans un cas générique où les divers canaux pouvaient interagir avec plusieurs environnements (indépendants ou non) et entre eux. Tout est prêt pour une implémentation numérique que je n'ai malheureusement pas eu le temps d'effectuer, ce qui explique que cette étude n'aie pas trouvé sa place dans ce manuscrit. Cependant, elle devrait pouvoir être terminée bientôt, et j'espère que des résultats intéressants pour notre communauté pourront en être tirés.

Pour terminer ce résumé, et après ce bref aperçu des travaux que j'ai commencé mais pas encore tout à fait terminé, je vais présenter en quelques lignes la seconde catégorie de perspectives pour l'optique quantique électronique en général. Ces domaines commencent tout juste à se développer, et pourraient devenir bien plus importants dans les prochaines années.

Tout d'abord, la démonstration récente de corrélations supraconductrices dans les canaux de bord de l'effet Hall quantique [102, 121, 70] pose la question de l'interaction entre les concepts de l'optique quantique électronique et ceux de la supraconductivité. En particulier, la présence de supraconducteurs pourrait mener à des corrélateurs de la forme $\langle\psi\psi\rangle$ non nuls, ce qui modifierait complètement la façon dont les cohérences se comportent et évoluent dans notre approche. Pour moi, il ne fait aucun doute que ce domaine est voué à augmenter d'intérêt (et de taille) extrêmement rapidement.

Enfin, cela ne sera pas une surprise pour quiconque d'un peu familier avec l'effet Hall quantique de me voir mentionner l'effet Hall quantique fractionnaire. [164, 100, 154]. Ce nouvel état de la matière se manifeste sous la forme de nouveaux plateaux dans la résistance de Hall pour des facteurs de remplissage fractionnaires de la forme p/q, p et q étant premiers entre eux. Dans ces états, il a été montré que les porteurs de

charges n'étaient plus les électrons mais des fermions composites [87] portant une charge $e^* = e/q$. Expérimentalement, cela a pu être observé pour différentes valeurs de q [127, 132], et de nombreuses expériences étudiant le bruit de grenaille de telles excitations [141] ont été réalisées pour sonder la charge de ces excitations. D'un point de vue théorique, les fermions composites sont des particules intéressantes, car il a été montré que leur statistique pouvaient permettre de créer des anyonss [87], un type de particule tel que l'état d'une paire prenne une phase qui n'est ni 0 ni π lorsque l'on échange les deux particules. Plusieurs propositions ont été faites dans le domaine de l'information quantique pour utiliser ces anyons dans la création d'ordinateurs quantiques résistants aux erreurs [94]. Du point de vue de l'optique quantique électronique, les anyons pourraient mener à un physique complètement nouvelle, mais la situation devrait être beaucoup plus compliquée puisque nous ne connaissons pas de lames semi-réfléchissantes pour ces particules. Malgré cette limite, plusieurs tentatives ont été faites pour étendre le formalisme de l'optique quantique électronique au cas fractionnaire, avec des propositions portant sur l'émission de quasi-particule unique [42], des études sur les excitations minimales dans un régime d'effet Hall quantique fractionnaire [130, 168] ou leur bruit photoassisté [167], ainsi que sur des expériences de Hong-Ou-Mandel utilisant des trains de Levitons dans le régime de l'effet Hall quantique fractionnaire [133].

Bibliography

[1] C. Altimiras, H. le Sueur, U. Gennser, A. Cavanna, D. Mailly, and F. Pierre. "Non-equilibrium edge-channel spectroscopy in the integer quantum Hall regime". In: *Nature Physics* 6 (2010), pp. 34–39. DOI: 10.1038/nphys1429.

[2] C. Altimiras, H. le Sueur, U. Gennser, A. Cavanna, D. Mailly, and F. Pierre. "Tuning Energy Relaxation along Quantum Hall Channels". In: *Phys. Rev. Lett.* 105 (22 Nov. 2010), p. 226804. DOI: 10.1103/PhysRevLett.105.226804.

[3] L. Amico, R. Fazio, A. Osterloh, and V. Vedral. "Entanglement in many-body systems". In: *Rev. Mod. Phys.* 80 (2 May 2008), pp. 517–576. DOI: 10.1103/RevModPhys.80.517.

[4] C. Bäuerle, D. C. Glattli, T. Meunier, F. Portier, P. Roche, P. Roulleau, S. Takada, and X. Waintal. "Coherent control of single electrons: a review of current progress". In: *Reports on Progress in Physics* 81.5 (2018), p. 056503.

[5] G. Baym. "The physics of Hanbury Brown - Twiss intensity interferometry: from stars to nuclear collisions". In: *Acta Physical Polonica B* 29 (1998), p. 1839.

[6] C. Beenakker. "Electron-hole entanglement in the Fermi sea". In: *Quantum computers, Algorithms and Chaos*. Ed. by G. Casati, D. Shepelyansky, P. Zoller, and G. Benenti. Vol. 162. International School of Physics Enrico Fermi. Amsterdam: IOS Press, 2006, pp. 307–347.

[7] C. H. Bennett and G. Brassard. "Quantum cryptography: Public key distribution and coin tossing". In: *Proceedings of IEEE International Conference on Computers, Systems and Signal Processing*. Vol. 175. IEEE, 1984, pp. 175–179.

[8] K.-F. Berggren, T. J. Thornton, D. J. Newson, and M. Pepper. "Magnetic depopulation of 1D subbands in a narrow 2D electron gas in a GaAs:AlGaAs heterojunction". In: *Physical Review Letters* 57 (Oct. 1986), pp. 1769–1772. DOI: 10.1103/PhysRevLett.57.1769.

[9] P. Bertet, A. Auffeves, P. Maioli, S. Osnaghi, T. Meunier, M. Brune, J. M. Raimond, and S. Haroche. "Direct Measurement of the Wigner Function of a One-Photon Fock State in a Cavity". In: *Phys. Rev. Lett.* 89 (20 Oct. 2002), p. 200402. DOI: 10.1103/PhysRevLett.89.200402.

[10] A. Bertoni, P. Bordone, R. Brunetti, C. Jacoboni, and S. Reggiani. "Quantum Logic Gates based on Coherent Electron Transport in Quantum Wires". In: *Phys. Rev. Lett.* 84 (25 June 2000), pp. 5912–5915. DOI: 10.1103/PhysRevLett.84.5912.

[11] A. Bertoni. "Perspectives on solid-state flying qubits". In: *Journal of Computational Electronics* 6.1 (Sept. 2007), pp. 67–72. DOI: 10.1007/s10825-006-0076-8.

[12] E. Bieri, M. Weiss, O. Göktas, M. Hauser, C. Schönenberger, and S. Oberholzer. "Finite-bias visibility dependence in an electronic Mach-Zehnder interferometer". In: *Phys. Rev. B* 79 (24 June 2009), p. 245324. DOI: 10.1103/PhysRevB.79.245324.

[13] E. Bocquillon, V. Freulon, J.-M. Berroir, P. Degiovanni, B. Plaçais, A. Cavanna, Y. Jin, and G. Fève. "Coherence and Indistinguishability of Single Electrons Emitted by Independent Sources". In: *Science* 339.6123 (2013), pp. 1054–1057. DOI: 10.1126/science.1232572.

[14] E. Bocquillon, V. Freulon, J. Berroir, P. Degiovanni, B. Plaçais, A. Cavanna, Y. Jin, and G. Fève. "Separation between neutral and charge modes in one dimensional chiral edge channels". In: *Nature Communications* 4 (2013), p. 1839. DOI: 10.1038/ncomms2788.

[15] E. Bocquillon, F. D. Parmentier, C. Grenier, J.-M. Berroir, P. Degiovanni, D. C. Glattli, B. Plaçais, A. Cavanna, Y. Jin, and G. Fève. "Electron Quantum Optics: Partitioning Electrons One by One". In: *Phys. Rev. Lett.* 108 (19 May 2012), p. 196803. DOI: 10.1103/PhysRevLett.108.196803.

[16] E. Bocquillon. “Electron quantum optics in quantum Hall edge channels”. PhD thesis. Université Pierre et Marie Curie - Paris VI, Nov. 2012.

[17] E. Bocquillon, V. Freulon, F. D. Parmentier, J.-M. Berroir, B. Plaçais, C. Wahl, J. Rech, T. Jonckheere, T. Martin, C. Grenier, D. Ferraro, P. Degiovanni, and G. Fève. “Electron quantum optics in ballistic chiral conductors”. In: *Annalen der Physik* 526.1-2 (2014), pp. 1–30. DOI: 10.1002/andp.201300181.

[18] J. Brendel, N. Gisin, W. Tittel, and H. Zbinden. “Pulsed Energy-Time Entangled Twin-Photon Source for Quantum Communication”. In: *Phys. Rev. Lett.* 82 (12 Mar. 1999), pp. 2594–2597. DOI: 10.1103/PhysRevLett.82.2594.

[19] M. Brune, J. Bernu, C. Guerlin, S. Deléglise, C. Sayrin, S. Gleyzes, S. Kuhr, I. Dotsenko, J. M. Raimond, and S. Haroche. “Process Tomography of Field Damping and Measurement of Fock State Lifetimes by Quantum Nondemolition Photon Counting in a Cavity”. In: *Phys. Rev. Lett.* 101 (24 Dec. 2008), p. 240402. DOI: 10.1103/PhysRevLett.101.240402.

[20] M. Brune, E. Hagley, J. Dreyer, X. Maître, A. Maali, C. Wunderlich, J. M. Raimond, and S. Haroche. “Observing the Progressive Decoherence of the “Meter” in a Quantum Measurement”. In: *Phys. Rev. Lett.* 77 (24 Dec. 1996), pp. 4887–4890. DOI: 10.1103/PhysRevLett.77.4887.

[21] O. Brune. “Synthesis of a finite two-terminal network whose driving-point impedance is a prescribed function of frequency”. In: *J. Math. and Phys.* 10 (1931), pp. 191–236.

[22] M. Büttiker. “Absence of backscattering in the quantum Hall effect in multiprobe conductors”. In: *Phys. Rev. B* 38 (14 Nov. 1988), pp. 9375–9389. DOI: 10.1103/PhysRevB.38.9375.

[23] M. Büttiker. “Quantized transmission of a saddle-point constriction”. In: *Phys. Rev. B* 41 (11 Apr. 1990), pp. 7906–7909. DOI: 10.1103/PhysRevB.41.7906.

[24] W. Cauer. “Die Verwirklichung der Wechselstromwiderst ände vorgeschriebener Frequenzabh ängigkeit”. In: *Archiv für Elektrotechnik* 17 (1926), pp. 355–388.

[25] L. Chirolli, V. Giovannetti, R. Fazio, and V. Scarani. "Time-bin entanglement of quasiparticles in semiconductor devices". In: *Phys. Rev. B* 84 (19 Nov. 2011), p. 195307. DOI: 10.1103/PhysRevB.84.195307.

[26] T. Christen and M. Büttiker. "Low-frequency admittance of quantized Hall conductors". In: *Phys. Rev. B* 53 (4 Jan. 1996), pp. 2064–2072. DOI: 10.1103/PhysRevB.53.2064.

[27] N. M. Chtchelkatchev, G. Blatter, G. B. Lesovik, and T. Martin. "Bell inequalities and entanglement in solid-state devices". In: *Phys. Rev. B* 66 (16 Oct. 2002), p. 161320. DOI: 10.1103/PhysRevB.66.161320.

[28] C. Cohen-Tannoudji. *Interactions résonnantes ou quasi-résonnantes d'un atome ou d'une molécule avec une ou plusieurs ondes électromagnétiques intenses et monochromatiques*. Lectures at Collège de France. 1977.

[29] D. Dasenbrook, J. Bowles, J. B. Brask, P. P. Hofer, C. Flindt, and N. Brunner. "Single-electron entanglement and nonlocality". In: *New Journal of Physics* 18.4 (2016), p. 043036.

[30] D. Dasenbrook and C. Flindt. "Dynamical generation and detection of entanglement in neutral leviton pairs". In: *Phys. Rev. B* 92 (16 Oct. 2015), p. 161412. DOI: 10.1103/PhysRevB.92.161412.

[31] C. C. Dean and M. Pepper. "The transition from two- to one-dimensional electronic transport in narrow silicon accumulation layers". In: *Journal of Physics C: Solid State Physics* 15.36 (1982), p. L1287.

[32] P. Degiovanni, C. Grenier, and G. Fève. "Decoherence and relaxation of single-electron excitations in quantum Hall edge channels". In: *Phys. Rev. B* 80 (24 Dec. 2009), p. 241307. DOI: 10.1103/PhysRevB.80.241307.

[33] P. Degiovanni, C. Grenier, G. Fève, C. Altimiras, H. le Sueur, and F. Pierre. "Plasmon scattering approach to energy exchange and high-frequency noise in $\nu = 2$ quantum Hall edge channels". In: *Phys. Rev. B* 81 (12 Mar. 2010), p. 121302. DOI: 10.1103/PhysRevB.81.121302.

[34] S. Deléglise, I. Dotsenko, C. Sayrin, J. Bernu, M. Brune, J.-M. Raimond, and S. Haroche. "Reconstruction of non-classical cavity field states with snapshots of their decoherence". In: *Nature* 455 (Sept. 2008), pp. 510–514. DOI: 10.1038/nature07288.

[35] J. von Delft and H. Schoeller. "Bosonization for beginners – refermionization for experts". In: *Annalen der Physik* 7.4 (1998), pp. 225–305. DOI: 10.1002/(SICI)1521-3889(199811)7:4<225::AID-ANDP225>3.0.CO;2-L.

[36] M. Devoret. *Circuits et signaux quantiques (I)*. Lectures at Collège de France. 2008.

[37] J. Dubois, T. Jullien, C. Grenier, P. Degiovanni, P. Roulleau, and D. C. Glattli. "Integer and fractional charge Lorentzian voltage pulses analyzed in the framework of photon-assisted shot noise". In: *Phys. Rev. B* 88 (8 Aug. 2013), p. 085301. DOI: 10.1103/PhysRevB.88.085301.

[38] J. Dubois, T. Jullien, F. Portier, P. Roche, A. Cavanna, Y. Jin, W. Wegscheider, P. Roulleau, and D. Glattli. "Minimal excitation states for electron quantum optics using Levitons". In: *Nature* 502 (Oct. 2013), p. 659. DOI: 10.1038/nature12713.

[39] T. J. Dunn, I. A. Walmsley, and S. Mukamel. "Experimental Determination of the Quantum-Mechanical State of a Molecular Vibrational Mode Using Fluorescence Tomography". In: *Phys. Rev. Lett.* 74 (6 Feb. 1995), pp. 884–887. DOI: 10.1103/PhysRevLett.74.884.

[40] H. Everett. "The many worlds interpretation of quantum mechanics". PhD thesis. Princeton university, 1957.

[41] D. Ferraro, A. Feller, A. Ghibaudo, E. Thibierge, E. Bocquillon, G. Fève, C. Grenier, and P. Degiovanni. "Wigner function approach to single electron coherence in quantum Hall edge channels". In: *Phys. Rev. B* 88 (20 Nov. 2013), p. 205303. DOI: 10.1103/PhysRevB.88.205303.

[42] D. Ferraro, J. Rech, T. Jonckheere, and T. Martin. "Nonlocal interference and Hong-Ou-Mandel collisions of single Bogoliubov quasiparticles". In: *Phys. Rev. B* 91 (7 Feb. 2015), p. 075406. DOI: 10.1103/PhysRevB.91.075406.

[43] D. Ferraro, T. Jonckheere, J. Rech, and T. Martin. "Electronic quantum optics beyond the integer quantum Hall effect". In: *physica status solidi (b)* 254.3 (2017), p. 1600531. DOI: 10.1002/pssb.201600531.

[44] G. Fève, A. Mahé, J.-M. Berroir, T. Kontos, B. Plaçais, D. C. Glattli, A. Cavanna, B. Etienne, and Y. Jin. "An On-Demand Coherent Single-Electron Source". In: *Science* 316.5828 (2007), pp. 1169–1172. DOI: 10.1126/science.1141243.

[45] G. Floquet. "Sur les équations différentielles linéaires à coefficients périodiques". In: *Ann. Ecole Norm. Sup.* 12 (1883), p. 47.

[46] J.-C. Forgues, F. B. Sane, S. Blanchard, L. Spietz, C. Lupien, and B. Reulet. "Noise intensity-intensity correlations and the fourth cumulant of photo-assisted shot noise". In: *Scientific reports* 3 (2013), p. 2869. DOI: 10.1038/srep02869.

[47] R. M. Foster. "A Reactance Theorem". In: *Bell System Technical Journal* 3.2 (1924), pp. 259–267. DOI: 10.1002/j.1538-7305.1924.tb01358.x.

[48] M. Fox. *Quantum Optics: An Introduction*. Oxford University Press, 2006.

[49] J. D. Franson. "Bell inequality for position and time". In: *Phys. Rev. Lett.* 62 (19 May 1989), pp. 2205–2208. DOI: 10.1103/PhysRevLett.62.2205.

[50] J. D. Franson. "Two-photon interferometry over large distances". In: *Phys. Rev. A* 44 (7 Oct. 1991), pp. 4552–4555. DOI: 10.1103/PhysRevA.44.4552.

[51] V. Freulon, A. Marguerite, J.-M. Berroir, B. Plaçais, A. Cavanna, Y. Jin, and G. Fève. "Hong-Ou-Mandel experiment for temporal investigation of single-electron fractionalization". In: *Nature Communications* 6 (Apr. 2015). Article, p. 6854. DOI: 10.1038/ncomms7854.

[52] V. Freulon. "Étude de la décohérence de paquets d'onde monoélectroniques dans les canaux de bord de l'effet Hall quantique entier". PhD thesis. Ecole Normale Supérieure, Oct. 2014.

[53] J. Gabelli. "Mise en évidence de la cohérence quantique des conducteurs en régime dynamique". PhD thesis. Université Pierre et Marie Curie - Paris VI, Jan. 2006.

[54] D. Gabor. “Theory of communication. Part 1: The analysis of information”. English. In: *Journal of the Institution of Electrical Engineers - Part III: Radio and Communication Engineering* 93 (26 Nov. 1946), 429–441(12).

[55] G. Gasse, C. Lupien, and B. Reulet. “Observation of Squeezing in the Electron Quantum Shot Noise of a Tunnel Junction”. In: *Phys. Rev. Lett.* 111 (13 Sept. 2013), p. 136601. DOI: 10.1103/PhysRevLett.111.136601.

[56] U. Gavish, Y. Levinson, and Y. Imry. “Detection of quantum noise”. In: *Phys. Rev. B* 62 (16 Oct. 2000), R10637–R10640. DOI: 10.1103/PhysRevB.62.R10637.

[57] T. Giamarchi. *Quantum Physics in One Dimension*. International Series of Monogr. Clarendon Press, 2004.

[58] V. Giovannetti, D. Frustaglia, F. Taddei, and R. Fazio. “Electronic Hong-Ou-Mandel interferometer for multimode entanglement detection”. In: *Phys. Rev. B* 74.11 (Sept. 2006), p. 115315. DOI: 10.1103/PhysRevB.74.115315.

[59] V. Giovannetti, D. Frustaglia, F. Taddei, and R. Fazio. “Characterizing electron entanglement in multiterminal mesoscopic conductors”. In: *Phys. Rev. B* 75 (24 June 2007), p. 241305. DOI: 10.1103/PhysRevB.75.241305.

[60] D. C. Glattli. “Quantum shot noise of conductors and general noise measurement methods”. In: *The European Physical Journal Special Topics* 172.1 (June 2009), pp. 163–179. DOI: 10.1140/epjst/e2009-01049-y.

[61] R. J. Glauber. “Coherent and Incoherent States of the Radiation Field”. In: *Phys. Rev.* 131 (6 Sept. 1963), pp. 2766–2788. DOI: 10.1103/PhysRev.131.2766.

[62] R. J. Glauber. “Photon Correlations”. In: *Phys. Rev. Lett.* 10 (3 Feb. 1963), pp. 84–86. DOI: 10.1103/PhysRevLett.10.84.

[63] R. J. Glauber. “The Quantum Theory of Optical Coherence”. In: *Phys. Rev.* 130 (6 June 1963), pp. 2529–2539. DOI: 10.1103/PhysRev.130.2529.

[64] I. Gradshteyn, A. Jeffrey, and I. Ryzhik. *Table of Integrals, Series, and Products*. Academic Press, 1996.

[65] C. Grenier, J. Dubois, T. Jullien, P. Roulleau, D. C. Glattli, and P. Degiovanni. "Fractionalization of minimal excitations in integer quantum Hall edge channels". In: *Phys. Rev. B* 88 (8 Aug. 2013), p. 085302. DOI: 10.1103/PhysRevB.88.085302.

[66] C. Grenier, R. Hervé, E. Bocquillon, F. D. Parmentier, B. Plaçais, J. M. Berroir, G. Fève, and P. Degiovanni. "Single-electron quantum tomography in quantum Hall edge channels". In: *New Journal of Physics* 13.9 (2011), p. 093007. DOI: 10.1088/1367-2630/13/9/093007.

[67] C. Grenier. "Electronic quantum optics". PhD Thesis. École Normale Supérieure de lyon, June 2011.

[68] A. L. Grimsmo, F. Qassemi, B. Reulet, and A. Blais. "Quantum Optics Theory of Electronic Noise in Coherent Conductors". In: *Phys. Rev. Lett.* 116 (4 Jan. 2016), p. 043602. DOI: 10.1103/PhysRevLett.116.043602.

[69] L. K. Grover. "A Fast Quantum Mechanical Algorithm for Database Search". In: *Proceedings of the Twenty-eighth Annual ACM Symposium on Theory of Computing*. STOC '96. Philadelphia, Pennsylvania, USA: ACM, 1996, pp. 212–219. DOI: 10.1145/237814.237866.

[70] S. Guiducci, M. Carrega, G. Biasiol, L. Sorba, F. Beltram, and S. Heun. *Quantum Hall Effect in a Josephson Junction*. 2018. eprint: arXiv:1805.02862.

[71] M. Gündoğan, P. M. Ledingham, K. Kutluer, M. Mazzera, and H. de Riedmatten. "Solid State Spin-Wave Quantum Memory for Time-Bin Qubits". In: *Phys. Rev. Lett.* 114 (23 June 2015), p. 230501. DOI: 10.1103/PhysRevLett.114.230501.

[72] D. B. Gutman, Y. Gefen, and A. D. Mirlin. "Bosonization out of equilibrium". In: *EPL (Europhysics Letters)* 90.3 (2010), p. 37003. DOI: 10.1209/0295-5075/90/37003.

[73] G. Haack, M. Moskalets, J. Splettstoesser, and M. Büttiker. "Coherence of single-electron sources from Mach-Zehnder interferometry". In: *Phys. Rev. B* 84 (8 Aug. 2011), p. 081303. DOI: 10.1103/PhysRevB.84.081303.

[74] F. D. M. Haldane. "'Luttinger liquid theory' of one-dimensional quantum fluids. I. Properties of the Luttinger model and their extension to the general 1D interacting spinless Fermi gas". In: *Journal of Physics C: Solid State Physics* 14.19 (1981), p. 2585.

[75] R. Hanbury Brown and R. Twiss. "A Test of a New Type of Stellar Interferometer on Sirius". In: *Nature* 178 (1956), p. 1046. DOI: doi:10.1038/1781046a0.

[76] R. Hanbury Brown and R. Twiss. "Correlation between photons in two coherent beams of light". In: *Nature* 177 (1956), p. 27. DOI: doi:10.1038/177027a0.

[77] S. Haroche and J.-M. Raimond. *Exploring the quantum: atoms, cavities, and photons*. Oxford university press, 2006.

[78] M. Hashisaka, N. Hiyama, T. Akiho, K. Muraki, and T. Fujisawa. "Waveform measurement of charge- and spin-density wavepackets in a chiral Tomonaga–Luttinger liquid". In: *Nature Physics* 13 (Feb. 2017), pp. 559–562. DOI: 10.1038/nphys4062.

[79] M. Henny, S. Oberholzer, C. Strunk, T. Heinzel, K. Ensslin, M. Holland, and C. Schönenberger. "The Fermionic Hanbury Brown and Twiss Experiment". In: *Science* 284.5412 (1999), pp. 296–298. DOI: 10.1126/science.284.5412.296.

[80] P. P. Hofer and M. Büttiker. "Emission of time-bin entangled particles into helical edge states". In: *Phys. Rev. B* 88 (24 Dec. 2013), p. 241308. DOI: 10.1103/PhysRevB.88.241308.

[81] P. P. Hofer, D. Dasenbrook, and C. Flindt. "On-demand entanglement generation using dynamic single-electron sources". In: *physica status solidi (b)* 254.3 (), p. 1600582. DOI: 10.1002/pssb.201600582.

[82] C. K. Hong, Z. Y. Ou, and L. Mandel. "Measurement of subpicosecond time intervals between two photons by interference". In: *Phys. Rev. Lett.* 59 (18 Nov. 1987), pp. 2044–2046. DOI: 10.1103/PhysRevLett.59.2044.

[83] P.-A. Huynh, F. Portier, H. le Sueur, G. Faini, U. Gennser, D. Mailly, F. Pierre, W. Wegscheider, and P. Roche. "Quantum Coherence Engineering in the Integer Quantum Hall Regime". In: *Phys. Rev. Lett.* 108 (25 June 2012), p. 256802. DOI: 10.1103/PhysRevLett.108.256802.

[84] G.-L. Ingold and Y. V. Nazarov. "Charge Tunneling Rates in Ultrasmall Junctions". In: *Single Charge Tunneling: Coulomb Blockade Phenomena In Nanostructures*. Ed. by H. Grabert and M. H. Devoret. Boston, MA: Springer US, 1992, pp. 21–107. DOI: 10.1007/978-1-4757-2166-9_2.

[85] A. Inhofer and D. Bercioux. "Proposal for an on-demand source of polarized electrons into the edges of a topological insulator". In: *Phys. Rev. B* 88 (23 Dec. 2013), p. 235412. DOI: 10.1103/PhysRevB.88.235412.

[86] R. Ionicioiu, G. Amaratunga, and F. Udrea. "Quantum Computation with Ballistic Electrons". In: *International Journal of Modern Physics B* 15.02 (2001), pp. 125–133. DOI: 10.1142/S0217979201003521.

[87] J. Jain. *Composite Fermions*. Cambridge University Press, 2007.

[88] Y. Ji, Y. Chung, D. Sprinzak, M. Heiblum, D. Mahalu, and H. Shtrikman. "An electronic Mach–Zehnder interferometer". In: *Nature* 422 (Mar. 2003), pp. 415–418. DOI: 10.1038/nature01503.

[89] E. Joos and H. D. Zeh. "The emergence of classical properties through interaction with the environment". In: *Zeitschrift für Physik B Condensed Matter* 59.2 (June 1985), pp. 223–243. DOI: 10.1007/BF01725541.

[90] T. Jullien, P. Roulleau, B. Roche, A. Cavanna, Y. Jin, and D. C. Glattli. "Quantum tomography of an electron". In: *Nature* 514 (Oct. 2014), pp. 603–607. DOI: 10.1038/nature13821.

[91] H. Kamata, T. Ota, K. Muraki, and T. Fujisawa. "Voltage-controlled group velocity of edge magnetoplasmon in the quantum Hall regime". In: *Phys. Rev. B* 81 (8 Feb. 2010), p. 085329. DOI: 10.1103/PhysRevB.81.085329.

[92] B. E. Kane. "A silicon-based nuclear spin quantum computer". In: *Nature* 393 (May 1998). Article, pp. 133–137. DOI: 10.1038/30156.

[93] J. Keeling, I. Klich, and L. S. Levitov. "Minimal Excitation States of Electrons in One-Dimensional Wires". In: *Phys. Rev. Lett.* 97 (11 Sept. 2006), p. 116403. DOI: 10.1103/PhysRevLett.97.116403.

[94] A. Kitaev. “Fault-tolerant quantum computation by anyons”. In: *Annals of Physics* 303.1 (2003), pp. 2–30. DOI: https://doi.org/10.1016/S0003-4916(02)00018-0.

[95] I. Klich and L. Levitov. “Quantum Noise as an Entanglement Meter”. In: *Phys. Rev. Lett.* 102 (10 Mar. 2009), p. 100502. DOI: 10.1103/PhysRevLett.102.100502.

[96] K. von Klitzing, G. Dorda, and M. Pepper. “New Method for High-Accuracy Determination of the Fine-Structure Constant Based on Quantized Hall Resistance”. In: *Phys. Rev. Lett.* 45 (6 Aug. 1980), pp. 494–497. DOI: 10.1103/PhysRevLett.45.494.

[97] N. Kumada, H. Kamata, and T. Fujisawa. “Edge magnetoplasmon transport in gated and ungated quantum Hall systems”. In: *Phys. Rev. B* 84 (4 July 2011), p. 045314. DOI: 10.1103/PhysRevB.84.045314.

[98] N. Kumada, P. Roulleau, B. Roche, M. Hashisaka, H. Hibino, I. Petkovi ć, and D. C. Glattli. “Resonant Edge Magnetoplasmons and Their Decay in Graphene”. In: *Phys. Rev. Lett.* 113 (26 Dec. 2014), p. 266601. DOI: 10.1103/PhysRevLett.113.266601.

[99] L. Landau. “The theory of a Fermi liquid”. In: *Soviet Physics Jetp-Ussr* 3.6 (1957), pp. 920–925.

[100] R. B. Laughlin. “Anomalous Quantum Hall Effect: An Incompressible Quantum Fluid with Fractionally Charged Excitations”. In: *Phys. Rev. Lett.* 50 (18 May 1983), pp. 1395–1398. DOI: 10.1103/PhysRevLett.50.1395.

[101] M. Le Bellac. *Des phénomènes critiques aux champs de jauge*. Savoirs actuels. EDP Sciences, 1988.

[102] G.-H. Lee, K.-F. Huang, D. K. Efetov, D. S. Wei, S. Hart, T. Taniguchi, K. Watanabe, A. Yacoby, and P. Kim. “Inducing superconducting correlation in quantum Hall edge states”. In: *Nature Physics* 13 (Apr. 2017). Article, pp. 693–698. DOI: 10.1038/nphys4084.

[103] D. Leibfried, D. M. Meekhof, B. E. King, C. Monroe, W. M. Itano, and D. J. Wineland. “Experimental Determination of the Motional Quantum State of a Trapped Atom”. In: *Phys. Rev. Lett.* 77 (21 Nov. 1996), pp. 4281–4285. DOI: 10.1103/PhysRevLett.77.4281.

[104] L. S. Levitov, H. Lee, and G. B. Lesovik. "Electron counting statistics and coherent states of electric current". In: *Journal of Mathematical Physics* 37.10 (1996), pp. 4845–4866. DOI: 10.1063_1.531672.

[105] I. P. Levkivskyi and E. V. Sukhorukov. "Dephasing in the electronic Mach-Zehnder interferometer at filling factor $\nu = 2$". In: *Phys. Rev. B* 78 (4 July 2008), p. 045322. DOI: 10.1103/PhysRevB.78.045322.

[106] L. V. Litvin, H.-P. Tranitz, W. Wegscheider, and C. Strunk. "Decoherence and single electron charging in an electronic Mach-Zehnder interferometer". In: *Phys. Rev. B* 75 (3 Jan. 2007), p. 033315. DOI: 10.1103/PhysRevB.75.033315.

[107] J. M. Luttinger. "An Exactly Soluble Model of a Many-Fermion System". In: *Journal of Mathematical Physics* 4.9 (1963), pp. 1154–1162. DOI: 10.1063/1.1704046.

[108] A. Mahé, F. D. Parmentier, G. Fève, J.-M. Berroir, T. Kontos, A. Cavanna, B. Etienne, Y. Jin, D. C. Glattli, and B. Plaçais. "Subnanosecond Single Electron Source in the Time-Domain". In: *Journal of Low Temperature Physics* 153.5 (Dec. 2008), pp. 339–349. DOI: 10.1007/s10909-008-9839-x.

[109] I. Marcikic, H. de Riedmatten, W. Tittel, V. Scarani, H. Zbinden, and N. Gisin. "Time-bin entangled qubits for quantum communication created by femtosecond pulses". In: *Phys. Rev. A* 66 (6 Dec. 2002), p. 062308. DOI: 10.1103/PhysRevA.66.062308.

[110] I. Marcikic, H. de Riedmatten, W. Tittel, H. Zbinden, M. Legré, and N. Gisin. "Distribution of Time-Bin Entangled Qubits over 50 km of Optical Fiber". In: *Phys. Rev. Lett.* 93 (18 Oct. 2004), p. 180502. DOI: 10.1103/PhysRevLett.93.180502.

[111] A. Marguerite, E. Bocquillon, J.-M. Berroir, B. Plaçais, A. Cavanna, Y. Jin, P. Degiovanni, and G. Fève. "Two-particle interferometry in quantum Hall edge channels". In: *physica status solidi (b)* 254.3 (2017), p. 1600618. DOI: 10.1002/pssb.201600618.

[112] A. Marguerite. "Two-particle interferometry for quantum signal processing". PhD thesis. Université Pierre et Marie Curie - Paris VI, July 2017.

[113] D. C. Mattis and E. H. Lieb. “Exact Solution of a Many-Fermion System and Its Associated Boson Field”. In: *Journal of Mathematical Physics* 6.2 (1965), pp. 304–312. DOI: 10.1063/1.1704281.

[114] U. C. Mendes and C. Mora. “Cavity squeezing by a quantum conductor”. In: *New Journal of Physics* 17.11 (2015), p. 113014. DOI: 10.1088/1367-2630/17/11/113014.

[115] E. Montambaux G. et Akkermans. *Physique mésoscopique des électrons et des photons*. EDP Sciences, 2004.

[116] M. Moskalets. “First-order correlation function of a stream of single-electron wave packets”. In: *Phys. Rev. B* 91 (19 May 2015), p. 195431. DOI: 10.1103/PhysRevB.91.195431.

[117] M. Moskalets. “Two-electron state from the Floquet scattering matrix perspective”. In: *Phys. Rev. B* 89 (4 Jan. 2014), p. 045402. DOI: 10.1103/PhysRevB.89.045402.

[118] M. Moskalets, G. Haack, and M. Büttiker. “Single-electron source: Adiabatic versus nonadiabatic emission”. In: *Phys. Rev. B* 87 (12 Mar. 2013), p. 125429. DOI: 10.1103/PhysRevB.87.125429.

[119] M. Moskalets. *Scattering Matrix Approach to Non-stationary Quantum Transport*. Imperial College Press, 2012.

[120] S. Oberholzer, M. Henny, C. Strunk, C. Schönenberger, T. Heinzel, K. Ensslin, and M. Holland. “The Hanbury Brown and Twiss experiment with fermions”. In: *Physica E: Low-dimensional Systems and Nanostructures* 6.1 (2000), pp. 314–317. DOI: https://doi.org/10.1016/S1386-9477(99)00162-9.

[121] G.-H. Park, M. Kim, K. Watanabe, T. Taniguchi, and H.-J. Lee. “Propagation of superconducting coherence via chiral quantum-Hall edge channels”. In: *Scientific Reports* 7.1 (2017), p. 10953. DOI: 10.1038/s41598-017-11209-w.

[122] F. D. Parmentier, A. Mahé, A. Denis, J.-M. Berroir, D. C. Glattli, B. Plaçais, and G. Fève. “A high sensitivity ultralow temperature RF conductance and noise measurement setup”. In: *Review of Scientific Instruments* 82.1 (2011), p. 013904. DOI: 10.1063/1.3518945.

[123] F. Parmentier. “Short-time Hanbury-Brown and Twiss correlation of a single-electron beam in ballistic conductors”. PhD thesis. Université Pierre et Marie Curie - Paris VI, Nov. 2010.

[124] J. P. Paz, S. Habib, and W. H. Zurek. “Reduction of the wave packet: Preferred observable and decoherence time scale”. In: *Phys. Rev. D* 47 (2 Jan. 1993), pp. 488–501. DOI: 10.1103/PhysRevD.47.488.

[125] M. E. Peskin and D. V. Schroeder. *An Introduction to quantum field theory*. Reading, USA: Addison-Wesley, 1995.

[126] I. Petković, F. Williams, and D. Glattli. “Edge magnetoplasmons in graphene”. In: *J. Phys. D: Appl. Phys.* 47 (9 Feb. 2014), p. 094010. DOI: 10.1088/0022-3727/47/9/094010.

[127] R. de Picciotto, M. Reznikov, M. Heiblum, V. Umansky, G. Bunin, and D. Mahalu. “Direct observation of a fractional charge”. In: *Physica B: Condensed Matter* 249-251 (1998), pp. 395–400. DOI: https://doi.org/10.1016/S0921-4526(98)00139-2.

[128] A. Prêtre, H. Thomas, and M. Büttiker. “Dynamic admittance of mesoscopic conductors: Discrete-potential model”. In: *Phys. Rev. B* 54 (11 Sept. 1996), pp. 8130–8143. DOI: 10.1103/PhysRevB.54.8130.

[129] A. Rauschenbeutel, G. Nogues, S. Osnaghi, P. Bertet, M. Brune, J.-M. Raimond, and S. Haroche. “Step-by-Step Engineered Multiparticle Entanglement”. In: *Science* 288.5473 (2000), pp. 2024–2028. DOI: 10.1126/science.288.5473.2024.

[130] J. Rech, D. Ferraro, T. Jonckheere, L. Vannucci, M. Sassetti, and T. Martin. “Minimal Excitations in the Fractional Quantum Hall Regime”. In: *Phys. Rev. Lett.* 118 (7 Feb. 2017), p. 076801. DOI: 10.1103/PhysRevLett.118.076801.

[131] J.-G. Ren, P. Xu, H.-L. Yong, L. Zhang, S.-K. Liao, J. Yin, W.-Y. Liu, W.-Q. Cai, M. Yang, L. Li, K.-X. Yang, X. Han, Y.-Q. Yao, J. Li, H.-Y. Wu, S. Wan, L. Liu, D.-Q. Liu, Y.-W. Kuang, Z.-P. He, P. Shang, C. Guo, R.-H. Zheng, K. Tian, Z.-C. Zhu, N.-L. Liu, C.-Y. Lu, R. Shu, Y.-A. Chen, C.-Z. Peng, J.-Y. Wang, and J.-W. Pan. “Ground-to-satellite quantum teleportation”. In: *Nature* 549 (Aug. 2017), pp. 70–73. DOI: 10.1038/nature23675.

[132] M. Reznikov, R. de Picciotto, T. G. Griffiths, M. Heiblum, and V. Umansky. "Observation of quasiparticles with one-fifth of an electron's charge". In: *Nature* 399 (May 1999), pp. 238–241. DOI: 10.1038/20384.

[133] F. Ronetti, L. Vannucci, D. Ferraro, T. Jonckheere, J. Rech, T. Martin, and M. Sassetti. *Crystallization of Levitons in the fractional quantum Hall regime*. 2017. eprint: arXiv:1712.07094.

[134] P. Roulleau, F. Portier, P. Roche, A. Cavanna, G. Faini, U. Gennser, and D. Mailly. "Noise Dephasing in Edge States of the Integer Quantum Hall Regime". In: *Phys. Rev. Lett.* 101 (18 Oct. 2008), p. 186803. DOI: 10.1103/PhysRevLett.101.186803.

[135] P. Roulleau, F. Portier, P. Roche, A. Cavanna, G. Faini, U. Gennser, and D. Mailly. "Tuning Decoherence with a Voltage Probe". In: *Phys. Rev. Lett.* 102 (23 June 2009), p. 236802. DOI: 10.1103/PhysRevLett.102.236802.

[136] P. Roulleau. "Quantum coherence in the integer quantum Hall regime". Theses. Université Pierre et Marie Curie - Paris VI, Nov. 2008.

[137] P. Roulleau, F. Portier, P. Roche, A. Cavanna, G. Faini, U. Gennser, and D. Mailly. "Direct Measurement of the Coherence Length of Edge States in the Integer Quantum Hall Regime". In: *Phys. Rev. Lett.* 100 (12 Mar. 2008), p. 126802. DOI: 10.1103/PhysRevLett.100.126802.

[138] B. Roussel. "Autopsy of a quantum electrical current". PhD thesis. Université de Lyon, Dec. 2017.

[139] A. Roy and M. Devoret. "Introduction to parametric amplification of quantum signals with Josephson circuits". In: *Comptes Rendus Physique* 17.7 (2016). Quantum microwaves / Micro-ondes quantiques, pp. 740–755. DOI: https://doi.org/10.1016/j.crhy.2016.07.012.

[140] I. Safi. "A dynamic scattering approach for a gated interacting wire". In: *The European Physical Journal B - Condensed Matter and Complex Systems* 12.3 (Dec. 1999), pp. 451–455. DOI: 10.1007/s100510051026.

[141] L. Saminadayar, D. C. Glattli, Y. Jin, and B. Etienne. "Observation of the $e/3$ Fractionally Charged Laughlin Quasiparticle". In: *Phys. Rev. Lett.* 79 (13 Sept. 1997), pp. 2526–2529. DOI: 10.1103/PhysRevLett.79.2526.

[142] P. Samuelsson and M. Büttiker. "Quantum state tomography with quantum shot noise". In: *Phys. Rev. B* 73 (4 Jan. 2006), p. 041305. DOI: 10.1103/PhysRevB.73.041305.

[143] P. Samuelsson, E. V. Sukhorukov, and M. Büttiker. "Orbital Entanglement and Violation of Bell Inequalities in Mesoscopic Conductors". In: *Phys. Rev. Lett.* 91 (15 Oct. 2003), p. 157002. DOI: 10.1103/PhysRevLett.91.157002.

[144] P. Samuelsson, E. V. Sukhorukov, and M. Büttiker. "Two-Particle Aharonov-Bohm Effect and Entanglement in the Electronic Hanbury Brown and Twiss Setup". In: *Phys. Rev. Lett.* 92 (2 Jan. 2004), p. 026805. DOI: 10.1103/PhysRevLett.92.026805.

[145] C. Sayrin, I. Dotsenko, X. Zhou, B. Peaudecerf, T. Rybarczyk, S. Gleyzes, P. Rouchon, M. Mirrahimi, H. Amini, M. Brune, J.-M. Raimond, and S. Haroche. "Real-time quantum feedback prepares and stabilizes photon number states". In: *Nature* 477 (Sept. 2011), pp. 73–77. DOI: 10.1038/nature10376.

[146] R. Schuster, E. Buks, M. Heiblum, D. Mahalu, V. Umansky, and H. Shtrikman. "Phase measurement in a quantum dot via a double-slit interference experiment". In: *Nature* 385 (Jan. 1997), pp. 417–420. DOI: doi:10.1038/385417a0.

[147] Y. Sherkunov, N. d'Ambrumenil, P. Samuelsson, and M. Büttiker. "Optimal pumping of orbital entanglement with single-particle emitters". In: *Phys. Rev. B* 85 (8 Feb. 2012), p. 081108. DOI: 10.1103/PhysRevB.85.081108.

[148] P. W. Shor. "Algorithms for quantum computation: discrete logarithms and factoring". In: *Proceedings 35th Annual Symposium on Foundations of Computer Science*. Nov. 1994, pp. 124–134. DOI: 10.1109/SFCS.1994.365700.

[149] C. Smith, M. Pepper, H. Ahmed, J. Frost, D. Hasko, R. Newbury, D. Peacock, D. Ritchie, and G. Jones. "One dimensional electron tunneling and related phenomena". In: *Surface Science*

228.1 (1990), pp. 387–392. DOI: https://doi.org/10.1016/0039-6028(90)90334-5.

[150] I. Snyman and S. Florens. "Microscopic bosonization of band structures: x-ray processes beyond the Fermi edge". In: *New Journal of Physics* 19.11 (2017), p. 113031.

[151] J. Splettstoesser and R. J. Haug. "Single-electron control in solid state devices". In: *physica status solidi (b)* 254.3 (), p. 1770217. DOI: 10.1002/pssb.201770217.

[152] J. Splettstößer, M. Moskalets, and M. Büttiker. "Two-Particle Nonlocal Aharonov-Bohm Effect from Two Single-Particle Emitters". In: *Phys. Rev. Lett.* 103 (7 Aug. 2009), p. 076804. DOI: 10.1103/PhysRevLett.103.076804.

[153] M. Stone. *Bosonization*. WORLD SCIENTIFIC, 1994. DOI: 10.1142/2436. eprint: https://www.worldscientific.com/doi/pdf/10.1142/2436.

[154] H. L. Stormer. "Nobel Lecture: The fractional quantum Hall effect". In: *Rev. Mod. Phys.* 71 (4 July 1999), pp. 875–889. DOI: 10.1103/RevModPhys.71.875.

[155] H. le Sueur, C. Altimiras, U. Gennser, A. Cavanna, D. Mailly, and F. Pierre. "Energy Relaxation in the Integer Quantum Hall Regime". In: *Phys. Rev. Lett.* 105 (5 July 2010), p. 056803. DOI: 10.1103/PhysRevLett.105.056803.

[156] V. I. Talyanskii, J. M. Shilton, M. Pepper, C. G. Smith, C. J. B. Ford, E. H. Linfield, D. A. Ritchie, and G. A. C. Jones. "Single-electron transport in a one-dimensional channel by high-frequency surface acoustic waves". In: *Phys. Rev. B* 56 (23 Dec. 1997), pp. 15180–15184. DOI: 10.1103/PhysRevB.56.15180.

[157] S. Tewari, P. Roulleau, C. Grenier, F. Portier, A. Cavanna, U. Gennser, D. Mailly, and P. Roche. "Robust quantum coherence above the Fermi sea". In: *Phys. Rev. B* 93 (3 Jan. 2016), p. 035420. DOI: 10.1103/PhysRevB.93.035420.

[158] K. Thibault, J. Gabelli, C. Lupien, and B. Reulet. "Pauli-Heisenberg Oscillations in Electron Quantum Transport". In: *Phys. Rev. Lett.* 114 (23 June 2015), p. 236604. DOI: 10.1103/PhysRevLett.114.236604.

[159] E. Thibierge. “Cohérence à un et deux électrons en optique quantique électronique”. PhD thesis. École Normale Supérieure de lyon, June 2015.

[160] K. H. Thomas and C. Flindt. “Entanglement entropy in dynamic quantum-coherent conductors”. In: *Phys. Rev. B* 91 (12 Mar. 2015), p. 125406. DOI: 10.1103/PhysRevB.91.125406.

[161] T. J. Thornton, H. Ahmed, M. Pepper, D. Andrews, and G. J. Davies. “One-dimensional conduction in the 2D electron gas of a GaAs-AlGaAs heterojunction”. In: *Physical Review Letters* 56 (Mar. 1986), pp. 1198–1201. DOI: 10.1103/PhysRevLett.56.1198.

[162] S.-i. Tomonaga. “Remarks on Bloch’s Method of Sound Waves applied to Many-Fermion Problems”. In: *Progress of Theoretical Physics* 5.4 (1950), pp. 544–569. DOI: 10.1143/ptp/5.4.544.

[163] D. Tong. *The Quantum Hall effect*. Lectures at Cambridge University. 2016.

[164] D. C. Tsui, H. L. Stormer, and A. C. Gossard. “Two-Dimensional Magnetotransport in the Extreme Quantum Limit”. In: *Phys. Rev. Lett.* 48 (22 May 1982), pp. 1559–1562. DOI: 10.1103/PhysRevLett.48.1559.

[165] G. Vallone, D. Bacco, D. Dequal, S. Gaiarin, V. Luceri, G. Bianco, and P. Villoresi. “Experimental Satellite Quantum Communications”. In: *Phys. Rev. Lett.* 115 (4 July 2015), p. 040502. DOI: 10.1103/PhysRevLett.115.040502.

[166] M. Vanević, Y. V. Nazarov, and W. Belzig. “Electron and electron–hole excitations in a driven Fermi sea”. In: *physica status solidi (b)* 254.3 (2017), p. 1600551. DOI: 10.1002/pssb.201600551.

[167] L. Vannucci, F. Ronetti, D. Ferraro, J. Rech, T. Jonckheere, T. Martin, and M. Sassetti. “Photoassisted shot noise spectroscopy at fractional filling factor”. In: *Journal of Physics: Conference Series* 969.1 (2018), p. 012143. DOI: 10.1088/1742-6596/969/1/012143.

[168] L. Vannucci, F. Ronetti, J. Rech, D. Ferraro, T. Jonckheere, T. Martin, and M. Sassetti. “Minimal excitation states for heat transport in driven quantum Hall systems”. In: *Phys. Rev. B* 95 (24 June 2017), p. 245415. DOI: 10.1103/PhysRevB.95.245415.

[169] J. Ville. “Théorie et applications de la notion de signal analytique”. In: *Cables et Transmission* 1 (1948), pp. 61–74.

[170] V. Volkov and S. Mikhailov. “Edge magnetoplasmons: low frequency weakly damped excitations in inhomogeneous two-dimensional electron systems”. In: *Sov. Phys. JETP* 67 (1988), p. 1639.

[171] C. Wahl, J. Rech, T. Jonckheere, and T. Martin. “Interactions and Charge Fractionalization in an Electronic Hong-Ou-Mandel Interferometer”. In: *Phys. Rev. Lett.* 112 (4 Jan. 2014), p. 046802. DOI: 10.1103/PhysRevLett.112.046802.

[172] B. J. van Wees, H. van Houten, C. W. J. Beenakker, J. G. Williamson, L. P. Kouwenhoven, D. van der Marel, and C. T. Foxon. “Quantized conductance of point contacts in a two-dimensional electron gas”. In: *Phys. Rev. Lett.* 60 (9 Feb. 1988), pp. 848–850. DOI: 10.1103/PhysRevLett.60.848.

[173] B. J. van Wees, L. P. Kouwenhoven, E. M. M. Willems, C. J. P. M. Harmans, J. E. Mooij, H. van Houten, C. W. J. Beenakker, J. G. Williamson, and C. T. Foxon. “Quantum ballistic and adiabatic electron transport studied with quantum point contacts”. In: *Phys. Rev. B* 43 (15 May 1991), pp. 12431–12453. DOI: 10.1103/PhysRevB.43.12431.

[174] D. S. Wei, T. van der Sar, J. D. Sanchez-Yamagishi, K. Watanabe, T. Taniguchi, P. Jarillo-Herrero, B. I. Halperin, and A. Yacoby. “Mach-Zehnder interferometry using spin- and valley-polarized quantum Hall edge states in graphene”. In: *Science Advances* 3.8 (2017). DOI: 10.1126/sciadv.1700600.

[175] J. Weis and K. von Klitzing. “Metrology and microscopic picture of the integer quantum Hall effect”. In: *Philosophical Transactions of the Royal Society of London A: Mathematical, Physical and Engineering Sciences* 369.1953 (2011), pp. 3954–3974. DOI: 10.1098/rsta.2011.0198.

[176] V. Weisskopf and E. Wigner. “Berechnung der natürlichen Linienbreite auf Grund der Diracschen Lichttheorie”. In: *Zeitschrift für Physik* 63.1 (Jan. 1930), pp. 54–73. DOI: 10.1007/BF01336768.

[177] X. G. Wen. “Chiral Luttinger liquid and the edge excitations in the fractional quantum Hall states”. In: *Phys. Rev. B* 41 (18 June 1990), pp. 12838–12844. DOI: 10.1103/PhysRevB.41.12838.

[178] G. Wendin. “Quantum information processing with superconducting circuits: a review”. In: *Reports on Progress in Physics* 80.10 (2017), p. 106001.

[179] D. A. Wharam, T. J. Thornton, R. Newbury, M. Pepper, H. Ahmed, J. E. F. Frost, D. G. Hasko, D. C. Peacock, D. A. Ritchie, and G. A. C. Jones. “One-dimensional transport and the quantisation of the ballistic resistance”. In: *Journal of Physics C: Solid State Physics* 21.8 (1988), p. L209.

[180] G. C. Wick. “The Evaluation of the Collision Matrix”. In: *Phys. Rev.* 80 (2 Oct. 1950), pp. 268–272. DOI: 10.1103/PhysRev.80.268.

[181] G. C. Wick, A. S. Wightman, and E. P. Wigner. “The Intrinsic Parity of Elementary Particles”. In: *Phys. Rev.* 88 (1 Oct. 1952), pp. 101–105. DOI: 10.1103/PhysRev.88.101.

[182] E. Wigner. “On the Quantum Correction For Thermodynamic Equilibrium”. In: *Phys. Rev.* 40 (5 June 1932), pp. 749–759. DOI: 10.1103/PhysRev.40.749.

[183] E. Wolf. *Introduction to the Theory of Coherence and Polarization of Light*. Cambridge University Press, 2007.

[184] T. Zibold, P. Vogl, and A. Bertoni. “Theory of semiconductor quantum-wire-based single- and two-qubit gates”. In: *Phys. Rev. B* 76 (19 Nov. 2007), p. 195301. DOI: 10.1103/PhysRevB.76.195301.

[185] W. H. Zurek. “Environment-induced superselection rules”. In: *Phys. Rev. D* 26 (8 Oct. 1982), pp. 1862–1880. DOI: 10.1103/PhysRevD.26.1862.

[186] W. H. Zurek, S. Habib, and J. P. Paz. “Coherent states via decoherence”. In: *Phys. Rev. Lett.* 70 (9 Mar. 1993), pp. 1187–1190. DOI: 10.1103/PhysRevLett.70.1187.

[187] W. H. Zurek. “Decoherence, einselection, and the quantum origins of the classical”. In: *Rev. Mod. Phys.* 75 (3 May 2003), pp. 715–775. DOI: 10.1103/RevModPhys.75.715.

Own publications

[OP1] C. Cabart, B. Roussel, G. Fève, and P. Degiovanni. "Taming electronic decoherence in 1D chiral ballistic quantum conductors". In: *Submitted to Phys. Rev. B.* (2018). eprint: arXiv:180404054.

[OP2] D. Ferraro, B. Roussel, C. Cabart, E. Thibierge, G. Fève, C. Grenier, and P. Degiovanni. "Real-Time Decoherence of Landau and Levitov Quasiparticles in Quantum Hall Edge Channels". In: *Phys. Rev. Lett.* 113 (16 Oct. 2014), p. 166403. DOI: 10.1103/PhysRevLett.113.166403.

[OP3] A. Marguerite, C. Cabart, C. Wahl, B. Roussel, V. Freulon, D. Ferraro, C. Grenier, J.-M. Berroir, B. Plaçais, T. Jonckheere, J. Rech, T. Martin, P. Degiovanni, A. Cavanna, Y. Jin, and G. Fève. "Decoherence and relaxation of a single electron in a one-dimensional conductor". In: *Phys. Rev. B* 94 (11 Sept. 2016), p. 115311. DOI: 10.1103/PhysRevB.94.115311.

[OP4] A. Marguerite, B. Roussel, R. Bisognin, C. Cabart, M. Kumar, J.-M. Berroir, E. Bocquillon, B. Plaçais, A. Cavanna, U. Gennser, Y. Jin, P. Degiovanni, and G. Fève. "Extracting single electron wavefunctions from a quantum electrical current". In: *Submitted to Phys. Rev. Lett.* (2017). eprint: arXiv:1710.11181.

[OP5] B. Roussel, C. Cabart, G. Fève, E. Thibierge, and P. Degiovanni. "Electron quantum optics as quantum signal processing". In: *physica status solidi (b)* 254.3 (2017). 1600621, p. 1600621. DOI: 10.1002/pssb.201600621.

[OP6] É. Thibierge, D. Ferraro, B. Roussel, C. Cabart, A. Marguerite, G. Fève, and P. Degiovanni. "Two-electron coherence and its

measurement in electron quantum optics". In: *Phys. Rev. B* 93 (8 Feb. 2016), p. 081302. DOI: 10.1103/PhysRevB.93.081302.

Summary

Over the last few years, extensive experimental efforts have been devoted to the development of quantum nanoelectronics tools aiming at controlling electronic transport down to the single electron level. These advances led to a paradigm shift in the domain of coherent electronic transport, giving birth to electron quantum optics, which is the domain of this work.

This manuscript is devoted to two problems. The first of these is the one of Coulomb interactions between electrons, which lead to a decoherence phenomenon that must be characterized and predicted in order to be controlled. Using an analytical and numerical approach, it became possible to predict the effect of interactions on an experimentally relevant system, a prediction that was then confirmed in the experiment. After this result, this manuscript displays some ideas aiming at controlling interactions and proposes some ways to test them experimentally.

In this work, I also took on the problem of characterizing complex quantum states. In particular, following the experimental demonstration of a tomography protocol for first order coherences, I tried to extend this protocol to more complex states that could exhibit two-electron coherences, or more. These states being also sensitive to Coulomb interactions, an extension of the tools used to treat interactions to this multi-electronic state is also presented in this work.

Keywords: electron quantum optics, quantum coherence, electronic interferences, Coulomb interaction

Résumé

Ces dernières années, de considérables efforts expérimentaux ont été dévoués au développement d'outils de nanoélectronique quantique, dans le but d'atteindre un niveau de contrôle sur le transport électronique quantique à l'échelle de l'électron unique. Ces avancées ont poussé à un changement de paradigme dans le domaine du transport électronique cohérent et donné naissance à l'optique quantique électronique, domaine dans lequel cette thèse s'inscrit.

Cette thèse est consacrée à deux problématiques. Tout d'abord, elle s'intéresse au problème des interactions Coulombiennes entre électrons, qui donnent lieu à un phénomène de décohérence qu'il est nécessaire de caractériser et de prédire au mieux afin de le contrôler. En utilisant une approche analytique et numérique, il a été possible de prédire l'effet de ces interactions sur un système expérimentalement accessible, prédiction qui a ensuite été confirmée par l'expérience. Dans la foulée de ce résultat, cette thèse présente des possibilités de contrôle de ces interactions, et propose un moyen de les mettre en œuvre qui devrait pouvoir être testé dans une expérience.

Je me suis également confronté à la problématique de la caractérisation d'états quantiques complexes. En particulier, suite à la démonstration expérimentale d'un protocole de tomographie pour des états mono-électroniques, je me suis tourné vers l'extension de ce protocole à des états plus complexes, pouvant exhiber des propriétés de cohérence à deux électrons, voire plus. Ces états étant également sensibles aux interactions de Coulomb, une extension au cas multi-électronique des outils utilisés pour traiter ces interactions est proposée dans cette thèse.

Mots-clés: optique quantique électronique, cohérence quantique, interférences électroniques, interaction Coulombienne